Cost-effective design and operation of variable speed wind turbines

Closing the gap between the control engineering and the wind engineering community

Cost-effective design and operation
of variable speed wind turbines

Closing the gap between the control engineering and the wind
engineering community

Proefschrift

ter verkrijging van de graad van doctor
aan de Technische Universiteit Delft,
op gezag van de Rector Magnificus prof. dr. ir. J.T. Fokkema
voorzitter van het College voor Promoties,
in het openbaar te verdedigen op dinsdag 18 februari 2003 om 16.00 uur
door

David-Pieter MOLENAAR

werktuigkundig ingenieur
geboren te Middelie

Dit proefschrift is goedgekeurd door de promotor:
Prof. ir. O.H. Bosgra

Samenstelling promotiecommissie:

Rector Magnificus	voorzitter
Prof. ir. O.H. Bosgra	Technische Universiteit Delft, promotor
Dr. Sj. Dijkstra	Technische Universiteit Delft, toegevoegd promotor
Prof. dr. ir. G.A.M. van Kuik	Technische Universiteit Delft
Dr. ir. M.J. Hoeijmakers	Technische Universiteit Delft
Prof. dr. ir. D.J. Rixen	Technische Universiteit Delft
Prof. dr. ir. Th. van Holten	Technische Universiteit Delft
Prof. dr. ir. M. Steinbuch	Technische Universiteit Eindhoven

Printed in The Netherlands

For free
and still too
expensive

"Er is geen gunstige wind voor hen
die niet weten waar ze heen gaan"

Willem I, Prins van Oranje
(1533-1584)

Voorwoord

Promoveren? Daaf gaat promoveren? Deze reactie kreeg ik 6 jaar geleden vlak na mijn afstuderen te horen. Ik moest zelf ook even aan het idee wennen, maar de uitdaging om uit te zoeken of de stelling "windenergie: gratis en toch duur" ontkrachtigd kon worden sprak mij zeer aan. De vrijheid (en dus de mogelijkheden) bij de sectie Systeem en Regeltechniek om dit doel te bereiken was voor mij de belangrijkste reden om voor de Technische Universiteit Delft en niet voor het ECN in Petten of Stork Product Engineering in Amsterdam te kiezen.

Ik behoor tot de groep promovendi die puur voor het onderwerp gekozen heeft. Windenergie intrigeerde me eigenlijk als kind al. Mijn vader wilde een windmolen in de tuin zetten om elektriciteit op te wekken en dat vond ik zeer interessant. Helaas is dàt er nooit van gekomen, hoewel hij er onlangs weer over begon...

Onderzoek doen is leuk (zeker naar windenergie gezien het brede en maatschappelijke karakter van het onderwerp). Maar helaas, het werk zit erop en dus is het moment gekomen een aantal mensen te bedanken voor hun positieve bijdrage op het verloop van mijn onderzoek. Van deze groep wil ik de volgende personen graag met naam noemen.

Allereerst wil ik Maarten Steinbuch bedanken voor het feit dat hij mij het laatste zetje gegeven heeft. Maarten, ik heb er geen moment spijt van gehad! Natuurlijk was dit project nooit tot stand gekomen als Okko Bosgra mij niet de gelegenheid had gegeven de traditie op de sectie voort te zetten. Speciale dank gaat ook uit naar Gregor van Baars voor het beschikbaar stellen van zijn vrije tijd om de overgang van student naar promovendus te versoepelen.

Verder wil ik de sectie bedanken voor de stimulerende werkomgeving. In het bijzonder Sjoerd Dijkstra voor de morele en politieke ondersteuning en Peter Valk voor de soft- en hardware ondersteuning. De "woensdag-after-lunch" presentaties met de bijbehorende discussies evenals de (soms onzinnige) bijdragen tijdens de lunch heb ik zeer gewaardeerd. Hans, Dick, Joost, Judi, Marco, Edwin, Thomas, Sjirk, Rob, A3, Martijn, Branko, Gideon, Eduard, Camile, Les, Jogchem, Leon, Dennis, Alex, Maria, Maria M., Els, Jacqueline, Marjolein, Debby, Agnes, "kroketten" Cor, Frits, Ton, Guus, John, Ad, Carsten, Peter H. en Paul: bedankt. Daarnaast hebben sommige afstudeerders op mij een onvergetelijke indruk achter gelaten. Martin, Jurjen,

Mario en Mark, ook al staan niet al jullie resultaten vermeld in dit proefschrift, toch bedankt voor jullie (inhoudelijke) bijdragen.

Tijdens mijn promotie heeft een aantal mensen een essentiële bijdrage geleverd aan de experimenten uitgevoerd op de Lagerwey LW-50/750 windturbine. André Pubanz, Martin Hoeijmakers, John Vervelde, Bert Bosman, Jan Lucas, Cees van Everdinck, Rob Tousain, Koert de Kok, Robert Verschuren en Berit van Hulst: bedankt voor jullie inzet en vooral geduld. Zonder jullie zou dit proefschrift minstens de helft dunner en lang niet zo waardevol zijn. Daarnaast wil ik Bart Roorda en Henk Heerkes bedanken voor het beschikbaar stellen van respectievelijk de Polymarin en AERPAC rotorblad gegevens. Tevens wil ik Hans van Leeuwen, Gerben de Winkel, Don van Delft, Arno van Wingerde en Peter Joosse bedanken voor het beschikbaar stellen van de modale testresultaten van diverse rotorbladen en hun assistentie bij het analyseren van de data.

Vervolgens wil ik Sylvia bedanken voor de altijd gezellige ontvangst op de 6de. Hans en Jan bedankt voor jullie enthousiasme, kritische houding, samenwerking en gezelligheid. Ik hoop dat al onze plannen uitkomen en dat in navolging van jullie meer DUWIND-ianen de Mekelweg over durven te steken.

Ik wil Richard Luijendijk (Siemens Nederland N.V.) bedanken voor het feit dat hij mij de mogelijkheid heeft geboden de wind (tijdelijk) vanuit een andere positie te bekijken. In de periode dat ik bij Siemens aan het NSWP (North Sea Wind Power) project gewerkt heb, heb ik veel van jou en onze samenwerking geleerd. Daarnaast heb ik de bevestiging gekregen dat dit proefschrift een belangrijke bijdrage kan leveren in het verbeteren van de concurrentiepositie van windenergie.

Monique: super dat je de omslag van mijn proefschrift hebt willen vormgeven. Ik hoop dat de vormgeving de dikte een beetje compenseert.

Mijn ouders, "Pap en Mam", hartstikke bedankt voor alle goede zorgen. Zonder jullie steun had ik dit nooit kunnen doen. Wat ik het meest in jullie bewonder is dat jullie zowel Dirk-Jacob als mij de ruimte en kans hebben gegeven dingen te doen die jullie vroeger door de andere omstandigheden nooit hebben kunnen doen.

Tenslotte wil ik mijn vriendin Nannila bedanken. Niet alleen voor de liefde en steun tijdens mijn promotie, maar ook voor het af en toe dichtgooien van mijn laptop.

Zo, nu is het weer tijd voor een goed boek,

David-Pieter "Daaf" Molenaar
Delft, 1 december 2002.

Note to the reader

Consciousness is raising in the wind engineering community that control design should be an integral part of the complete wind turbine design. Obviously, the dynamics of a controller interact with the dynamics of the wind turbine and so have implications for, among other things, the energy production, fatigue life and the wind turbine configuration. In an ideal situation the wind turbine components (including controller) should be designed taking into account their behavior in the complete wind turbine. This will lead to an integrated and optimal wind turbine design as well as optimal operation. It must be emphasized that designing a controller afterwards (*i.e.* after the turbine has already been constructed) is certainly not cost-effective.

I have tried to make the contents of this thesis to be digestible for readers living in both the control system community and the wind engineering community in an attempt to reduce the significant gap that exists between the two communities. This lack of fruitful multidisciplinary interaction obviously limits the technological improvements required to achieve economic viability of the use of wind power.

Contents

x

Chapter 1

Introduction

In the 1970s the concern about the limited fossil fuel resources and their impact on the environment awakened. Due to this growing concern, interest revived in using renewable energy sources in order to meet the constantly rising world electricity demand. In addition, the oil crises of 1973 and 1979 led to the awareness that the amount of energy import should be decreased so as to become less dependent of oil exporting countries. The Gulf-war (1990-1991) confirmed this concern. One way to use renewable energy sources is to generate electricity using wind turbines.

1.1 Motivation and background

The wind is a vast, worldwide renewable source of energy. Since ancient times, mankind has harnessed the power of the wind. The earliest known use of wind power is the sailboat. Wind energy propelled boats sailed up the Nile against the current as early as 5000 B.C. By 1000 A.D. the Vikings had explored and conquered the North Atlantic. The wind was also the driving force behind the voyages of discovery of the Verenigde Oost-Indische Compagnie (VOC) between 1602 and 1799. Windmills have been providing useful mechanical power for at least the last thousand years, while wind turbines generate electricity since 1888.

1.1.1 History: from windmill to wind turbine

The historic development of using wind as a source of power shows an evolution from simple drag-type vertical-axis windmills generating mechanical power for local use, via stand-alone wind turbines designed for battery charging and single grid-connected wind turbines producing AC power using aerodynamic lift, to wind farms supplying electricity to the utility grid for distribution to the consumers. In this subsection we shall briefly review this transition from windmills to wind turbines. The next subsection presents an outlook on the future of wind power. Finally, the required improvements in both wind turbine design and operation to achieve and maintain cost-effective wind turbines are discussed.

1000 A.D. - 1180 A.D.

The first windmills were developed to automate the tasks of grain-grinding and water-pumping. Although the Chinese reportedly invented the windmill, the earliest-documented design is the vertical-axis windmill used in the region Sīstān in eastern Persia for grinding grain and hulling rice in the tenth century A.D. [279]. One of the most important climatic features of this extensive border region of present day Afghanistan and Iran is a northerly wind that blows unceasingly during the summer months of June to September at velocities ranging between 27 and 47 meters per second. This wind is locally referred to as "the wind of 120 days".

The Persian windmills were usually laid out in a single line that was built at the top of a mountain, hill or tower with high walls separating them as illustrated in Fig. 1.1 [321]. The famous example near the town of Neh had one line of 75 windmills. The lines were oriented perpendicular to the prevailing wind direction. Each individual windmill consisted of a two-storey structure made of sun-dried bricks. The upper part of the structure contained the millstones (about 2 m in diameter), while the lower part contained a vertical spindle (or wind-wheel) which was fitted with between six and twelve radial arms as illustrated in Fig. 1.2. Each of these arms was covered with fabric that is allowed to bulge in order to catch the wind. In the walls of the lower part containing the wind-wheel were apertures being aligned with the primary wind direction. As a consequence, this kind of windmill can only work in a region where there is a steady prevailing wind. The apertures were wider on the outside than on the inside, forcing the wind to increase its velocity as it enters the wheel-house and rotate the wind-wheel, which then directly drives the millstones. In addition, a series of shutters were used (presumably on the outside of the structure) to admit or shut out the wind, and thereby regulate the rotational speed.
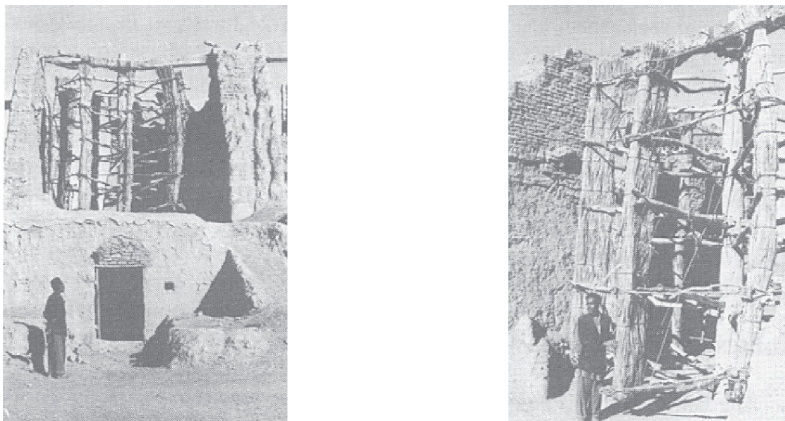
Figure 1.1: *Left photograph: Downwind view of a vertical-axis windmill of the Persian type in the town of Neh. Right photograph: Close-up view of the working surface made of bundles of reed [321]. Reprinted by permission of The MIT Press.*
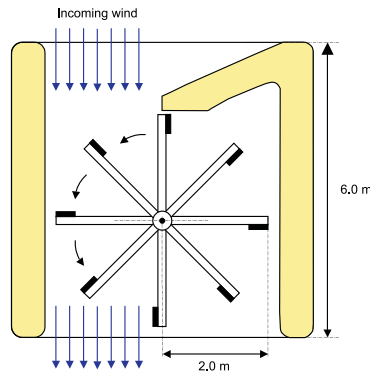
Figure 1.2: *Cross-section of the wind-wheel of a Persian windmill showing the apertures being aligned with the primary wind direction.*

Vertical-axis windmills of this basic design were still operating in Iran in 1977 (and may be still used today) [105]. This means that the basic design has lasted at least 1000 years, although a major change has taken place: the millstones have been placed below the rotor as already shown in Fig. 1.1. The advantage of having the sails above the millstones was that the working surface could be substantially enlarged. Another noticeable change is the use of bundles of reeds instead of fabric to provide the working surface. It must be noted that the Persian windmill never came into use in Northwest Europe.

1180 A.D. - 1888 A.D.

The history of the Western windmill begins with the first documented appearance of the European or "Dutch" windmill in Normandy, France in the year 1180 [80]. The "Dutch" windmill had four sails and was of the horizontal-axis configuration. Wooden cog-and-ring gears were used to translate the motion of the horizontal-axis to a vertical movement to turn a grindstone. The reason for the sudden evolution from the vertical-axis Persian design is unknown, but the fact that European water wheels also had a horizontal-axis configuration – and apparently served as the technological model for the early windmills – may provide part of the answer. Another reason may have been the higher structural efficiency of drag-type horizontal machines over drag-type vertical machines. In addition, the omnidirectional wind, as opposed to the Sīstān environment, may have called for an adaptation to suit the conditions.

Windmills spread rapidly throughout Europe in the thirteenth century. In a relatively short time, tens of thousands were in use for a variety of duties. The applications ranged from grinding grain, shredding tobacco, sawing timber, processing spices and paint pigments, milling flax, pressing oil or pumping water for polder drainage. The performance increased greatly between the twelfth and nineteenth

century with the introduction of metal parts. A primary improvement of the European windmills was their designer's use of sails that generated aerodynamic lift. This feature provided improved rotor efficiency compared with the Persian mills by allowing an increase in rotor speed, which also allowed for superior grinding as well as pumping action.

The lower cost of wind power to water power and the fact that more sites were available for windmills than there were for water mills caused an increase in the use of windmills. In The Netherlands, this growth contributed to the country's golden age (from 1590 till about 1670). As late as 1850, 90 % of the power used in Dutch industry came from the wind. Steam supplied the rest. Industrialization, first in Europe and later in America, led to a gradual decline in the use of windmills. The steam engine took over the tasks previously performed by windmills.

In 1896, at the height of the industrial revolution, wind still pumped 41 % of the polders in The Netherlands. However, in 1904, wind provided only 11 % of Dutch industrial energy. These windmills had a rotor diameter and hub height of 25 m and 30 m respectively, and were capable of producing the equivalent of 25–50 kW in mechanical form. For comparison, modern wind turbines of the same size are capable of extracting ten times more power from the wind [80]. As steam power developed, the uncertain power of the wind became less and less economic (in particular after cheap coal came available), and we are left today with a tiny fraction of the elegant structures that once extracted power from the wind. These remaining windmills, scattered throughout the world, are a historic, and certainly very photogenic, reminder of a past technological age.

1888 A.D. - 1973 A.D.

The first wind turbine to harness the wind for the generation of electricity was built by Charles F. Brush in Cleveland, Ohio, USA in 1888. The so-called "Brush" windmill was featured with a 17-m diameter multi-blade rotor mounted on an 18-m high rectangular tower as illustrated in Fig. 1.3. The upwind rotor consisted of 144 thin wooden blades, and a large fantail to turn the rotor out of the wind. The turbine was equipped with a 12 kW direct-current generator, and a belt-and-pulley transmission with a step-up ratio of (50:1). The DC generator was located on the basement of the tower. The power output was used for charging storage batteries. Despite its relative success in operating for 20 years, the Brush windmill demonstrated the limitations of the low-speed, high-solidity rotor for the generation of electricity [279].

The next important step in the transition from windmills to wind turbines was taken by P. la Cour in 1891 in Askow, Denmark. He developed the first variable speed wind turbine that incorporated the aerodynamic design principles (low-solidity, four-bladed rotors incorporating primitive airfoil shapes and blade twist) used in the best Dutch windmills. The resulting higher speed of the La Cour rotor made this type of wind turbine quite practical for electricity generation.

By the late 1930s, the pioneering machines of Brush and La Cour had evolved into two- or three bladed horizontal-axis wind turbines with the rotor upwind of the tower and low solidity, using a tail vane to position the rotor at right angles with
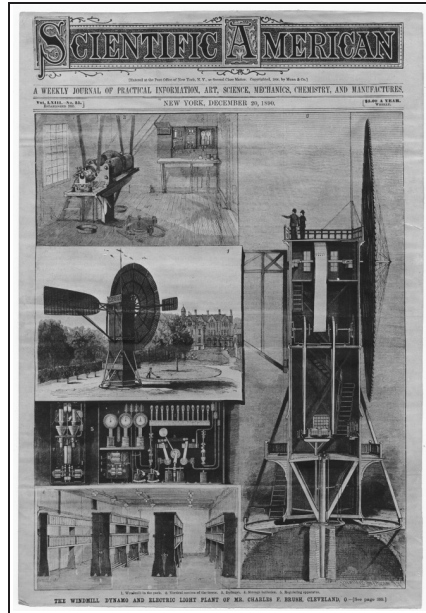
Figure 1.3: *"The windmill dynamo and electric light plant of Mr. Charles F. Brush",
Scientific American, December 20, 1890. Copy of an original in the Department of
Special Collections, Case Western Reserve University Library Cleveland, Ohio.*

the wind direction. The majority of these direct-current producing turbines were
operated at variable speed with fixed pitch angle rotor blades. The turbines were
generally reliable and long-lived machines giving reasonable maintenance. They did
not, however, have the cost-effectiveness and capacity to compete with conventional
power systems.

The majority of the wind turbines built before 1970 were small machines de-
signed for battery charging. The 1.25 MW Smith-Putnam wind turbine constituted
a notable exception. This constant speed turbine, built in 1941, had a two-bladed
rotor of 53.3-meter diameter mounted on a 33.5 m high truss tower. It featured
full-span active control of the blade pitch angle using a fly-ball governor, active yaw
control by means of a servomotor, and flapping hinges to reduce gyroscopic loads
on the rotor shaft. The turbine was erected on the top of a hill called "Grandpa's
Knob" near Rutland, Vermont, USA. It supplied AC power to the local grid for 695
hours from October 1941 till March 1945 when a blade failure due to fatigue disabled
the turbine [225] (in 1943 a bearing failed which could not be replaced for two years
due to the Second World War [80]).

During the period 1945–1970 new growth in wind turbine technology develop-
ment took place mainly in western Europe, but at a very modest pace [279]. By
1970, there was little or no activity world-wide for producing electricity using wind
turbines. The energy crisis of 1973 renewed interest in wind power from both govern-

mental and environmentalist sides. From an environmental point of view, generating electricity using wind turbines consumes no feedstock of fuel, emits no greenhouse gases (*e.g.* carbon dioxide, methane, nitrous oxide, or halocarbons), and creates almost no waste products. Although the aforementioned gases all contribute to global warming, carbon dioxide in itself accounts for 66-74 percent of the warming [317]. As a consequence of this, the market is highly dependent on the political situation and willingness to support wind power in return for a cleaner environment[1].

1973 A.D. - 2002 A.D.

During the years 1973–2002, the commercial wind turbine market evolved from small grid-connected machines in the 1 to 99 kilowatt size range for rural and remote use, via medium-scale turbines (100 to 999 kW) for remote community or industrial market use, to utility interconnected wind farms consisting of megawatt sized turbines. For the purpose of illustration, Fig. 1.4 shows the gradual increase in the average installed power size of cumulative installation in the period 1994–2001. Observe that the average installed power size of all wind turbines installed globally doubled in the period 1997-2001. The growth in installed power size is also reflected by the following figures: the average installed power size of all wind turbines installed globally by the end of 2001 is 445 kW, while the average installed power size of the turbines installed in 2001 is 915 kW [34].
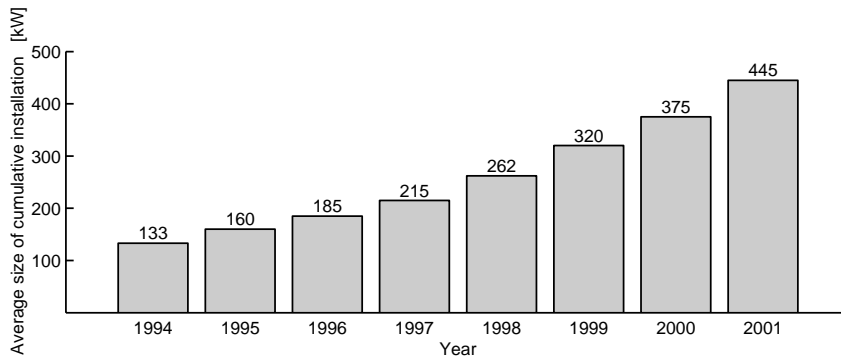
Figure 1.4: *Development of the average wind turbine installed power size of cumulative installation in the period 1994–2001 [34].*

The globally installed wind power capacity reached 24.93 GW by the end of 2001 as shown in Fig. 1.5 [34]. This is an average increase of over 28 % per year in the displayed period. Observe that the installed capacity has increased more than fourfold in the period 1996–2001, and that last year's growth was almost 36 %. This strong growth eclipses that of all other fuel sources: oil, natural gas, and nuclear power are growing at a rate of 1.9 % or less each year, while the coal consumption

---

[1]It must be noted that, at present, wind is still an environmental driven market, although common market aspects are finally beginning to play a more important role.

had an average annual growth rate of -0.6 % in the 1990s. In 1999, natural gas - the cleanest fossil fuel - has become the fuel of choice for power generation, replacing coal. Solar photovoltaics, which convert sunlight in electricity, had an annual average global growth of 17 % in the last decade, while hydropower, geothermal power, and biomass energy have experienced a steady growth over the same period ranging from 1 to 4 percent annually [317]. These figures not only indicate that wind energy is trending towards the preferred renewable electricity source, but also show that wind is the fastest growing energy source in the world.
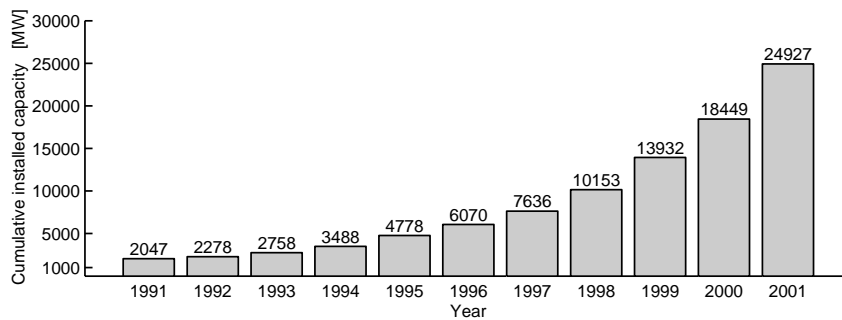
Figure 1.5: *Global installed cumulative wind power [33, 34].*

Most of the installed wind power capacity is located in Europe (*i.e.* 71.5 %), followed by the United States of America (18.4 %) and Asia (9.0 %). The global wind-generated electricity production in 2001 was about 50.3 TWh. Even though this figure looks impressive from a wind power point of view, wind power still only accounted for approximately 0.32 % of total electricity generation (partly due to the (also) constantly rising worldwide demand for electricity). The development of this share is depicted in Fig. 1.6 for the period 1996–2001 [34].
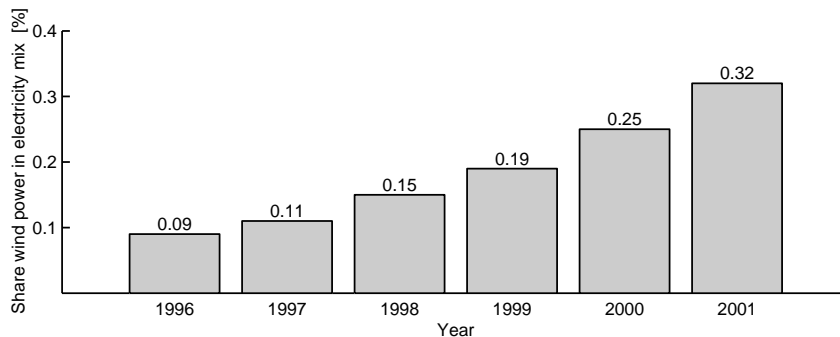
Figure 1.6: *The development of the share of wind power in the global electricity mix in the period 1996–2001. A capacity factor (see Definitions) of 0.23 is assumed [34].*

7

Over the last 20 years the cost of electricity from onshore wind power has dropped substantially: from 23-38 euro cents per kilowatt-hour in the early 1980s to 3-8 euro cents today for a mean wind speed of respective 10 and 5 m/s at hub height [203, 260]. But the price for conventional power plant generated electricity also declined [84]. The costs of wind power came down largely because of improved reliability. Advances in technology and learning curve made turbines cheaper to produce and far more reliable. At present, about 70 % of the cost per kWh comes from the capital cost of initial investment [172].

Despite the improved reliability and technical understanding even in the past few years a number of serious failures, such as broken blades, bearing damages and wear on gearbox teeth, occurred *see e.g.* [94, 146, 310, 311, 312]. The origin of these failures can be twofold: i) direct failures due to extreme loading, or ii) failures due to fatigue loads. It is now generally accepted that fatigue loads are the main cause of failure in the present onshore wind turbines [284]. In addition, it is also expected that fatigue will be the design driver when considering the combined wind and water wave loading acting on offshore wind turbines.

Obviously, premature field failures lead to a relatively high kilowatt-hour price due to increased maintenance cost, costly retrofits and, indirectly, increased design conservatism. At present, a realistic value for the operation and maintenance (O&M) cost lies between 0.44 and 0.87 euro cents per kilowatt-hour [34]. This implies that the O&M cost make up 6–29 % of the cost per kilowatt-hour. It should be noted that the O&M cost for offshore wind farms are even higher due to fact that the wind farms are exposed to a more aggressive and less known environment. In addition, safe access for maintenance is either very expensive or limited by a narrow weather window.

Nevertheless, onshore wind power is, at excellent wind sites, as competitive if not more competitive as the lowest cost traditional fuel, natural gas. In Fig. 1.7 the electricity generation cost of coal, natural gas, nuclear, and both onshore and offshore wind are compared. Observe that there is no single price that can be assigned to any source of generation. In particular, the kilowatt-hour price of nuclear power as well as onshore wind power span a wide range. The wide range of the latter can be easily explained by recognizing that the cost of wind power are critically dependent on site wind speeds since the power available in the wind is proportional to the cube of the mean wind velocity. The mean wind velocity, in turn, varies widely across a country because of obstacles (*e.g.* buildings, line of trees) to the wind, and varying surface roughness of the terrain. Therefore, it is expected that the move from onshore to offshore sites offers a very appealing opportunity for the future of wind power.

The aforementioned premature field failures have not only resulted in a relatively high price of electricity generated by wind turbines, but also in a public image of wind energy as being not very reliable. The public opinion is reflected in headlines like "Wind energy encounters head winds" [25], "Nobody wants a wind turbine" [31], "Benefit of wind turbines is negligible" [75], "Wind energy parasitizes on conventional power plants" [87] and "The wind war" [244].

From the preceding it can be concluded that in the past decades the wind industry has grown from a niche business serving the environmentally aware into one that has
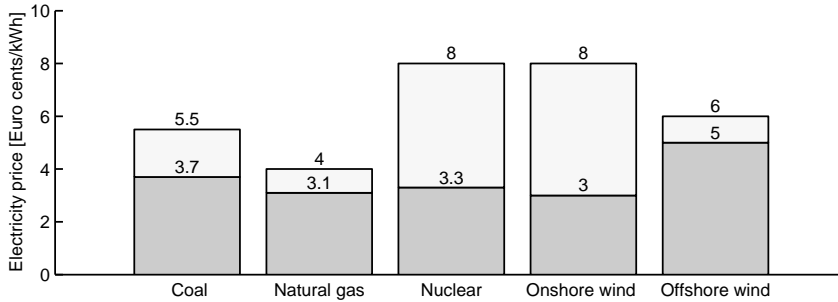
Figure 1.7: *Cost comparison of producing electricity: traditional fuel sources versus wind power [49]. Grey column: minimum cost, and white column: maximum cost in euro cents per kilowatt-hour.*

established itself as the most competitive form of renewable energy. Nonetheless, wind energy is not yet cost-effective, and consequently, the share of wind power in the global electricity mix is almost negligible. Furthermore, it should be stressed that establishing a reliable image is of paramount importance for successful penetration into the electricity market. This implies that development and deployment of new technology will be crucial to successful large-scale application of wind energy.

1.1.2 The future of wind power

The proliferation of wind turbines as a source of electricity in the future depends upon various economical, political, environmental, social and technical factors. The most important potential barriers for the large-scale development of both onshore and offshore wind energy are the relatively high kilowatt-hour price of wind-generated electricity, the public acceptance (especially in densely populated areas and coastal regions) and the impact on flora, fauna and landscape. On the other hand, the potential of wind power can be enhanced through an increase of the fossil-fuel prices, by means of fiscal instruments, and last but not least by technological advancements aiming at both cost reduction and performance increase.

Wind power has the technical potential to meet larger portions of the worlds electricity demand than it does now, but under current market conditions the economic potential is limited. It should be noted that the worldwide demand for electricity is expected to have an annual average growth rate of 3 % until 2020: 1.9 % for OECD (Organisation for Economic Co-operation and Development) countries, and significantly higher rates are predicted for non-OECD countries (5.4 % for China and 5.0 % in both India and East Asia) [114]. This means that the key to commercial success of wind power are further reductions of the kilowatt-hour price of wind-generated electricity. Although in the past two decades significant reductions enabling wind power commercialization at the best wind sites have already been achieved, additional improvements are still necessary since there are large areas around the world that only have moderately strong winds. This implies that any improvements that result in

economic generation of electricity from areas with slightly poorer wind resources than at the best sites will have a big impact on the future of wind power. It must be stressed that large-scale cost-effective application of wind energy implies also a need for a close co-operation of the investors and/or project developers with both public and environmental organizations. After all, the public acceptance increases with the higher level of information and economic participation.

At the current consumption rate, it is generally assumed that both oil and natural gas will become scarce within the next 50 years causing their kilowatt-hour price to rise substantially [84]. Although coal will not become scarce within this time scale, the cost of exploiting increasingly remote resources will make large-scale reliance on coal uneconomic with respect to wind power. The competitiveness of wind power will be further strengthened if the external cost associated with conventional power plant generated electricity are included in the market price and/or if the hidden subsidies to conventional sources will be removed.

Fiscal instruments like the REB (Regulerende Energiebelasting or "ecotax") can (temporarily) improve the competitive position of wind power by leveling the market playing field for sales of wind generated electricity. At present, in The Netherlands, electrical power obtained from renewable energy sources (so-called "groene stroom") is available for the consumers at a price comparable to conventionally generated electrical power [183]. However, uncertainties in the green power price within a project term due to uncertainties in future ecotax legislation will limit the project's financial viability. As a consequence, fiscal instruments may not necessarily improve the competitive position of wind energy.

Structural improvements in the economic viability of wind power can be achieved by not only improving the current wind turbine design and operation, but also by the development and deployment of new (non-wind turbine) technology. After all, widespread use of wind power will also require advances in the fields of information technology, energy storage systems, and control engineering to overcome the unpredictable character of wind. The main technological advancements that would improve the prospects of wind power are:

- The design of cost-effective, grid-connected wind turbines that are operating continuously at the best possible performance. Research and development needs to be continued in a number of areas to reach optimized wind turbine designs. The most important areas are:

    - Scaling-up the present wind turbine size to the multi-megawatt class

    - Integrated design aiming at, for example, reduction of mass

    - Implementation of advanced control systems exploiting the advantages of variable speed in both wind turbine design and operation

    - Direct-drive generator design

    - Wind resource modeling and site assessment

    - Grid integration and wind farm control

Each of the aforementioned items require validated design tools which offer not only reliable dynamic models describing the relevant physical wind turbine properties, but also provide the ease of use required by the designers;

- The (further) development of offshore wind farms. Offshore wind energy is an extremely promising application of wind power, particularly in countries with dense populations. The Dutch government stimulates this development by means of a 100 MW demonstration project, the so-called "Near Shore Wind Farm" (NSW), within the Netherlands Exclusive Economic Zone (EEZ) in the North Sea. The demonstration wind farm is planned to be constructed in 2004, and is primarily intended for acquiring the knowledge and experience required for constructing cost-effective offshore wind farms located in deep water. In addition to this, the impact on nature and environment will be carefully assessed.

  Although offshore projects require initially higher investments than onshore, mainly due to increased support structure, O&M, installation, and grid connection costs, it is expected that the increase in mean wind velocity and economies of scale will compensate for this [172];

- Breakthroughs in reduction of transport losses and electricity storage for different time scales (ranging from minutes to months) at market shares above $15-20\%$ [113]. Because wind is an intermittent (*i.e.* unpredictable) generation source, viable electricity transportation and storage is essential for turning wind energy into a mainstream electricity source. The most versatile energy storage system, and the best "energy carrier", is hydrogen [317]. Coupling wind energy with hydrogen production (via electrolysis of (sea)water) has the potential to overcome this disadvantage of wind power. After all, surplus wind power can be stored as hydrogen at off-peak times, and used at a later stage in fuel cells or gas turbines to generate electricity to meet peaks in the electricity demand. Alternatively, wind energy can also be combined with hydro power.

In 2010, wind power is expected to achieve economic viability (at sites with moderate to high average wind speeds) as a result of technological improvements, economies of scale (resulting from expanding markets), and raised fossil fuel prices (the result of the depletion of fossil fuel resources) [85]. The wind power market is expected to show a continued rapid growth through 2020. Simultaneous with the increasing role of wind power, the climate-destabilizing greenhouse gas emissions will be reduced[2] and a more diversified energy mix will be obtained.

1.1.3 Cost-effective wind turbine design and operation

Designing the cost-effective, grid-connected wind turbines that are required to materialize the presented outlook is a challenge given the fact these turbines are constantly competing with conventional power systems on the world market on the basis of the

---

[2]Hereby assuming that the reduction in emissions is not counterbalanced by the expected increase in the worldwide electricity consumption.

cost price of electricity per kilowatt-hour. At present, the conversion of wind power to electrical power is still too expensive at sites with a low to moderate average wind speed. This in spite of the fact that the wind resource is available for free, and that already a significant reduction in cost per kilowatt-hour has been achieved in the past decades.

From the preceding subsection it should be clear that obtaining economic viability of wind power, and subsequently increasing the share of wind power in the global electricity mix can be obtained in various ways. However, if the fossil fuel prices do not increase sharply, and if the governments do not introduce new fiscal instruments that substantially improve the competitive position of wind power, the rate at which costs will further decline depends solely on advances in wind turbine design and operation. While considerable technical progress has been made over the last 20 years, additional improvements are still possible. This is mainly because the modern wind turbine technology is still in an early stage of development, and consequently not as mature as the technology involved in conventional power plants.

A breakdown of the cost of onshore wind turbines shows that the O&M cost and the capital cost account for the bulk of the cost per kilowatt-hour [34, 172]. Their respective shares are $6-29\,\%$ and $70\,\%$. Thus wind energy is a highly capital-intensive technology, and consequently the economics of wind power are highly sensitive to both the size of the capital investment and the interest rate charged on that capital. This in turn means that the cost can be most effectively reduced by reducing the capital cost. This is in direct contrast to conventional electricity generation where the main driver of cost per kWh is the price of the fuel (*e.g.* natural gas or coal) that is being used. Besides capital cost reduction, the competitive position of wind power can also be improved by ensuring that the turbine is operating continuously at the best possible performance as well as by minimizing the difference between the technical and economic lifetime.

It can thus be concluded that in order to achieve, and subsequently maintain the desired global economic competitiveness, steady improvements in both wind turbine design and operation are of vital importance. Eventually, a cost-effective wind turbine will have:

- Low capital cost

- A technical lifetime that equals the economic lifetime

- Low operations and maintenance cost

- Efficient energy conversion

In order to achieve this goal, the design and operation of the complete wind turbine system has to be optimized with respect to both cost and performance. In view of the complex wind turbine dynamic behavior, which is related to various design parameters and control system design, accurate and reliable dynamic wind turbine models are a prerequisite to the design and operation of such cost-effective turbines. When implemented in a user-friendly design tool, these models enable the wind turbine designer to evaluate different wind turbine configurations to support

design decisions and to explore how the selected configuration would perform under extreme conditions. This will lead to better wind turbine designs with improved system performance and will reduce dependence on the development of prototypes and testing. The former will reduce the cost price of electricity by capturing maximum energy at minimum fatigue loads, while the latter will shorten the design cycle and reduce development costs.

1.2   Problem formulation

With this motivation and background in mind, the following problem can be formulated:

> *"Develop a systematic methodology that generates accurate and reliable dynamic models suited for cost-effective design and operation of structurally flexible, variable speed wind turbines."*

It is recognized that solving the above problem is a huge challenge within the limited capacity and time available. As a consequence, we will confine our research to grid-connected, 3-bladed, horizontal-axis wind turbines equipped with a direct-drive synchronous generator. The rotor is located upwind of the tower. The main reasons for this are: i) the aforementioned configuration has a high potential to reach cost-effectiveness in the near future, ii) the system offers the implementation of advanced control systems exploiting the advantages of variable speed operation, and iii) we have the possibility to take measurements from a wind turbine belonging to this specific class (*i.e.* the Lagerwey LW-50/750 wind turbine located near Nieuwe-Tonge, Province of Zuid-Holland, The Netherlands). Since this turbine is located on land, we will further restrict our attention to onshore wind turbines.

It should be stressed that the systematic methodology under development, however, should not possess in any form fundamental restrictions for proper inclusion of other and larger wind turbine configurations. Furthermore, it should also allow for a straightforward incorporation of the computation of hydrodynamic forces resulting from waves acting on the support structure since the future of wind power lies offshore.

The solution to the confined problem statement is achieved by solving first the wind turbine modeling sub-problem, subsequently the model validation sub-problem, and finally the model based control design sub-problem.

Sub-problem 1.2.1 (Modeling of flexible wind turbines) *Acquire or develop a non-linear dynamic model describing the relevant physical properties of flexible, variable speed wind turbines.*

Before we can solve this first sub-problem, it should be clear what is demanded from the model. We aim at developing models suited for the cost-effective design and operation of flexible, variable speed wind turbines. This implies that we are mainly interested in the complete wind turbine behavior (including all bilateral couplings between the different wind turbine parts) as well as the interactions with

the surroundings. Consequently, the models are not suited for the detailed physical design of individual wind turbine components (*e.g.* rotor blades, generator or power converter) although an unambiguous exchange of data between the two must be possible. Basically, the models should:

- support design choices to evaluate their impact on the performance of the complete wind turbine. In the previous section it was motivated that in order to arrive at cost-effective designs the design must be done with great care, implying that proper design support is crucial. Design choices include the following issues: rotor diameter, hub height, support structure type, type and location of sensors and actuators, gearbox or direct-drive, fixed or variable speed, operation and maintenance strategies;

- be suited for the design of optimal operating strategies. This means that the model must have a limited complexity (model order restricted to about a hundred), must be equipped with a straightforward and automated transfer from physical data available during the design of a new wind turbine to model parameters, and the model relations must be validated against measured data. This opens the possibility to establish a bilateral coupling between the design of a new wind turbine and the design of its control system;

- allow for the prediction and analysis of the dynamic behavior of the complete system before the turbine is actually built. It is demanded for feedback to the wind turbine designer that the model is fully parametric with physical meaningful parameters (*i.e.* the model parameters should be directly related to for example geometry and material properties).

The system boundary will be tightly chosen around the wind turbine. This means that both the undisturbed wind velocity and the waves act as external inputs to the model. Furthermore, it is assumed that the utility grid can be modeled as an infinite bus (*i.e.* source of constant voltage and frequency). Notice that this assumption might be too restrictive in the case of weak grids as well as in the case that a wind farm instead of a single wind turbine is connected to the grid.

To begin with, an inventory of the state-of-the-art wind turbine design codes will be made in order to provide an answer to the question whether or not the models available in the existing codes are suited for our purpose. From this inventory it will be concluded that the existing models are not adequate to solve the main thesis problem. As a consequence, a new wind turbine design code will be developed that overcomes the observed shortcomings. This code must include a systematic procedure transferring the physical data (*e.g.* dimension, mass distribution) to model parameters. It is evident that a systematic modeling approach is preferred over an application specific wind turbine model.

Sub-problem 1.2.2 (Model validation) *Investigate the validity of the model by confronting it with as much as information about the process that is necessary.*

Model validation, as it is usually performed in the wind energy community, is rather limited. Basically, time-domain model simulations are compared with measurements

taken from an operating wind turbine. In general, this does not meet the high validation demands associated with the intended model use. The main two reasons are that the wind acts as a stochastic input and the fact that the bilateral couplings between the different modules makes it impossible to separate the measured responses.

It can be concluded that, at present, no satisfactory model validation procedure seems to be available. Consequently, to arrive at a validated wind turbine model suited to solve the main thesis problem, a systematic model validation approach needs to be developed.

From a model validation point of view, the fact that physical laws are applied to arrive at the wind turbine model (*i.e.* the model parameters have a clear physical interpretation) offers a main advantage with respect to black-box models: it is also possible to compare the estimated parameter values with information from other sources, such as likely ranges and values in the literature.

Sub-problem 1.2.3 (Model based control design) *Design a controller on the basis of the validated model such that the cost price of electricity per kilowatt-hour is minimal.*

The question is how a controller can be designed that minimizes a specified economic objective function. This function must encompass all aspects of both performance and costs related to wind turbine construction and operation (including electricity yield, lifetime, maintenance and quality of power).

Obviously, there is thus a need for a methodology that translates the manufacturer's specifications and site-specific data automatically in a purpose-made controller. Together with the systematic modeling approach that enables wind turbine designers and control engineers to rapidly and easily build accurate dynamic wind turbine models with physically meaningful parameters this will lead to an integrated and optimal design. Consequently, the solution to the main thesis problem is achieved.

It must be stressed that the gap that exists between the control engineering and the wind engineering community will be closed only if the controlled wind turbine behavior *in situ* corresponds to the predicted behavior. This implies that the designed controller needs to be implemented in the real turbine under investigation and the true performance must be evaluated. The so-called implementation sub-problem, however, is not dealt with in this thesis due to practical, resource, and time limitations.

1.3 Outline

The remainder of this thesis consists of five main parts. A brief overview of these parts and accompanying chapters will now be presented.

- Part I: **Modeling of flexible wind turbines**. The first part, comprising Chapter 2 and Chapter 3, addresses sub-problem 1.2.1. In Chapter 2, the minimum requirements a design code should meet are listed, after which an

inventory of the state-of-the-art of wind turbine design codes is made. Chapter 3 is devoted to the modeling of flexible wind turbines, resulting in the development of DAWIDUM: a new wind turbine design code;

- Part II: **Model validation issues**. The second part, comprising Chapter 4 and Chapter 5, addresses sub-problem 1.2.2. Chapter 4 deals with the verification and validation of DAWIDUM's mechanical and electrical module, while Chapter 5 describes how the physical mechanical model parameters can be updated in order to achieve better correlation with test data when available;

- Part III: **Model based control design**. The third part, comprising Chapter 6 and Chapter 7, addresses sub-problem 1.2.3. In Chapter 6 an improved frequency converter controller is developed for the synchronous generator of the Lagerwey LW-50/750 wind turbine. In Chapter 7 the first steps towards the systematic synthesis of model based controllers aiming at cost-effectiveness are made;

- Part IV: **Conclusions and recommendations**. The conclusions are presented in Chapter 8, and the recommendations for future research are given in Chapter 9;

- Part V: **Appendices**. The final part presents the appendices A to I in which essential (background) information is gathered and some proofs are listed.

1.4 Typographical conventions

The following typographical conventions are used in this thesis:

- Names of software packages are typeset in SMALL CAPITALS;

- Scalar symbols such as x and z are typeset in *italic*, while **boldface** symbols represent vectors or matrices;

- Instantaneous values of variables such as voltage, current and power that are functions of time are typeset in lower-case letters u, i, and p respectively. We may or may not show that they are functions of time, for example, using u rather than $u(t)$. The upper-case symbols U and I refer to their average values. They generally refer to an average value in DC quantities and a root-mean-square (rms) value in AC quantities;

- A `typewriter` font is used when commands are to be entered by the user at the MATLAB® command window. This font is also used for SD/FAST® commands;

- Names of SIMULINK® and SD/FAST® systems (*i.e.* MEX-files) as well as MATLAB® functions and data files are denoted by their file names (with extensions .mdl, .dll, .m, and .mat respectively) which are typeset in Sans Serif style.

Part I:

Modeling of flexible wind turbines

Chapter 2

State-of-the-art of wind turbine design codes

In the introduction it was motivated that the availability of a dynamic model of a complete wind turbine is a necessity in view of the cost-effective design and operation of flexible, variable speed wind turbines. In the wind energy community there is a wide variety in different design codes that can be used to model a wind turbine's dynamic behavior. Each of them with advantages and disadvantages.

In this chapter an inventory of the state-of-the-art of wind turbine design codes is made in order to judge the appropriateness of using one of these to solve the main thesis problem. In Section 2.1 the main specifications are listed that a design tool should at least meet. Section 2.2 presents an overview of the design codes used in the wind energy community. In Section 2.3 the most important features of the aforementioned codes will be described, explained, and – where possible – compared. Finally, in Section 2.4, the conclusions are listed.

2.1 Introduction

The challenge of wind energy research lies in developing wind turbines that are optimized with respect to both cost and performance. A prerequisite for the cost-effective design of such turbines is the availability of a systematic methodology that generates accurate and reliable dynamic models of the complete system within the design phase with relatively low modeling effort. The methodology and resulting models needs to be encased in a user-friendly simulation environment to be able to fully exploit the gained model knowledge. The basic requirements that such a design code must meet are:

- It should have a modular structure. This offers the possibility to easily adapt the model configuration (*e.g.* two or three rotor blades) and/or model complexity (*i.e.* number of degrees of freedom) by interchanging modules such that the resulting configuration is appropriate for the intended application;

- Models must accurately describe the couplings between the different wind turbine modules as well as the interactions with the surroundings;

- It must be possible to extract linear models (preferably in state-space form) from the created non-linear wind turbine models. Linear models are indispensable for i) analyzing the model behavior in different operating points and ii) design and optimization of control strategies. In addition, it must allow for rapid and easy (real-time) controller implementation.

In addition, it is desired that the package:

- Is equipped with an extensive module library containing models describing a wide range of wind turbines with a different level of complexity. Each model must be validated against measured data;

- Is part of a general-purpose (simulation) program with access to sophisticated and reliable mathematical algorithms. Data exchange with standard programs (including MATLAB$^®$, and Microsoft Excel);

- Offers the computation of several steady-state characteristics (including rotor power versus undisturbed wind velocity (P-V_w curve), or thrust versus undisturbed wind velocity (D_{ax}-V_w curve) or is able to perform other standard wind turbine related analyses;

- Is equipped with a Graphical User Interface (GUI) to simplify the operations involved with creating, optimizing, analyzing, simulating and animating the wind turbine models as well as facilitating controller design. This allows the user to focus the attention on the design, rather than handling of the model.

We will next present an overview of the wind turbine design codes that are commonly used in the wind energy community.

2.2   Overview wind turbine design codes

In the wind energy community the following design codes are commonly used to model and simulate the wind turbine dynamic behavior, as well as to carry out design calculations:

- **ADAMS/WT** (Automatic Dynamic Analysis of Mechanical Systems - Wind Turbine) [57]. ADAMS/WT is an add-on package for the general-purpose, multibody package ADAMS. ADAMS/WT is developed by Mechanical Dynamics, Inc. (MDI) under contract to the National Renewable Energy Laboratory (NREL), specifically for modeling horizontal-axis wind turbines of different configurations. The ADAMS-code is intended for detailed calculations in the final design stage [318]. Both the subroutine packages AeroDyn (computes the aerodynamic forces for the blades) and YawDyn (blade flap and machine yaw), developed at the University of Utah, can be incorporated in the package [102]. In the 2.0 release, ADAMS/WT is limited to fixed- or free yaw, horizontal-axis wind turbines with two-bladed teetering or 3, 4 or 5-bladed rigid hubs;

- **BLADED** for Windows - Offshore Upgrade [29, 74]. BLADED for Windows is an integrated software package offering the full range of performance and loading calculations required for the design and certification of both onshore and offshore wind turbines. This code is developed at Garrad Hassan & Partners Ltd., Bristol, England, and has been accepted by Germanischer Lloyd for the calculation of wind turbine loads for design and certification;

- **DUWECS** (Delft University Wind Energy Convertor Simulation program) [20, 21, 22, 23, 143]. The development of this code started in 1986 at the Mechanical Engineering Systems and Control Group of Delft University of Technology, The Netherlands, in order be able to optimize controlled, flexible horizontal-axis onshore wind turbines. In 1993 DUWECS has been extended to be able to deal with offshore wind turbines. Since 1994, this code is maintained by the Institute for Wind Energy, also from Delft University of Technology;

- **FAST** (Fatigue, Aerodynamics, Structures, and Turbulence) [66, 306, 309]. The design code FAST has been developed at Oregon State University under contract to the Wind Technology Branch of the National Renewable Energy Laboratory (NREL). There are two versions of FAST, notably: a two-bladed version called FAST-2, and a three bladed version called FAST-3. The FAST-code is intended to obtain loads estimates for intermediate design studies. The number of degrees of freedom is limited in order to reduce runtimes for a wind turbine model simulation. Typical runtimes with FAST-2 take about one-sixth the time required for a similar ADAMS/WT run for a similar wind turbine model [318]. In 1996, NREL has modified FAST to use the AeroDyn subroutine package developed at the University of Utah to calculate the aerodynamic forces along the blade. This version has been called FAST-AD;

- **FLEX5** [48, 207, 208, 289, 297]. The design code FLEX5 has been developed at the Fluid Mechanics Department of the Technical University of Denmark. FLEX5 simulates the dynamic behavior of both onshore and offshore wind turbines wind turbines with 1 to 3 rotor blades, fixed or variable speed, pitch or stall controlled. The aero-elastic model is formulated in the time-domain, and uses a relatively limited number of degrees of freedom to describe rigid body motions and elastic deformations. In the present version FLEX5 is limited to monopile foundations;

- **FLEXLAST** (FLEXible Load Analysing Simulation Tool) [15, 299]. The development of FLEXLAST started at Stork Product Engineering, Amsterdam, The Netherlands, in 1982. Since 1990 the code has been used for the design and certification for Dutch companies as well as for foreign companies;

- **FOCUS** (Fatigue Optimization Code Using Simulations) [239, 240]. FOCUS is an integrated design tool for structural optimization of rotor blades. It is developed by Stork Product Engineering, the Stevin Laboratory, and the Institute for Wind Energy, the latter two from Delft University of Technology, The Netherlands. FOCUS consists of four main modules, SWING (stochastic

wind generation), FLEXLAST (calculation load time cycles), FAROB (structural blade modeling), and Graph (output handling);

- **GAROS** (General Analysis of ROtating Structures) [235]. GAROS is a general purpose program for the dynamic analysis of coupled elastic rotating and non-rotating structures with special attention to horizontal-axis wind turbines. The development of GAROS started in 1979 at *aerodyn* Energiesysteme GmbH;

- **GAST** (General Aerodynamic and Structural Prediction Tool for Wind Turbines) [236, 302]. GAST is developed at the Fluids Section of the National Technical University of Athens, Greece for performing complete simulations of the behavior of wind turbines over a wide range of different operational conditions. It includes a simulator of turbulent wind fields, time-domain aero-elastic analysis of the full wind turbine configuration, and post-processing of loads for fatigue analysis;

- **HAWC** (Horizontal Axis Wind Turbine Code) [150, 215]. The aero-elastic code HAWC is developed at the Wind Energy Department of Risø National Laboratory, Denmark. Besides acting as a "test stand" for improved aero-elastic modeling, this code is used for intermediate horizontal-axis wind turbine design studies;

- **PHATAS-IV** (Program for Horizontal Axis wind Turbine Analysis and Simulation, version IV) [160, 161, 162, 163, 164, 165, 275]. The PHATAS code is developed at the Dutch Energy Research Foundation (ECN) unit Renewable Energy, Petten, The Netherlands for the calculation of the non-linear dynamic behavior and the corresponding loads of a horizontal-axis, wind turbine (both onshore and offshore) in time domain;

- **TWISTER** [145, 168]. The program TWISTER is developed at Stentec B.V., Heeg, The Netherlands, in order to analyse the behavior of horizontal-axis wind turbines. TWISTER is the successor of FKA;

- **VIDYN** [69, 70]. VIDYN is a simulation program for static and dynamic analysis of horizontal-axis wind turbines. The development of VIDYN began in 1983 at Teknikgruppen AB, Sollentuna, Sweden, as part of the evaluation projects concerning two large, Swedish prototypes Maglarp and Nässuden;

- **YawDyn** (Yaw Dynamics computer program) [97, 99]. YawDyn is developed at the Mechanical Engineering Department of University of Utah, United States of America with the support of the National Renewable Energy Laboratory (NREL) Wind Research Branch for the analysis of the yaw motions or loads of a horizontal-axis constant rotational speed wind turbine with a rigid or teetering hub, and two or three blades. The aerodynamic subroutines from YawDyn, *i.e.* AeroDyn, have been modified for use with the ADAMS/WT program. This code is intended to be used to obtain quick estimates of preliminary design loads [318], since the structural dynamics model contained in YawDyn is extremely simple [98].

2.3 Main features overview

In this section the most important features (*i.e.* rotor aerodynamics, structural dynamics, generator description, wind field description, wave field description, and control design) of the aforementioned state-of-the-art wind turbine design codes are summarized by a short description. It should be noted that only features of upwind, horizontal-axis wind turbines are covered. Finally, these features are listed in two tables in order to enable the reader to get quick and comparative information.

2.3.1 Rotor aerodynamics

Rotor aerodynamics refers to the interaction of the wind turbine rotor with the incoming wind. The treatment of rotor aerodynamics in all current design codes is based on Glauerts well-known, and well established blade element momentum (BEM) theory [81, 83]. This theory is an extension of the Rankine-Froude actuator-disk model (introduced by R.E. Froude in 1889 [68], after W.J.M. Rankine [231] has introduced the momentum theory) in order to overcome the unsatisfactory accuracy performance predictions based on this model.

The blade element momentum theory divides the rotor blades into a number of radial blade sections (elements), each at a particular angle of attack. These blade elements are assumed to have the same aerodynamic properties as an infinitely long (or 2-D) rotor blade with the same chord, and aerofoils. This implies that 2-D aerofoil data (*i.e.* lift, drag and moment coefficients) obtained from wind tunnel experiments are assumed to be valid. The airflow from upstream to downstream of the elements is, in turn, divided into annular stream tubes (*see* Fig. 3.5 on page 50). It is assumed that each stream tube can be treated independently from adjacent ones. Subsequently, the theory behind the Rankine-Froude actuator-disk model is applied to each blade element, instead of to the rotor disk as a whole. Finally, the total load on the blades is calculated by adding up the forces from all the elements.

The basic BEM-theory has, however, a number of limitations which are frequently encountered in wind turbine applications. Many of these limitations can be overcome using (semi) empirical relations derived from either helicopter, propellor, or wind turbine experience. The major problem with semi-empirical models is, however, the uncertainty regarding their reliability across a range of wind turbines with different configurations and aerofoils. The most common corrections applied to the quasi-steady momentum theory are: i) blade tip and root effects, ii) turbulent wake state, iii) dynamic inflow, iv) dynamic stall, and v) 3-D corrections.

Blade tip and root effects

The BEM theory does not account for the effect of a finite number of rotor blades. Therefore a correction has to be applied for the interaction of the shed vorticity with the blade's bound vorticity. This effect is usually greatest near the blade tip, and it significantly affects the rotor torque and thrust. In principle, either an approximate solution by Prandtl [221] or a more exact solution by Goldstein [88] can be used to account for the non-uniformity of the induced axial velocity [55]. Both

approximations give similar results. The expression obtained by Prandtl is however commonly used, since this has a simple closed form, whereas the Goldstein solution is represented by an infinite series of modified Bessel functions.

Prandtl's expression is in literature denoted by the misleading term tip-loss factor. Misleading because it corrects for the fact that induction is not uniform over the annulus under consideration due to the finite number of blades, and not for the finite length of the blades.

Turbulent wake state

For high induced velocities (exceeding approximately $40\,\%$ of the free-stream velocity), the momentum and vortex theory are no longer applicable because of the predicted reversal of flow in the turbine wake. The vortex structure disintegrates and the wake becomes turbulent and, in doing so, entrains energetic air from outside the wake by a mixing process. Thereby thus altering the mass flow rate from that flowing through the actuator disk. The turbine is now operating in the so-called "turbulent wake state", which is an intermediate state between windmill, and propellor state (*see* Appendix B for an overview of the different flow states of a wind turbine rotor).

In the turbulent wake state the relationship between the axial induction factor and the thrust coefficient according to the momentum theory (*i.e.* $C_{dax} = 4a(1-a)$, with a the axial induction factor and C_{dax} the thrust coefficient) has to be replaced by an empirical relation ($a = f(C_{dax})$ for $C_{dax} > C_{dax}^{th}$. Note that the threshold value C_{dax}^{th} depends on the empirical relation). The explanation for this is that the momentum theory predicts a decreasing thrust coefficient with an increasing axial induction factor, while data obtained from wind turbines show an increasing thrust coefficient [279]. Thus, the momentum theory is considered to be invalid for axial induction factors larger than 0.5. This is consistent with the fact that when $a = 0.5$ the far wake velocity vanishes (*i.e.* a condition at which streamlines no longer exist), thereby violating the assumptions on which the momentum theory is based.

Most design codes include an empirical relation for induced velocities for these high disk loading conditions in order to improve agreement between theory and experiment. The following approximations are commonly used: Anderson [2], Garrad Hassan [29], Glauert [55, 82], Johnson [118], and Wilson [280, 308].

These five empirical relations are compared in Fig. 2.1 for perpendicular flow. The simple expression for the thrust coefficient, as derived from the momentum theory is added for comparison. Obviously, disagreement exists about how to model the flow field through a wind turbine under heavily loaded conditions, and the applied empirical approximations must thus be regarded as being only approximate at best.

With the recent developments towards wind turbines operating at variable speed, however, the importance of this phenomenon will become of lesser importance. After all, a wind turbine typically operates in turbulent wake state when the tip-speed ratio λ exceeds 1.3 or 1.4 times the value for which $C_{p,max}$ is achieved [267]. For a constant rotational speed wind turbine this implies that it occurs at wind velocities much lower than the rated wind velocity, while for a variable speed wind turbine it may not occur at all during normal operation.
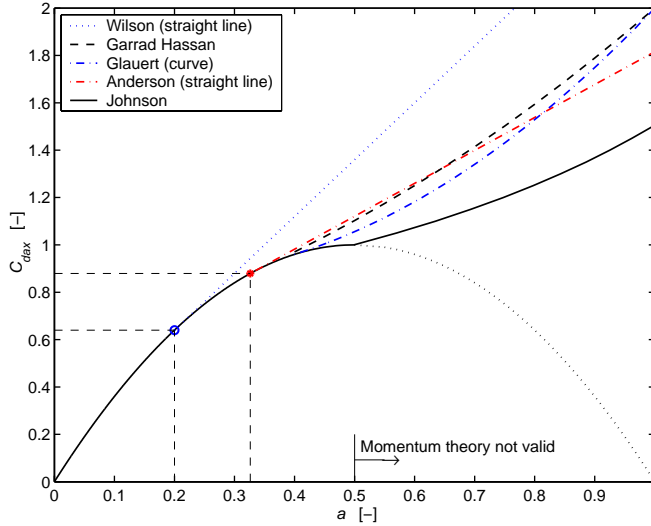
Figure 2.1: *Thrust coefficient C_{dax} as function of axial induction factor a. Solid curve: Johnson, dashed curve: Garrad Hassan, dashed-dotted straight line: Anderson, $*$: transition point, dotted straight line: Wilson, o: junction point, dashed-dotted curve: Glauert. The equations are given on page 64-65.*

Dynamic inflow

The aerodynamic forces are, following the blade element momentum theory, calculated in a quasi-steady fashion, assuming at any instant in time an equilibrium between the load situation and the induced velocity. In other words: the blade element momentum theory assumes that the induced velocity flow field react instantaneously to changes in blade loading. This treatment is in literature known as the equilibrium wake model.

In the actual operation of a wind turbine its load situation is changing continuously, either because of wind velocity fluctuations, blade movements or through blade pitch control at full load (in case that of pitchable blades). When the load situation changes, the change in the induced velocities will lag behind, since the mass of the air in the wake makes it impossible to respond instantaneously to a change in rotor loading. The dynamics associated with this process is in literature commonly referred to as "dynamic inflow". The study of dynamic inflow was initiated nearly 40 years ago in the helicopter aerodynamics. The difference between steady and dynamic inflow is illustrated in Fig. 2.2 for a stepwise change in pitch angle on one blade element.

From comparisons of computational results with measurements it is shown by different researchers, including Snel and Schepers [269, 271, 272, 273], that under certain circumstances, notably pitching transients, important and systematic differences occur which can be attributed to unsteadiness and the time lag in the adjust-
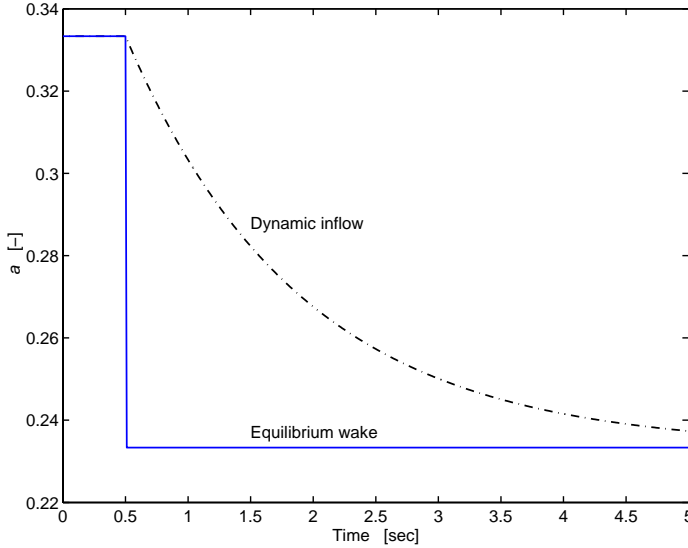
Figure 2.2: *Influence of dynamic inflow on the axial induction factor a. Solid curve: Equilibrium wake, dashed-dotted curve: Dynamic inflow. It is assumed that the axial induction factor is described by the following linear, first order system: $a = \frac{1}{\tau_a \cdot s + 1} \cdot a_o$, with a_o calculated from the blade element momentum theory equations, and the time constant τ_a set to 1.4 seconds.*

ment in the induced velocities. Furthermore, Montgomerie and Zdunek [193] report that fatigue loads may be underestimated if the effect of wake inertia is neglected by considering steady aerodynamics only. The unsteady character must be included in the computation of the aerodynamic loads. The characteristic time scale for this phenomenon is $\frac{D}{V_w}$, where D the rotor diameter, and V_w the undisturbed wind velocity [269]. Hence, the importance of dynamic inflow increases with the pitching speed and the size of the turbine. Dynamic inflow must be distinguished from the other unsteady aerodynamic effect "dynamic stall" which has a length scale of the order of the chord length. Dynamic stall will be discussed in the next paragraph.

Dynamic inflow can be modeled by realizing that the distribution of vortices in the wake is responsible for the induced velocity in the rotor plane. By following the creation and transport of wake vorticity in time, and calculating the velocity induced by it in the rotor plane, a so-called free vortex model is obtained [270]. Such a model is, however, computationally expensive. Therefore, in the state-of-the-art wind turbine design codes, the blade element momentum theory is adapted by transforming the algebraic equilibrium equations into first order differential equations reflecting the dynamics of the inflow process. Nowadays, two alternative models are used to describe dynamic inflow: a first order system (FOS) [193, 209] and the Pitt and Peters model [71, 72, 218].

In literature, another way of analyzing dynamic inflow has been put forward,

notably vortex wake calculation. Although this method is inherently more satisfying since it enables one to directly calculate the motion of the vortex trajectories without the necessity to make assumptions regarding the time constant of the flow it is not suitable for use with the blade element momentum theory. At this time there is not sufficient data available to determine whether this more complex method is more accurate than the first order system (FOS) or Pitt and Peters model.

Dynamic stall

Transient aerodynamics have another facet, called "dynamic stall". Dynamic stall or stall hysteresis is a dynamic effect which occurs on aerofoils if the angle of attack changes more rapidly than the air flow around the blade (or blade element) can adjust. Dynamic stall was shown to occur under a variety of inflow conditions, including turbulence, tower shadow, and yawed flow [100]. The result is aerofoil lift and drag coefficients which depend not only on the instantaneous angle of attack (quasi-steady aerodynamics assumption), but also on the recent angle of attack history. In particular, the lift and drag coefficients depend on the angle of attack as well as its first time derivative. These changes can produce hysteresis loops which, in turn, lead to cyclic pressure loadings that are not predictable from conventional lift and drag data obtained at steady angles of attack. Fig. 2.3 (from Leishman & Beddoes [157]) shows a typical rotating blade dynamic stall measurement compared to 2-D wind tunnel data.
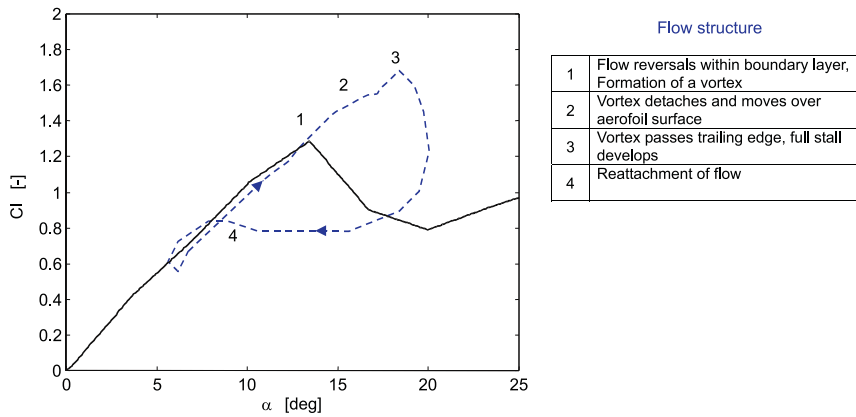
Figure 2.3: *Typical dynamic stall behavior of the lift coefficient C_l of a fictive aerofoil as function of the angle of attack α compared with 2-D wind tunnel data. Solid curve: 2-D wind tunnel data, dashed curve: Dynamic stall.*

Increased excitation of the blade structural dynamic modes becomes a possibility during dynamic stall. In case of torsionally soft rotor blades, severe stall may even excite the blade torsion mode at its natural frequency, leading to a dynamic instability known as stall-flutter [157].

27

Now that the structural dynamic modeling has reached a good level of maturity (*see* Section 2.3.2), it is also required that the relatively simple quasi-steady representation for the aerodynamics of stall regulated wind turbines is replaced by more accurate, but still computationally efficient, models that incorporate the unsteady behavior of the blade sections. At present it is possible to model dynamic stall in considerable detail, and accuracy using Computational Fluid Dynamics (CFD) methods. For example, numerical solutions to the unsteady Navier-Stokes equations are becoming increasingly feasible [277]. Unfortunately, these solutions are extremely complex, implying that implementation in a design code would exceed the practical limits of the computational power.

In order to include the unsteady behavior in the design codes, it is thus necessary to make use of semi-empirical models. Such models describe the sectional force coefficients in terms of angle of attack and some time derivatives in differential equation form allowing straightforward implementation in the aerodynamic routines based on the blade element momentum theory. The CFD methods can be used to check the validity of these models.

Prior to 1988 dynamic stall was not incorporated in wind turbine design codes [100] although most wind turbines were stall regulated. At present, the unsteady aerodynamics with a length scale of the order of the chord length are modeled in five ways in the state-of-the-art design codes, *i.e.* Beddoes [157] (or Beddoes-Leishman), Gormont [89, 103] (or Boeing-Vertol Gamma Function), ONERA [216, 217, 293], SIMPLE [192], and Stig Øye [206]. All models are semi-empirical in nature, and require some a priori knowledge of aerofoil characteristics. In Molenaar [190] it is shown by comparing hysteresis loops calculated for an oscillating NACA-0012 aerofoil (where "00" means zero camber implying a symmetrical aerofoil, and "12" indicates a maximum thickness to chord ratio of 12 %) that no preference for either of the mentioned dynamic stall models exists.

This conclusion is confirmed by *e.g.* Bierbooms [10], Snel [266], and Yeznasni *et al.* [322]. Hansen [99], on the other hand, reports that the Gormont model is able to predict the correct hysteresis loop when the two empirical constants are known *a priori.* The main cause for the observed differences is that dynamic stall depends on such a large number of parameters (including aerofoil geometry, pitching frequency, Mach number, Reynolds number). This implies that the phenomenon is difficult to analyze. Research is continuing to explore the most accurate and practical method to implement this aspect of unsteady aerodynamics. Riziotis *et al.* [237], for example, suggests to use the more advanced vortex models to check and calibrate the semi-empirical models.

3-D corrections

In the state-of-the-art design codes 2-D aerofoil data obtained from wind tunnel experiments at the appropriate Reynolds number is used to represent the aerodynamic properties of wind turbine rotor blades. Recall that wind tunnel data is obtained from measurements on non-rotating aerofoil sections, whereas the resulting lift, drag and moment coefficients are applied to rotating wind turbine blades. This approach leads to reasonable prediction of wind turbine loads for attached or equivalently un-

separated flow, but is known to become unsatisfactory for (partially) separated flow conditions [268]. Experiments on rotating blades show a stall-delay and increased lift coefficients at angles of attack beyond the 2-D stall point. The main cause for this is the effect of rotation [14].

Although in principle relevant for all types of wind turbines, the above problem is especially important for stall regulated wind turbines. The interested reader is referred to Snel *et al.* [274] for the physical explanation of the differences between 2-D stall and 3-D separation on rotating blades as well as for a review of the theoretical and experimental work done on 3-D effects on rotating blades.

Consequently, the 2-D aerofoil data has to be corrected to provide accurate predictions of the aerodynamic forces in stall. For a non-rotating blade (*i.e.* wing) it is common to use the Prandtl correction equations [23]. In case of a rotating blade the 3-D effects become more complex because of the centrifugal forces acting on the air particles in the boundary layer of the rotor blade. At present, there is no (simple) theory to account for these effects. Hence, semi-empirical methods are to be used. The measured 2-D lift coefficients in stall are corrected by either the Snel *et al.* [274] or Viterna & Corrigan (semi-empirical) method [9, 279, 300].

In Fig. 2.4 the 2-D lift C_l as well as drag C_d coefficients of a NACA-63615-2D aerofoil are corrected using the aforementioned semi-empirical correction methods. A section with a chord-to-radius ratio of 0.25 is applied because 3-D effects are more pronounced near the blade root. The Snel *et al.* 3-D correction results in a stall-delay and increased lift coefficients at angles of attack beyond the 2-D stall point. The Viterna & Corrigan 3-D correction results in a smaller lift gradient, equal maximum value for C_l, and a smooth curve in the post-stall region. The drag coefficient is larger for attached flow, but smaller for stalled flow.
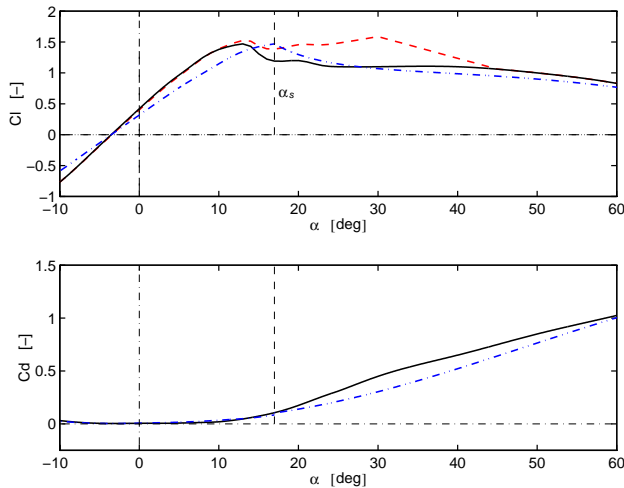
Figure 2.4: *Effect of 3D-correction on 2D-lift coefficient $C_l^{[2D]}$ as function of the angle of attack α of NACA-63615-2D aerofoil for $\frac{c}{r} = 0.25$. Solid line: 2D-data, Dashed line: Snel et al., and Dashed-dotted line: Viterna & Corrigan.*

Obviously, the correction methods for 3-D effects in stall implemented in the state-of-the-art design codes result in quite different modified aerofoil characteristics. As 3-D correction is especially important for stall regulated wind turbines, it will become of lesser importance due to recent developments towards wind turbines operating at variable speed.

In Table 2.1, and Table 2.2 on page 40, and 41 respectively, it is summarized *which* correction (*i.e.* blade tip and root, turbulent wake state, dynamic inflow, dynamic stall and 3-D) is implemented in *which* state-of-the-art design code. It can be concluded that in the state-of-the-art design codes the rotor aerodynamics are – without exception – treated with Glauerts blade element momentum theory. Although the Glauert blade element momentum theory is well-established and widely used, it is necessary to have experimental verification of it for wind turbine rotor analysis. Furthermore, more research is needed to determine the most appropriate turbulent wake state model. The most challenging problem, however, for modelling rotor aerodynamics for stall regulated wind turbines is to improve the predictions of 3-D effects and that of dynamic stall. With the recent developments towards wind turbines operating at variable speed, however, these phenomena will become of lesser importance.

Relevant for all types of wind turbines, on the other hand, is accurate prediction of yawed flow. From the practical point of view, yawed flow (yaw misalignment, skewed wake effects or oblique flow) is a fact of life, and is of paramount importance since an important part of fatigue lifetime consumption of rotor blades can be attributed to these conditions. In addition, it is of importance to the load spectra of yaw bearing, tower, and rotor shaft. Hence, corrections must be made to the blade element momentum theory when the rotor operates at a yaw angle. Although considerable progress has been made, the results are not yet sufficiently accurate when compared with measurements.

2.3.2   Structural dynamics

In the early days of the wind industry, the effects of structural dynamics were either ignored completely, or included through the use of estimated dynamic magnification (*i.e.* safety) factors [228]. The increasing structural flexibility of wind turbines implies that their dynamic behavior, and our ability to model flexibility accurately, becomes more important [73]. Nowadays, the structural dynamics of wind turbines are approximated in three ways, notably using a multibody, finite element, and modal approach. These three approaches are briefly described below:

- **Multibody**. In the multibody or MBS approach, a real mechanical system is approximated with a finite number of rigid bodies, coupled by inelastic joints (*e.g.* slider, pin) to the Newtonian reference frame. Consequently, such a system can be described with a finite number of ordinary differential equations. The essential dynamics of stiff mechanical systems that undergo large displacements as well as large rotations can be well reproduced in this way. Since the number of equations of motion remains comparatively small, this approach is very appropriate for control system design. Soft mechanical systems, on the

other hand, consists of deformable bodies that undergo rigid body motion as
well as elastic deformations. In view of the multibody methodology, such a
system can be approximated with a collection of rigid, and flexible bodies.
Inclusion of these flexible bodies in the MBS approach is essential in order to
reach the same level of accuracy as for stiff mechanical systems. The price to
be paid is, of course, an increased model order;

- **Finite Element**. The finite element approach is one of the two most common
  spatial discretization methods of a continuous system. This approach leads
  to linear, finite dimensional, continuous time equations of motion for approxi-
  mation the dynamics of flexible systems. In the Finite Element approach, the
  real flexible structure is regarded as an assembly of a finite, but large number
  geometrically simple, discrete elements. In general, the number of elements
  varies between a hundred and some thousands. Finite Element systems (FES)
  are appropriate for the analysis of static loads, and small dynamic motions
  referred to an inertial system. The resulting dynamic models are usually of
  high order, and therefore not suitable for control system design without order
  reduction. Finite Element systems, however, may be very useful for layout
  and design, because stress calculations give important hints for design and
  dimensioning of the structural elements;

- **Modal**. The modal approach is the other spatial discretization method. The
  structural dynamics can also be modeled by a modal representation (modal
  frequency, modal damping coefficient, and modeshape). The modal frequency
  as well as mode shape are determined from the eigenvalues and eigenvectors
  of a finite element analysis of the wind turbine's mechanical structure. A
  disadvantage of the modal approach is that the centrifugal loads are often
  neglected since they correspond to modes caused by the axial deformation (*i.e.*
  in the direction of the blade radius) of the blades. These modes usually have
  relatively high frequencies and are normally not calculated. The result being
  that the centrifugal loads must be calculated by a separate static analysis.

In Table 2.1, and Table 2.2 on page 40, and 41 respectively, it is summarized which
approach to approximate the structural dynamics of wind turbines is implemented
in which design code. It can be concluded that the state-of-the-art of wind turbine
structural dynamic modeling includes representations of rotor blade bending modes
in both flap and lead-lag directions, rotor teeter, drive train torsion, tower bending
in two directions, nacelle yaw and/or tower torsion. At present, it is uncommon to
model rotor blade torsionally flexibility, since current commercial blades are rela-
tively stiff in torsion. The representation of torsional dynamics will become more
important as rotor blades become more flexible in the future.

It should be noted, however, that the difference between a finite element and a
multibody model can be small. For example, the finite element model of a wind
turbine's mechanical structure modeled within *e.g.* BLADED, and GAROS is built
up with beam elements. FES $\mapsto$ MBS implies in Table 2.1, and Table 2.2 that a
detailed finite element is used to deduce the first eigenfrequency of the wind tur-
bine's structural dynamics. Subsequently, this eigenfrequency is used to compute

the equivalent stiffness and damping of the Mass-Spring-Damper system in order to represent the flexibility. Note that a Mass-Spring-Damper system (or Inertia-Spring-Damper system) can be seen as a MBS consisting of 1 rigid body, and that a hinge model can be seen as a MBS consisting of 2 rigid bodies connected by a joint.

From a control design point of view, the multibody approach is most suited because it results in limited order models with physically interpretable model parameters. What is missing in most design codes, however, is an easy transfer from physical data available during the design of a new wind turbine (*e.g.* CAD-drawings or 3-D models) to model parameters. Therefore attention should be paid to the development of an automated structural modeling procedure in which the physical data can be entered an interactive way. Furthermore, it should be possible to select a model with the desired number of degrees of freedom out of a library within an environment suitable for control design (*e.g.* MATLAB®/SIMULINK® [264]). Ideally, this will result in a situation in which control design has become an integral part of wind turbine design.

2.3.3 Generator description

The generator of a horizontal-axis wind turbine is housed in the nacelle and converts the mechanical power into electrical power. Until recently, the classification into constant or variable rotational speed wind turbines was determined by the choice of the electrical generator. For the grid-connected wind turbines, two types of generators were commonly used, asynchronous (or induction) generators and synchronous generators with AC-DC-AC converter. Asynchronous generators were used by many Danish wind turbine manufacturers during the 1980's en 1990's and had no possibility to influence the electrical conversion system. The result being that the rotational speed of the generator was almost constant. The synchronous generator plus AC-DC-AC converter offers the possibility to influence the electrical conversion directly (*i.e.* by means of controlling the power electronics and/or the field excitation), making variable rotational speed possible.

Variable speed implies, in contrast to constant speed generators which are directly coupled to the public grid, a conversion step from mechanical energy at variable turbine speed to electrical energy fed into the constant frequency grid. Part of this conversion could be performed mechanically, for instance using a continuous variable transmission. In most cases a more economical solution is electrical conversion by means of an electrical power converter. In essence, power electronics ensure that the utility line "sees" a 50 Hz current even as the rotor speed changes with wind velocity and generator frequency fluctuates.

Due to the development in the power electronic converters, offering both higher power handling capability and lower price per kW, this distinction has become less clear today. It is even possible to use an asynchronous generator (with suitable power converters) for variable speed operation. The interested reader is referred to Hansen *et al.* [101] were an overview of the generators and power electronic configurations commonly applied in wind turbines can be found. Future concepts are treated as well.

From Table 2.1, and Table 2.2 on page 40, and 41 it can be concluded that in most design codes (in particular the aero-elastic ones) the generator (or to be more precisely: the electromagnetic part of the generator plus conversion system) is described by a static relationship. It is common to express the torque as a function of the generator speed (and sometimes voltage), while the total losses are represented by an efficiency ratio. Obviously, this approach neglects the mutual coupling between the structural dynamics and the electromagnetic part of the generator plus conversion system. It is important that the dynamics will be included in the design codes in more detail in the near future (especially when fast torque control is required for cost-effective design).

2.3.4 Wind field description

It has long been recognized that wind simulation should be an integral part of wind turbine structural design, and analysis. Now that the structural models become more sophisticated, adequate input to these models is essential in order to make full use of the increased accuracy. The wind input required to receive a license is laid down in design standards (*e.g.* IEC-1400-1 standard [112], NVN 11400-0 [198] or Germanischer Lloyd [77]). In addition, a realistic wind input is also requisite in order to be able to evaluate the performance of a wind turbine regarding the obtained fatigue load reduction. After all, the fatigue loading depends strongly on the wind characteristic used as input for the simulation [186]. Hence realistic modeling of three-dimensional wind fields is essential in the cost-effective design, and operation of a wind turbine.

From field experiments it is known that the undisturbed wind velocity is variable in space, time and direction, see Fig. 2.5. The rotor blades move at high speed (compared to the wind velocity) through this spatially, and non-uniform wind field. This gives rise to excitation of the rotor with dominant frequencies at integer multiples of the rotational speed [50, 141]. The spatial structure of the atmospheric turbulence is mainly responsible for this so-called "rotational sampling effect". Obviously, this effect is more pronounced for constant speed turbines than for variable speed turbines.
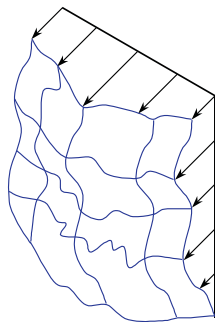
Figure 2.5: *The undisturbed wind velocity: variable in space, time and direction.*

The undisturbed wind velocity is in the current design codes decomposed into a deterministic, and a stochastic (*i.e.* turbulent) wind description. Deterministic wind inputs are very useful to study and verify the global wind turbine behavior, while stochastic wind inputs are to be used for the prediction of the loads which a wind turbine will experience during its life-time. The state-of-the-art with regard to the deterministic part is a representation that includes a linear (or more accurately bi-linear), Power Law (or exponential) or logarithmic model of wind shear together with two, almost identical representations of the tower shadow effect, *viz.* the (1-cos) and the potential flow (or dipole) model.

A model of the turbulent wind field suitable for loading calculations requires good representation of both the temporal and spatial structure of turbulence [229]. Calculations based on a turbulence simulation which assumes a fully coherent cross-wind spatial structure will not take into account the crucial important "eddy slicing" transfer of rotor load from low frequencies to those associated with rotational speed and its higher harmonics. This "eddy slicing" or "rotational sampling effect", associated with rotating blades slicing through the turbulent structure of the wind, is a significant source of fatigue loading. Although early models concentrated on representation of the longitudinal component of turbulence only, the state-of-the-art is to base load calculations on a model of all three turbulent velocity components of the wind field [228].

The most "correct" method to simulate such a turbulent wind field would probably be to solve the Navier-Stokes equations of an atmospheric flow bounded from below by an aerodynamically rough surface directly by Direct Numerical Simulation (DNS) [174]. However, the computational cost of this would be enormous. A cheaper way to do it would be to use Large Eddy Simulation (LES), which is an approximate solution to the Navier-Stokes equations where the motions of the smallest scales are not solved directly, but modelled. Still, this requires supercomputers, and is usually not justified for practical engineering use.

Therefore, in wind engineering, empirical information is generally used in the methods developed for the simulation of turbulent wind. All these methods use, as a starting point, auto-spectral and coherence descriptions of the turbulence. There are several of such descriptions available with the most common being the Von Kármán and Kaimal spectral models. A more comprehensive method is that due to Mann [173, 174] developed at Risø National Laboratory, Denmark. This method is in principle a special case of the general method of Shinozuka and Jan [263]. Another method is the Veers turbulence simulation method, often referred to as SANDIA or SNLWIND method [132] which is originally proposed by Veers, and is again based on the method of Shinozuka and Jan [263].

All these descriptions are encoded in so-called stochastic 3D wind field generators. The following stochastic 3D wind field generators are commonly used: EWS [145, 168], Mann [174], Shinozuka/Jan [263], SNLWIND-3D [132], Sosisw [69, 70], SWIFT (Simulation WInd Field in Time) [315], SWING-4 (Stochastic WINd Generator) [11, 13], Veers [296] and WIND3D [226]. In Table 2.1, and Table 2.2 on page 40, and 41 respectively, it is summarized which wind generator is used in which wind turbine design code.

2.3.5 Wave field description

The future of wind energy will be in large-scale offshore wind farms located in deep water. The main reasons are: i) the wind energy potential offshore is several times higher compared with the resources on land, ii) the average mean wind speed is substantially higher implying an increased electricity yield, iii) both wind shear and atmospheric turbulence are substantially lower due to the smoother surface implying reduced fatigue loading, and iv) NIMBY (not-in-my-backyard) related phenomena as noise emission and optical pollution are of secondary importance.

Conversely, the wind farms are exposed to a more aggressive environment: water waves, currents, (floating) ice, marine fouling, and corrosion due to the salinity and humidity of the salt water environment. The water waves have a particular importance since their frequencies may coincide with the structural eigenfrequencies [143]. This implies that it is of paramount importance for the design and operation of cost-effective offshore wind turbines that the design code is capable to deal with wind as well as water wave (and current) loading. Interestingly, research has shown that the fatigue damage predicted by a coupled simulation of wind and waves is significantly less than a summation of the damages caused by the two effects in isolation [38]. This observation stresses the need of an integrated design approach implemented in a user-friendly design tool.

Deterministic versus stochastic

For the design of an offshore wind turbine the wind generated waves are the most important [143]. The other types (*e.g.* planetary waves, tsunamis, and capillary waves) are either occurring beyond the relevant frequency range or their energy content is too small. Wind generated water waves are random in nature and contain energy in the frequency range of 0.05-0.5 Hz [144].

The wave velocity of these random waves is in the current design codes decomposed into a deterministic, and a stochastic wave description. Deterministic wave inputs are used to model extreme sea waves, while stochastic wave inputs are to be used for the prediction of the wave loads which an offshore wind turbine will experience during its life-time.

The deterministic or design wave approach represents a single wave by a wave period and a wave height (*e.g.* the maximum wave height at the site under investigation). The main reason for using this approach is the simplicity in the design analysis and easy determination of the response due to extreme wave conditions [43]. For proper analysis it is recommended that several possible single design waves of varying periods and heights are analyzed and that the wind turbine has to be designed to withstand the worst of the considered load cases.

The stochastic or wave energy spectrum approach, on the other hand, selects a suitable wave energy spectrum representing an appropriate density distribution of the sea waves at the site under investigation. The standard wave energy spectra are the Pierson-Moskowitz (P-M) and the JONSWAP (Joint North Sea Wave Project) spectrum. The P-M spectrum describes a fully developed sea state, while the JONSWAP spectrum represents a not fully developed sea state. A sea state is

defined as a period of 3 hours and is considered as a stationary stochastic process. Consequently, to account for the variability of the sea, a family of sea states should be used. Both spectra have a significant wave height and the mean wave period as parameters.

Wave theories

The wave field is thus described by a number of waves, either obtained by the design wave approach or by decomposing a wave energy spectrum. The next step is to determine the kinematics of the water particles at a number of locations on the submerged support structure. Although the ocean waves are random in nature, all common wave theories describe wave profiles that are regular (*i.e.* wave form does not change due to interaction with structure) and periodic with prescribed wave height, wave period, and water depth.

The simplest and consequently most often used wave theory is the Airy theory which provides a linear expression for the water particle velocity from the sea bottom up to the still water level (SWL). This implies that the Airy theory gives symmetric profiles about the SWL. The Airy theory can also be regarded as a first order Stokes' theory. Other commonly used wave theories are i) Stokes second- and third-order theory, ii) Stokes fifth-order theory, iii) Cnoidal theory and iv) Stream function theory. Generally, the higher the order of the wave theory, the higher the limiting height for which it is valid [8]. The interested reader is referred to Chakrabarti [43] where regions of validity of the aforementioned wave theories are presented. These regions are described in terms of the three basic parameters (*i.e.* wave height H, wave period T, and water depth d). The shallow, intermediate and deep water wave ranges correspond to $\frac{d}{gT^2} < 0.0025$, $0.0025 \leq \frac{d}{gT^2} \leq 0.08$ and $\frac{d}{gT^2} > 0.08$ respectively (with g the gravity constant) [247].

Wave forces

The water wave forces on an offshore structure are dependent upon the size and shape of the (submerged part of the) support structure as well as the wave characteristics. It is common practice in offshore engineering to calculate the wave forces using one of the following three methods:

- **Morison equation**

- **Froude-Krylov theory**

- **Diffraction theory**

The regions of validity of the aforementioned methods for the calculation of forces on a vertical cylinder are depicted in Fig. 2.6 [143]. The double logarithmic plot shows the Keulegan-Carpenter number KC (ratio between drag and inertia force) against the relative size of the (submerged part of the) support structure. The relative size is expressed by the cross-section dimension of structure D divided by the wave length L. Both axes are limited for increasing values by the slope of the deep water breaking wave curve ($L/H = 7$, with L the wave length and H the wave height).
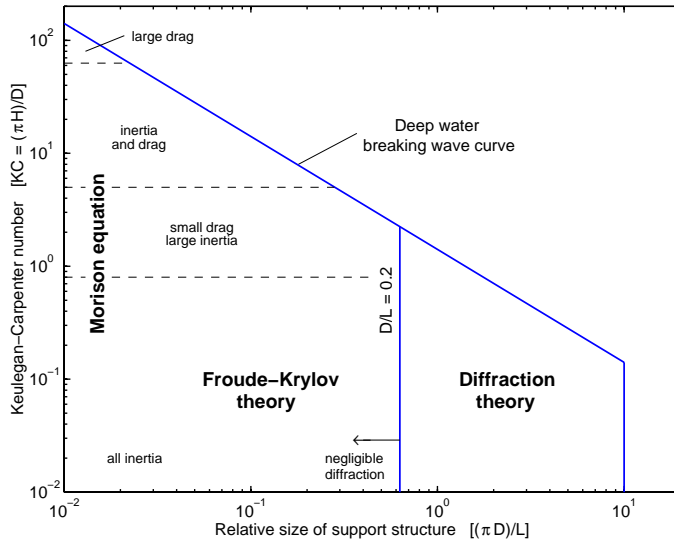
Figure 2.6: *Regions of validity of the Morison equation, Froude-Krylov theory and the diffraction theory, with H the wave height, D the cross-section dimension, and L the wave length [143].*

From Fig. 2.6 it can be concluded that:

- When the (submerged part of the) support structure is small compared to the predominant water wave lengths (*i.e.* $D/L < 0.2$), it can be assumed that the incident wave field is not significantly deformed by the presence of the support structure. In this case, wave loads can be calculated from the Morison equation, where the total force is simply given by the linear combination of drag and inertia forces;

- When the drag force is small and the inertia force predominates, and the structure is still relatively small, the Froude-Krylov theory can be applied;

- When the structure is not small compared to predominant wave lengths ($D/L > 0.2$), the incident wave field is significantly deformed by the presence of the support structure. In this case, the diffraction theory has to be used to compute the wave forces to include the effects of wave scattering around the support structure.

In Table 2.1, and Table 2.2 on page 40, and 41 respectively, it is listed which of the aforementioned design codes is equipped with a wave module. From this table it can be concluded that all codes use the Morison equation to compute the wave forces. In addition, PHATAS-IV uses ROWS (Random Ocean Wave Simulator) [314] to generate the waves.

2.3.6 Control design

The economic cost of electricity generated by wind turbines can be reduced by decreasing the construction cost, while increasing the life-time and efficiency of the energy conversion. The question is to what extent a (feedback) control system can contribute to this reduction of cost.

In general, the purpose of using feedback is to combat uncertainty [169]. After all, if there were *no* disturbances, or in other words if there were *no uncertainty* about the behavior of the plant, then open-loop series compensation would suffice. Of course, such an ideal situation never occurs, and is very rarely even approached. It will be shown below that using feedback it is also possible to alter the following linear system properties: stability, disturbance rejection, and robustness.

Consider thereto the "classical" feedback system in Fig. 2.7. In this feedback system the reference signals r, filtered by F, are compared with the measured output y which is corrupted by a disturbance v. Based on this difference, the controller C produces an input u to the plant (*i.e.* wind turbine) P. The output y as function of r and v is given by:

$$y = \frac{L}{I+L}Fr + \frac{I}{I+L}v = TFr + Sv \qquad (2.1)$$

with $L = PC$ the loop gain, $S = (I + L)^{-1}$ the sensitivity function and $T = (I + L)^{-1}(L)$ the complementary sensitivity function of the closed-loop system.
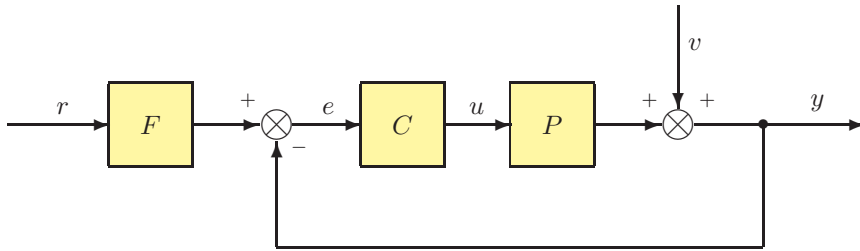
Figure 2.7: *Classical feedback system.*

From Eq. (2.1) follows that stability of the feedback system is related to stability of $(I + L)^{-1}(L)$ and consequently can be altered by a controller C. Disturbances can be attenuated by reducing S in some sense. It should be added that the "disturbance" v can represent various sources of uncertainty in the plant (including model uncertainty) and hence by attenuating disturbances the robustness of the closed-loop system is improved. A detailed analysis can be found in [21, 169].

It can be concluded that a feedback controller interacts with the dynamics of the wind turbine and has implications for, among others, the energy production and fatigue life. Ideally, use of a controller should imply an optimal energy production and increased fatigue life.

Nowadays, industrial standard PID-type (proportional-integral-derivative) controllers are normally used for wind turbine control [24, 30, 115, 283]. These are model-free, single-input-single-output (SISO), and hence single-objective approaches for which no controller synthesis algorithm is available. This implies that the controller parameters are to be determined by using rules of thumb. For a comprehensive survey of tuning methods of PID controllers, the reader is referred to Åström and Hägglund [5]. More advanced tuning methods use optimization theory to determine the PID controller parameters. The SISO controller structure, however, is not capable of simultaneously satisfying the more or less conflicting control objectives [186]. The conflicting nature of these objectives is caused by substantial interaction between the inputs (wind, pitch angle, and electromechanical torque) and outputs (electrical power and dynamic loads) of the wind turbine.

Recent advances in power electronics applied to wind turbines have drawn the attention to turbines which possess the ability to continuously adapt the rotational speed to the actual felt wind velocity. Such variable rotational speed wind turbines are multi-input-multi-output (MIMO) systems and this opens the possibility to exploit the interactions between the inputs and outputs in the system to reduce dynamic loads as well as maintaining a desired amount of energy production.

The key issue in model based control design is the use of accurate mathematical models of the system to be controlled. In general, the following holds true: "The more accurate the model describes reality, the higher the achievable performance will be". The majority of the state-of-the-art design codes has been developed for dealing with wind turbine design calculations and time-domain simulations, and consequently do not include the linearization step to obtain linear model descriptions of the complete wind turbine required for control design. Only ADAMS/WT, DUWECS, and GAROS provide a facility for linearizing the non-linear wind turbine model around an operating point. The linearization module of ADAMS/WT (*i.e.* ADAMS/WT/linear), however, neglects rotating frame effects due to the fact that the wind turbine modes can be extracted only in parked position. The result being that the significant gyroscopic coupling effects of a rotating wind turbine are neglected [171, 283]. This limitation excludes the design of controllers that exploit the dependency on both azimuth (*i.e.* rotor position) and rotational speed.

Generally it can be said that consciousness is raising that the control design should be integral part of the design of the complete system, since the dynamics of a controller interact with the rest of the dynamics of the wind turbine and so have implications for the behavior and performance of the complete system, including energy production and fatigue life.

2.3.7 Summary main features in tabular form

The aforementioned features of the discussed state-of-the-art wind turbine design codes are summarized in two tables, Table 2.1, and Table 2.2, on the next two pages. The tabular form enables the reader to get quick and comparable information. It should be noted that the design codes are listed in alphabetical order; *i.e.* the order does not express any rating.

Component	WIND TURBINE DESIGN CODES					
	ADAMS/WT	BLADED	DUWECS	FAST-AD	FLEXLAST	FLEX5
Rotor aerodynamics						
Loading	Modified BEM	BEM	BEM	BEM	BEM	BEM
Induced velocities	axial/tangential	axial/tangential	axial/tangential	axial/tangential	axial	axial/tangential
Tip effects	Prandtl	Prandtl	Prandtl	Prandtl	Prandtl	Prandtl
Root effects	–	Prandtl	Prandtl	Prandtl	–	–
Turbulent Wake State	Wilson	Garrad Hassan	Anderson	Wilson	Empirical	Glauert
Dynamic Inflow	Pitt and Peters	Pitt and Peters	FOS	Pitt and Peters	FOS	FOS
Dynamic Stall	Beddoes	Beddoes	Gormont	Beddoes	Stig Øye	Stig Øye
3D-correction	V&C	–	V&C	V&C	Snel et al.	•
Structural dynamics						
Rotor blades	Hinge + MBS	Modal	Hinge	Modal	Hinge	Modal
Lead-lag	•	6	1st-mode	1	1st-mode	2
Flap	•	6	1st-mode	2	1st-mode	2
Torsion	–	–	–	–	–	–
Hub connection	Rigid + Teeter	Rigid + Teeter	Rigid + Teeter	Rigid + Teeter	Rigid + Teeter	Rigid + Teeter
Tower	MBS	Modal	Modal	Modal	MSD	Modal
Forward bending	•	3	•	2	1st	2
Sideward bending	•	3	•	2	1st	2
Torsion	–	–	•	–	–	1
Drive Train						
Torsion	•	1st-mode	1st-mode	•	1st-mode	•
Generator description	Static	•	•	Static	Static	Static
Wind field description						
Deterministic:						
Wind shear	Linear, PL	PL, Log	Linear	Linear, PL	PL, Log, Lin	PL
Tower shadow	$(1-\cos^2)$	Dipole	$(1-\cos)$	$(1-\cos^2)$	Dipole	Dipole
Stochastic:	Veers (Snlwind-3D)	Veers (Wind3D)	White noise	Veers (Snlwind-3D)	SWING, SWIFT	Veers
Wave field description						
Deterministic:						
Wave theory	–	Airy + Non-lin	Airy, Dean	–	–	Streamline
Stochastic:						
Input spectrum	–	P-M, JONSWAP	P-M	–	–	P-M, JONSWAP
Wave theory	–	Airy	Airy	–	–	Airy
Force calculation	–	Morison	Morison	–	–	Morison
Control design						
Linearization	•		•	–	–	–

Design code features, with •: implemented in the design code, –: not not implemented in the design code, BEM: Blade-Element-Momentum theory, FOS: First-Order-System, V&C: Viterna & Corrigan, MSD: Mass-Spring-Damper system, ISD: Inertia-Spring-Damper system, FO: First-Order, PL: Power Law, and P-M: Pierson-Moskowitz.

Table 2.1: *State-of-the-art design codes features.*

WIND TURBINE DESIGN CODES

Component	GAROS	GAST	HAWC	PHATAS-IV	TWISTER	VIDYN
Rotor aerodynamics						
Loading	BEM	Modified BEM‡	BEM	BEM	BEM	BEM
Induced velocities	axial	axial/tangential	axial/tangential	axial/tangential	axial/tangential	axial/tangential
Tip effects	Prandtl	Prandtl	Prandtl	Prandtl	Prandtl	Prandtl
Root effects	–	Prandtl		Prandtl	Prandtl	–
Turbulent Wake State	?	Empirical	Glauert	Wilson ($a_c = 0.38$)	Glauert	Anderson
Dynamic Inflow	?	FOS	FOS	FOS	FOS	FOS
Dynamic Stall	?	ONERA	Stig Øye, B/L	SIMPLE†	SIMPLE	Stig Øye
3D-correction	?	Snel $et\ al.$	Manual	Snel $et\ al.$	Snel $et\ al.$	–
Structural dynamics						
Rotor blades	Modal	MBS/FES	FES	FES	FES $\mapsto$ MSD	Modal
Lead-lag	●	●	●	●	1st-mode	●
Flap	●	●	●	●	1st-mode	●
Torsion	●	●	●	●		–
Hub connection	Arbitrary	Rigid + Teeter	Arbitrary	Rigid + Teeter	Rigid + Teeter	Rigid + Teeter
Tower	FES/Modal	MBS/FES	FES	Modal	FES $\mapsto$ MSD/ISD	Modal
Forward bending	●	●	●	8	$1^{st} + 2^{nd}$	2
Sideward bending	●	●	●	8	1st	2
Torsion				1	1st	–
Drive Train						
Torsion	●	●	●	●	1st-mode	1st-mode
Generator description	–	–	Static + FO	Static + FO	Static	●
Wind field description						
Deterministic:						
Wind shear	Power Law	Arbitrary	Arbitrary	Power Law, Log, Lin	Arbitrary	Linear, Power Law
Tower shadow	(1-cos)	Dipole	Dipole	Dipole	Dipole	Dipole
Stochastic:	Shinozuka/Jan	Veers, Mann	Veers, Mann	SWIFT	EWS	Sosisw
Wave field description						
Deterministic:						
Wave theory	–	–	–	Non-linear 5th order Stokes ROWS wave field	–	–
Stochastic:						
Input spectrum	–	–	–	P-M, JONSWAP	–	–
Wave theory	–	–	–	Airy	–	–
Force calculation	–	–	–	Morison	–	–
Control design						
Linearization	●		–	–	–	–

Table 2.2: *State-of-the-art design codes features (continued).*

41

Design code features, with ●: implemented in the design code, –: not not implemented in the design code, BEM: Blade-Element-Momentum theory, FOS: First-Order-System, B/L: Beddoes/Leishman, ISD: Inertia-Spring-Damper system, MSD: Mass-Spring-Damper system, FO: First-Order, P-M: Pierson-Moskowitz, ‡: Optional Vortex model, †: The dynamic stall model ONERA is only implemented in a "garage" version.

2.4 Conclusions

In this chapter the main features of the state-of-the-art wind turbine design codes have been investigated in order to judge the appropriateness of using one of these to solve the main thesis problem. When comparing the design tool demands listed in Section 2.1 with the design code overview presented in Section 2.2 and the main features listed in Table 2.1 and Table 2.2, the following conclusions can be drawn:

- There is a wide variety in wind turbine design codes for modeling a wind turbine's dynamic behavior or to carry out design calculations. Most of the design codes, however, have been specially developed to deal with wind turbine design calculations and time-domain simulations. The intended use is either for intermediate design studies or for detailed design studies in the final stage;

- The sophistication of these codes has increased enormously over the last two decades. This development has been driven mainly by the trend to reduce unnecessary design conservatism in order to reach cost-effective wind turbines. However, no consensus has been reached on the best modeling approach and basic features to be included. In addition, despite all recent progress in wind turbine aerodynamics, the state-of-the-art wind turbine design codes still suffer from a substantial semi-empirical content;

- The validation of the various design codes has received little attention, although all codes claim that the models have been validated against experimental data [32, 214, 227, 230, 251]. This holds especially for flexible, variable speed wind turbines since validation for this type of turbines is described in a few cases only. This situation should change given the trend towards increasingly lightweight and structurally flexible wind turbines operating at variable speed [228].

  In addition, the experimental data has been acquired from wind turbines in the 500 kW class. Present wind turbine sizes are in multi-megawatt class, implying that the design codes are used outside their range of validity [146];

- Most wind turbine design codes currently in use rely on a formulation that is adequate for simulation, but not for the design (and easy implementation) of optimal operating strategies.

Judged from our point of view, the most obvious shortcomings are that the indispensable bilateral coupling between the design of a new wind turbine and the design and implementation of its control system is missing in the existing design codes and that model validation has not received the attention required for obtaining economic viability of wind power. In addition, the modeling of the electromagnetic part of the generator plus conversion system has received too little attention.

Combination of the aforementioned conclusions leads to the overall conclusion that it is advisable to develop a new wind turbine design code. This code should provide wind turbine designers and control engineers with a tool that enables them to rapidly and easily build accurate dynamic models of wind turbines. Preferably

within the MATLAB®/SIMULINK® environment. The main reasons for this are: SIMULINK® is a *general-purpose* simulation program with access to sophisticated and reliable mathematical algorithms. In addition, this environment offers rapid and easy (real-time) controller design and implementation due to the seamless integration with MATLAB® and dSPACE®. The main disadvantage is that it is time-consuming to implement the state-of-the-art features of wind turbine design codes in a new environment.

Chapter 3

Dynamic wind turbine model development

In Chapter 2 it has been concluded that the current wind turbine design codes are not suitable for design, and easy implementation of optimal operating strategies. Consequently, it is sensible to develop a new wind turbine design code. The models within this code should meet the requirements specified in Section 1.2. The fundamental requirement is, of course, that the models are suited for the design of optimal operating strategies.

The layout of this chapter is as follows. Section 3.1 presents the general wind turbine model setting. Next, in Section 3.2 the main properties of the wind module are discussed. Section 3.3 treats the aerodynamic modeling. In Section 3.4 a systematic, rapid method of determining accurate dynamic structural models of flexible wind turbines is developed. Section 3.5 treats the modeling of the electrical module. Finally, Section 3.6 summarizes the main modeling features.

3.1   Introduction: general wind turbine model

A horizontal-axis wind turbine basically consists of five physical components, *viz.* rotor, transmission, generator, tower (including foundation) and control system. The rotor converts wind power into mechanical power, which is represented by the product of torque and angular velocity of the rotor shaft. This velocity is increased by the transmission in order to come to an angular velocity well-suited for the generator. The generator in its turn converts the mechanical power into electrical power. The transmission as well as the generator are housed in the nacelle. The tower plus foundation are needed to support the nacelle and besides that, they place the rotor into more windswept layers of air. Finally, the main goal of the control system is to enhance the closed-loop performance.

Judged from the point of view of control design, the most obvious shortcoming in most of the design codes listed in the previous chapter, is the lack of possibilities for

integration of the design of a new wind turbine and the design of its control system. In order to enable this integrated design, we have developed a novel design tool called DAWIDUM. DAWIDUM is equipped with a Graphical User Interface (GUI) in order to simplify the operations involved with creating accurate dynamic models of wind turbines as well as facilitating controller design. DAWIDUM has been developed in the MATLAB®/SIMULINK® environment. For a detailed survey of the features of DAWIDUM the reader is referred to the User's Guide [187]. Implementation issues are also discussed in this guide.

Within DAWIDUM any wind turbine system is modeled as a set of bilaterally coupled modules as illustrated in Fig. 3.1. Bilateral couplings imply that the transfer of power is the result of mutual interaction instead of being imposed upon the system or upon the surroundings. To have one system impose power transfer to another system regardless of the state of the receiving system is physically not conceivable, and hence bilateral couplings should therefore be preferred. The general wind turbine model consists of the following five modules:

- **Wind**

- **Aerodynamic**

- **Mechanical**

- **Electrical**

- **Controller**

The aerodynamic module converts the 3-D stochastic wind field generated in the wind module into aerodynamic forces. These forces are the input to the mechanical module which, in turn, converts these to velocities. The mechanical part of a generator is modeled in this module. The electrical module describes the electromagnetic part of a generator. Here mechanical power is converted into electrical power using torque set-points calculated by the controller.
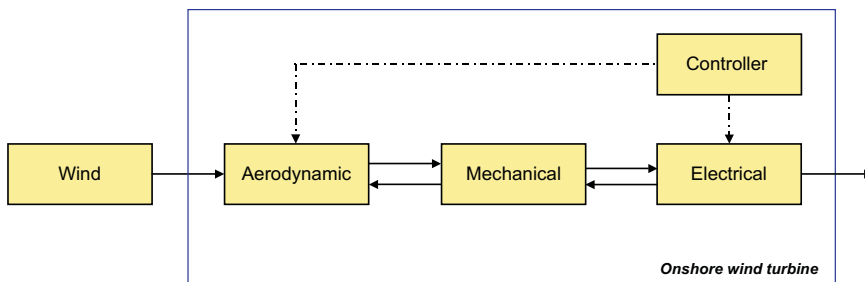
Figure 3.1: *Wind turbine modeled as a set of four interacting modules (i.e. aerodynamic, mechanical, electrical, and controller) and one input module (i.e. wind).*

Notice that if the electromechanical torque equals the aerodynamic torque, an equilibrium is achieved, and as a result the wind turbine's rotational speed will be

constant. Acceleration and deceleration to new speed set-points will be achieved by decreasing or increasing the electromechanical torque, respectively. Furthermore, if there are also mechanical means of controlling the aerodynamic torque, *e.g.* pitch control (indicated by the dashed arrow in Fig. 3.1), greater operational flexibility is achieved [106]. This can be easily seen by recognizing that pitch control can now be used to follow minute-to-minute fluctuations in aerodynamic power, while the (almost instantaneous) torque control can focus on fatigue load reduction.

It should also be mentioned that the presented model structure can be easily extended to being able to handle offshore wind turbines as well. The resulting model structure is shown in Fig. 3.2. The hydrodynamic module converts the wave field generated in the wave module into hydrodynamic forces. It is assumed that the structural dynamics are not influencing the wave field.
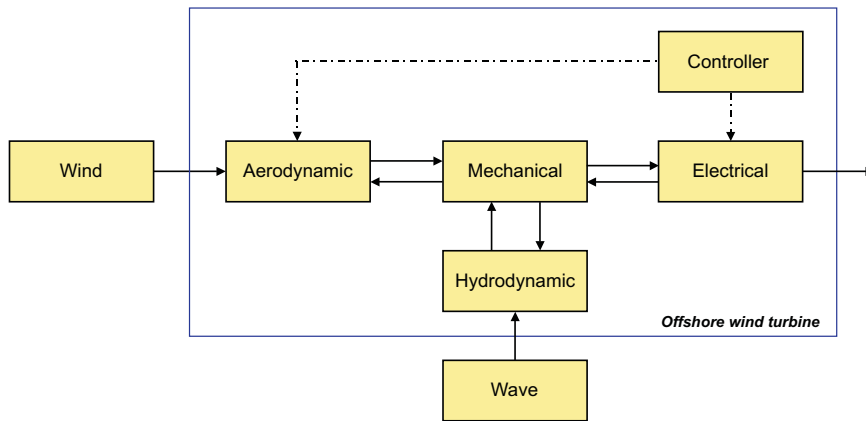
Figure 3.2: *Wind turbine model structure of Fig. 3.1 extended with a wave and hydrodynamic module required for offshore applications.*

The division of the complete wind turbine model into modules is based on the assumption that the modules are interacting via specified interaction variables. This creates a modular structure in which the user can easily exchange modules. Linked together correctly the modules will describe the complete wind turbine behavior. Hence, the user can compose a specific wind turbine configuration by choosing for each type of module (electrical, mechanical *et cetera*) the appropriate one out of the available DAWIDUM library. Moreover, any module can be modified or can be written totally new by the user as long as it is compatible with the presented model structure.

In the next sections we will discuss the main properties of the aforementioned modules as well as the interaction variables. We start with the wind module.

3.2 Wind module

Wind, in the macro-meteorological sense, are movements of air masses in the atmosphere. These large-scale movements are generated primarily by differences in temperature within the atmosphere. These temperature differences are due to the unequal heating of the crust of the earth by the sun: the equatorial regions receive more solar energy than the polar regions [65]. The variations in wind velocity and direction due to atmospheric turbulence, on the other hand, form the micro-meteorological range. Consequently, the behavior and structure of the wind will vary from site to site dependent on the general climate of the region, the physical geography of the locality, the surface condition of the terrain around the site, and various other factors.

Meteorologists estimate that about 1% of the incoming solar radiation is converted to wind energy ($\approx 1.2 \cdot 10^{15}$ W). According to the World Meteorological Organization it is possible to extract about $2 \cdot 10^{13}$ W from the atmosphere due to limitations in height and accessibility. Compare this figure with the world electricity consumption (1999) of $12.8 \cdot 10^{12}$ kWh (*i.e.* an average of $0.15 \cdot 10^{13}$ W) [58].

To be able to predict the yield of wind turbines accurate information about the undisturbed wind velocity V_w is essential. This knowledge is also necessary if the turbines are designed to withstand the imposed loads with safety and at cost that are competitive with conventional energy production (fossil or nuclear fuel) and other renewable energy sources (including biomass, photovoltaics, waterpower and sun collectors). Combination of both results leads to the conclusion that wind simulation should be an integral part of wind turbine structural design, and analysis.

DAWIDUM's wind module consists of two submodules, *viz.* "deterministic" and "stochastic". Both contain different wind models. All models have an input-output configuration as depicted in Fig. 3.3. It is assumed that neither the aerodynamics nor the structural dynamics are influencing the undisturbed wind part. Consequently, the only output of this module is the undisturbed wind velocity (vector) V_w. Observe that the wind vector can be a one, two or three-dimensional function of time, depending on the chosen wind model. The wind vector is described with respect to the blade element reference frame (*see* Fig. 3.11 on page 58).
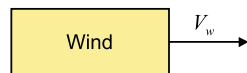
Figure 3.3: *Wind module input-output configuration.*

The deterministic submodule allows the following undisturbed wind inputs to be specified: a uniform wind field (*i.e.* V_w is constant both in space and time), a sequence of upward and downward stepwise changes in the wind velocity, and a user specified WindData.mat file. The stochastic submodule is able to read the output generated by SWING-4 (*see* Subsection 2.3.4 for detailed information about this wind field generator).

3.3 Aerodynamic module

This section treats the aerodynamics. DAWIDUM's aerodynamic module has an input-output configuration as depicted in Fig. 3.4. The only input to this module is the undisturbed wind velocity V_w generated by the wind module. The aerodynamic module is bilaterally coupled to the mechanical module through the velocity vector $\dot{x}$ (containing the blade movements with respect to the blade element reference frame), and the aerodynamic forces F_{aero}. In other words, the interaction between the aerodynamics and the structural dynamics takes place via the blade movements and the aerodynamic forces. This interaction is indispensable for accurate modeling of the aero-elastic behavior of, in particular, flexible wind turbines.
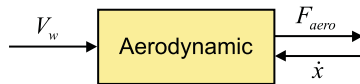
Figure 3.4: *Aerodynamic module input-output configuration.*

3.3.1 Introduction

The accurate computation of the aerodynamic forces is a very challenging problem. First of all, the wind environment in which wind turbines generally operate is variable both in space and time and has a strong stochastic content. Because the dimensions of atmospheric turbulence are of the same order as the rotor diameter, individual blades can be engulfed in coherent turbulence bells which lead to severe fatigue loading that significantly can reduce the lifetime of the structure. Secondly, the blade sections can see highly variable, large angle unsteady flows at reduced frequencies, so that non-linear and unsteady aerodynamic effects are significant. Finally, the rotor blades as well as the support structure will in the (near) future become more and more flexible due to the move from relatively small and rigid constant speed wind turbines towards increasingly lightweight and structurally flexible wind turbines operating at variable speed.

Obviously, we need to have models that accurately describes the mutual coupling between the aerodynamics and the structural mechanics in order to make it possible to identify and resolve such (aero-elastic) stability problems already in the design phase of a wind turbine. The starting point of the modeling of the aerodynamics is the Rankine-Froude actuator-disk model which will be discussed below.

3.3.2 Rankine-Froude actuator-disk model

The simplest and oldest mathematical model which describes the wind turbine dynamics is the Rankine-Froude actuator-disk model. The concept was introduced by R.E. Froude in 1889 [68], after W.J.M. Rankine [231] had introduced the momentum theory. In this model the rotor is replaced by an "actuator-disk", which is a circular

surface of zero thickness than can support a pressure difference, and thus decelerate the air through the disk. Physically, the disk could be approximated by a rotor with an infinite number of very thin, draggles blades rotating with a tip speed much higher than the wind velocity. The actuator-disk model is thus an approximation of a real wind turbine rotor (which has only a small number of blades). As a result the flow of the actuator-disk will be very different from that of a real rotor, which is unsteady, with a wake of discrete vorticity corresponding to the discrete loading.

The principal use of the actuator-disk model is to obtain a first estimate of the wake-induced flow, and hence the total induced power loss. Note that the actual induced power loss will be larger than the actuator-disk result because of the non-uniform and unsteady induced velocity. The assumptions on which the Rankine-Froude actuator-disk theory are based are as follows:

1. Steady, homogeneous wind;

2. No obstructions to wind flow either upstream or downstream;

3. Uniform flow velocity at disk;

4. Wind flow passing through disk separable from remaining flow by well-defined streamtube (*see* Fig. 3.5);

5. Wind flow incompressible (*i.e.* air density, ρ, is constant);

6. No rotation of flow produced by disk.

Assumption 3 requires that the disk slows the wind equally at each radius, which is equivalent to assuming uniform thrust loading at the disk. Uniform thrust loading is, in turn, equivalent to considering an infinite number of rotor blades.
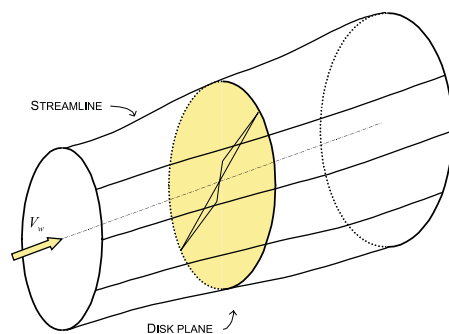
Figure 3.5: *The energy extracting streamtube of a wind turbine. By removing some of the kinetic energy in the wind, the wind flow that passes through the disk plane will slow down. Assuming incompressible wind flow, the cross-sectional area of the streamtube must expand in order to accomodate the slower moving air.*

Now consider the flow diagram of Fig. 3.6 for a cylindrical control volume of cross-sectional area S and note sections 0, 3, 2, and 1. Let A be the area of the rotor disk and ρ be the air density. Wind approaches the rotor at velocity V_w far upstream at section 0 at static pressure p_0. Kinetic energy is extracted by the rotor, and the reduced velocity causes the the streamline to expand.
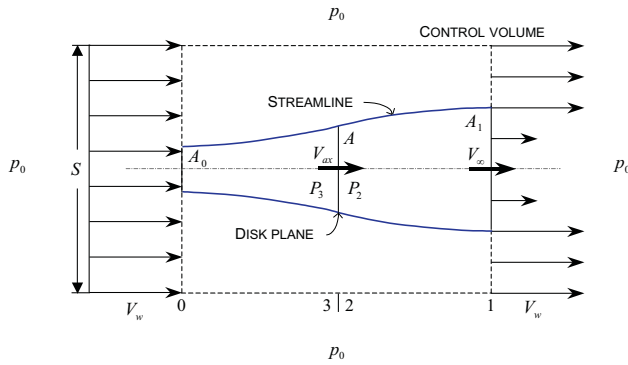
Figure 3.6: *One-dimensional flow past the disk plane of an actuator-disk.*

Fig. 3.7 shows this principle for a non-loaded and loaded machine. For instance, for a turbine with zero loading, the wind velocity in the rotor plane (V_{ax}) is equal to the undisturbed wind velocity (V_w), while an operating and hence loaded turbine slows down the wind velocity to a lower value. If the velocity decrease induced by the rotor is v, then the velocity at the disk is $V_w - v = V_{ax}$, while far downstream at section 1 the wind has been slowed further to velocity V_∞ and the pressure has returned to p_0. The difference between the axial component of the wind velocity and the axial flow velocity in the rotor plane is usually called the "induced" velocity, the velocity induced by the presence of the turbine.
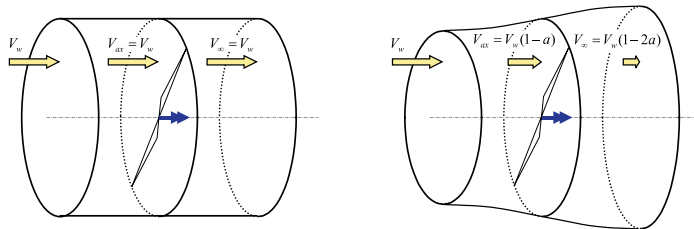
Figure 3.7: *Wind turbine with (r) and without (l) loading. V_w is the undisturbed wind velocity, V_{ax} is the wind velocity at the rotor disk position, and V_∞ is the velocity far downstream, in the turbine wake. The unloaded wind turbine is transparent to the wind, the loaded turbine decelerates the wind. A change in loading implies a change in "induced" velocity.*

The momentum loss of the fluid is the result of the thrust D_{ax} that the rotor exerts against the flow, combined with the net resultant of the external pressure on the control volume, as shown in Fig. 3.6. Since the static atmospheric pressure, p_0 acts on the entire control volume, its net resultant is zero.

Within the streamtube, continuity requires that $V_w A_0 = V_{ax} A = V_\infty A_1$. Writing the continuity equation for flow outside the streamtube between sections 0 and 1, it follows that there must be a net flow, Φ_f, out the sides of the control volume equal to the following:

$$\Phi_f = V_w \left[(S - A_0) - (S - A_1)\right] = V_w (A_1 - A_0) \tag{3.1}$$

Newton's second law or equivalently *law of motion* can be generalized from particles to fluids: "At any instant in steady flow the resultant force acting on the moving fluid within a fixed volume of space equals the net rate of outflow of momentum from the closed surface bounding that volume". This is known as the *momentum theorem*. Writing the momentum theorem for the cylindrical control volume, it follows

$$\rho V_w^2 S - D_{ax} = \rho V_w^2 (S - A_1) + \rho V_\infty^2 A_1 + \rho \Phi_f V_w \tag{3.2}$$

Substituting Φ_f from Eq. (3.1) and $V_w A_0 = V_\infty A_1$ gives the thrust as

$$D_{ax} = \rho A_1 V_\infty (V_w - V_\infty) \tag{3.3}$$

To slow the wind, a force must be manifested as a pressure drop across the disk. After all, a sudden step change in velocity is not possible because of the enormous accelerations and forces this would require. The static pressure drop just ahead the disk is p_3 and just behind the disk p_2. Since it is assumed that these pressures do not vary with time, it is also assumed that there is no periodicity in the flow velocity at the rotor plane, a condition that is strictly true only for an infinite number of blades. Applying the Bernoulli theorem from section 0 to section 3 and again from section 2 to section 1, we have

$$\frac{1}{2}\rho V_w^2 + p_0 = \frac{1}{2}\rho V_{ax}^2 + p_3 \tag{3.4}$$
$$\frac{1}{2}\rho V_{ax}^2 + p_2 = \frac{1}{2}\rho V_\infty^2 + p_0 \tag{3.5}$$

The thrust on the rotor is then

$$D_{ax} = A(p_3 - p_2) \tag{3.6}$$

Solving for the pressure difference using Eq. (3.4) and (3.5) gives

$$D_{ax} = \frac{1}{2}\rho A (V_w^2 - V_\infty^2) \tag{3.7}$$

Equating Eq. (3.3) and (3.7) and using $A V_{ax} = A_1 V_\infty$, we find that

$$V_{ax} = \frac{1}{2}(V_w + V_\infty) \tag{3.8}$$

Thus, the velocity at the disk is the average of the upstream and downstream velocities. Defining an axial induction factor, a, as the fractional decrease in wind velocity between the free stream and the rotor plane represented by

$$a = \frac{v}{V_w} \tag{3.9}$$

it follows that

$$V_{ax} = V_w(1 - a) \tag{3.10}$$

Also

$$V_\infty = V_w(1 - 2a) \tag{3.11}$$

For $a = 0$, the wind is not decelerated and no power is extracted, whereas for $a = 0.5$, the far wake velocity vanishes, and, without presence of flow behind the turbine, no power is generated. The power extracted from the wind by the rotor is:

$$P = \tfrac{1}{2}\rho V_w^2 A V_{ax} - \tfrac{1}{2}\rho V_\infty^2 A V_{ax} \quad = \quad \tfrac{1}{2}\rho A V_{ax}(V_w^2 - V_\infty^2) \tag{3.12}$$

$$= \quad \tfrac{1}{2}\rho A V_{ax}(V_w + V_\infty)(V_w - V_\infty) \tag{3.13}$$

Substituting V_{ax} from Eq. (3.10) and V_∞ from Eq. (3.11), we find that

$$P = \tfrac{1}{2}\rho A V_w^3 4a(1 - a)^2 \tag{3.14}$$

A power coefficient C_p is then defined as

$$C_p = \frac{P}{\tfrac{1}{2}\rho A V_w^3} \tag{3.15}$$

where the denominator represents the kinetic energy of the free-stream wind contained in a streamtube with an area equal to the disk area. Substituting Eq. (3.14) in Eq. (3.15) results in

$$C_p = 4a(1 - a)^2 \tag{3.16}$$

The maximum value of the power coefficient C_p occurs when

$$\frac{d}{da}C_p = 4(1 - a)(1 - 3a) = 0$$

which gives a value of $a = \tfrac{1}{3}$. Hence

$$C_{p,max} \quad = \quad \tfrac{16}{27} \cong 0.59259 \tag{3.17}$$

$$V_{ax} \quad = \quad \tfrac{2}{3}V_w \tag{3.18}$$

$$V_\infty \quad = \quad \tfrac{1}{3}V_w \tag{3.19}$$

Thus the maximum amount of energy extraction from the wind equals the $\tfrac{16}{27}$th part of the kinetic energy in the wind. This limit is often referred to as the "Betz limit", or more accurately the "Lanchester-Betz limit". The power coefficient C_p versus the induction factor a is shown in Fig. 3.8. This plot illustrates that the sensitivity of C_p to changes in a in the region $0.2 \leq a \leq 0.5$, is much less than for $a < 0.2$. The

power coefficient C_p has proved to be the most useful measure of the effectiveness of a wind turbine [261]. The actuator disk "efficiency" η_{ad} (*i.e.* power output divided by power input), on the other hand, is

$$\eta_{ad} = \frac{P}{\frac{1}{2}\rho V_w^2 V_{ax} A} = 4a(1-a) \tag{3.20}$$

since the mass flow rate through the actuator disk is not $\rho A V_w$, but $\rho A V_{ax}$ or equivalently $\rho A V_w(1-a)$ using Eq. (3.10). The maximum efficiency of 1 occurs at $a = \frac{1}{2}$ implying zero velocity in the wake ($V_\infty = 0$) and a power coefficient of $\frac{1}{2}$. The actuator disk efficiency is $\frac{8}{9} \cong 0.889$ at the maximum power coefficient of 0.59259.
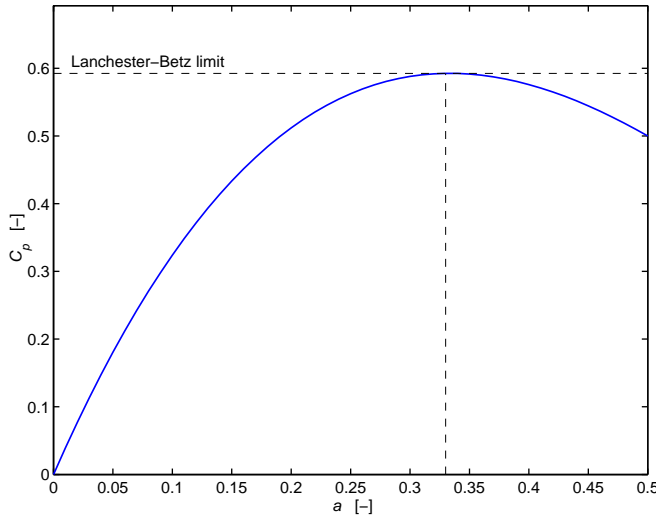
Figure 3.8: *Power coefficient C_p as function of the axial induction factor a. Solid line: $C_p = 4a(1-a)^2$. The maximum value of C_p occurs when $a = \frac{1}{3}$ and is equal to $C_{p,max} = \frac{16}{27} = 0.59259$.*

It must be noted that according to Van Kuik [139] the radial force assumption does not hold true owing to an edge singularity of the actuator disk flow, and that the "real" maximum of the power coefficient is to be expected to be slightly higher than the Betz limit. Apart from this, it is possible to reach much higher power coefficients (*i.e.* to by-pass the optimum of Betz) with additional devices like tip vanes [262]. These devices are all based on the concentrator and/or ejector principle. But to date almost no such devices have progressed beyond the experimental stage, mainly due to their higher complexity and expense in comparison to the free-running turbine.

The pressure and velocity relationships of an energy extracting actuator-disk are shown in Fig. 3.9.
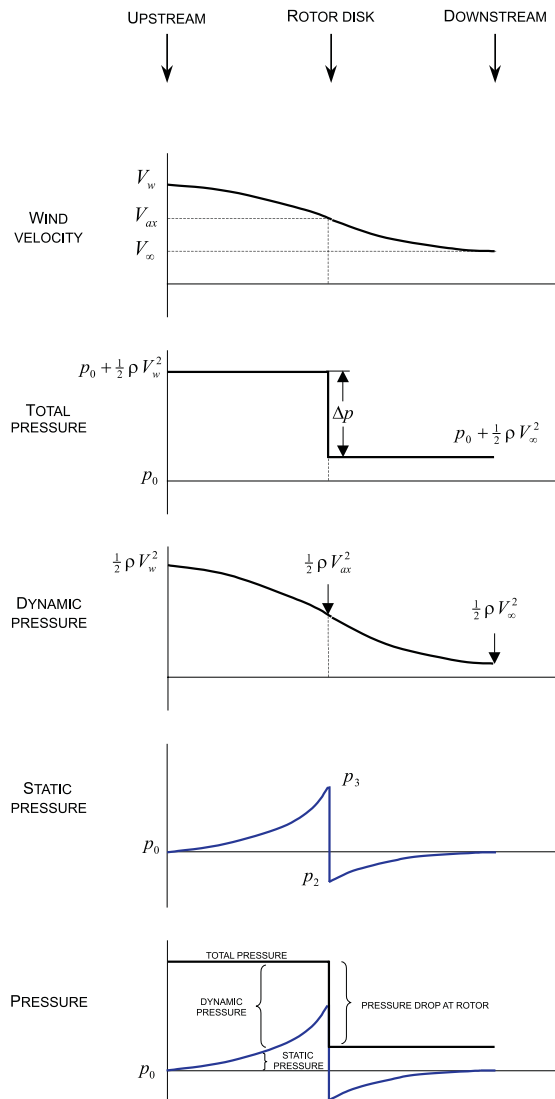
Figure 3.9: *Pressure relationships of an energy extracting actuator-disk. A wind turbine extracts kinetic energy from the wind by slowing down the wind. This results in a rise in the static pressure. Across the rotor swept area there is a drop in static pressure such that, on leaving, the air is below atmospheric pressure. As the air proceeds downstream the pressure climbs back to the atmospheric value causing a futher slowing down of the wind. Thus, between upstream and downstream conditions, no change in static pressure exists but there is a reduction in kinetic energy.*

55

The Rankine-Froude actuator-disk model has the following implications:

- The wind velocity at the rotor plane is always less than the free-stream velocity when power is being absorbed (*i.e.* $V_{ax} < V_w$);

- This model assumes no wake rotation, *i.e.* no energy wasted in kinetic energy of a twirling wake;

- Even with the best rotor design, it is evidently not possible to extract more than about 60 percent of the kinetic energy in the wind.

Note that the range of the axial induction factor, a, is from zero for no energy extraction to one-half, at which point the wind theoretically slows to zero velocity behind the rotor. Outside this range, the assumptions made in deriving this model are violated.

Additional data that can be derived from this model include the thrust loading on the rotor. The thrust on the rotor is:

$$D_{ax} = \tfrac{1}{2}\rho A(V_w^2 - V_\infty^2) \tag{3.21}$$

which for $V_\infty = V_w(1 - 2a)$ simplifies to

$$D_{ax} = \tfrac{1}{2}\rho V_w^2 A\left[4a(1 - a)\right] = qA\left[4a(1 - a)\right] \tag{3.22}$$

where q is the dynamic pressure.

If we were thinking of the rotor as a propeller, we would define a thrust coefficient, as follows:

$$C_t = \frac{D_{ax}}{qA} \tag{3.23}$$

On the other hand, if we were to think of D_{ax} as a drag force on an equivalent flat plate of area equal to that of a rotor disk, we can define a drag coefficient, as follows:

$$C_{dax} = \frac{D_{ax}}{qA} \tag{3.24}$$

In either case, it is apparent from Eq. (3.16) that for these definitions

$$C_t = C_{dax} = 4a(1 - a) \tag{3.25}$$

Since a flat plate has a drag coefficient of about 1.28, we can note that, for $a = \tfrac{1}{3}$, we obtain an equivalent drag coefficient of $\tfrac{8}{9}$ for a rotor operating at the maximum C_p condition. Thus the rotor thrust is about 30 percent less than that of a flat plate equal in diameter to the rotor. Therefore, it is easy to see that the thrust loads generated by continuing to operate in high winds can be very large, requiring a very strong rotor and tower.

The Glauert limit

The Rankine-Froude actuator-disk model neglects both aerofoil drag and wake rotation (or "swirl"). As a result, the maximum possible level of extracted power will therefore be lower than that predicted by the Lanchester-Betz limit. Glauert developed a simple model for a rotating actuator-disk (*i.e.* with an infinite number of draggles blades) that includes the effect of wake rotation. The interested reader is referred to Spera [279] for derivation of this model. The corresponding limit is referred to as the "Glauert limit" and is illustrated by the solid line in Figure 3.10. At low tip-speed ratios, the maximum possible power coefficient is reduced because of large rotational kinetic energy captured in the wake. At high tip-speed ratios, the power coefficient approaches $C_{p,max} \cong 0.59259$ (Lanchester-Betz limit) and the wake rotation reduces to zero. The tip-speed ratio is defined here as the ratio between the rotor circumferential speed and the undisturbed wind velocity. Furthermore, typical effects of changing the number of blades N_b and changing the design drag to lift ratio D/L on the power coefficient C_p are added using the empirical relation of Wilson *et al.* [307]:

$$C_p = 0.59259 \cdot \left[\frac{\lambda N_b^{0.67}}{1.48 + (N_b^{0.67} - 0.04)\lambda + 0.0025\,\lambda^2} - \frac{1.92\lambda^2 N_b}{1 + 2\lambda N_b} \cdot D/L \right] \quad (3.26)$$

Note that for an infinite number of draggles blades (*i.e.* $N_b \to \infty$ and $D/L = 0$) the maximum power coefficient predicted by the empirical relation (3.26) equals the Lanchester-Betz limit for all tip-speed ratios λ.
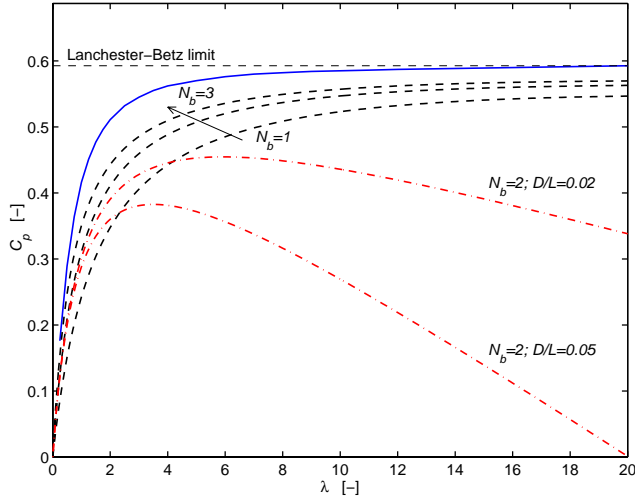
Figure 3.10: *Typical effect of the number of blades N_b and the design drag to lift ratio D/L on the power coefficient C_p. Solid line: Glauert limit, dashed lines: $N_b = 1, 2, 3$ and $D/L = 0$, and dashed-dotted lines: $N_b = 2$, $D/L = 0.02$ and $D/L = 0.05$ respectively.*

3.3.3 Blade element momentum model

The combined blade element and momentum theory is an extension of the Rankine-Froude actuator disk theory described in Section 3.3.2. The blade element momentum theory divides the rotor blades into a number of radial blade sections (elements), each at a particular angle of attack. These blade elements are assumed to have the same aerodynamic properties as an infinitely long (or 2-D) rotor blade with the same chord, and aerofoils. This implies that 2-D aerofoil data (*i.e.* lift, drag and moment coefficients) obtained from wind tunnel experiments may be used. The airflow from upstream to downstream of the elements is, in turn, divided into annular stream tubes. It is assumed that each stream tube can be treated independently from adjacent ones. Subsequently, the theory outlined in the preceding section is applied to each blade element, instead of to the rotor disk as a whole. The velocity component in the span-wise direction (*i.e.* perpendicular to the blade cross-section) is ignored. Finally, the total load is calculated by adding up the forces from all the elements.

The contribution of each blade element to the lift and drag force can be derived as follows. Consider an annular cross-section of a rotor blade as depicted in Fig. 3.11, and examine an element of length Δr of one blade.
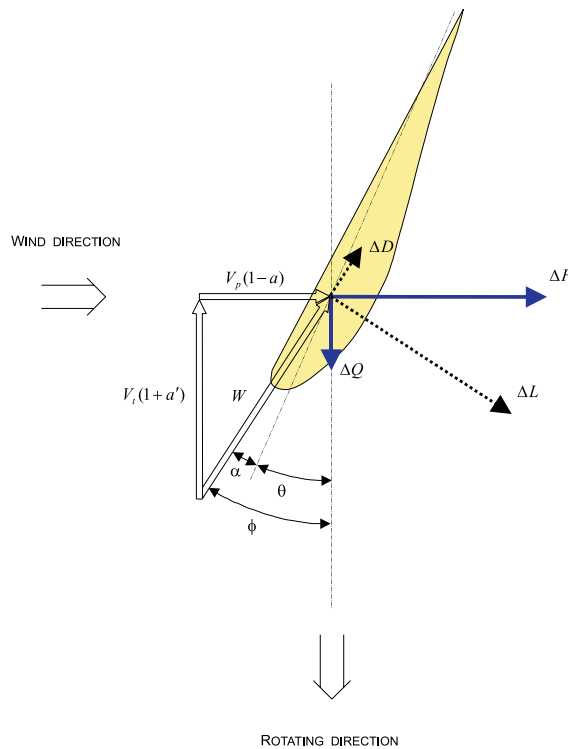
Figure 3.11: *Blade element velocities, and aerodynamic forces w.r.t the blade local coordinate frame with the chord line as reference.*

ΔL	Blade element lift force
ΔD	Blade element drag force
ΔF	Axial components of aerodynamic forces
ΔQ	Tangential components of aerodynamic forces
α	Angle of attack of aerodynamic (or resultant) velocity
θ	Pitch angle of rotor blade
ϕ	Direction of aerodynamic velocity related to the rotor plane
V_p	Local, undisturbed, perpendicular wind velocity
V_t	Local, undisturbed, tangential wind velocity
W	Local, undisturbed, aerodynamic wind velocity
a	Axial induction factor: represents the fractional decrease in wind velocity between the free stream and rotor plane
a'	Tangential induction factor: represents the swirl velocity of the air

The net effect on air flowing through this annular section of the rotor disk results from the forces and moments on all the blades. The instantaneous relative undisturbed wind velocity experienced by a blade element is

$$W = \sqrt{(V_p(1 - a))^2 + (V_t(1 + a'))^2} \tag{3.27}$$

under an angle

$$\phi = \arctan \frac{V_p\,(1 - a)}{V_t\,(1 + a')} \tag{3.28}$$

It must be noted that the tangential induction factor a' in the above equation is as a rule an order smaller than the axial induction factor a.

Due to the special profile of a rotor blade, higher velocities will occur at the top of the blade rather than on the bottom side. According to the Bernoulli theorem, this leads to an underpressure at the first mentioned side of the blade and an overpressure at the latter. This air pressure difference is the driving force behind the rotation of the rotor. More precisely, the pressure distribution around an aerofoil can be represented by two forces, a lift L and a drag D force, and one torque, the pitching moment M. Both forces and the pitching moment are usually applied at a location $\frac{1}{4}$ chord back from the leading edge (*i.e.* the so-called aerodynamic center) since, on most low speed aerofoils, the magnitude of the pitching moment is essentially constant up to maximum lift at that specific location. For symmetric aerofoils, the aerodynamic moment about the aerodynamic center is zero for all angles of attack. With camber, the moment is non-zero (normally negative for positive camber) and constant for thin aerofoils. Using the aerodynamic center as the location where the aerodynamic forces are applied simplifies the aerodynamic analysis. The effect of the pitching moment, however, is neglected in most design codes.

The angle of attack of the relative wind velocity (α) is determined by the difference between the angle of inflow (ϕ) and the pitch angle (θ):

$$\alpha = \phi - \theta \tag{3.29}$$

Due to the resultant velocity W the blade cross-section exerts a quasi-steady aero-dynamic lift force ($\Delta L \perp W$)

$$\Delta L = \tfrac{1}{2}\rho\, c\, W^2 C_l^{[2D]}(\alpha)\Delta r \qquad (3.30)$$

and a quasi-steady aerodynamic drag force ($\Delta D \parallel W$)

$$\Delta D = \tfrac{1}{2}\rho\, c\, W^2 C_d^{[2D]}(\alpha)\Delta r \qquad (3.31)$$

with

c	Local blade chord (varies along the blade: $c = f(r)$)
$C_l^{[2D]}$	Blade element 2-D lift coefficient
$C_d^{[2D]}$	Blade element 2-D drag coefficient
ρ	Air density
Δr	Length of blade section

The dimensionless aerodynamic coefficients C_l, C_d, and C_m are – among other things – functions of the angle of attack α, Reynolds number Re and Mach number Ma (compressibility of the airflow). These coefficients have to be either determined for each type of aerofoil separately by means of stationary windtunnel experiments and/or CFD computations or can be obtained from a database. An example of such a database is the Aërodynamische Tabel Generator (ATG) described by Timmer *et al.* [290].

Typical variation of these coefficients are shown in Fig. 3.12. The sudden change in the coefficients at $14°$ is due to flow separation from the suction side of the aerofoil; this is called stall.

The Reynolds number varies in practice between zero and $2 \cdot 10^6$ [119] depending on chord and undisturbed wind velocity of a blade-element. However, this dependency is often neglected, although the Reynolds number significantly affects the values for the lift and drag coefficients (*see* either Sharpe [259] or the aerofoil data option on DAWIDUM's Plot menu for the variation of aerofoil characteristics with the Reynolds number).

From the above discussion it follows that the quasi-steady aerodynamic lift and drag forces are proportional to the local blade chord c, are quadratic in resultant wind velocity W, and are approximately linear in the angle of attack α in the attached flow region.

In order to calculate the lift ΔL, and drag ΔD on a section of a rotor blade it suffices to determine the local, undisturbed, resultant wind velocity W, which consists of four components: the undisturbed wind velocity V_w (including yawed flow, wind shear, and tower shadow, see Section 2.3.4), the velocity of the blade element itself (including rotor shaft rotation, flap motion, lead-lag motion and the velocity of the tower top, resulting from the mechanical model which will be discussed in Section 3.4) and the induced velocities. Next, the determination of the induced wind velocities shall be described.
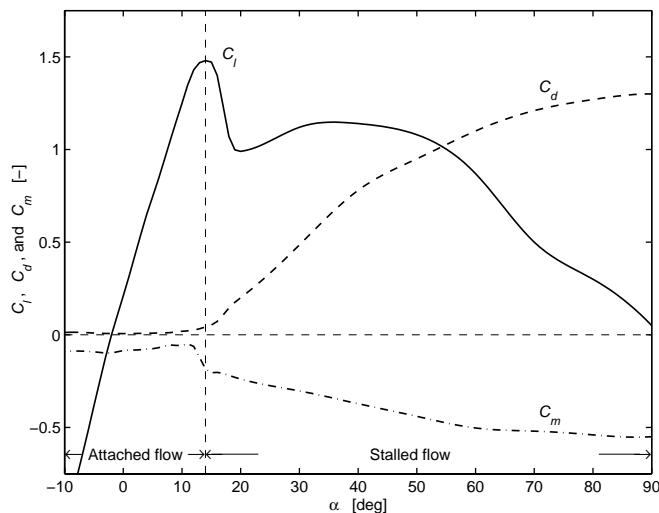
Figure 3.12: *Typical variation of the 2-D lift, drag, and moment coefficient as function of the angle of attack α. Solid curve: lift coefficient C_l, dashed curve: drag coefficient C_d, and dashed-dotted curve: moment coefficient C_m about the aerodynamic center.*

Induced velocities

In the equilibrium situation, the axial flow in the rotor plane of a wind turbine, depends on the wind velocity, and on the degree of loading (*i.e.* the size of axial force $D_{ax} = \sum \Delta F$) of the turbine. For instance, for a turbine with zero loading, the wind velocity at the rotor disk position (V_{ax}) is equal to the undisturbed wind velocity (V_w), while an operating, and hence loaded turbine slows down the wind velocity to a lower value (see Fig. 3.7 on page 51). The difference between the axial component of the wind velocity and the axial flow velocity in the rotor plane is usually called the "axial induced" velocity, the velocity induced by the presence of the turbine. The tangential flow, on the other hand, is induced by the swirl velocity of the air flow around the blade.

Horizontal-axis wind turbine rotors are usually not aligned with the wind due to the continuously changing wind direction and the fact that no rotor is capable of following this variability. Furthermore, upwind rotors are sometimes tilted in order to increase the tower clearance, and hence to reduce tower shadow. In effect, the rotor is then yawed about a horizontal axis. For all these reasons it is thus necessary to include in the blade element momentum theory the effects of yaw. Here we will consider only the simple case of perpendicular flow.

The axial induced velocity can be determined by expressing the axial thrust ΔF on a blade element either as the rate of change of momentum in the annular ring swept out by this element

$$\Delta F = 4\rho\pi r V_p^2 a(1-a)\Delta r \tag{3.32}$$

61

using Eq. (3.22) with $A \simeq \pi(r + \frac{1}{2}\Delta r)^2 - \pi(r - \frac{1}{2}\Delta r)^2 = 2\pi r \Delta r$ the area of the annular ring, or as the force exerted by the wind on a blade element

$$
\begin{aligned}
\Delta F &= N_b(\Delta L \cos\phi + \Delta D \sin\phi) \\
&= \tfrac{1}{2}\rho W^2 N_b\, c\, \underbrace{\left(C_l^{2D}\cos\phi + C_d^{2D}\sin\phi\right)}_{C_N} \Delta r
\end{aligned}
\qquad (3.33)
$$

where N_b is the number of rotor blades. Assuming equality of Eqs. (3.32) and (3.33) gives

$$
4a(1-a) = \underbrace{\frac{W^2 N_b\, c\, (C_l^{2D}\cos\phi + C_d^{2D}\sin\phi)}{2\pi r V_p^2}}_{C_{dax}}
\qquad (3.34)
$$

The right-hand side term is defined as the dimensionless thrust coefficient C_{dax} (see Eq. (3.25)). Solving the above equation gives

$$
\begin{aligned}
4a(1-a) &= C_{dax} \\
\Rightarrow \quad a &= \tfrac{1}{2} - \tfrac{1}{2}\sqrt{1 - C_{dax}}
\end{aligned}
\qquad (3.35)
$$

as an expression for the axial induction factor in case of perpendicular flow. Alternatively, the axial induction factor can be calculated as

$$
a = \frac{\sigma_r C_N}{4\sin^2(\phi) + \sigma_r C_N}
\qquad (3.36)
$$

by substituting

$$
\begin{aligned}
C_N &= C_l^{2D}\cos\phi + C_d^{2D}\sin\phi \\
\sin(\phi) &= \frac{V_p(1-a)}{W} \\
\sigma_r &= \frac{N_b\, c}{2\pi r}
\end{aligned}
$$

in Eq. (3.34) and solving for a. The term σ_r (which is a function of the radius r) is called the local solidity or chord solidity.

The tangential induced velocity can, on the other hand, be determined by expressing the torque ΔQ on a blade element either as the rate of change of angular momentum

$$
\Delta Q = 4\rho\pi r \Delta r(1-a)V_p V_t\, r a'
\qquad (3.37)
$$

or as the torque exerted by the wind on a blade element

$$
\begin{aligned}
\Delta Q &= N_b(\Delta L \sin\phi - \Delta D \cos\phi)r \\
&= \tfrac{1}{2}\rho W^2 N_b\, c\, \underbrace{\left(C_l^{2D}\sin\phi - C_d^{2D}\cos\phi\right)}_{C_T} r\Delta r
\end{aligned}
\qquad (3.38)
$$

assuming N_b blades. Again assuming equality between the above expressions of the torque on a blade element we have

$$a' = \frac{W^2 N_b c \, (C_l^{2D} \sin\phi - C_d^{2D} \cos\phi)}{8\pi V_t V_p \, r(1-a)} \qquad (3.39)$$

as an expression for the tangential induction factor. Alternatively, the tangential induction factor can be calculated as

$$a' = \frac{\sigma_r C_T}{4\sin(\phi)\cos(\phi) - \sigma_r C_T} \qquad (3.40)$$

with

$$C_T = C_l^{2D} \sin\phi - C_d^{2D} \cos\phi$$

and

$$
\begin{aligned}
\sin(\phi) &= \frac{V_p \, (1-a)}{W} \\
\cos(\phi) &= \frac{V_t \, (1+a')}{W} \\
\sigma_r &= \frac{N_b \, c}{2\pi r}
\end{aligned}
$$

Thus, Eqs. (3.35)/(3.36) and (3.39)/(3.40) are the set of non-linear relations that determine the dimensionless induced velocities a, and a' in case of perpendicular flow. Before these equations can be used, however, the local thrust coefficient must be modified to account for two effects: the departure of the local thrust coefficient from the momentum relation, and the non-uniformity of the induced velocities in the flow. These so-called tip losses will be considered after the treatment of the turbulent wake state.

Turbulent wake state

For heavily loaded wind turbines, which implies a high axial induction factor a as well as a high tangential induction factor a', the momentum and vortex theory are no longer applicable because of the predicted reversal of flow in the turbine wake. The vortex structure disintegrates and the wake becomes turbulent and, in doing so, entrains energetic air from outside the wake by a mixing process. Thereby thus altering the mass flow rate from that flowing through the actuator disk. The turbine is now operating in the so-called "turbulent wake state", which is an intermediate state between windmill, and propellor state (*see* Appendix B for an overview of the different flow states of a wind turbine rotor).

In the turbulent wake state the relationship between the axial induction factor and the thrust coefficient according to the momentum theory, Eq. (3.35), has to be replaced by an empirical relation. The explanation for this is that the momentum theory predicts a decreasing thrust coefficient with an increasing axial induction

factor, while data obtained from wind turbines show an increasing thrust coefficient [279]. Thus, the momentum theory is considered to be invalid for axial induction factors larger than 0.5. This is consistent with the fact that when $a = 0.5$ the far wake velocity vanishes (*i.e.* a condition at which streamlines no longer exist), thereby violating the assumptions on which the momentum theory is based. The following approximations are implemented in DAWIDUM:

1. **Anderson** [2]. The empirical relation of Anderson is defined as:

$$a = 1 + \frac{C_{dax} - C_{dax1}}{4(\sqrt{C_{dax1}} - 1)} \quad \text{for} \quad a \geq a_T \tag{3.41}$$

or equivalently

$$C_{dax} = 4(a_T)^2 + 4(1 - 2a_T) \cdot a \quad \text{for} \quad C_{dax} > 4a_T(1 - a_T) \tag{3.42}$$

where

$$a_T = 1 - \tfrac{1}{2}\sqrt{C_{dax1}}$$

with $C_{dax1} = 1.816$ as "best" fit [21]. Thus $a_T = 0.3262$ and $C_{dax}(a_T) = 0.8792$. The empirical relation of Anderson is a straight line in the $C_{dax} - a$ diagram, and this line lies tangential to the momentum theory parabola at the transition point a_T (marked $*$ in Fig. 2.1);

2. **Garrad Hassan** [29]. The empirical relation of Garrad Hassan is defined as:

$$C_{dax} = 0.6 + 0.61\,a + 0.79\,a^2 \quad \text{for} \quad a > 0.4 \tag{3.43}$$

or equivalently

$$a = \frac{61}{158} + \frac{1}{158}\sqrt{-15239 + 31600 \cdot C_{dax}} \quad \text{for} \quad C_{dax} > 0.96 \tag{3.44}$$

3. **Glauert** [55, 82]. The empirical relation of Glauert is defined as:

$$a = 0.143 + \sqrt{0.6427 \cdot C_{dax} - 0.55106} \quad \text{for} \quad C_{dax} > 0.96 \tag{3.45}$$

4. **Johnson** [118]. The empirical relation of Johnson is obtained from interpolation of the expressions for the wind turbine and propellor state by a third order polynomial:

$$a = 1.991 - \frac{1.491}{C_{dax}} \quad \text{for} \quad C_{dax} \geq 1 \tag{3.46}$$

or equivalently

$$C_{dax} = \frac{1.491}{1.991 - a} \quad \text{for} \quad a \geq 0.5 \tag{3.47}$$

5. **Wilson** [280, 308]. The empirical relation of Wilson is defined as:

$$C_{dax} = 4 \left[a_c^2 + (1 - 2a_c)a \right] \quad \text{for} \quad a > a_c \tag{3.48}$$

or equivalently

$$a = \tfrac{1}{4} \cdot \frac{C_{dax} - 4a_c^2}{1 - 2a_c} \quad \text{for} \quad C_{dax} > 4a_c(1 - a_c) \tag{3.49}$$

where

$$a_c \approx 0.2$$

This is a linear extrapolation of the from the momentum theory parabola at the transition point a_C (marked o in Fig. 2.1);

Observe that the empirical relation of Wilson is identical to that of Anderson, only the location of the transition point is different. The five mentioned approximations were already compared in Fig. 2.1 on page 25 for perpendicular flow. From the observed differences it has been concluded that the listed empirical approximations must be regarded as being only approximate at best. The prediction is, nevertheless, more realistic than the one from the momentum theory as illustrated in Fig. B.1 on page 228. It must be noted that, in general, the value of the axial induction factor rarely exceeds 0.6 and for a well-designed blade it will be in the vicinity of 0.33 for much of its operating range [37].

Thus for values of C_{dax} greater than the (empirical model dependent) transition point, the right-hand side term of Eq. (3.34) needs to be substituted in one of the above mentioned empirical relations (*i.e.* either Eq. (3.41), (3.44), (3.45), (3.46), or (3.49)) to compute a.

Blade tip and root effects

The blade momentum theory, as previously developed, does not account for the effect of a finite number of rotor blades. Therefore a correction has to be applied for the interaction of the shed vorticity with the blade's bound vorticity. This effect is usually greatest near the blade tip, and it significantly affects the rotor torque and thrust.

Either an approximate solution by Prandtl or a more exact solution by Goldstein can be used to account for the non-uniformity of the induced axial velocity [55]. Both approximations give similar results. The expression obtained by Prandtl is however commonly used, since this has a simple closed form, whereas the Goldstein solution is represented by an infinite series of modified Bessel functions.

This expression is in literature denoted with the misleading term tip-loss factor. Misleading because it corrects for the fact that induction is not uniform over the annulus under consideration owing to the finite number of blades, and not for the finiteness of the blades. Prandtl's tip-loss factor is defined as

$$F_{tip} = \frac{2}{\pi} \arccos e^{-\frac{(R - r_i) N_b}{2 r_i \sin \phi_i}} \tag{3.50}$$

with

> R Length of rotor blade
> r_i Radial position of blade section i
> N_b Number of blades
> ϕ_i Angle between relative wind vector and the plane of rotation
>   at blade section i

Note that at the blade tips, where $r = R$, the factor equals zero, as can be reasoned by the fact that the circulation at the blade tips is reduced to zero by the wake vorticity.

A similar loss takes place at the blade root where, as at the blade tip, the bound circulation must fall to zero, and therefore a vortex must be trailed into the wake. The blade root-loss factor is defined as

$$F_{root} = \frac{2}{\pi} \arccos e^{-\frac{(r_i - r_0)N_b}{2r_0 \sin \phi_i}} \tag{3.51}$$

with r_0 the radial position of start root loss (typically 10% to 30% of the blade radius [118]).

The effective total loss factor at any blade section is, according to Eggleston and Stoddard [55], then the product of the two:

$$F_L = F_{tip} \cdot F_{root} \tag{3.52}$$

Figure 3.13 shows Prandtl's combined blade tip and blade root loss factor F_L as a function of the normalized radius $\tilde{r} = r/R$.

The incorporation of the combined blade tip and root loss factor F_L into the expressions for the induction factors depends upon whether the azimuthal averaged values of the induction factors, or the maximum values (local to a blade element) are to be determined. If the former alternative is chosen then, in the momentum terms the induction factors remain unmodified, but in the blade element terms the induction factors must appear as the average value divided by F_L. The latter choice, however, allows the simplest modification of Eqs. (3.35)/(3.36) and (3.39)/(3.40). In this case, the induction factors in the momentum terms are to be multiplied by F_L while the values of ϕ and C_N that are obtained from the blade element calculations are not multiplied by F_L. Equation (3.35) then becomes

$$a = \frac{1 - \sqrt{1 - C_{dax}}}{2F_L} \tag{3.53}$$

for a wind turbine operating in windmill state or, when the turbine is operating in turbulent wake state, by dividing the right-hand side of either Eq. (3.41), (3.44), (3.45), (3.46), or (3.49) by F_L. In addition, Eq. (3.39) becomes

$$a' = \frac{W^2 N_b \, c \, (C_l^{2D} \sin \phi - C_d^{2D} \cos \phi)}{8\pi V_t V_p \, r(1 - aF_L)F_L} \tag{3.54}$$
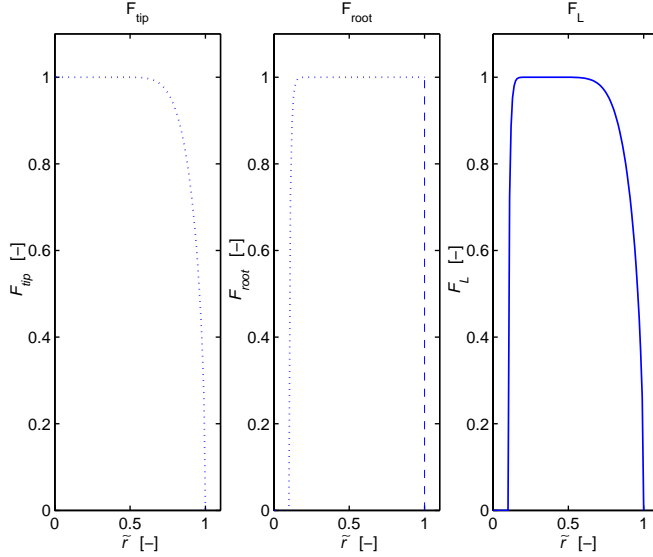
Figure 3.13: *Prandtl's combined blade tip and blade root loss factor F_L as function of the normalized radius $\tilde{r}$. It is assumed that the inflow angle ϕ_i is constant over the radius of the blade, and r_0 is taken as $0.10 \cdot \tilde{r}$.*

3.3.4 Calculation of the blade element forces

The aforementioned equations form the core of the aerodynamic description of the rotor behavior in DAWIDUM. Observe from Fig. 3.11 on page 58 or Eq. (3.27) on page 59 that the instantaneous undisturbed wind velocity W is composed of the vector sum of the perpendicular wind velocity V_p (corrected for axial induction), and the tangential wind velocity V_t (corrected for tangential induction). Obviously, V_p and V_t are expressed in the blade element local frame of reference and result from the decomposition of the vector sum of the free stream wind velocity V_w (corrected for wind shear and tower shadow), and the blade movements $\dot{x}$.

This implies that the lift and drag forces, Eq. (3.30) and Eq. (3.31), can be calculated once the induced velocities are known (assuming a given air density ρ, chord c, pitch angle θ, blade element length Δr and aerofoil). The induced velocities, in turn, are a function of the blade loads. This coupling implies that a set of non-linear equations needs to be solved. The conventional approach to the calculation of the forces acting on a blade element is to proceed as follows:

a.) Assume initial values of a and a' ($a = a' = 0$ is a common choice to start);

b.) Calculate the angle ϕ using Eq. (3.28);

c.) Calculate the local angle of attack α using Eq. (3.29), and the known value of the pitch angle θ;

67

d.) Determine the lift coefficient C_l and drag coefficient C_d by substituting the calculated values for α in a look-up table containing both $C_l(\alpha)$ and $C_d(\alpha)$ of the aerodynamic profile for the correct Reynolds number;

e.) Calculate total loss factor F_L using Eq. (3.52);

f.) Calculate C_{dax} using right-hand side term of Eq. (3.34) and determine in which flow state the turbine is operating;

g.) Calculate a new value of a using either Eq. (3.53) (windmill state) or using one of the empirical relations divided by F_L (either Eq. (3.41), (3.44), (3.45), (3.46), or (3.49)) in case the turbine is operating in turbulent wake state;

h.) Calculate a new value of a' using Eq. (3.54);

i.) Incrementally adapt a and a' and repeat steps b.) to h.) until convergence occurs (difference between two successive estimates of a and a' is smaller than the prescribed tolerance) or for a specified maximum number of iterations.

Once the iterations have converged, the blade element forces can be computed for each blade as follows:

$$\Delta F_p = \tfrac{1}{2}\rho\,W^2\,c\,\left(C_l^{2D}\cos\phi + C_d^{2D}\sin\phi\right)\Delta r \qquad (3.55)$$

$$\Delta F_t = \tfrac{1}{2}\rho\,W^2\,c\,\left(C_l^{2D}\sin\phi - C_d^{2D}\cos\phi\right)\Delta r \qquad (3.56)$$

with $F_p \parallel V_p$ and $F_t \parallel V_t$. These forces are input to the mechanical module describing the structural dynamics. This module is discussed in the next section. Finally, the next time step can be computed.

Within DAWIDUM, the adaptation is performed by minimization of the following objective function

$$F_{obj} = (a - a_{old})^2 + (a' - a'_{old})^2$$

using the Nelder and Mead Simplex method [199]. This is a direct search method that does not use numerical or analytic gradients. The interested reader is referred to Chapter 5 for a detailed treatment of this method. The aerodynamic module is coded as an M-File S-Function[1] named BEM. In this S-Function, deterministic effects as wind shear, tower shadow and the ten-minute average wind speed at hub height are added to the zero-mean stochastic components of SWING-4 before the forces are computed.

Up to now, the selection of the number of blade elements N_s has not been dealt with. A common choice is to select N_s from the range $10 < N_s < 20$. The actual number of blade elements, however, depends on various factors, including the following ones:

- chord variation over the rotor blade;

- number of aerodynamic profiles per blade;

---

[1]An M-File S-Function is a computer language description of a SIMULINK block written in MATLAB.

- number of rigid bodies used to model the structural dynamics.

At present, an optimization procedure that calculates the minimum number of blade elements for a given wind turbine configuration is not available. Within DAWIDUM the number of blade elements can be changed easily to evaluate the effect this number has on the performance. Moreover, the number can be chosen independently of the number of rigid bodies the flexible rotor blade has been subdivided in.

One last point about the BEM theory. The basic assumption is that the force acting on a blade element is solely responsible for the change of momentum of the air which passes through the annulus swept by that element. It is therefore assumed that there is no radial interaction between adjacent annuli. This condition is, strictly, only true if the axial induction factor does not vary radially. The axial induction factor, however, varies not only radially, but also azimuthally due to various reasons (including unsteady wind and yawed flow). The question remains: is it legitimate to apply the BEM theory for the cost-effective design and operation of a flexible wind turbines operating in turbulent wind? At present, neither an affirmative or a negative answer can be given. It is strongly recommended to perform validation experiments in order to reveal whether it is satisfactory to use this approach to determine the forces acting on each blade (element).

3.4 Mechanical module

In this section a systematic procedure for modeling the structural dynamics of flexible wind turbines is developed. The mechanical module has an input-output configuration as depicted in Fig. 3.14. This module is bilaterally coupled to the aerodynamic module through the velocity $\dot{x}$, and the aerodynamic forces $F_{aero} = [F_{p,1}(1 : N_s)\ F_{t,1}(1 : N_s) \cdots F_{p,N_b}(1 : N_s)\ F_{t,N_b}(1 : N_s)]$ (with N_s the number of blade elements and N_b the number of rotor blades), and is bilaterally coupled to the electrical module through the mechanical speed ω_m, and the electromechanical torque T_{em}.
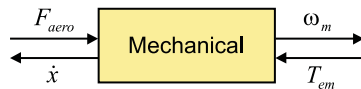
Figure 3.14: *Mechanical module input-output configuration with the interaction variables.*

3.4.1 Introduction

At present, four different kinds of mechanical models are commonly used to model (flexible) mechanical structures: Finite Element (FES), Multibody (MBS), Continuous, and Hybrid Multibody systems (HMBS) [190]. The complexity of the mechanical models increases in the mentioned order. Without exception, all different kinds of mechanical models are based on the classical mechanics formulated by Sir

Isaac Newton (1642-1727) in his book *Philosophiæ Naturalis Principia Mathematica* in 1687 [200].

The general guideline in mechanical modeling always should be: devise a model as simple as possible. It is the combination of theoretical knowledge, and practical experience which leads to models well suited for the intended use. Due to the extensiveness of the subject and the wide range of literature on this topic, a number of aspects of the mentioned mechanical models will be reviewed in bird's-eye view.

In the FES method, a real flexible structure is regarded as an assembly of a finite, but large number of geometrically simple, discrete elements. In general, the number of elements varies between a hundred and some thousands. Each element consists of a number of nodes (ranging from 2 to 27 nodes per element) with 1 to 12 degrees of freedom at each node [176]. Models based on this method have thus many degrees of freedom, with the associated high computational cost. Finite Element models are appropriate for the analysis of static loads, small dynamic motions referred to an inertial system, and may be very useful for layout and design, because stress calculations give important hints for design and dimensioning of the structural elements [140]. These models are, however, not suitable for control system design if not combined with an order reduction.

In the Multibody System (MBS) approach, a real mechanical system is approximated with a finite number of rigid bodies, coupled by inelastic joints (*e.g.* slider, pin) to the Newtonian reference frame. Consequently, such a system can be described with a finite number of differential equations. The essential dynamics of stiff mechanical systems that undergo large displacements as well as large rotations can be well reproduced in this way. However, when the deformation of (a part of) the system has a significant effect on the dynamic behavior, the elasticity can no longer be neglected. Inclusion of elasticity by so-called flexible bodies is essential in order to reach the level of accuracy of stiff mechanical systems. The price to be paid is, of course, an increased model order. Since the number of equations of motion remains comparatively small, this approach is very appropriate for control system design.

A Continuous System (COS) consists of flexible bodies of which the distribution of mass and stiffness can be exactly mathematically represented. The resulting set of partial differential equations (PDE's) can be solved exactly only in a few simple cases. An example of a continuous system is an Euler-Bernoulli beam of which the exact solution is given in Section 4.2. Due to this limitation, approximate finite-dimensional equations of motion are normally used [128]. Moreover, the description of the dynamics by partial differential equations is not suited for control design [21]. In the most common approximation technique, a spatial discretization is used, whereby the partial differential equations are replaced by ordinary differential equations (ODE's). Note that while spatial discretization is used, the resulting ordinary differential equations are still continuous with respect to time. Time discretization can also be used, of course, and the resulting equations would be of the difference type. The two most common spatial discretization methods are the assumed modes, and the finite element method respectively. Both approaches lead to linear, finite dimensional, continuous time equations of motion for approximation the dynamics of flexible systems. Remark: the widely adopted term "assumed

modes" is sometimes confusing, because the real system normal modes of vibration are approximated by a linear combination of the assumed modes.

A Hybrid Multibody System (HMBS) may be built up of a combination off all three methods of modeling mentioned above, leading to the most complex model of a mechanical system.

An overview of the main features of the four modeling concepts is given in Table 3.1. From this table it can be concluded that many physical systems of interest, and of practical importance can be effectively modeled as multibody systems. "Effectively" means that this approach results in a limited order model of the real system under consideration. In addition, the model parameters have a clear physical interpretation (*i.e.* are related to geometry and material properties). Such a model is well suited for time-domain simulation, analysis of dynamic loads, and control system design. The COS mechanical modeling method, on the other hand, can only be applied to very simple geometric structures (*e.g.* beams). The Finite Element approach results in complex, high order models mainly suited for layout, design, and thorough system analysis.

Mechanical modeling concepts			
Modeling	HMBS		
	MBS	COS	FES
Body	rigid and/or flexible	flexible	flexible
Geometry	complex	simple	complex
Deflections	large non-linear and/or small linear	large non-linear	small linear and/or non-linear
Description of deformation	reduced	available	available
Forces/moments	discrete	smoothly distributed	discrete
Suitability for time-domain simulation	good	poor	poor
Suitability for control system design	good	after reduction	conditional, after reduction

Table 3.1: *Overview of the four modeling variants, with MBS: Multibody System, COS: Continuous System, FES: Finite Element System, and HMBS: Hybrid Multibody System.*

Based on these conclusions, we have chosen the multibody approach to be most suited for our goal. There are several ways of modeling flexible bodies within the MBS methodology, for an overview see *e.g.* Shabana [257, 258]. The simplest way is to equally distribute the mass of the flexible body into lumped masses, interconnected by ideal, massless springs and dampers. This is the so-called "lumped-mass method". A more accurate model is obtained by using the concept of the so-called "superelement" as introduced by Rauh and Schiehlen [232, 233]. The interested reader is referred to Appendix C where the exact calculated eigenfrequencies of an Euler-Bernoulli beam are compared with those of the finite element, lumped-mass and the superelement method.

3.4.2 Superelement approach

In the superelement approach, a (part of a) flexible body is approximated with a number of so-called superelements. Each symmetric superelement consists of 3 rigid bodies connected by joints (marked ○ in Fig. 3.15) containing ideal torsional springs that model the elastic properties in bending direction. The attractive feature of modeling the flexibility by joint springs and dampers is that the spring and damper forces are readily incorporated into the standard (rigid) multibody body packages (*e.g.* SD/FAST® [109]).

It should be noted that the centre body of a superelement can be divided in two parts of equal length to include axial deflection, and torsion deformation as well. In this thesis we limit ourselves (initially) to bending since the first torsional mode and the first two (non-rotating) bending modes of the Lagerwey LW-50/750 wind turbine are sufficient apart (*see* Table A.2 on page 223). That is, for the Lagerwey LW-50/750 wind turbine it is not necessary to take the torsional mode of vibration into account.
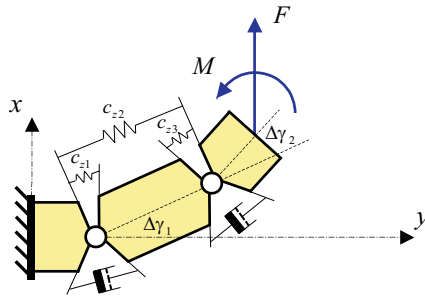
Figure 3.15: *Deflections and slopes of a superelement with bending stifness EI, and length L. Each (symmetric) superelement consists of three rigid bodies (with lengths kL, $(1 - 2k)L$, and kL) connected by joints (○).*

The main question is "What should the values of the spring constants be in order to produce a comprehensive and accurate dynamic model of a flexible body?"

Accurate in the sense that i) the elastic deformations of the superelement under a static load should be equal to those of a flexible beam, ii) the superelement should have the same mass and inertia properties as a rigid beam with identical dimensions, and iii) the eigenfrequencies of the superelement should be as close as possible to those of a continuous beam. Next, we will derive the spring constants in bending direction required in the superelement approach. The interested reader is referred to Molenaar [189] for the determination of the spring constants representing the axial deflection and the torsion deformation.

Continuous bending expressions

If it is assumed that both the shear deformation and rotational inertia of the flexible body cross-sections are negligible if compared with bending deformation and translational inertia, the spring constants can be derived from the differential equation of the deflection curve of a prismatic beam (*i.e.* beam with constant cross section throughout its length). This equation is given in Gere & Timoshenko [76] as

$$\frac{d^2 v}{dy^2} = -\frac{M}{EI} \tag{3.57}$$

with

v	Transverse displacement $(v \perp y)$	[m]
y	Distance from the origin	[m]
M	Bending moment	[Nm]
E	Modulus of elasticity	[Pa]
I	Area moment of inertia	[m^4]

It should be noted that Eq. (3.57) is valid only when Hooke's law applies for the material, and when the slope of the deflection curve is very small. Also, since effects of shear deformations are disregarded, the equation describes only deformations due to pure bending.

For a tapered beam, the presented relationship gives satisfactory results provided that the angle of taper is small (*i.e.* < 10°). In that case, Eq. (3.57) has to be written in the following form

$$\frac{d^2 v}{dy^2} = -\frac{M}{EI(y)} \tag{3.58}$$

in which $I(y)$ is the area moment of inertia of the cross-section at distance y from the origin.

Determination parameters superelement

The superelement parameters (*i.e.* the torsional spring constants c_{z1}, c_{z2}, and c_{z3} *see* Fig. 3.15) are found by comparing the deflection and the angle of rotation at

the free end of a Euler-Bernoulli beam (*i.e.* a prismatic beam with length L, cross-section area A, constant flexural rigidity EI_z, and uniformly distributed mass per unit length $\rho = m/L$, where m is the total mass of the beam) subjected to a load F and couple M at the free end of the beam (*see* Fig. 3.16). Since this is a case of pure bending, we may use Eq. (3.57) to determine the total deflection δ and the total angle of rotation θ at the free end [76].

Substituting the expression for the bending moment, the differential equation becomes

$$EI_z v'' = -M = FL - Fy$$

with $v'' = \frac{d^2 v}{dy^2}$. The first integration of this equation gives

$$EI_z v' = FLy - \frac{Fy^2}{2} + C_1$$

The constant of integration C_1 can be found from the condition that the slope of the beam is zero at the support; thus $v'(0) = 0$, which results in $C_1 = 0$. Therefore

$$EI_z v' = FLy - \frac{Fy^2}{2} \tag{3.59}$$

Integration of this equation yields

$$EI_z v = \frac{FLy^2}{2} - \frac{Fy^3}{6} + C_2$$

The boundary condition on the deflection at the support is $v(0) = 0$, which shows that $C_2 = 0$. Thus, the equation of the deflection curve is

$$v = \frac{Fy^2}{6EI_z}(3L - y) \tag{3.60}$$

The angle of rotation θ_F and the deflection δ_F at the free end of the beam loaded by a force F are readily found by substituting $y = L$ into Eqs. (3.59) and (3.60) respectively.

The equation of the deflection curve for an Euler-Bernoulli beam loaded by a couple M at the end of the beam (*see* Fig. 3.16) can be determined analogously. The results for both cases are summarized in the following equation

$$\begin{bmatrix} \delta \\ \theta \end{bmatrix} = \frac{1}{6EI_z} \begin{bmatrix} 2L^3 & 3L^2 \\ 3L^2 & 6L \end{bmatrix} \begin{bmatrix} F \\ M \end{bmatrix} \tag{3.61}$$

Inversion of this equation results in

$$\begin{bmatrix} F \\ M \end{bmatrix} = \frac{EI_z}{L^3} \begin{bmatrix} 12 & -6L \\ -6L & 4L^2 \end{bmatrix} \begin{bmatrix} \delta \\ \theta \end{bmatrix} \tag{3.62}$$

From Fig. 3.15 it can be easily derived that

$$\begin{bmatrix} c_{z1} + c_{z2} & c_{z2} \\ c_{z2} & c_{z2} + c_{z3} \end{bmatrix} \begin{bmatrix} \Delta\gamma_1 \\ \Delta\gamma_2 \end{bmatrix} = \begin{bmatrix} (1-k)L & 1 \\ Lk & 1 \end{bmatrix} \begin{bmatrix} F \\ M \end{bmatrix} \tag{3.63}$$
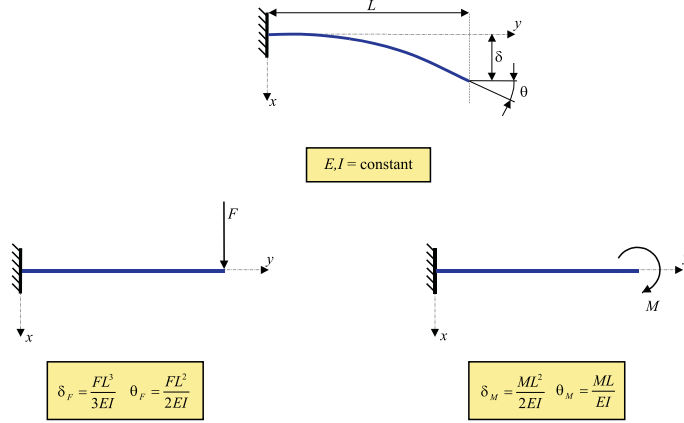
Figure 3.16: *Deflections and slopes of an Euler-Bernoulli beam with bending stiffness EI, and length L.*

and that the following relation holds

$$\begin{bmatrix} \delta \\ \theta \end{bmatrix} = \begin{bmatrix} L(1-k) & kL \\ 1 & 1 \end{bmatrix} \begin{bmatrix} \Delta\gamma_1 \\ \Delta\gamma_2 \end{bmatrix} \tag{3.64}$$

with k the partitioning coefficient. Substituting Eq. (3.64) in Eq. (3.62) and back-substituting the result in Eq. (3.63) gives

$$\begin{bmatrix} c_{z1} + c_{z2} & c_{z2} \\ c_{z2} & c_{z2} + c_{z3} \end{bmatrix} \begin{bmatrix} \Delta\gamma_1 \\ \Delta\gamma_2 \end{bmatrix} =$$
$$\frac{EI_z}{L} \begin{bmatrix} 12k^2 - 12k + 4 & -12k^2 + 12k - 2 \\ -12k^2 + 12k - 2 & 12k^2 - 12k + 4 \end{bmatrix} \begin{bmatrix} \Delta\gamma_1 \\ \Delta\gamma_2 \end{bmatrix} \tag{3.65}$$

The spring coefficients c_{z1}, c_{z2}, and c_{z3} are found by comparing the elements in the above equation. The resulting spring coefficients are

$$c_{z1} = c_{z3} = \frac{6EI_z}{L}(1-2k)^2 \tag{3.66}$$

and

$$c_{z2} = \frac{2EI_z}{L}(-1 + 6k - 6k^2) \tag{3.67}$$

in which EI_z represents the flexural rigidity. The partitioning coefficient k ($0 < k < \frac{1}{2}$) of the superelement exerts influence on the kind of approximation of the eigenfrequencies. In Rauh [232] is has been concluded that choosing a partitioning coefficient from the range $\frac{1}{5} \leq k \leq \frac{1}{4}$ results in models that approximate the exact eigenfrequencies with a limited number of superelements. Furthermore, with $k = \frac{1}{2}(1 - \frac{1}{\sqrt{3}}) \approx 0.211$ it follows that $c_{z2} = 0$, and that Eq. (3.66) reduces to

$$c_{z1} = c_{z3} = \frac{2EI_z}{L} \tag{3.68}$$

75

Consequently, a relatively simple, and compact model structure has been obtained. It will be shown in Section 4.2 that, in this case, some eigenfrequencies are smaller, and some are larger than in reality, while the errors decrease very fast with an increasing number of superelements.

3.4.3   Generation of the equations of motion of MBS

For a multibody system, the equations of motion are a set of ordinary differential equations (ODE) relating the accelerations to the time, the positions, the velocities, and the parameters of the system. There are various methods to derive the equations of motion of multibody systems. In order to be able to understand the differences between these methods, we will first highlight the roots of multibody system dynamics.

Roots of multibody system dynamics

As mentioned, the dynamics of multibody systems is based on classical mechanics. The most simple element of a multibody system is a free particle (or point mass) which can be treated by Newton's laws. The rigid body as principle element of a MBS was introduced in 1776 by Euler in his contribution entitled "Nova methodus motum corporum rigidarum determinandi" [59]. For the modeling of constraints and joints, Euler already used the free body principle resulting in reaction forces. The equations obtained are known in the multibody dynamics as Newton-Euler equations.

A system of constraint rigid bodies was considered in 1743 by d'Alembert in his "Traité de Dynamique"[52] where he distinguished between applied and reaction forces. D'Alembert called the reaction forces "lost forces" having the principle of virtual power in mind. A mathematical consistent formulation of d'Alembert's principle is due to Lagrange [149] combining d'Alemberts fundamental idea with the principle of virtual work. As a result a minimal set of ordinary differential equations of second order is found.

A systematic analysis of constraint mechanical systems was established in 1788 by Lagrange [149], too. The variational principle applied to the total kinetic and potential energy of the system considering its kinematical constraints and the corresponding generalized coordinates result in the Lagrangian equations of the first and second kind. Lagrange's equations of the first kind represent a set of differential-algebraic equations (DAE), while the second kind leads to a minimal set of ordinary differential equations (ODE).

An extension of d'Alembert's principle valid for holonomic systems only was presented in 1909 by Jourdain [125]. For non-holonomic systems the variations with respect to the translational and rotational velocities resulting in generalized velocities are required. Then, a minimal set of ordinary differential equations of first order is obtained. The approach for generalized velocities, identified as partial velocities, was also introduced by Kane and Levinson in 1985 [130]. The resulting Kane's equations represent a compact description of multibody systems. Interestingly, when Kane's equations were introduced in 1961, there was little - if any - interest in

multibody dynamics. More details on history of classical mechanics including rigid body dynamics can be found in Päsler [213] and Szabó [288].

Summarizing, either one of the following methods can be used to derive the equations of motion of multibody systems:

- Newton-Euler;

- D'Alembert (or Virtual Work);

- Lagrange;

- Hamilton (or state space form of Lagrange);

- Jourdain (or Virtual Power);

- Kane;

The question is: "Which method is most suitable for multibody system dynamics analysis?" [292], or in other words: "Which method formulates the equations of motion most efficiently? Kane's method (sometimes called "Langrange's form of d'Alembert's principle", "Jourdain's principle", or the "Principle of virtual power"), is preferable to the use of each of the other mentioned methods, particularly for the automated numerical analysis of large multibody systems [127], because it leads directly to the simplest possible equations of motion (*i.e.* Euler's dynamical equations when applied to a single rigid body) [131, 243]. The Euler dynamical equations are exceedingly compact, uncoupled in the highest derivatives, and free of trigonometric functions. Furthermore, since Kane's method focuses its attention on motions rather than on configurations, it offers the designer maximum physical insight [130].

Automatic versus manual generation

In general, the equations of motion can be generated either by hand, or automatically. Generating the equations of motion for complex multibody systems with a large number of degrees of freedom (DOF) is very time-consuming with pencil and paper, even if the best suited method is used. For this reason, various computer programs for automatic equation generation have been developed.

The first programs were on an numerical basis (*i.e.* the equations produced are given as implicit formulas, or in other words: numerical formalisms combine the generation and solution of the equations of motion). Examples are ADAMS [4, 56], SIMPACK, and SPACAR [121]. This approach has obviously a number of drawbacks: it requires starting the computations all over again for each new set of input data, and it does not provide all the insight provided by analytical equations. Moreover, for controller design numerically generated equations are of no help. Therefore, most recent program are analytical based (*i.e.* the equations produced are given as explicit formulas, or in other words: symbolic formalisms generate the equations of motion independent of the integration routine used). Examples are AUTOLEV [129, 234, 250], MESA VERDE, NEWEUL [253], and SD/FAST [109].

The symbolic representation has the advantage that the equations of motion are to be generated only once, and the expressions have only to be evaluated during time-integration. The cost for the formulation of one symbolic set of equations is higher than once running through a numerical formalism. However, symbolic equations are an exact basis for the model under consideration, and combined with a package for numerical analysis, and simulation (*e.g.* MATLAB®/SIMULINK®) they result in ten or even more times faster computations than a purely numerical approach would require [62, 140, 201, 243]. See Schiehlen [252] for a more detailed comparison of important multibody system dynamics software.

We have decided to use SD/FAST® for the generation of the equations of motion of flexible wind turbines within DAWIDUM's mechanical module. The main reasons are twofold. First, SD/FAST® uses Kane's method for the derivation of the equations of motion. Second, it is able to generate SIMULINK® MEX-files.

Main features of SD/FAST

SD/FAST®, a product of Symbolic Dynamics, Inc., is a *general-purpose* multibody program whose function it is to create *special-purpose* simulation code employing explicit equations of motion for particular multibody configurations of interest. Computer symbol manipulation is used to simplify the general form of the equations of motion as appropriate to the system at hand (*i.e.* repeated terms are removed in order to arrive at the computationally simplest equations).

Any mechanical system that can be described as a collection of hinge-connected rigid bodies can be modeled in SD/FAST®. The system topology can either be open-loop, tree, or closed-loop (*see* Fig. 3.17 for a graphical illustration). The systems can be "free-flying" (*e.g.* a spacecraft) or "grounded" (*e.g.* a wind turbine). The system complexity is limited to 300 rigid bodies and 1000 degrees of freedom.

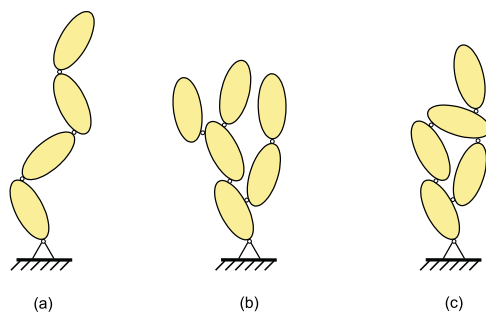|		
(a)	(b)	(c)

Figure 3.17: *Topological structures of multibody systems: (a) open-loop (or chain), (b) tree, and (c) closed-loop.*

The connection between the bodies, or between a body and the ground is established by means of joints (*e.g.* translational joints, rotational joints, or spherical joints). These connections typically impose constraints on the relative motion be-

tween the bodies. SD/FAST$^\circledR$ has eleven pre-defined joint types, ranging from a weld joint (a zero DOF joint) to a free joint (a completely free, 6-DOF joint with three translational plus three rotational DOF's). It should be noted that all joints can be used as a tree or a loop joint. For a more detailed survey the reader is referred to the SD/FAST User's Manual [109].

SD/FAST$^\circledR$ generates the equations of motion describing the dynamic behavior of the system in either C or FORTRAN as requested, based on a user-written input file (sdinputs()), a system description file (System Descripion), and a user-written output file (sdoutputs()). In the system description file the basic geometry, mass properties, and gravity are specified. In the sdinputs() file, the inputs to the SD/FAST$^\circledR$ block are defined, while in the sdoutputs() file the outputs from the SD/FAST$^\circledR$ block are defined. Using the SD/FAST$^\circledR$ Interface for SIMULINK$^\circledR$ it is possible to built out of these three files a single MEX-file, which appears as a SIMULINK$^\circledR$ block [255, 295]. This implies that it is possible to simulate virtually any mechanical system within the SIMULINK$^\circledR$ environment. This relationship is illustrated in Fig 3.18. Examples of these files can be found in Molenaar [189].
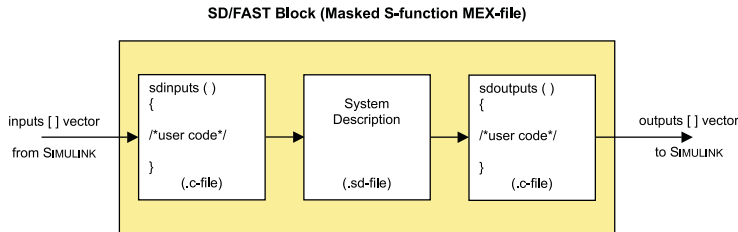
Figure 3.18: *Relationship between the SD/FAST block interface files.*

3.4.4 Automated structural modeling procedure

In Chapter 2 it has been observed that in most state-of-the-art wind turbine design codes an easy transfer from physical data available during the design of a new wind turbine to model parameters is missing. This situation should be changed in order to achieve an integrated and optimal wind turbine design.

The superelement approach presented in Subsection 3.4.2 requires the specification of the mass, centroidal mass moment of inertia, length, location of the center of gravity, interconnection vectors of the rigid bodies within each superelement as well as the aforementioned spring constants. In addition, the modulus of elasticity and the area moment of inertia needs to be specified.

This implies that the user must supply the correct mass and stiffness distribution as well as the number of superelements the structure has to be subdivided in. In order to facilitate the conversion from the user input to the above mentioned parameters, the following automated procedure has been developed:

- **Step 1:** Convert the physical data from the manufacturer (stored in Microsoft Excel spreadsheets, each sheet contains the data of a specific rotor blade, tower

or beam) into a multidimensional array stored in a MAT-file (*i.e.* RotorBlade-Data, TowerData, or BeamData respectively);

- **Step 2:** Select the model with the desired number of degrees of freedom out of the available mechanical module library (*see* Appendix I.2.3 for an overview);

- **Step 3:** Convert data in the MAT-file to SD/FAST$^{\circledR}$ input parameters by running MATLAB$^{\circledR}$ M-file. The required SD/FAST parameters are stored in a rotor blade/tower/beam specific file with the specified number of superelements appended to the basename "Blade", "Tower" or "Beam" (*e.g.* Blade2.mat contains the SD/FAST data of a blade divided into 2 superelements);

- **Step 4:** Build SIMULINK$^{\circledR}$ MEX-file containing equations of motion by running SD/FAST$^{\circledR}$.

This systematic procedure has been implemented in DAWIDUM providing both structural designers and control engineers with a tool that enables them to rapidly and easily build accurate dynamic models of flexible mechanical structures. In Table I.1 on page 273 an overview is given of the CPU time used to generate the equations of motion of several DAWIDUM models. It shows that this takes only a few seconds even for the most complex structural model. In addition, because the user can determine the model complexity by specifying the number of superelements, the resulting models can be made suited for time-domain simulation, analysis of dynamic loads, or control design purposes. This implies that a bidirectional communication between the structural wind turbine design and the controller design has been established.

It should be stressed that the presented mechanical module contains a model of the structural dynamics of a complete flexible wind turbine. The spacers, hub, nacelle and both the stator and rotor of the generator are in general treated as rigid, while the support structure and rotor blades are to be modeled as flexible bodies. Flexible body dynamics are approximated using the aforementioned superelements. This integrated approach overcomes the shortcomings regarding the incomplete modeling of the "rotor - support structure"-interaction reported in Kühn [144] and Wilson [306].

3.4.5 Soil dynamics

Up to now, the effect of the flexibility of the foundation and its supporting soil has not been dealt with in this thesis. Soil is a non-linear material in which the stifness progressively decreases with increasing shear stress until, at a sufficient high stress level, plastic deformation takes place. Furthermore, when subjected to cyclic loading, soil exhibits damping which increases with increasing shear amplitude. Soil damping comprises two parts: internal and radiation. The internal damping (also called material, structural or hysteric damping) is mainly caused by viscous and frictional effects within the soil. The radiation damping is an elastic property associated with stress waves being propagated away from an area. Obviously, the soil properties vary from place to place, and many of the properties vary in time too.

In this chapter it is assumed that the flexibility of the foundation and its supporting soil can be modeled by a torsional spring plus viscous damper in the two bending directions. This assumption will be (in)validated in Section 4.2 where the results from a full-scale modal test on the Lagerwey LW-50/750 wind turbine are described.

The flexibility of the soil makes the mechanical wind turbine structure less stiff than if the wind turbine were on a fixed base. This reduces the eigenfrequencies of the wind turbine in transverse vibration which in turn tends to increase the dynamic response of the mechanical structure. Figure 3.19 illustrates that the lowest modes are most affected because they tend to involve the highest proportion of soil response in the mode shape. In this figure the relative frequency shift as function of the foundation spring stiffness is depicted for Tower2f (*i.e.* tower plus foundation modeled as a torsional spring, *see* Appendix I.2.3 for a detailed description of the Tower2f module). This shift is defined as:

$$\Delta \omega_f = \frac{\text{Eigenfrequencies of Tower2f}}{\text{Eigenfrequencies of Tower2}} \cdot 100 - 100 \qquad [\%]$$

In other words: the relative frequency shift converges to zero with increasing foundation spring stiffness, since it then will approximate the infinitely rigid foundation modeled in Tower2. The dashed vertical line in the figure indicates the measured value of foundation spring stiffness at the location in Nieuwe-Tonge. This value is experimentally determined by Jacobs [116]. Obviously, small inaccuracies in the determination of this value will have significant impact on the model quality.
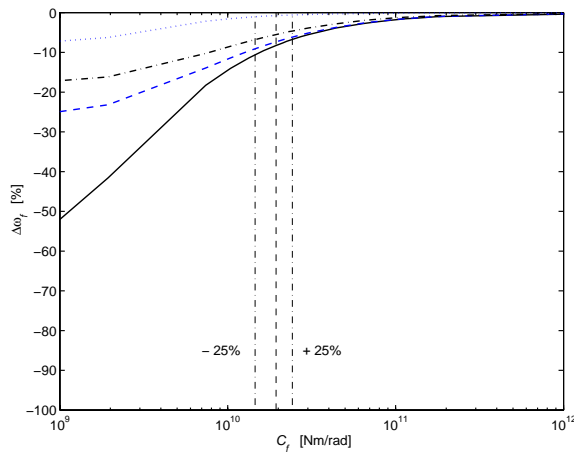
Figure 3.19: *Effect of foundation spring stiffness C_f on the first four uncoupled eigenfrequencies of the Lagerwey LW-50/750 tower. Solid line: first mode, dashed line: second mode, dashed-dotted line: third mode, dotted line: fourth mode, dashed vertical line: $C_f = 19.4 \cdot 10^9$ [Nm/rad], and dashed-dotted vertical lines: - 25% and + 25% error bound respectively.*

3.4.6 Example: three bladed wind turbine

For the purpose of illustration, Fig. 3.20 shows a superelement approximation of a three bladed wind turbine. Observe that both the tower and rotor blades are approximated by one superelement. Each superelement consists of three rigid bodies connected by two joints (marked ○). Each joint (*i.e.* a universal joint since both blade and tower torsion is not considered in this thesis) has two degrees of freedom. This implies that this system has 18-DOF (exclusive pitch and azimuth). Obviously, the total number of degrees of freedom required for proper modeling depends on both the wind turbine and site under investigation.

Three bladed wind turbine   Superelement approximation
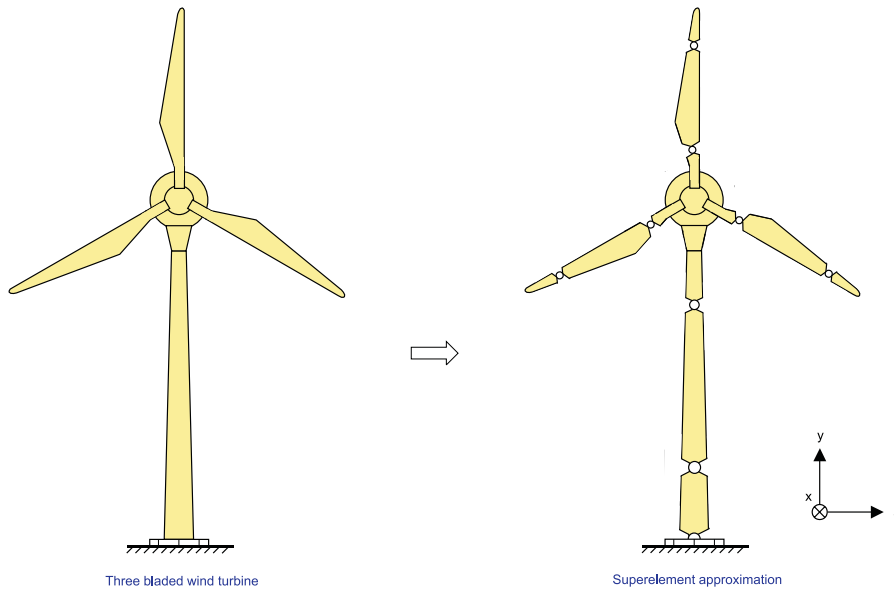
Figure 3.20: *Superelement approximation of a three bladed wind turbine, with ○: universal joints (2-DOF rotational joints). Both the tower and rotor blades are approximated by one superelement consisting of 3 rigid bodies connected by ideal torsional springs. The flexibility of the foundation is approximated by a torsional spring.*

Please remember that the resulting model accuracy strongly depends on the quality of the input data (*i.e.* garbage-in is by definition garbage-out). For example, in case of a wind turbine the uncertain (mechanical) parameters are particularly found in the area of foundation stiffness and damping. Obviously, when the correlation with the test data is not satisfactory, there is a need to modify the model by tuning/updating the model parameters. Since ad hoc procedures (trial and error) become impractical for more than three or four parameters, a systematic procedure has to be developed. This subject is treated in Chapter 5.

3.5 Electrical module

The electrical module has an input-output configuration as depicted in Fig. 3.21. This module is bilaterally coupled to the mechanical module through the mechanical speed ω_m, and the electromechanical torque T_{em}. The electrical module receives a set-point for the electromechanical torque T_{em}^{set} from the controller module. The output of the electrical module is the generated electric power P_{elec}.
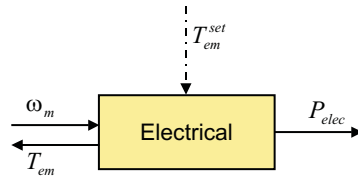
Figure 3.21: *Electrical module input-output configuration.*

3.5.1 Introduction

Continuous advances in power electronics applied to wind turbines have now drawn the attention of almost all wind turbine manufacturers to turbines which possess the ability to continuously vary rotational speed with the wind velocity, although world wide they are still outnumbered by constant rotational speed wind turbines. Constant speed operation has not been the choice of wind turbine designers, but rather a necessity brought about by the fixed relationship between the speed of the AC generators and the fixed utility grid frequency. The two main advantages of variable speed operation over constant speed operation are additional energy capture at partial load and potential reduction of fatigue loads on rotor and drive-train. At present, however, the convincing argument is the ability to meet the (stringent) power quality requirements.

This can be easily seen by recognizing that the power available in the wind varies with the cube of the wind velocity. Therefore it is desirable to let the wind turbine speed vary over a wide range to an optimum value depending on the operating conditions. This would not be possible if the (three-phase) generator were directly connected to the utility grid. To allow the generator (*i.e.* wind turbine) rotational speed to vary, a power electronic interface is needed. In such an interface the three-phase generator output is, in general, rectified into DC and subsequently interfaced with the three-phase utility source by means of a power electronic converter as illustrated in Fig. 3.22. In general, a rectifier at the generator side as well as an inverter at the utility grid site is required to provide both control and power quality requirements (*e.g.* power factor). Both the rectifier and the inverter act as a voltage and frequency changer.

In addition, variable speed operation enables reduction of periodic torque pulsations, caused by *e.g.* tower shadow or wind shear, by short-term kinetic energy
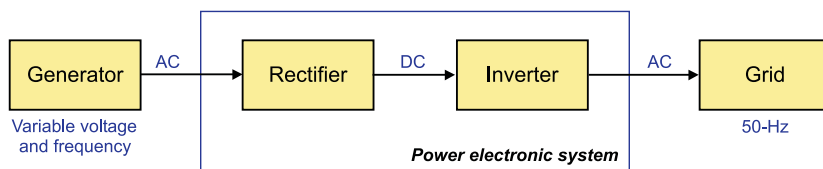
Figure 3.22: *General variable rotational speed generator configuration: the cascade of rectifier and inverter converts the AC of varying frequency and voltage to the fixed utility grid frequency of 50 Hz.*

storage in the rotor. Fatigue load reduction, however, is the most important and still underestimated advantage of variable rotational speed operation. After all, in 1994 it has already been demonstrated by Bongers [21] on an experimental test-rig (consisting of a drive-train of a variable speed wind turbine with a torque generator replacing the rotor system) that fatigue loads acting on the wind turbine structure can be significantly reduced by means of advanced controller design and implementation. Whether these advantages outweigh the disadvantages (higher initial costs, increased complexity and potential lower reliability respectively) is dependent on the design of the complete wind turbine.

However, in general, the bandwidth of the active blade pitch system is too small to achieve fatigue load reduction. As a result, pitch control has to be used to follow minute-to-minute fluctuations in aerodynamic power, while the electromechanical torque control will focus on fatigue load reduction. The design of a robust frequency converter controller for high dynamic performance of a variable speed generator requires an accurate dynamic model of the electromagnetic part. In essence, there are two aspects of a generator that need to be modeled, *viz.* the mechanical and the electromagnetic part. The mechanical part can be modeled using the techniques outlined in the previous section. In this section we will restrict ourselves to the dynamic modeling of the electromagnetic part.

3.5.2 Synchronous generator: physical description

In this subsection the physics of synchronous generators will be discussed since most electric power today is produced by synchronous generators [107]. In addition, the Lagerwey LW-50/750 is equipped with a synchronous generator. Synchronous generators are synchronous machines used to convert mechanical power into electrical power.

Construction

Physically, most synchronous generators consist of a stationary part, called the stator, and a rotating part driven by an external torque, called the rotor. The stator is, in general, connected to the utility grid, and consists of a three-phase winding on a ferromagnetic core. The core is constructed of thin laminations to reduce eddy current losses. Mostly, the rotor has a winding through which a direct current is

84

flowing: the field winding. The field winding produces a rotor magnetic field. This rotating magnetic field induces a three-phase set of AC voltages within the stator windings of the generator. The magnetic field created by the stator windings reacts with the rotating field thereby producing an electromagnetic torque. This torque is the mechanism through which the synchronous generator converts mechanical to electrical energy.

Since the rotor is rotating, a special arrangement is required to get the DC power to the field windings. There are two common approaches: either via an external DC source by means of slip rings and brushes or via a special DC power source mounted directly on the synchronous generator shaft. Slip rings and brushes were used on all smaller synchronous machines, while on larger generators and motors the DC power is provided by the latter approach [44]. The DC power required for excitation takes approximately one to a few percent of the rating of the synchronous generator [63].

The DC excitation of the field winding can also be provided by permanent magnets. Permanent magnet excitation brings the following benefits: i) higher torque or output power per volume, and ii) elimination of rotor copper losses due to the absence of electrical excitation, implying a substantial increase in the efficiency [92, 286]. The main disadvantages are: i) the field is uncontrollable [108], and ii) the assembly is a tricky job.

Depending on the rotor construction, a synchronous machine may be either a round-rotor (or cylindrical), or a salient-pole type. Figure 3.23 shows the cross-sections of both types. The salient-pole construction is mostly used in low-speed applications where the diameter to length ratio can be made larger to accommodate the higher pole number (20 up to 120 poles). This results in ring-generators. An example of this type is the synchronous generator used in waterwheel turbines. The round-rotor construction is favoured in high-speed applications where the diameter to length ratio has to be kept small to keep the mechanical stresses from centrifugal forces within acceptable limits. Examples are synchronous generators driven by steam or gas turbines.
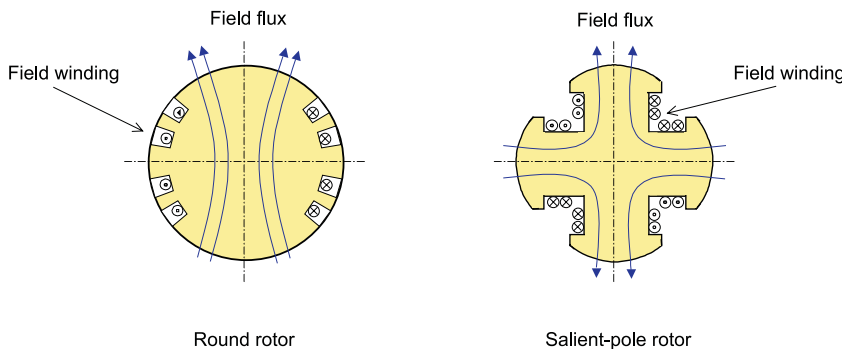
Figure 3.23: *Cross-section of a two-pole round, and on a four-pole salient-pole rotor.*

Synchronous speed

Synchronous generators are by definition *synchronous*, meaning that the produced electrical angular frequency with constant rotor field excitation is locked in or synchronized with the mechanical speed of the stator magnetic field, or equivalently the generator shaft speed. The produced frequency is completely determined by the generator shaft speed and the number of pole-pairs

$$f = \frac{p \cdot n}{60} \tag{3.69}$$

where f the produced frequency in hertz, p the number of pole-pairs, and n is the speed of the generator shaft expressed in rotations per minute (r.p.m.). For example, to generate 50-Hz power in a four pole machine, the rotor must turn at 1500 r.p.m. This relationship is depicted in Table 3.2.

p [-]	1	2	3	4	5	6	30	60	75	100
n [r.p.m.]	3000	1500	1000	750	600	500	100	50	40	30

Table 3.2: *Relationship between number of pole-pairs p, and rotational speed n of a three-phase synchronous generator linked to a grid with a fixed 50-Hz frequency.*

Large wind turbines have relatively low rotor shaft speeds, typically from 50 to 15 r.p.m. in the power range from 300 to 1500 kW, while wind turbine generators typically have 2, 3, or 4 pole-pairs (with base speeds of 1500, 1000 and 750 r.p.m. respectively at 50-Hz grid frequency, *see* Table 3.2). Consequently, if we want to link such a wind turbine driven generator to the grid with a fixed 50-Hz frequency, a mechanical transmission with a speed ratio between 10 and 100 is required to increase the angular velocity of the rotor shaft in order to come to an angular velocity well-suited for the (high-speed) generator. Most wind turbines are equipped with a rotor-transmission-generator drive-train where the combination of generator base speed and transmission ratio is selected such that the drive-train costs are minimized [106].

The interest in low-speed generators (which are directly connected to the shaft of the turbine and hence eliminating the transmission) has increased significantly in the past decade [92]. These so-called direct-drive generators necessarily have a large diameter, because it follows from basic generator theory that the torque that can be produced is directly related to the volume of the generator [298]. This construction offers a number of advantages in comparison to its counterpart with transmission. The most important advantages are a reduced noise level and a reduction of installation costs [186]. In addition, when combined with efficient, variable frequency power supply allowing the rotational speed to vary with the wind velocity, the aforementioned advantages can be obtained. The main disadvantages are the relatively high generator mass and the present purchase price.

3.5.3 Synchronous generator: mathematical description

The aim of this section is to set up a theoretical model of a synchronous generator suited for both time-domain simulation, and model based control design.

From a modeling point of view all synchronous generators have similar representations. They differ only with respect to some model parameters. Because the round-rotor synchronous generator is a special case of the salient-pole rotor synchronous generator, we will treat only the latter for an arbitrary number of pole-pairs p in this section.

Fig. 3.24 depicts a salient-rotor synchronous generator with only one pole-pair ($p = 1$ for illustration purposes). The machine has the usual three stator windings, each 120 (electrical) degrees apart. The stator windings are star connected. The rotor has one accessible circuit, the field or excitation winding, and two sets of inaccessible circuits, called damper windings. Damper windings are real or fictitious windings that can be used to represent, for example, the damping effects of eddy currents in the machine. In Fig. 3.24, one damper winding is located along the direct-axis, and one along the quadrature-axis (represented by ψ_{1d} and ψ_{1q} in Fig. 3.24). When the DC excitation of the field winding is provided by permanent magnets, the field windings can be replaced by fictitious ones carrying constant field currents.
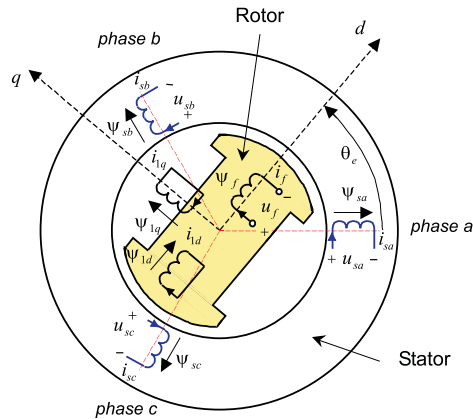
Figure 3.24: *Schematic representation of an elementary three-phase, two-pole synchronous generator.*

3.5.4 Dynamic generator model

The operation of a (synchronous) generator is based on the Maxwell's second equations or equivalently, Faraday's law of electromagnetic induction. This law states that when the field is excited and rotated, voltages will be induced in the three stator phases.

The fields produced by the stator winding currents are assumed to be sinusoidally distributed around the airgap. This assumption ignores the space harmonics and as a result, the induced stator voltages (or electromagnetic force EMF) will vary sinusoidally with time. In steady-state, the three sine waves will be displaced 120° electrical degrees in time as a result of the phases being displaced 120° in space. Using generator sign convention, the stator currents are defined positive flowing out of the machines terminals and the expressions for the induced stator voltages become

$$
\begin{aligned}
u_a &= -R_a \cdot i_a - \frac{d\psi_a}{dt} \\
u_b &= -R_b \cdot i_b - \frac{d\psi_b}{dt} \\
u_c &= -R_c \cdot i_c - \frac{d\psi_c}{dt}
\end{aligned}
\tag{3.70}
$$

with R_a, R_b, and R_c the resistance of stator a-phase, b-phase and c-phase, i_a, i_b and i_c the stator currents, and ψ_a, ψ_b and ψ_c the stator flux linkages respectively. The stator resistances are constant when skin effect and effects of temperature are neglected [219].

The equation for the field winding voltage is

$$
-u_f = -R_f \cdot i_f - \frac{d\psi_f}{dt}
\tag{3.71}
$$

with R_f, i_f and ψ_f the field winding resistance, current, and flux linkage respectively. The equations for the short-circuited (*i.e.* $u_{1d} = 0$) direct-axis damper winding and short-circuited (*i.e.* $u_{1q} = 0$) quadrature-axis damper winding are

$$
\begin{aligned}
u_{1d} &= -R_{1d} \cdot i_{1d} - \frac{d\psi_{1d}}{dt} = 0 \\
u_{1q} &= -R_{1q} \cdot i_{1q} - \frac{d\psi_{1q}}{dt} = 0
\end{aligned}
\tag{3.72}
$$

with R_{1d} (R_{1q}), i_{1d} (i_{1q}) and ψ_{1d} (ψ_{1q}) the d (q)-axis damper resistance, current, and flux linkages respectively. Here it is assumed that the damping can be adequately represented by one damper winding on the direct-axis and one on the quadrature-axis.

The voltage equations of the rotor and stator windings can be arranged in the following matrix form

$$
\begin{bmatrix} \mathbf{u_s} \\ \mathbf{u_r} \end{bmatrix} = - \begin{bmatrix} \mathbf{R_s} & 0 \\ 0 & \mathbf{R_r} \end{bmatrix} \cdot \begin{bmatrix} \mathbf{i_s} \\ \mathbf{i_r} \end{bmatrix} - \frac{d}{dt} \begin{bmatrix} \psi_\mathbf{s} \\ \psi_\mathbf{r} \end{bmatrix}
\tag{3.73}
$$

where

$$
\begin{aligned}
\mathbf{u_s} &= \begin{bmatrix} u_a & u_b & u_c \end{bmatrix}^T \\
\mathbf{u_r} &= \begin{bmatrix} -u_f & 0 & 0 \end{bmatrix}^T \\
\mathbf{R_s} &= \mathrm{diag} \begin{bmatrix} R_a & R_b & R_c \end{bmatrix}
\end{aligned}
$$

$$\mathbf{R_r} = \mathrm{diag}\begin{bmatrix} R_f & R_{1d} & R_{1q} \end{bmatrix}$$

$$\mathbf{i_s} = \begin{bmatrix} i_a & i_b & i_c \end{bmatrix}^T$$

$$\mathbf{i_r} = \begin{bmatrix} i_f & i_{1d} & i_{1q} \end{bmatrix}^T$$

$$\psi_{\mathbf{s}} = \begin{bmatrix} \psi_a & \psi_b & \psi_c \end{bmatrix}^T$$

$$\psi_{\mathbf{r}} = \begin{bmatrix} \psi_f & \psi_{1d} & \psi_{1q} \end{bmatrix}^T$$

It is assumed that the flux linkages $\psi_{\mathbf{s}}$, and $\psi_{\mathbf{r}}$ in Eq. (3.73) are linearly related to the six currents i_a, i_b, i_c, i_f, i_{1d}, and i_{1q} by a 6×6 inductance matrix

$$\begin{bmatrix} \psi_a \\ \psi_b \\ \psi_c \\ \hline \psi_f \\ \psi_{1d} \\ \psi_{1q} \end{bmatrix} = \left[\begin{array}{ccc|ccc} L_{aa} & L_{ab} & L_{ac} & L_{af} & L_{a1d} & L_{a1q} \\ L_{ba} & L_{bb} & L_{bc} & L_{bf} & L_{b1d} & L_{b1q} \\ L_{ca} & L_{cb} & L_{cc} & L_{cf} & L_{c1d} & L_{c1q} \\ \hline L_{fa} & L_{fb} & L_{fc} & L_{ff} & L_{f1d} & L_{f1q} \\ L_{1da} & L_{1db} & L_{1dc} & L_{1df} & L_{1d1d} & L_{1d1q} \\ L_{1qa} & L_{1qb} & L_{1qc} & L_{1qf} & L_{1q1d} & L_{1q1q} \end{array} \right] \cdot \begin{bmatrix} i_a \\ i_b \\ i_c \\ \hline i_f \\ i_{1d} \\ i_{1q} \end{bmatrix} \quad (3.74)$$

where self-inductances are denoted by two like subscripts, and mutual inductances are denoted by two unlike subscripts. In matrix form

$$\begin{bmatrix} \psi_{\mathbf{s}} \\ \psi_{\mathbf{r}} \end{bmatrix} = \begin{bmatrix} \mathbf{L_{ss}} & \mathbf{M_{sr}} \\ \mathbf{M_{rs}} & \mathbf{L_{rr}} \end{bmatrix} \cdot \begin{bmatrix} \mathbf{i_s} \\ \mathbf{i_r} \end{bmatrix} \quad (3.75)$$

where $\mathbf{L_{ss}}$ represents the stator self-inductance matrix, and $\mathbf{L_{rr}}$ represents the rotor self-inductance matrix. The stator-rotor and rotor-stator mutual inductances are represented by $\mathbf{M_{sr}}$ and $\mathbf{M_{sr}}$ respectively.

The synchronous generator is thus represented as a group of magnetically coupled circuits. The circuits are shown schematically in Fig. 3.25. Each of the windings has thus its own resistance, self-inductance and mutual inductances with respect to every other winding. Notice that most inductances in Eq. (3.75) depend on the angular position of the rotor [222].

Inductances of salient-pole generator

The self-inductance of any stator winding varies periodically from a maximum (when the direct-axis coincides with the phase axis) to a minimum (when the quadrature-axis is in line with the phase axis). The self-inductance L_{aa} for example, will reach a maximum for $\theta_e = 0°$, a minimum for $\theta_e = 90°$ and maximum again for $\theta_e = 180°$ and so on. That is, L_{aa} has a period of $\theta_e = 180$ electrical degrees and can be exactly represented by a series of cosines of even harmonics of angle [246]. Because of the rotor symmetry, the diagonal elements of the submatrix $\mathbf{L_{ss}}$ are represented as

$$\begin{aligned} L_{aa} &= L_s + L_m \cos 2\left(\theta_e\right) \\ L_{bb} &= L_s + L_m \cos 2\left(\theta_e - \tfrac{2}{3}\pi\right) \\ L_{cc} &= L_s + L_m \cos 2\left(\theta_e + \tfrac{2}{3}\pi\right) \end{aligned} \quad (3.76)$$
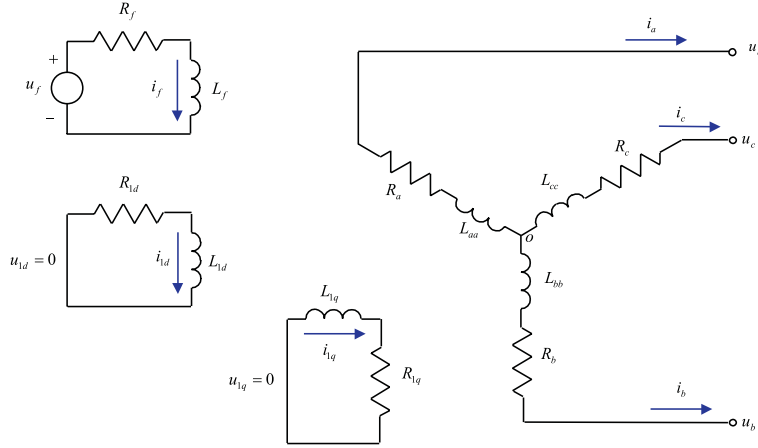
Figure 3.25: *Schematic representation of mutually coupled circuits.*

where both L_s and L_m are constants $(L_s > L_m)$, and θ_e is the angle between the direct-axis and the magnetic axis of phase a in electrical degrees as shown in Fig. 3.24. Since the angle included in one pole pair p is 360 electrical degrees, the angle θ_e in electrical units is related to the mechanical angle θ_m through the number of pole-pairs p as follows

$$\theta_e = p\,\theta_m$$

The air gap of a salient-pole synchronous generator varies along the inner circumference of the stator. Consequently the mutual inductances between any two stator phases are also periodic functions of the electrical angle θ_e, and hence vary with time. It can be concluded from symmetry considerations that the mutual inductance between phase a and b should have a negative maximum when the pole axis is lined up 30° behind phase a, or 30° ahead of phase b, and a negative minimum when it is midway between the two phases. Thus, for a machine with sinusoidally-distributed windings, the variations of the stator mutual inductances, *i.e.* the off-diagonal elements of submatrix $\mathbf{L_{ss}}$ can be represented as follows

$$
\begin{aligned}
L_{ab} &= L_{ba} = -M_s - L_m \cos 2\left(\theta_e + \tfrac{1}{6}\pi\right) \\
L_{bc} &= L_{cb} = -M_s - L_m \cos 2\left(\theta_e - \tfrac{1}{2}\pi\right) \\
L_{ca} &= L_{ac} = -M_s - L_m \cos 2\left(\theta_e + \tfrac{5}{6}\pi\right)
\end{aligned}
\tag{3.77}
$$

where $|M_s| > L_m$ [246]. Notice that the signs of the mutual inductance terms depend upon assumed current directions and circuit orientation.

The elements of the submatrix $\mathbf{L_{rr}}$ consist of rotor self-inductances and mutual inductance between any two circuits both in direct-axis (or in quadrature-axis). All the rotor self-inductances, *i.e.* the diagonal elements of submatrix $\mathbf{L_{rr}}$, are constant since the effects of stator slots and saturation are neglected. They are represented

with single subscript notation

$$
\begin{aligned}
L_{ff} &= L_f \\
L_{1d1d} &= L_{1d} \\
L_{1q1q} &= L_{1q}
\end{aligned}
\tag{3.78}
$$

The mutual inductance between any two circuits both in direct-axis (or both in quadrature-axis) is constant. The mutual inductance between any rotor direct-axis circuit and quadrature-axis circuit does not exist, thus

$$
\begin{aligned}
L_{f1d} &= L_{1df} = M_r \\
L_{f1q} &= L_{1qf} = 0 \\
L_{1d1q} &= L_{1q1d} = 0
\end{aligned}
\tag{3.79}
$$

This are the off-diagonal elements of submatrix $\mathbf{L_{rr}}$.

Finally, consider the mutual inductances between stator and rotor circuits. Obviously, these are periodic functions of the electrical angle θ_e. Because only the space-fundamental component of the produced flux links the sinusoidally distributed stator, all stator-rotor mutual inductances vary sinusoidally, reaching a maximum when the two windings in question align. Thus, their variations can be written as follows

$$
\begin{aligned}
L_{af} &= L_{fa} = M_f \cos\theta_e \\
L_{bf} &= L_{fb} = M_f \cos\left(\theta_e - \tfrac{2}{3}\pi\right) \\
L_{cf} &= L_{fc} = M_f \cos\left(\theta_e + \tfrac{2}{3}\pi\right) \\
L_{a1d} &= L_{1da} = M_{1d} \cos\theta_e \\
L_{b1d} &= L_{1db} = M_{1d} \cos\left(\theta_e - \tfrac{2}{3}\pi\right) \\
L_{c1d} &= L_{1dc} = M_{1d} \cos\left(\theta_e + \tfrac{2}{3}\pi\right) \\
L_{a1q} &= L_{1qa} = M_{1q} \sin\theta_e \\
L_{b1q} &= L_{1qb} = M_{1q} \sin\left(\theta_e - \tfrac{2}{3}\pi\right) \\
L_{c1q} &= L_{1qc} = M_{1q} \sin\left(\theta_e + \tfrac{2}{3}\pi\right)
\end{aligned}
\tag{3.80}
$$

It follows from above equations that the rotor-stator mutual inductance matrix is equal to the transpose of the stator-rotor mutual inductance matrix. Thus, $\mathbf{M_{sr}} = \mathbf{M_{rs}^T}$ in Eq. (3.75).

The dynamic behavior of a synchronous, salient-pole generator is thus described by Eq. (3.73) and the time-varying coefficients are given by Eqs. (3.76)-(3.80). Analysis of the dynamic behavior can thus be accomplished by the solution of a set of simultaneous coupled-circuit differential equations. The solution of these equations is complicated due to the fact that the inductances between the stator-phase windings and the rotor circuits are a function of the rotor angle θ_e (and hence change with time). This complication can be avoided by using Park's transformation [211, 212].

Park's transformation

The key idea of Park's transformation is to express the stator flux linkages in the rotating d, q reference system instead of the normal stator fixed reference system. The stator windings are replaced with two fictitious windings which are fixed with respect to the rotor. One winding is chosen to coincide with the direct-axis, and the other with the quadrature-axis.

Since the axes of the rotor windings are already along the direct and quadrature-axes, the transformation needs only to be applied to the stator quantities. In order to ensure that the rotor quantities remain unaffected, Park's transformation matrix $\mathbf{T}_{0dq}$ is expanded with a 3×3 identity matrix $\mathbf{I}_3$ as follows

$$\mathbf{C} = \begin{bmatrix} \mathbf{T}_{0dq} & \mathbf{0} \\ \mathbf{0} & \mathbf{I_3} \end{bmatrix} \tag{3.81}$$

with

$$\mathbf{T}_{0dq} = \sqrt{\tfrac{2}{3}} \begin{bmatrix} \frac{1}{\sqrt{2}} & \frac{1}{\sqrt{2}} & \frac{1}{\sqrt{2}} \\ \cos(p\,\theta_m) & \cos(p\,\theta_m - \tfrac{2}{3}\pi) & \cos(p\,\theta_m + \tfrac{2}{3}\pi) \\ \sin(p\,\theta_m) & \sin(p\,\theta_m - \tfrac{2}{3}\pi) & \sin(p\,\theta_m + \tfrac{2}{3}\pi) \end{bmatrix} \tag{3.82}$$

Notice the resemblance between Park's transformation matrix and the presence of the sine and cosine terms in Eq. (3.80).

By definition, the transformed voltages, currents and flux linkages of the stator are given by

$$\begin{aligned} \mathbf{u_{0dq}} &= \mathbf{T}_{0dq} \cdot \mathbf{u}_s \\ \mathbf{i_{0dq}} &= \mathbf{T}_{0dq} \cdot \mathbf{i}_s \\ \psi_{\mathbf{0dq}} &= \mathbf{T}_{0dq} \cdot \psi_s \end{aligned}$$

where

$$\begin{aligned} \mathbf{u_{0dq}} &= \begin{bmatrix} u_0 & u_d & u_q \end{bmatrix}^T \\ \mathbf{i_{0dq}} &= \begin{bmatrix} i_0 & i_d & i_q \end{bmatrix}^T \\ \psi_{\mathbf{0dq}} &= \begin{bmatrix} \psi_0 & \psi_d & \psi_q \end{bmatrix}^T \end{aligned}$$

Premultiplying Eq. (3.75) by the transformation matrix $\mathbf{C}$, the flux linkage equations become

$$\underbrace{\begin{bmatrix} \mathbf{T}_{0dq} & \mathbf{0} \\ \mathbf{0} & \mathbf{I_3} \end{bmatrix} \begin{bmatrix} \psi_{\mathbf{s}} \\ \psi_{\mathbf{r}} \end{bmatrix}}_{\begin{bmatrix} \psi_{\mathbf{0dq}} \\ \psi_{\mathbf{r}} \end{bmatrix}} =$$

$$= \begin{bmatrix} \mathbf{T}_{0dq} & \mathbf{0} \\ \mathbf{0} & \mathbf{I_3} \end{bmatrix} \begin{bmatrix} \mathbf{L_{ss}} & \mathbf{M_{sr}} \\ \mathbf{M_{rs}} & \mathbf{L_{rr}} \end{bmatrix} \begin{bmatrix} \mathbf{T}_{0dq}^{-1} & \mathbf{0} \\ \mathbf{0} & \mathbf{I_3} \end{bmatrix} \cdot \underbrace{\begin{bmatrix} \mathbf{T}_{0dq} & \mathbf{0} \\ \mathbf{0} & \mathbf{I_3} \end{bmatrix} \begin{bmatrix} \mathbf{i_s} \\ \mathbf{i_r} \end{bmatrix}}_{\begin{bmatrix} \mathbf{i_{0dq}} \\ \mathbf{i_r} \end{bmatrix}}$$

or equivalently

$$
\begin{bmatrix} \psi_{\mathbf{0dq}} \\ \psi_{\mathbf{r}} \end{bmatrix} = \begin{bmatrix} \mathbf{T}_{0dq} & \mathbf{0} \\ \mathbf{0} & \mathbf{I_3} \end{bmatrix} \begin{bmatrix} \mathbf{L_{ss}} & \mathbf{M_{sr}} \\ \mathbf{M_{rs}} & \mathbf{L_{rr}} \end{bmatrix} \begin{bmatrix} \mathbf{T}_{0dq}^{-1} & \mathbf{0} \\ \mathbf{0} & \mathbf{I_3} \end{bmatrix} \cdot \begin{bmatrix} \mathbf{i_{0dq}} \\ \mathbf{i_r} \end{bmatrix} \tag{3.83}
$$

Substituting the expressions for $\mathbf{T}_{0dq}$, $\mathbf{T}_{0dq}^{-1}$ and the inductances given by Eqs. (3.76)-(3.80), it can be shown that the above equation reduces to the following expression in which all the inductances are independent of the rotor angle θ_e

$$
\begin{bmatrix} \psi_0 \\ \psi_d \\ \psi_q \\ \hline \psi_f \\ \psi_{1d} \\ \psi_{1q} \end{bmatrix} = \underbrace{\left[\begin{array}{ccc|ccc} L_o & 0 & 0 & 0 & 0 & 0 \\ 0 & L_d & 0 & k\,M_f & k\,M_{1d} & 0 \\ 0 & 0 & L_q & 0 & 0 & k\,M_{1q} \\ \hline 0 & k\,M_f & 0 & L_f & M_r & 0 \\ 0 & k\,M_{1d} & 0 & M_r & L_{1d} & 0 \\ 0 & 0 & k\,M_{1q} & 0 & 0 & L_{1q} \end{array} \right]}_{\mathbf{L}} \cdot \begin{bmatrix} i_0 \\ i_d \\ i_q \\ \hline i_f \\ i_{1d} \\ i_{1q} \end{bmatrix} \tag{3.84}
$$

where

$$
\begin{align}
L_0 &= L_s - 2M_s \tag{3.85} \\
L_d &= L_s + M_s + \tfrac{3}{2}\,L_m \tag{3.86} \\
L_q &= L_s + M_s - \tfrac{3}{2}\,L_m \tag{3.87}
\end{align}
$$

the self-inductances of the equivalent circuits, and $k = \sqrt{\tfrac{3}{2}}$. Note that the inductance matrix $\mathbf{L}$ is sparse, symmetric and constant. The reader should compare it with the inductance matrix in Eq. (3.74) which depends on $\theta_e = p\,\theta_m$ in a complicated way.

Obviously, the coupling between the rotor and stator of the direct-axis involves the factor k, and similarly for the quadrature-axis. For example, the contribution to the direct-axis stator flux linkage ψ_d due to the field current i_f is $k\,M_f i_f$ and so on. The self-inductances L_0, L_d, and L_q are known as the zero-sequence inductance, the direct-axis synchronous inductance, and the quadrature-axis synchronous inductance, respectively [246].

Applying the transformation $\mathbf{C}$ to Eq. (3.73) gives the following voltage equations in the dq reference frame

$$
\begin{aligned}
\begin{bmatrix} \mathbf{u_{0dq}} \\ \mathbf{u_r} \end{bmatrix} &= - \begin{bmatrix} \mathbf{T}_{0dq} & \mathbf{0} \\ \mathbf{0} & \mathbf{I_3} \end{bmatrix} \begin{bmatrix} \mathbf{R_s} & \mathbf{0} \\ \mathbf{0} & \mathbf{R_r} \end{bmatrix} \begin{bmatrix} \mathbf{T}_{0dq}^{-1} & \mathbf{0} \\ \mathbf{0} & \mathbf{I_3} \end{bmatrix} \begin{bmatrix} \mathbf{i_{0dq}} \\ \mathbf{i_r} \end{bmatrix} \\
&\quad - \begin{bmatrix} \mathbf{T}_{0dq} & \mathbf{0} \\ \mathbf{0} & \mathbf{I_3} \end{bmatrix} \frac{d}{dt} \left(\begin{bmatrix} \mathbf{T}_{0dq}^{-1} & \mathbf{0} \\ \mathbf{0} & \mathbf{I_3} \end{bmatrix} \begin{bmatrix} \psi_{\mathbf{0dq}} \\ \psi_{\mathbf{r}} \end{bmatrix} \right)
\end{aligned} \tag{3.88}
$$

where

$$
\begin{align}
\mathbf{u_{0dq}} &= \begin{bmatrix} u_0 & u_d & u_q \end{bmatrix}^T \\
\mathbf{R_s} &= \text{diag} \begin{bmatrix} R_a & R_b & R_c \end{bmatrix} \\
\mathbf{i_{0dq}} &= \begin{bmatrix} i_0 & i_d & i_q \end{bmatrix}^T
\end{align}
$$

$$\psi_{\mathbf{0dq}} = \begin{bmatrix} \psi_0 & \psi_d & \psi_q \end{bmatrix}^T$$

$$\mathbf{u_r} = \begin{bmatrix} -u_f & 0 & 0 \end{bmatrix}^T$$

$$\mathbf{R_r} = \operatorname{diag}\begin{bmatrix} R_f & R_{1d} & R_{1q} \end{bmatrix}$$

$$\mathbf{i_r} = \begin{bmatrix} i_f & i_{1d} & i_{1q} \end{bmatrix}^T$$

$$\psi_{\mathbf{r}} = \begin{bmatrix} \psi_f & \psi_{1d} & \psi_{1q} \end{bmatrix}^T$$

Evaluating the first term while assuming that $R_a = R_b = R_c = R_s$, and obtaining the derivative of the second term in Eq. (3.88), yields

$$\begin{bmatrix} \mathbf{u_{0dq}} \\ \mathbf{u_r} \end{bmatrix} = -\begin{bmatrix} \mathbf{R_s} & 0 \\ 0 & \mathbf{R_r} \end{bmatrix}\begin{bmatrix} \mathbf{i_{0dq}} \\ \mathbf{i_r} \end{bmatrix}$$
$$-\begin{bmatrix} \mathbf{T}_{0dq} \cdot \frac{d}{dt}\left(\mathbf{T}_{0dq}^{-1}\right) & \mathbf{0} \\ \mathbf{0} & \mathbf{0} \end{bmatrix}\begin{bmatrix} \psi_{\mathbf{0dq}} \\ \psi_{\mathbf{r}} \end{bmatrix} - \frac{d}{dt}\begin{bmatrix} \psi_{\mathbf{0dq}} \\ \psi_{\mathbf{r}} \end{bmatrix} \quad (3.89)$$

The expression for $\mathbf{T}_{0dq} \cdot \frac{d}{dt}\left(\mathbf{T}_{0dq}^{-1}\right)$ can be written as

$$\mathbf{T}_{0dq}\frac{d}{dt}\left(\mathbf{T}_{0dq}^{-1}\right) = \mathbf{T}_{0dq}\frac{d\theta_m}{dt}\frac{d}{d\theta_m}\left(\mathbf{T}_{0dq}^{-1}\right) = \omega_m\,\mathbf{T}_{0dq}\frac{d}{d\theta_m}\left(\mathbf{T}_{0dq}^{-1}\right) \quad (3.90)$$

with

$$\frac{d}{d\theta_m}\mathbf{T}_{0dq}^{-1} = p\,\sqrt{\frac{2}{3}}\begin{bmatrix} 0 & -\sin(p\,\theta_m) & \cos(p\,\theta_m) \\ 0 & -\sin(p\,\theta_m - \frac{2}{3}\pi) & \cos(p\,\theta_m - \frac{2}{3}\pi) \\ 0 & -\sin(p\,\theta_m + \frac{2}{3}\pi) & \cos(p\,\theta_m + \frac{2}{3}\pi) \end{bmatrix} \quad (3.91)$$

Substituting this result, and $\mathbf{T}_{0dq}$ from Eq. (3.82) into Eq. (3.90) gives

$$\omega_m\,\mathbf{T}_{0dq}\frac{d}{d\theta_m}\left(\mathbf{T}_{0dq}^{-1}\right) = \begin{bmatrix} \frac{1}{\sqrt{2}} & \frac{1}{\sqrt{2}} & \frac{1}{\sqrt{2}} \\ \cos(p\,\omega_m) & \cos(p\,\omega_m - \frac{2}{3}\pi) & \cos(p\,\omega_m + \frac{2}{3}\pi) \\ \sin(p\,\omega_m) & \sin(p\,\omega_m - \frac{2}{3}\pi) & \sin(p\,\omega_m + \frac{2}{3}\pi) \end{bmatrix} \cdot$$
$$p\,\omega_m\,\frac{2}{3}\begin{bmatrix} 0 & -\sin(p\,\omega_m) & \cos(p\,\omega_m) \\ 0 & -\sin(p\,\omega_m - \frac{2}{3}\pi) & \cos(p\,\omega_m - \frac{2}{3}\pi) \\ 0 & -\sin(p\,\omega_m + \frac{2}{3}\pi) & \cos(p\,\omega_m + \frac{2}{3}\pi) \end{bmatrix}$$
$$= p\,\omega_m\begin{bmatrix} 0 & 0 & 0 \\ 0 & 0 & 1 \\ 0 & -1 & 0 \end{bmatrix} \quad (3.92)$$

Back-substituting the above results in Eq. (3.88) gives the following voltages equations of an ideal synchronous generator (*i.e.* linear magnetic circuit and stator windings are sinusoidally distributed along the stator circumference) in the dq reference frame in matrix form

$$\begin{bmatrix} \mathbf{u_{0dq}} \\ \mathbf{u_r} \end{bmatrix} = -\begin{bmatrix} \mathbf{R_s} & 0 \\ 0 & \mathbf{R_r} \end{bmatrix}\begin{bmatrix} \mathbf{i_{0dq}} \\ \mathbf{i_r} \end{bmatrix}$$

$$
-\left[\ p\,\omega_m
\begin{bmatrix}
0 & 0 & 0 \\
0 & 0 & 1 \\
0 & -1 & 0
\end{bmatrix}
\quad \mathbf{0} \\
\qquad \mathbf{0} \qquad\qquad \mathbf{0}
\right]
\begin{bmatrix}
\psi_{\mathbf{0dq}} \\
\psi_{\mathbf{r}}
\end{bmatrix}
-\frac{d}{dt}
\begin{bmatrix}
\psi_{\mathbf{0dq}} \\
\psi_{\mathbf{r}}
\end{bmatrix}
\tag{3.93}
$$

Notice that Eq. (3.93) contains both currents and flux linkages as variables. Since these two sets of variables are mutually dependent, it is also possible to select the flux linkages as state variables [3]. Another observation is that the zero-sequence equation

$$
u_0 = -R_0 \cdot i_0 - L_0 \frac{d}{dt} i_0
$$

is not coupled to the other equations. Therefore, it can be treated separately. In addition, in the vast majority of cases the generator is either connected in star such that the neutral current i_0 does not flow (*i.e.* neutral point is isolated) or is Delta connected (were no neutral exists), implying that the zero-sequence equation can be omitted [107, 202]. In the sequel the zero-sequence equation is omitted since the power in the Lagerwey LW-50/750 wind turbine is generated in two star connected three-phase systems with the neutral points isolated(*see* Appendix A.4).

Substituting Eq. (3.84) in Eq. (3.93), omitting the zero-sequence equation yields

$$
\begin{bmatrix}
u_d \\
-u_f \\
0 \\
\hline
u_q \\
0
\end{bmatrix}
=
$$

$$
-\left[
\begin{array}{ccc|cc}
R_s & 0 & 0 & p\,\omega_m L_q & p\,\omega_m kM_{1q} \\
0 & R_f & 0 & 0 & 0 \\
0 & 0 & R_{1d} & 0 & 0 \\
\hline
-p\,\omega_m L_d & -p\,\omega_m kM_f & -p\,\omega_m kM_{1d} & R_s & 0 \\
0 & 0 & 0 & 0 & R_{1q}
\end{array}
\right]
\begin{bmatrix}
i_d \\
i_f \\
i_{1d} \\
i_q \\
i_{1q}
\end{bmatrix}
$$

$$
-\left[
\begin{array}{ccc|cc}
L_d & k\,M_f & k\,M_{1d} & 0 & 0 \\
k\,M_f & L_f & M_r & 0 & 0 \\
k\,M_{1d} & M_r & L_{1d} & 0 & 0 \\
\hline
0 & 0 & 0 & L_q & k\,M_{1q} \\
0 & 0 & 0 & k\,M_{1q} & L_{1q}
\end{array}
\right]
\frac{d}{dt}
\begin{bmatrix}
i_d \\
i_f \\
i_{1d} \\
i_q \\
i_{1q}
\end{bmatrix}
\tag{3.94}
$$

This complete set of equations consisting of flux-linkage relations and voltage equations are known as Park's equations. The equations have been rearranged in order to show the coupling between the direct-axis and the quadrature-axis more clearly. From the above equation follows that if the generator speed $p\,\omega_m$ is constant, the resulting Park's equations are linear with constant coefficients. Notice that at standstill (*i.e.* $\omega_m = 0$), there is no interaction between the direct-axis and the quadrature-axis.

It should be noted that, in his original paper, R.H. Park used the non-power invariant transformation to transform the stator quantities onto the dq reference

frame that is fixed to the rotor. In the above derivation we have used the power-invariant version in order to ensure that in both reference frames the same power expressions are obtained. In addition, he used motor sign convention for the stator circuits.

Park's equations (reformulated)

Park's equations are in the presented form not suited for time-domain simulation since they contain a number of variables that can not be measured in practice (*i.e.* i_{1d}, i_{1q}, ψ_{1d}, and ψ_{1q}). It will be shown below that it is possible to eliminate these variables via substitution and rearranging of the aforementioned equations. When the generator speed is constant and equal to $p\omega_m$, the differential equations are linear with constant coefficients. This implies that Eq. (3.84) may be transformed to the Laplace domain as follows

$$
\begin{aligned}
\Psi_d &= L_d I_d + k M_f I_f + k M_{1d} I_{1d} \\
\Psi_q &= L_q I_q + k M_{1q} I_{1q} \\
\Psi_f &= k M_f I_d + L_f I_f + M_r I_{1d} \\
\Psi_{1d} &= k M_{1d} I_d + M_r I_f + L_{1d} I_{1d} \\
\Psi_{1q} &= k M_{1q} I_q + L_{1q} I_{1q}
\end{aligned}
\tag{3.95}
$$

where $k = \sqrt{\frac{3}{2}}$. Notice that capitals indicate Laplace-transformed quantities, and that zero initial conditions are assumed.

Applying the Laplace transform to Eq. (3.93) with the assumption of zero initial conditions gives

$$
\begin{aligned}
U_d &= -R_s I_d - s\Psi_d - p\omega_m \Psi_q \\
U_q &= -R_s I_q - s\Psi_q + p\omega_m \Psi_d \\
U_f &= R_f I_f + s\Psi_f \\
0 &= -R_{1d} I_{1d} - s\Psi_{1d} \\
0 &= -R_{1q} I_{1q} - s\Psi_{1q}
\end{aligned}
\tag{3.96}
$$

where it again is assumed that $R_a = R_b = R_c = R_s$. The zero-sequence equation has been omitted.

The transformed variables will now be eliminated via substitution and rearranging, first for the direct-axis, and secondly for the quadrature-axis:

- **Direct-axis**. The equation for the field winding voltage, and the equation for the voltage across the direct-axis damper are given by

$$
U_f = R_f I_f + s\Psi_f \qquad 0 = -R_{1d} I_{1d} - s\Psi_{1d}
$$

The flux linkage equations on the direct-axis are given by

$$
\begin{aligned}
\Psi_d &= L_d I_d + k M_f I_f + k M_{1d} I_{1d} \\
\Psi_f &= k M_f I_d + L_f I_f + M_r I_{1d} \\
\Psi_{1d} &= k M_{1d} I_d + M_r I_f + L_{1d} I_{1d}
\end{aligned}
$$

Rewriting the flux linkage expressions and substituting the results in the voltage equations allows elimination of I_f, I_{1d}, Ψ_f and Ψ_{1d}, resulting in the following equation for the direct-axis stator flux

$$
\begin{aligned}
\Psi_d \;=\;& L_d I_d \, \frac{1 + (\sigma_f \tau_f + \sigma_{1d}\tau_{1d})s}{1 + (\tau_f + \tau_{1d})s + (\sigma_r \tau_f \tau_{1d})s^{\,2}} \\
&+ L_d I_d \, \frac{(\tau_f \tau_{1d} \cdot (\sigma_r - \mu_{1d}(1-\sigma_f) - \mu_f(1-\sigma_{1d})))s^{\,2}}{1 + (\tau_f + \tau_{1d})s + (\sigma_r \tau_f \tau_{1d})s^{\,2}} \qquad (3.97) \\
&+ k M_f \, \frac{U_f}{R_f} \, \frac{1 + (\tau_{1d}\mu_{1d})s}{1 + (\tau_f + \tau_{1d})s + (\sigma_r \tau_f \tau_{1d})s^{\,2}}
\end{aligned}
$$

where

$$
\tau_f = \frac{L_f}{R_f} \qquad \tau_{1d} = \frac{L_{1d}}{R_{1d}}
$$

the rotor time constants for the direct-axis,

$$
\sigma_r = 1 - \frac{M_r^2}{L_f L_{1d}} \qquad \sigma_f = 1 - \frac{k^2 M_f^2}{L_d L_f} \qquad \sigma_{1d} = 1 - \frac{k^2 M_{1d}^2}{L_d L_{1d}}
$$

the leakage factors, and

$$
\mu_f = 1 - \frac{M_f M_r}{L_f M_{1d}} \qquad \mu_{1d} = 1 - \frac{M_{1d} M_r}{L_{1d} M_f}
$$

Furthermore, it is clear from Eq. (3.97) that the direct-axis stator flux is frequency dependent, and that its DC-gain is equal to L_d (for $u_f = 0$), or equal to $k M_f / R_f$ (for $i_d = 0$). In the sequel, these DC-gains are referred to as L_d^{DC}, and $-G_{fd}^{DC}$.

However, Eq. (3.97) is valid only for the situation that the (fictitious) damper winding can be adequately represented by one winding located on the direct-axis. Recall that the number of damper windings depends on both the physical construction of the rotor and the accuracy required by the model. More general, the direct-axis stator flux equation is described by

$$
\Psi_d(s) = L_d(s) I_d(s) - G_{fd}(s) U_f(s) \qquad (3.98)
$$

where $L_d(s)$ and $G_{fd}(s)$ transfer functions. The order of the numerator and denominator polynomials of $L_d(s)$ are equal to the number of damper windings located on the d-axis plus the field winding, while $G_{fd}(s)$ has the same denominator as $L_d(s)$, but a different numerator. The order of the numerator of $G_{fd}(s)$ is one less than the denominator. Both transfer functions depend on the design of the synchronous generator and $L_d(s)$ is usually referred to as "operational inductance".

In addition, it is shown in Appendix D that

$$
\Psi_d(s) = L_{do}(s) I_d(s) + L_{dfo}(s) I_f(s) \qquad (3.99)
$$

97

and that

$$\Psi_f(s) = L_{fdo}(s)I_d(s) + L_{fo}(s)I_f(s) \tag{3.100}$$

where $L_{do}(s)$, $L_{fdo}(s) = L_{dfo}(s)$, and $L_{fo}(s)$ are proper transfer functions, which depend on the design of the synchronous generator.

- **Quadrature-axis**. The equation for the voltage across the quadrature-axis damper is given by

$$0 = -R_{1q}I_{1q} - s\Psi_{1q}$$

The flux linkage equations on the quadrature-axis are given by

$$\begin{aligned}
\Psi_q &= L_q I_q + k M_{1q} I_{1q} \\
\Psi_{1q} &= k M_{1q} I_q + L_{1q} I_{1q}
\end{aligned}$$

Rearranging the latter two expressions and substituting the results in the voltage equation allows elimination of I_{1q} and Ψ_{1q}, resulting in the following equation for the quadrature-axis stator flux

$$\Psi_q = L_q I_q \frac{1 + \tau_{1q}\sigma_{1q} \cdot s}{1 + \tau_{1q} \cdot s} \tag{3.101}$$

where

$$\tau_{1q} = \frac{L_{1q}}{R_{1q}}$$

the rotor time constant for the quadrature-axis, and

$$\sigma_{1q} = 1 - \frac{k^2 M_{1q}^2}{L_q L_{1q}}$$

the leakage factor. Furthermore, it is clear from Eq. (3.101) that the quadrature-axis stator flux is frequency dependent, and that its DC-gain is equal to L_q. In the sequel, the DC-gain is referred to as L_q^{DC}.

However, Eq. (3.101) is valid only for the situation that the (fictitious) damper winding can be adequately represented by one winding located on the quadrature-axis. More general, the quadrature-axis stator flux equation is described by

$$\Psi_q(s) = L_q(s)I_q(s) \tag{3.102}$$

where $L_q(s)$ is a proper transfer function, which function depends on the design of the synchronous generator. The order of the numerator and denominator polynomials of $L_q(s)$ are equal to the number of damper windings located on the q-axis.

The voltage equations in the dq reference frame of the electromagnetic part of a synchronous generator have been given in matrix form in Eq. (3.93). Removing the

zero-sequence equation gives the following set of equations

$$
\begin{aligned}
u_d &= -R_s i_d - p\,\omega_m \psi_q - \frac{d}{dt}\psi_d \\
u_q &= -R_s i_q + p\,\omega_m \psi_d - \frac{d}{dt}\psi_q \\
-u_f &= -R_f i_f - \frac{d}{dt}\psi_f
\end{aligned}
\tag{3.103}
$$

with u_d the direct-axis voltage, R_s the stator-winding resistance, i_d the direct-axis current, $p\,\omega_m$ the generator speed, ψ_q the quadrature-axis winding flux, t time, ψ_d the direct-axis winding flux, u_q the quadrature-axis voltage, i_q the quadrature-axis current, u_f the field-winding voltage, R_f the field-winding resistance, i_f the field-winding current, and ψ_f the field-winding flux.

A few observations can be made, the most important one being that equations (3.103) are coupled via the fluxes. In addition, they depend on the generator speed $p\,\omega_m$, thereby introducing non-linearities. For time-domain simulation purposes, it is convenient to rewrite the this set of equations in the following form

$$
\begin{aligned}
\psi_d &= -\int \left(u_d + R_s i_d + p\,\omega_m \psi_q \right) dt \\
\psi_q &= -\int \left(u_q + R_s i_q - p\,\omega_m \psi_d \right) dt \\
\psi_f &= \int \left(u_f - R_f i_f \right) dt
\end{aligned}
\tag{3.104}
$$

with the fluxes as state variables.

The fluxes, in turn, have been given by

$$
\begin{aligned}
\Psi_d(s) &\overset{(3.99)}{=} L_{do}(s) I_d(s) + L_{dfo}(s) I_f(s) \\
\Psi_q(s) &\overset{(3.102)}{=} L_q(s) I_q(s) \\
\Psi_f(s) &\overset{(3.100)}{=} L_{fdo}(s) I_d(s) + L_{fo}(s) I_f(s)
\end{aligned}
\tag{3.105}
$$

with s the Laplace operator and $L_{do}(s)$, $L_{fdo}(s) = L_{dfo}(s)$, $L_q(s)$, $L_{fo}(s)$ proper transfer functions which can, for a finite number of damper windings, be expressed as a ratio of polynomials in s [147]. The direct-axis flux equations can be conveniently expressed in matrix form

$$
\begin{bmatrix} \Psi_d(s) \\ \Psi_f(s) \end{bmatrix} = \begin{bmatrix} L_{do}(s) & L_{fdo}(s) \\ L_{fdo}(s) & L_{fo}(s) \end{bmatrix} \cdot \begin{bmatrix} I_d(s) \\ I_f(s) \end{bmatrix}
\tag{3.106}
$$

It can be easily shown that the inverse transformation is given by

$$
\begin{bmatrix} I_d(s) \\ I_f(s) \end{bmatrix} = \frac{\begin{bmatrix} L_{fo}(s) & -L_{fdo}(s) \\ -L_{fdo}(s) & L_{do}(s) \end{bmatrix}}{L_{do}(s) \cdot L_{fo}(s) - L_{fdo}^2(s)} \cdot \begin{bmatrix} \Psi_d(s) \\ \Psi_f(s) \end{bmatrix}
\tag{3.107}
$$

99

It is shown in Appendix D that the denominators of $L_{do}(s)$, $L_{dfo}(s) = L_{fdo}(s)$, and $L_{fo}(s)$ are all the same. Consequently, the denominators in the above matrix equation are identical.

Finally, the inverse of the quadrature-axis flux equation is given by

$$I_q(s) = L_q(s)^{-1}\Psi_q(s) \tag{3.108}$$

The dynamic behavior of an ideal synchronous generator is thus fully described by the sets of equations (3.104), (3.107) and (3.108) expressed in the *dq* reference frame. These equations are implemented in DAWIDUM's Elec2 module (*see* Appendix I.2.4). The resulting block diagram is depicted in Fig. 3.26.
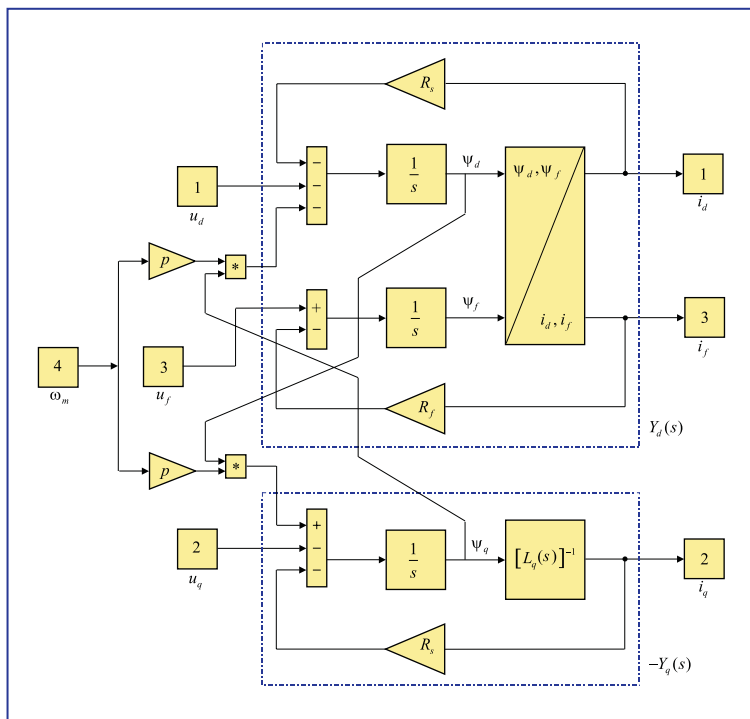
Figure 3.26: *Block diagram of an ideal synchronous machine.*

Obviously, for simulation as well as control design purposes, accurate information about the transfer functions $L_{do}(s)$, $L_{fdo}(s)$, $L_q(s)$ and $L_{fo}(s)$, as well as the resistances R_s and R_f, is required. In Section 4.3 a new procedure is developed for identifying the transfer functions $Y_d(s)$ and $Y_q(s)$ (*see* Fig. 3.26) of Park's *dq*-axis model of a synchronous generator from time-domain standstill test data. To complete the analysis, relations for power and torque are needed.

Electromagnetic torque

The instantaneous power output of a three-phase synchronous generator is simply the sum of the stator ui products

$$P_g = u_a \cdot i_a + u_b \cdot i_b + u_c \cdot i_c \qquad (3.109)$$

It can be shown that by applying Park's power-invariant transformation to Eq. (3.109), the following power output equation expressed in odq coordinates can be obtained

$$P_g = u_0 \cdot i_0 + u_d \cdot i_d + u_q \cdot i_q \qquad (3.110)$$

Assuming that the generator is star connected with the star point not used, this equation reduces to

$$P_g = u_d \cdot i_d + u_q \cdot i_q \qquad (i_0 = 0) \qquad (3.111)$$

Substitution of u_d and u_q from Eq. (3.93) in Eq. (3.111) gives

$$
\begin{aligned}
P_g &= \left(-R_s \cdot i_d - p\,\omega_m \psi_q - \frac{d\psi_d}{dt}\right) \cdot i_d + \left(-R_s \cdot i_q + p\,\omega_m \psi_d - \frac{d\psi_q}{dt}\right) \cdot i_q \\
&= \underbrace{-R_s \left(i_d^2 + i_q^2\right)}_{P_{cu}^s} - \left(\frac{d\psi_d}{dt} i_d + \frac{d\psi_q}{dt} i_q\right) + \underbrace{p\,\omega_m \left(\psi_d \cdot i_q - \psi_q \cdot i_d\right)}_{P_{em}} \qquad (3.112)
\end{aligned}
$$

The first term in Eq. (3.112) describes the power dissipated in the stator windings (the so-called stator copper losses). The second term corresponds to the time rate of change of the magnetic energy stored in the inductances of the generator, and the third term reflects the power transferred across the airgap [211]. This power is equal to the electromechanical power developed, hence

$$P_{em} = p\,\omega_m \left(\psi_d \cdot i_q - \psi_q \cdot i_d\right) \qquad (3.113)$$

Dividing the electromechanical power by the mechanical speed of the generator shaft (ω_m), the following expression is obtained for the instantaneous electromechanical torque developed by a synchronous generator with p pole-pairs

$$T_{em} = p\left(\psi_d \cdot i_q - \psi_q \cdot i_d\right) \qquad (3.114)$$

The value of T_{em} from the above expression is negative for motoring, and positive for generator operation.

Furthermore, it is assumed that the generated electrical power is equal to the generator power output minus the converter losses, the electric excitation losses (the so-called rotor copper losses) and the cable losses

$$P_{elec} = P_g - P_{conv} - P_{cu}^r - P_{cable} \qquad (3.115)$$

The converter losses include the switching losses in the power electronic interface and are, here, divided into no-load losses (which are constant) and losses which are proportional to the stator current squared

$$P_{conv} = C_1 + (1 - \eta_{conv} - C_1) \cdot P_{elec}^r \cdot \left(\frac{i_s}{i_s^r}\right)^2 \qquad (3.116)$$

where P_{elec}^r the rated electric power. The rotor copper losses are due to the excitation current flowing through the resistance of the field winding and are given by

$$P_{cu}^r = i_f^2 R_f \qquad (3.117)$$

with i_f and R_f the field winding current and resistance respectively. The power loss in the cables is given by

$$P_{cable} = (1 - \eta_{cable}^r) \cdot P_r^{elec} \cdot \left(\frac{i_s}{i_s^r}\right)^2 \qquad (3.118)$$

with η_{cable}^r the cable efficiency at rated electric power and i_s the stator current.

As noted in Section 3.5, in the development of the dynamic model of a synchronous generator we have ignored the losses in the magnetic material. There are two main sources of losses: hysteresis and eddy current losses. The hysteresis losses are due to the fact that all magnetic cores exhibit some degree of hysteresis in their B-H characteristic. Consequently, a time-varying flux in the core will dissipate power. Eddy current losses are due to the existence of circulating currents within the body of a ferromagnetic material under conditions of a time-varying flux. These currents cause an undesirable heating effect. The magnitude of these losses can be reduced by constructing the magnetic circuit from thin laminations of the ferromagnetic material rather than the solid. The details of the physical mechanisms that cause these losses are beyond the scope of this thesis, but can be found in the literature.

Taken together the hysteresis losses and eddy current losses are often described as the core, or iron losses. The iron losses are approximately proportional to the square of the voltage. However, in Polinder [219] it has been concluded that no simple and exact analytical expression for the iron losses can be derived. Thereto it is preferred to determine the core losses experimentally. To account for both friction and iron losses it is assumed that

$$P_{em} = P_{aero} - P_{fric} - P_{Fe}^s \qquad (3.119)$$

where P_{aero} the aerodynamic power, P_{fric} the total amount of friction in the drive train and P_{Fe}^s the stator iron losses. Summarizing, the power balance from aerodynamic power to generated electrical power is given by:

$$
\begin{aligned}
P_{elec} &\overset{(3.115)}{=} P_g - P_{conv} - P_{cu}^r - P_{cable} \\
&\overset{(3.112)}{=} (P_{em} - P_{cu}^s) - P_{conv} - P_{cu}^r - P_{cable} \quad \text{(steady-state)} \\
&= (P_{aero} - P_{fric} - P_{Fe}^s) - P_{cu}^s - P_{conv} - P_{cu}^r - P_{cable} \quad (3.120)
\end{aligned}
$$

This relationship is graphically depicted in Fig. 3.27.

This concludes the derivation of the equations describing a non-linear dynamic model of a salient-pole synchronous generator if saturation of the magnetic circuit is not considered. To account for saturation, it is necessary to replace the linear flux-current relationship, Eq. (3.74), by a non-linear one and subsequently repeating the
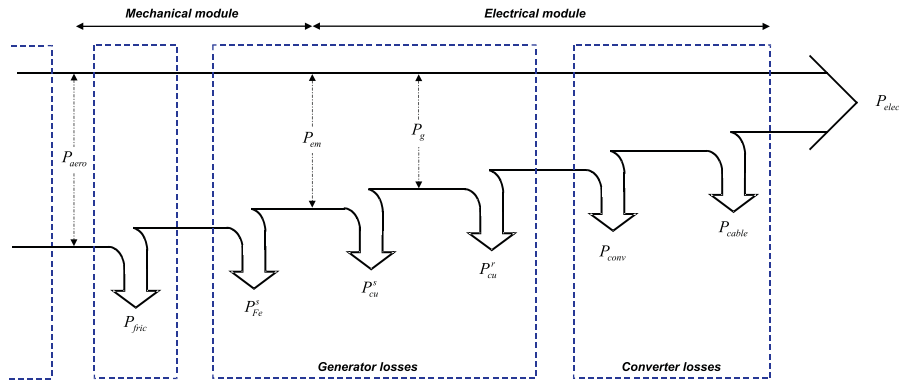
Figure 3.27: *Power balance from aerodynamic power to generated electrical power.*

analysis. For the Lagerwey LW-50/750 generator it is justified to neglect saturation since under normal operating conditions the generator doe not exhibit saturation [1]. In Chapter 6 a preliminary high bandwidth frequency converter controller will be designed on the basis of this model.

3.6   Summary

Within DAWIDUM it has been assumed that the general wind turbine model consists of one input module (*i.e.* wind) and four bilaterally coupled modules (*i.e.* aerodynamic, mechanical, electrical, and controller). In this section the main modeling features of the first four modules are summarized.

Wind module:

The undisturbed wind velocity is variable both in space and time. For system design analysis purposes the undisturbed wind velocity is decomposed in a deterministic, and a stochastic (*i.e.* turbulent) wind description. Deterministic wind inputs are very useful to study and verify the global wind turbine behavior, while stochastic wind inputs are to be used for the prediction of the loads which a wind turbine will experience during its life-time. It is assumed that neither the aerodynamics nor the structural dynamics are influencing the undisturbed wind part.

DAWIDUM's wind module allows the user to specify a uniform wind field (*i.e.* constant both in space and time) or a sequence of upward and downward changes in the wind velocity at hub height. It is also possible to specify a file that contains (measured) time-varying winds. Finally, the output of SWING-4 (a 3-D wind field simulation code) can also be used as input.

Aerodynamic module:

The blade aerodynamic forces are computed using the standard blade element momentum (BEM) theory coded as an M-File S-Function. In this S-Function, deterministic effects as wind shear, tower shadow and the ten-minute average wind speed at hub height are added to the zero-mean stochastic components of SWING-4 before the forces are computed. The values for both the axial and tangential induction factor are found by minimization of a quadratic objective function. DAWIDUM treats the aerodynamic loads as completely local and therefore with induction totally varying radially and azimuthally. The induced axial and tangential flow may be determined using one of the following five empirical models: Anderson, Garrad Hassan, Glauert, Johnson, and Wilson. Prandtl's tip-loss model is provided. The dimensionless aerodynamic coefficients C_l, C_d, and C_m are obtained from the Aërodynamische Tabel Generator (ATG) database.

Mechanical module:

Within DAWIDUM, the structural dynamics of flexible wind turbines are modeled as a collection of rigid and flexible bodies. This approach results in a limited order model of the real wind turbine. Such a model is well suited for the cost-effective design and operation of flexible, variable speed wind turbines. The rigid bodies include the spacers, hub, nacelle and both the stator and rotor of the generator, while the tower, and the rotor blades are modeled as flexible bodies. Flexible body dynamics are approximated using superelements.

The core of DAWIDUM's mechanical module is the combination of an automated physical data to model parameters conversion routine with SD/FAST®, a general-purpose multibody program capable of producing special-purpose simulation code. The equations of motion generated by SD/FAST® appear as a SIMULINK® MEX-file. SD/FAST® automatically accounts for all the non-linear inertial and geometric coupling and stiffening effects due to system motion and automatically takes care of internal reaction loads. SD/FAST® uses Kane's method to set up the equations of motion, which can be solved by numerical integration. This method greatly simplifies the equations of motion by directly using the generalized coordinates, and thus eliminating the need for separate constraint equations. The equations are easier to solve than those developed using methods of Newton or Lagrange and have fewer terms, hence reducing computer time.

Electrical module:

The electrical module contains a dynamic model of the electromagnetic part of an ideal synchronous generator. This model is obtained by rewriting Park's dq-axis model equations such that a model structure arises which can be translated in a simulation scheme. The rational transfer functions and parameters of the reformulated equations can be easily obtained from measured data. The order of the rational transfer functions is not fixed but is determined by the data, while the model parameters remain their physical meaningful interpretation. The resulting

model structure will be used for the design of a (robust) frequency converter controller that maximizes the electric energy yield whilst minimizing the fatigue loads of a wind turbine.

Part II:

Model validation issues

Chapter 4

Module verification and validation

In Chapter 3, a new wind turbine design code called DAWIDUM was described. For any practical application the models within DAWIDUM's module library cannot be used without both verification and experimental validation. The use of a model with invalidated model relations subsequent in controller design may lead to poor performance or even to premature field failures.

In literature, several model verification and validation techniques have been developed for determining whether a model is adequate for its intended use or not. The question is which method is most suited for (in)validating the developed dynamic wind turbine modules. This is the subject of this chapter.

The layout of this chapter is as follows. Section 4.1 presents the convention of model verification and validation adopted in this thesis. The validation of DAWIDUM is subdivided into three distinct parts: the mechanical module, the electrical module and the complete wind turbine. Both verification and validation of the first two parts are treated in this thesis. The validation of the complete wind turbine model has not been carried since a fully instrumented wind turbine has not become available. Section 4.2 treats the validation of mechanical module, while the electrical module is validated in Section 4.3. Finally, the conclusions are listed in Section 4.4.

4.1   Introduction

The economic cost of electricity generated by wind turbines can be reduced by decreasing the construction cost, while increasing the life-time and efficiency of the energy conversion. As explained in the introduction to this thesis, model based control can contribute to reach cost-effective wind turbines by improving the aerodynamic efficiency as well as by prolonging the life-time of the complete system.

The wind industry is showing a growing interest in increasingly lightweight and large (*i.e.* structurally flexible) wind turbines operating at variable speed [190]. This

development has been driven mainly by the trend to reduce cost and increase fatigue life. However, such turbines tend to be dynamically active, and are susceptible to resonances and instabilities. These problems need to be understood and solved before the full potential of such turbines can be realized. Therefore, accurate dynamic models are a basic need of modern wind turbine engineering. In order to develop such models, model verification and validation tools are required. This will lead, in combination with a systematic dynamic modeling method, to a wind turbine design tool enabling both optimal design and model based operation of wind turbines. In addition, it offers the possibility to solve dynamic problems in existing designs.

Because of this, model verification and validation is a topic of critical importance. Unfortunately, however, it is often a neglected aspect of the wind turbine design process. The process of checking the model quality too often appears to be regarded as an afterthought, rather than as a central part of the model development. It should be stressed that model verification and validation should be an integral part of the iterative process of the development of accurate mathematical wind turbine models within a simulation program in order to reach cost-effective wind turbines. Their importance should be reflected in the provision of specialised tools available for model verification and validation within the simulation environment.

4.1.1 Verification versus validation

We have used the words "verification" and "validation" associated with concepts of model accuracy and quality without stating the precise meaning. There is, however, no universal understanding about the meaning of these two words [195, 196]. To avoid questions about terminology, it is important to have precise and unambiguous definitions. Throughout this thesis, we will use the following definitions consistent with recommendations made in 1979 by the S.C.S. Technical Committee on Model Credibility [254]. It must be noted that in some application areas the definitions of verification and validation are, unfortunately, interchanged [196].

Definition 4.1 (Model verification) *The process of determining whether or not a computer simulation model is consistent with the underlying mathematical model to a specified accuracy level.*

Verification is often coupled to the adjective "internal" to stress that the main goal of verification is to check the implementation of the model equations in the time-domain simulation software (or wind turbine design code).

The first stage of verification is concerned with checking that the structure of the simulation program is consistent with the underlying mathematical model (*e.g.* by comparing the simulated steady-state values with those determined analytically from the mathematical model or visually inspect the correctness of the responses). The second stage of the verification is concerned with numerical accuracy. Simulation of mathematical models generally involves the integration of sets of ordinary differential equations. The performance in terms of accuracy and speed varies for different models and settings (including step size and tolerance). To select the most suited integration algorithm (*e.g.* Runge-Kutta fourth order (RK-45), Gear or Linsim),

the different algorithms can be compared at the same relative error per integration step. Furthermore, in the case of fixed step integration methods, comparisons can be made of results with a number of different integration step sizes.

Once the checks of the structure of the program has been completed satisfactory, and no algorithmic problems have been identified, the next step is to validate the verified model. Model validation is defined as:

Definition 4.2 (Model validation) *The process of determining whether or not the verified mathematical model of a system behaves similar to the real behavior associated with the intended model use.*

That is, validation is the process of proving that the verified model is an accurate approximation of the real system under investigation. Thereto, the model behavior has to be compared with real-life properties to check if the assumptions upon which it is based are satisfied. Validation is, as opposed to verification, closely linked to the adjective "external" to emphasize the connection with the real system under investigation. It is important to recognise that the validity of a model is closely linked to the intended use. That is, a model developed for one purpose may not be appropriate for another.

4.1.2 Model verification and validation approach

In the first place, there is no single best approach to the assesment of the validity of a mathematical model. Statements about model validity must always been made in the context of the intended application. In this thesis, the developed models are intended to be used for both model based control design and design optimization of flexible wind turbines. This means that there is thus interest in model accuracy in predicting the steady-state conditions as well as in model accuracy with which the transient behavior of the system is described. Both cover the complete operating area in the power generating mode (*see* Fig. E.1 on page 246 for an overview of the different wind turbine operating modes).

Model validation of wind turbine models, as it is usually performed in the wind energy community, is examined by direct comparison of time series, generated by the model, and data taken from an operating wind turbine. In general, this does not meet the high validation demands associated with the intended model use. The main two reasons are that the wind acts as a stochastic input and the fact that the interaction between the different modules makes it impossible to separate the measured responses. We have decided to subdivide the validation of the models within DAWIDUM's wind turbine module library in the following three parts:

- **Mechanical module**

- **Electrical module**

- **Complete wind turbine**

The main reasons are as follows: the mechanical as well as the electrical module can be validated independently from both the aerodynamic and controller module.

That is, under properly chosen experimental conditions, the bilateral couplings be-
tween these modules and the adjacent ones (*see* Fig. 3.14 on page 69) can be omitted.
The aerodynamic module, on the other hand, can only be validated using data from
an operating wind turbine. Observe that module verification can, for the greater
part, be carried out independently for each of the mentioned modules. The final
verification check is to compare steady-state characteristics as rotor power versus
undisturbed wind velocity (P-V_w curve), or thrust versus undisturbed wind velocity
(D_{ax}-V_w curve).

The first two verification and validation steps of the aforementioned approach
have been applied to the Lagerwey LW-50/750 wind turbine. We will start our
description with the verification and validation of the mechanical module.

4.2 Mechanical module verification and validation

In this section DAWIDUM's systematic structural modeling procedure will be vali-
dated to justify the use of this procedure and the resulting models for both model
based control design and design optimization purposes. Six cases are considered. In
the first case the procedure is verified using a test case before applying it to real
data. In the second till the fifth case measured non-rotating eigenfrequencies of wind
turbine rotor blades are compared with those from the superelement approximation.
Finally, in the sixth case, the procedure is validated by a full-scale experimental
modal test on the Lagerwey LW-50/750 wind turbine.

4.2.1 Case 1: Euler-Bernoulli beam (verification)

For verification of the proposed systematic structural modeling procedure, we will
present here the exact solutions to the frequency equation for transverse vibrations
of an Euler-Bernoulli beam for both the non-rotating and the rotating case [305].
That is, the Euler-Bernoulli beam will be analysed as an elastic body in which the
mass and deformation properties are continuously distributed. In general, it is very
difficult (if not impossible) to treat real mechanical structures as elastic continua
due to the complexity of their geometry. Elements that can, however, be handled
as continua include bars, shaft, cables, plates, and beams.

When analysing a body as an elastic continuum, it is considered to be composed
of an infinite number of particles. In order to specify the position of every point in
the body, an infinite number of displacement coordinates is required, resulting in an
infinite number of degrees of freedom. Because the mass is distributed, an elastic
body has an infinite number of vibration mode shapes, all with different frequencies.
In general, when an elastic body is deformed, all the eigenfrequencies will be excited
in various degrees depending on the shape of the particular deformation imposed.
The motion is then a superposition of the various mode shapes, each at different
amplitude.

Exact non-rotating eigenfrequencies

In Weaver *et al.* [305] it has been shown that the general solution for the transverse vibration of a uniform, non-rotating beam can be written as:

$$
\begin{aligned}
Y(x) \quad = \quad & C_1 \left(\cos(kx) + \cosh(kx) \right) + C_2 \left(\cos(kx) - \cosh(kx) \right) \\
+ \quad & C_3 \left(\sin(kx) + \sinh(kx) \right) + C_4 \left(\sin(kx) - \sinh(kx) \right)
\end{aligned}
\tag{4.1}
$$

where Y defines the shape of the natural mode of vibration. The constants C_1, C_2, C_3, and C_4 in this expression are determined by satisfying boundary conditions at the ends of the beam. In the derivation of Eq. (4.1) it is assumed that the material is homogeneous, isotropic, and that it follows Hooke's law. Furthermore, it is assumed that the displacements are sufficiently small that the response to dynamic excitations is always linearly elastic.

In our case the left end ($x = 0$) is built in as illustrated in Fig. 4.1, implying zero deflection and zero slope at the fixed end. That is, the boundary conditions are given by

$$
Y_{x=0} = 0 \qquad \text{and} \qquad \left(\frac{dY}{dx} \right)_{x=0} = 0
$$
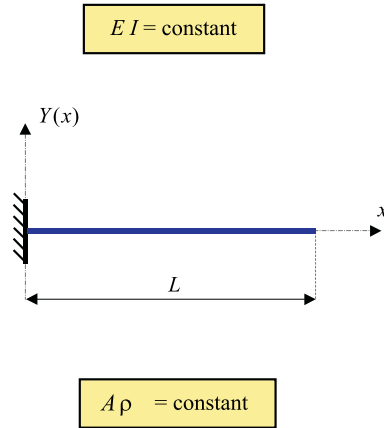
Figure 4.1: *Euler-Bernoulli beam (clamped-free situation).*

At the free right end ($x = L$), because the beam is uniform, both the bending moment and the shear force vanish, resulting in

$$
\left(\frac{d^2 Y}{dx^2} \right)_{x=L} = 0 \qquad \text{and} \qquad \left(\frac{d^3 Y}{dx^3} \right)_{x=L} = 0
$$

From the first two boundary conditions it follows that the constants C_1 and C_3 must be equal to zero, so that Eq. (4.1) reduces to

$$
Y(x) = C_2 \left(\cos(kx) - \cosh(kx) \right) + C_4 \left(\sin(kx) - \sinh(kx) \right)
\tag{4.2}
$$

From the remaining two boundary conditions we obtain

$$-\frac{C_2}{C_4} = \frac{\cosh(k_iL) + \cos(k_iL)}{\sinh(k_iL) - \sin(k_iL)} = \frac{\sinh(k_iL) + \sin(k_iL)}{\cosh(k_iL) + \cos(k_iL)} \qquad (4.3)$$

for each mode i. Rewriting Eq. (4.3) in matrix form gives

$$\begin{bmatrix} \sinh(k_iL) - \sin(k_iL) & \cosh(k_iL) + \cos(k_iL) \\ \cosh(k_iL) + \cos(k_iL) & \sinh(k_iL) + \sin(k_iL) \end{bmatrix} \cdot \begin{bmatrix} C_2 \\ C_4 \end{bmatrix} = \begin{bmatrix} 0 \\ 0 \end{bmatrix} \qquad (4.4)$$

The determinant of the matrix must be zero for a non-trivial solution to exists, that is,

$$(\sinh(k_iL) - \sin(k_iL)) \cdot (\sinh(k_iL) + \sin(k_iL)) + (\cosh(k_iL) + \cos(k_iL))^2 = 0$$

The above equation reduces to the frequency equation for transverse vibrations of an Euler-Bernoulli beam

$$\cos(k_iL)\cosh(k_iL) = -1 \qquad \text{for} \qquad i = 1, 2, 3, \cdots, \infty \qquad (4.5)$$

using

$$\cos^2(k_iL) + \sin^2(k_iL) = 1 \qquad \text{and} \qquad \cosh^2(k_iL) - \sinh^2(k_iL) = 1$$

Equation (4.5) must be solved numerically (using *e.g.* a mathematical manipulation package like MAPLE V [45]) and yields an infinity of solutions k_i. The first six non-zero positive roots of this equation are presented below in tabular, rather than graphical form so that the full ten-figure accuracy can be retained:

$$
\begin{aligned}
k_1 * L &= 1.875104069 \\
k_2 * L &= 4.694091133 \\
k_3 * L &= 7.854757438 \\
k_4 * L &= 10.99554073 \\
k_5 * L &= 14.13716839 \\
k_6 * L &= 17.27875953
\end{aligned}
$$

The eigenfrequencies in radians per second corresponding to these values of k_i are obtained as

$$\omega_i = k_i^2 \cdot \sqrt{\frac{EI}{\rho A}} \qquad (4.6)$$

where E the modulus of elasticity, I the area moment of inertia, ρ the mass density of the material, and A the cross-sectional area of the beam. Hence, the frequency of vibration of each mode is inversely proportional to square of the length, and proportional to the radius of gyration of the cross-section (*i.e.* $\sqrt{I/A}$). Thus for geometrically similar beams of the same material, the eigenfrequencies vary in direct proportion to the dimensions.

The form of the mode shapes is thus given by

$$
\begin{aligned}
Y_i(x) &= C_2 \left(\cos(k_i x) - \cosh(k_i x) \right) + C_4 \left(\sin(k_i x) - \sinh(k_i x) \right) \\
&= \left[\frac{C_2}{C_4} \cdot \left(\cos(k_i x) - \cosh(k_i x) \right) + \sin(k_i x) - \sinh(k_i x) \right] \cdot C_4 \quad (4.7)
\end{aligned}
$$

These modes can be shown to be orthogonal. Notice that although the ratio C_2/C_4 is uniquely given by Eq. (4.3), C_4 cannot be determined. This remaining coefficient becomes the arbitrary magnitude of the mode shape. The first three mode shapes for this beam are depicted in Fig. 4.2 Ⓐ - Ⓒ.
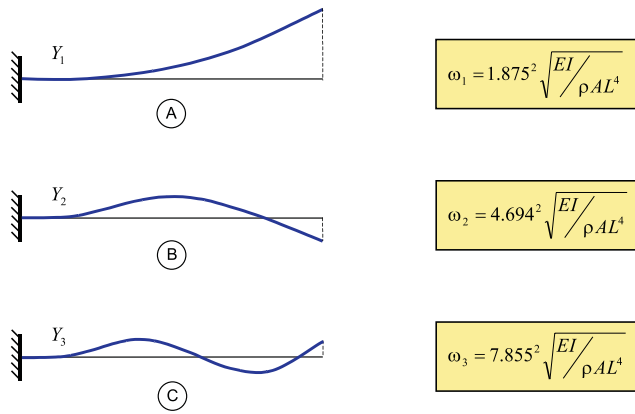
Figure 4.2: *Illustration of the first three mode shapes for the Euler-Bernoulli beam.*

The Euler-Bernoulli beam considered has length $L = 50$ m, modulus of elasticity $E = 21 \cdot 10^{10}$ N/m^2, area of beam cross-section $A = \pi$ m^2, mass density $\rho = 7850$ kg/m^3, and area moment of inertia $I = \frac{1}{4}\pi$ m^4. The first four exact frequencies are listed in Table 4.1, and will serve as reference solution.

Mode	Exact eigenfrequencies
1	3.637
2	22.79
3	63.82
4	125.1

Table 4.1: *The first four exact eigenfrequencies in radians per second of an Euler-Bernoulli beam with length $L = 50$ m, a constant flexural rigidity EI of $1.6493 \cdot 10^{11}$ Nm^2, a uniformly distributed mass density of 7850 kg/m^3, and a cross-sectional area of π m^2.*

Exact rotating eigenfrequencies

Now we will present exact solutions to the frequency equation for transverse vibrations of a rotating Euler-Bernoulli beam. The rotating beam is a particular case of the prestressed beam, of which the practical importance is considerable in the analysis of wind turbine rotor blades. It is a physical known fact that the eigenfrequencies of a rotating beam raise due to the component of the centrifugal acceleration field along the beam leading to an additional stiffening term. This effect is in the literature known as "centrifugal stiffening".

The non-dimensional frequency ratios for a variety of rotating beams can be found in Wright *et al.* [320]. We use the results for an Euler-Bernoulli beam which are repeated in Table 4.2. The exact values can be derived from the non-dimensional values listed in the table by applying the following transformation (*see* Van Woerkom [316]):

$$\omega_i = \frac{1}{p}\sqrt{(\omega_i^*)^2 - (\eta_i)^2} \qquad \text{for} \quad i = 1, 2, \cdots 5 \tag{4.8}$$

where

$$p = \sqrt{\frac{\rho A L^4}{EI}} \tag{4.9}$$

and ρ the mass density of the material, A the cross-sectional area, L the length, E the modulus of elasticity, I the area moment of inertia of the beam, and η the dimensionless rotation rate.

Frequency ratios of an Euler-Bernoulli beam					
η	ω_1^*	ω_2^*	ω_3^*	ω_4^*	ω_5^*
0.0	3.5160	22.0345	61.6972	120.9020	199.860
1.0	3.6817	22.1810	61.6418	121.0510	200.012
2.0	4.1373	22.6149	62.2732	121.4970	200.467
3.0	4.7973	23.3203	62.9850	122.2360	201.223
4.0	5.5850	24.2734	63.9668	123.2610	202.227
5.0	6.4495	25.4461	65.2050	124.5660	203.622
6.0	7.3604	26.8091	66.6840	126.1400	205.253
7.0	8.2996	28.3341	68.3860	127.9720	207.161
8.0	9.2568	29.9954	70.2930	130.0490	209.338
9.0	10.2257	31.7705	72.3867	132.3580	211.775
10.0	11.2023	33.6404	74.6493	134.8840	214.461
11.0	12.1843	35.5890	77.0638	137.6140	217.385
12.0	13.1702	37.6031	79.6145	140.5340	220.536

Table 4.2: *Non-dimensional frequency ratios of an Euler-Bernoulli beam as function of the dimensionless rotation rate η.*

Superelement approximation

In this case, the Euler-Bernoulli beam has been modeled using a number of superelements. Again, the beam is built in at the base. The torsional spring constants for each superelement are determined as follows:

$$c_{z1} = c_{z3} = \frac{2EI_z}{L_{se}} \qquad [\text{Nm}]$$

with E the modulus of elasticity, I_z the area moment of inertia, and L_{se} the length of the superelement which is, in turn, defined as

$$L_{se} = \frac{L}{N_{se}}$$

with L the length of the Euler-Bernoulli beam and N_{se} the number of superelements the beam is subdivided in.

The first four eigenfrequencies of the superelement approximation as function of the number of elements are listed in Table 4.3. The pattern is clear: dividing the beam into more superelements produces more eigenfrequencies (of which only the first four are shown), and improves the accuracy (compare columns with exact values listed in Table 4.1). The limiting case being an infinite number of superelements of which the eigenfrequencies equal to those of the exact solution.

Mode	Number of superelements N_{se}, with $k = \frac{1}{2}(1 - \frac{1}{\sqrt{3}})$								
	1	2	3	4	5	6	7	8	9
1	3.599	3.636	3.636	3.636	3.636	3.636	3.636	3.636	3.636
2	36.86	22.12	22.70	22.75	22.75	22.76	22.76	22.76	22.76
3	-	73.88	60.90	63.18	63.46	63.53	63.55	63.56	63.57
4	-	159.7	140.0	117.8	122.9	123.7	124.0	124.1	124.1

Table 4.3: *The first four eigenfrequencies in radians per second of the superelement approximation as function of the number of superelements.*

The exact analytical solution is used to evaluate the superelement approximation. In order to do so, the relative frequency errors are computed. This error is defined as:

$$\text{Relative error} = \frac{\text{Approximated eigenfrequency}}{\text{Exact eigenfrequency}} \cdot 100 - 100 \qquad [\%]$$

The relative errors for the first four eigenfrequencies of the superelement approximation are plotted in Fig. 4.3 as function of the number of superelements. Some eigenfrequencies are smaller, and some are larger than in reality, while the errors reach the indicated 1 % error bound rather fast.

It can be concluded that the superelement modeling method used to discritize the Euler-Bernoulli beam represents a consistent approximation to the exact model with an approximation accuracy that increases with an increasing number of superelements.
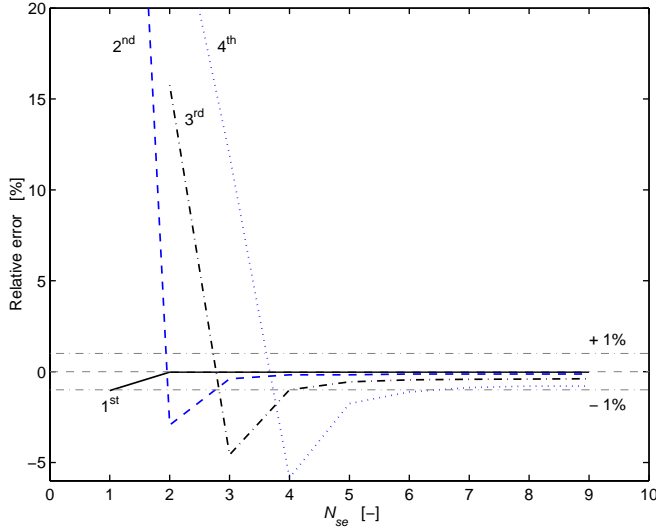
Figure 4.3: *The relative errors for the first four eigenfrequencies of the superelement approximation as function of the number of superelements N_{se} with $k = \frac{1}{2}(1 - \frac{1}{\sqrt{3}})$. Dashed-dotted lines: + 1 % and - 1 % error bound respectively.*

In addition, the mode shapes become also better defined with an increasing number of superelements, since information on more locations along the beam is available. Fig. 4.4 compares the first four analytical undamped mode shapes of an Euler-Bernoulli beam with those of the superelement approximation. The mode shapes are plotted from $x = 0$ to the full beam length of $L = 50$ m. The comparison shows that at least n superelements are required to accurately approximate the first n analytical mode shapes of an Euler-Bernoulli beam.

Recall that the form of the analytical mode shapes is given by Eq. (4.7). The mode shapes of the superelement approximation are computed by extracting the state-space matrices **A**: $n \times n$ state or system matrix, **B**: $n \times r$ input matrix, **C**: $p \times n$ output matrix, and **D**: $p \times r$ direct feedthrough matrix (with n number of states, r number of inputs, and p number of outputs) from the simulation model (*i.e.* Beam1sd, Beam2sd, Beam3sd and Beam4sd). For example, for Beam1sd $n = 4$, $r = 1$, and $p = 1$. Subsequently, the matrix eigenvalue problem is solved producing a diagonal matrix of generalized eigenvalues and a full matrix whose columns are the corresponding eigenvectors.

Each column of the eigenvector matrix contains the stacked vector of local joint position states (*i.e.* the angle of rotation of the 1 degree of freedom rotational joint expressed in the body-local frame of reference) and local joint velocity states. The modes are obtained by repeatedly picking an eigenvalue and selecting the associated vector of local position states out of the eigenvector matrix. Subsequently, the vector of local position states is converted to global displacements using the pin joint locations expressed in the Newtonian reference frame. Finally, the mode shapes are

scaled such that the displacement at the free end of the beam is identical to the displacement of the exact mode shape. Remember that a mode shape is just a measure of the motion of the beam and consequently can be scaled arbitrarily.
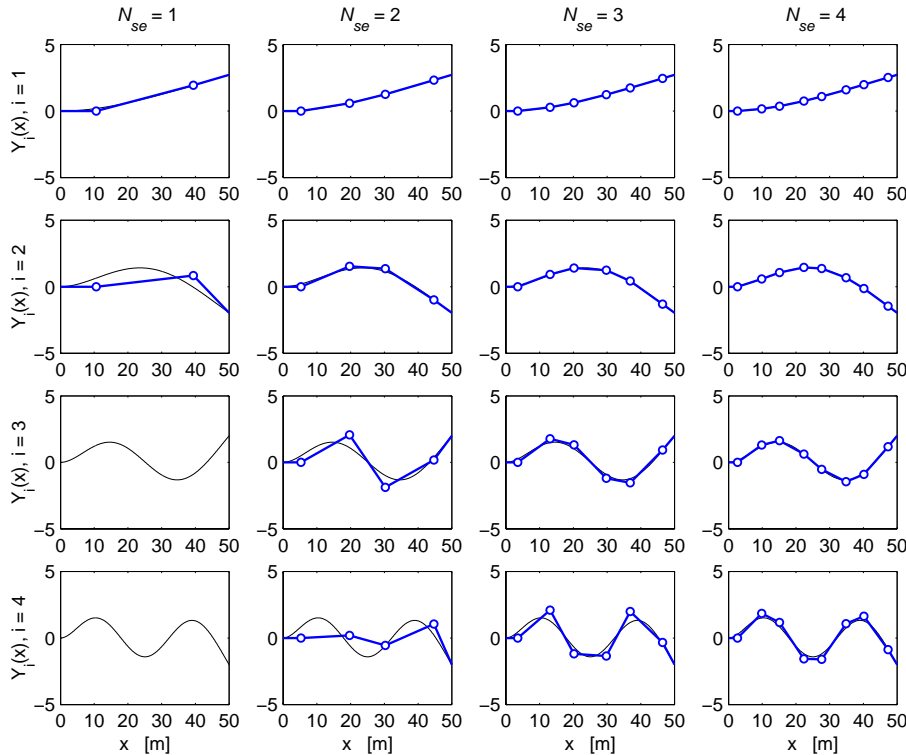

Figure 4.4: *Comparison of the first four mode shapes of an Euler-Bernoulli beam. Thin lines: analytical mode shapes (with $C_4 = 1$ for each mode), thick lines: superelement approximation for $N_{se} = 1$ to $N_{se} = 4$, with $\circ$: 1 degree of freedom rotational joints (i.e. pin joints).*

Finally, it is shown in Fig. 4.5 that the accuracy of approximating the centrifugal stiffening using the superelement approximation is near-perfect. In this figure the influence of centrifugal stiffening on the first four modes of an Euler-Bernoulli beam is plotted as function of the rotational speed. It is important to stress that the superelement modeling approach automatically acounts for centrifugal stiffening effects. After all, as the length of the rigid bodies within each superelement is constant, it follows that deformation of the blade automatically produces axial deformations and thereby automatically produces centrifugal stiffening.

It should be noted that the practical importance of centrifugal stiffening is considerable in the analysis of wind turbine rotor blades, since the eigenfrequencies of a spinning roter blade raise due to an additional stiffening term caused by the component of the centrifugal acceleration field along the blade.
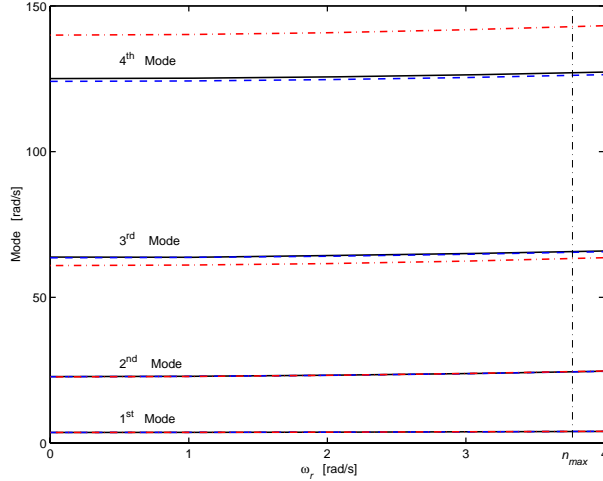
Figure 4.5: *The influence of centrifugal stiffening on the first four modes of an Euler-Bernoulli beam. Solid line: exact, dashed-dotted line: $N_{se} = 3$, dashed line: $N_{se} = 9$, and dashed-dotted vertical line: maximum rotor speed $n_{max} = 36$ [r.p.m] (see Table A.4 on page 226).*

4.2.2 Case 2: APX-45 rotor blade (validation)

In this subsection the measured non-rotating eigenfrequencies of an APX-45 wind turbine rotor blade are compared with those from the superelement approximation. The APX-45 rotor blades are designed by the Institute for Wind Energy of Delft University of Technology, The Netherlands [242], and manufactured by Aerpac Special Products B.V., Hengelo, The Netherlands [241]. The rotor blades are designed for both (full-span) pitch-controlled and (active) stall regulated 3-bladed wind turbines. The blade has a length of 21.75 m, and consists of two main parts: a 3.75 m long non-aerodynamic part where the cylindrical contour is transformed into an aerodynamic shaped root aerofoil, and an 18 m long aerodynamic part. The blade is mainly made of glass fibre reinforced epoxy (GRE). The interested reader is referred to Appendix A.2 for more detailed specifications.

We will use the blade definition file (*i.e.* FAROB[1] output file Table.flx), which is used to manufacture the blade, as a starting point. This file contains - among other things - the blade mass, and the flexural rigidity in the two principal bending directions at a number of locations beginning at the blade tip and ending with the blade root. Undefined locations are interpolated in a subsequent step after converting the file to a MATLAB MAT-file. The flexural rigidity in both flap and lead-lag direction as function of the local radius is shown in Fig 4.6. Both plots show a non-smooth increase in flexural rigidity from blade tip to blade root. The flexural rigidity in flap direction shows a local maximum at the radial position with the

---

[1]FAROB is the structural blade modeling module of the design code FOCUS.

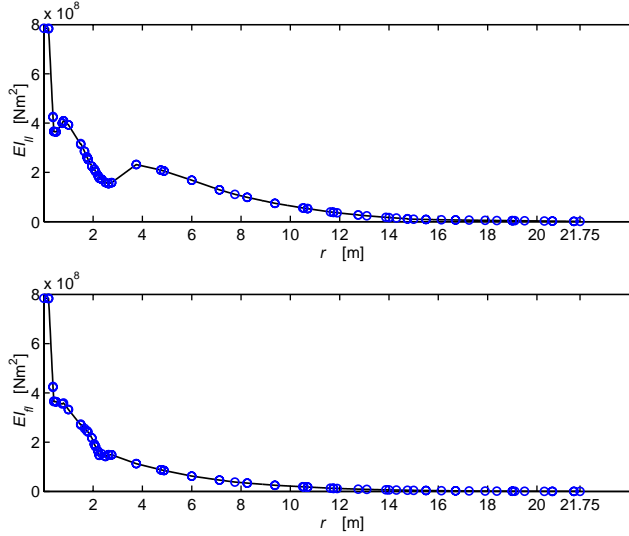maximum chord length (*see* Table A.1 on page 221) followed by a local minimum.

Figure 4.6: *Upper figure: flexural rigidity in lead-lag direction EI_{ll}, and lower figure: flexural rigidity in flap direction EI_{fl} of an APX-45 rotor blade as function of local radius r, with ∘: values defined in FAROB output file* Table.flx*, and solid line: linear interpolated values.*

The torsional spring constants for the superelement can be derived directly from the data in the MAT-file using the automated structural modeling procedure outlined in Section 3.4. Obviously, the resulting model accuracy depends strongly on the quality of the input data. Like the Euler-Bernouilli beam, the APX-45 rotor blade will be subdivided into an increasing number of superelements as illustrated in Fig. 4.7.

The non-rotating rotor blade eigenfrequencies obtained from the full-scale modal test performed by the Stevin Laboratory of Delft University of Technology [156] are used to evaluate the superelement approximation by comparing the relative frequency error

$$\text{Relative error} = \frac{\text{Superelement eigenfrequency}}{\text{Measured eigenfrequency}} \cdot 100 - 100 \qquad [\%]$$

The relative errors for the first two flap and lead-lag eigenfrequencies of the superelement approximation are plotted in Fig. 4.8. From this figure it is clear that the errors do not converge to zero with an increasing number of superelements. Numerical values are listed in the first column of Table 4.4. The reason for this bias might be one of the following:

- The model is used outside its range of validity and thereby violating the assumptions made in deriving the torsional spring constants;
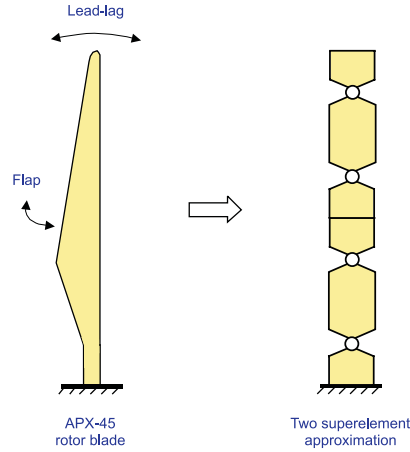
Figure 4.7: *Schematic of the APX-45 rotor blade and its two superelement approximation, with ○: 2 degrees of freedom rotational joints.*

- The blade structural properties in reality differ from their designed values due to uncertain material parameters and manufacturing tolerances. The APX-45 rotor blades are produced by moulding processes using composite materials of which the material properties are not known exactly. The upper and lower blade surfaces are manufactured separately in two moulds by hand-lay-up, and joined together using high strength adhesives. The result being that the blade mass and blade dimension are not precisely controllable;

- Quality of the applied experiments and determination of the eigenfrequencies from the measurements are not adequate. The natural frequencies of the APX-45 rotor blade have been determined from hand-excited displacement measurements in both lead-lag and flap direction. The displacements were measured at two locations using LVDT's (linear variable differential transducers);

- The flexibility of the test stand in which the blade has been mounted during the modal testing can not be neglected.

When the frequency errors for the first three flap and lead-lag eigenfrequencies of the superelement approximation are calculated relative to the eigenfrequencies as computed by FAROB, they converge to zero. It should be noted that the FAROB approximation also divides the blade in beam elements, but requires a significantly higher (> 100) number of elements. This illustrates (again) the power of the superelement approach.

Finally, the Finite Element program MARC [176] will be used to check whether the model assumptions are violated. The finite element mesh has been generated using the aforementioned blade definition file. The elements are eight noded, thick shell elements with 6 degrees of freedom at each node (MARC element type 22). The
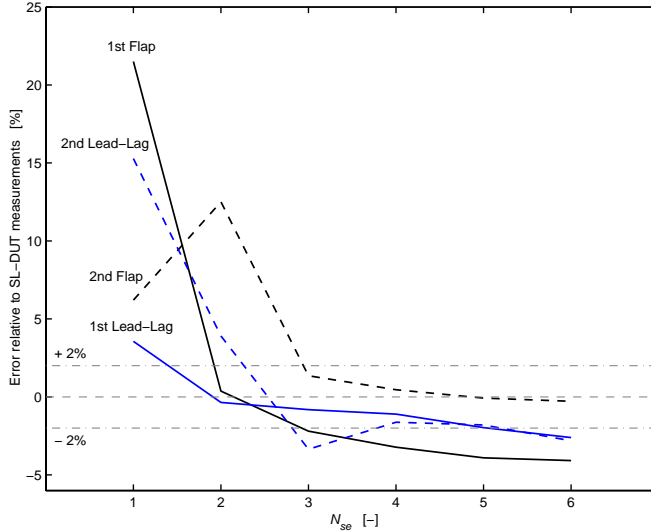
Figure 4.8: *The relative errors for the first two flap and lead-lag non-rotating eigen-frequencies of the APX-45 rotor blade as function of the number of superelements N_{se}. Dashed-dotted horizontal lines: + 2 % and - 2 % error bound respectively.*

elements have a composite layer structure. The layers of the composite are composed of orthotropic material. The total model contains 3137 elements, and 3055 nodes resulting in 18330 degrees of freedom. The first 15 eigenfrequencies were calculated using the Lanczos eigenvalue extraction algorithm. The resulting frequency errors of the first two flap and lead-lag eigenfrequencies of the APX-45 rotor blade are listed in the second column of Table 4.4.

APX-45 rotor blade		
Mode	Difference $N_{se} = 6$ w.r.t. SL-DUT measurements	Difference MARC w.r.t. SL-DUT measurements
1st flap	$-4.1\,\%$	$+1.0\,\%$
1st lead-lag	$-2.6\,\%$	$-9.1\,\%$
2nd flap	$-0.3\,\%$	$+3.0\,\%$
2nd lead-lag	$-2.8\,\%$	$-12.6\,\%$

Table 4.4: *Comparison of the first two flap and lead-lag non-rotating rotor blade eigenfrequencies calculated using the superelement approximation for $N_{se} = 6$ (left) and MARC (right) to the ones from a full-scale modal test performed by the Stevin Laboratory of Delft University of Technology (SL-DUT).*

It can be concluded that the effect of violating the model assumptions is probably negligible, but that the quality of the model is either limited by the quality of the input, or by the quality of the applied experiments and resulting eigenfrequency determination. In the next subsection we will further investigate the cause of the observed bias by examining an APX-70 rotor blade.

4.2.3   Case 3: APX-70 rotor blade (validation)

As discussed in the previous subsection, the relative frequency error is most likely to be associated with the fact that the blades are manufactured by hand-lay-up and quality of the applied experiments and resulting eigenfrequency determination. In order to check those assumptions, the measured non-rotating eigenfrequencies of an APX-70 wind turbine rotor blade are in this subsection compared with those from the superelement approximation. The APX-70 rotor blade is suited for pitch controlled turbines with a rated power of 1.5 MW and is designed, and manufactured by Aerpac Special Products B.V., Hengelo, The Netherlands [122].

The labour-intensive and inaccurate hand-lay-up manufacturing technique of the APX-45 blades has been replaced by a resin-infusion moulding (RIM) technique. With RIM the glass cloth is laid dry into the mould which is subsequently covered by plastic sheeting, sealed, and evacuated. The resin is then drawn in under the vacuum bag. Finally, the upper and lower blade surfaces are joined together using high strength adhesives.

The natural frequencies of the APX-70 rotor blade have been determined from hand-excited displacement measurements identical to those of the APX-45 blade [122], as well as by a more sophisticated modal analysis carried out by Netherlands Organization for Applied Scientific Research (TNO) [27]. In the latter case, both the input force (generated by instrumented hammer excitation) and the resulting responses are measured using a force transducer integrated in the hammer head and high-sensitivity accelerometers respectively. The blade was instrumented with 8 accelerometers in lead-lag direction and 16 accelerometers in flap direction (one positioned near the leading edge and one positioned near the trailing edge).

In the first column of Table 4.5 the eigenfrequencies determined from the hand-excited displacement measurements performed by the Stevin Laboratory (SL-DUT) are compared to the ones resulting from the modal analysis performed by TNO under contract of Delft University of Technology. It can be concluded based on the listed difference of maximum 1.8 % that the combination of hand-excitation with displacement measurements might be an explanation for the observed relative frequency error in the APX-45 case.

The errors for the first three flap and first two lead-lag eigenfrequencies of the APX-70 rotor blade are plotted relative to the TNO measurements as function of the number of superelements in Fig. 4.9. The bias of the first (-3.9%) and second mode (-1.8%) in flap direction are slightly larger than the ones observed in the APX-45 case. In lead-lag direction, however, the superelement approximation produces significantly higher values for the eigenfrequencies (the bias of the first mode is 11.0 %, while the bias of the second mode is 17.5 %).

APX-70 rotor blade		
Mode	Difference SL-DUT w.r.t. TNO measurements	Difference MARC w.r.t. TNO (SL-DUT) measurements
1st flap	$+1.8\%$	-0.2% (-2.0%)
1st lead-lag	$+1.8\%$	$+0.9\%$ (-0.9%)
2nd flap	-1.3%	$+1.4\%$ $(+2.7\%)$
2nd lead-lag	$+1.2\%$	$+6.6\%$ $(+5.3\%)$
3rd flap	$+0.0\%$	$+2.6\%$ $(+2.6\%)$

Table 4.5: *Comparison of eigenfrequencies determined from the displacement measurements performed by the Stevin Laboratory of Delft University of Technology (SL-DUT) to the ones resulting from the modal analysis performed by TNO (left) and comparison of the eigenfrequencies calculated by MARC relative to both the TNO and SL-DUT measurements (right) [122].*

Figure 4.9: *The relative errors for the first three flap and first two lead-lag eigenfrequencies of the APX-70 rotor blade as function of the number of superelements N_{se}. Dashed-dotted horizontal lines: + 2% and - 2% error bound respectively.*

Interestingly, the frequency errors of MARC with respect to either the TNO or the SL-DUT measurements do not show the increased bias in lead-lag direction. For the purpose of illustration, the numerical values are listed in the second column of Table 4.5 [313]. Clearly, this issue needs further research.

4.2.4 Case 4: RB-51 rotor blade (validation)

The Polymarin RB-51 rotor blade has been developed for wind turbines with a rated power of 750 kW. The blade has a length of 24.20 m. The natural frequencies of the RB-51 rotor blade have been determined from hand-excited displacement measurements carried out by the Stevin Laboratory (SL-DUT), as well as by a modal analysis carried out by TNO under contract of Delft University of Technology [123]. In the first column of Table 4.6 the resulting differences between the two methods are listed. It can be concluded that the second lead-lag mode has the largest difference and that the differences are larger than in the APX-70 case. The right column shows the comparison of the eigenfrequencies calculated by MARC relative to both the TNO and SL-DUT measurements.

RB-51 rotor blade		
Mode	Difference SL-DUT w.r.t. TNO measurements	Difference MARC w.r.t. TNO (SL-DUT) measurements
1st flap	$+ 2.4\,\%$	$- 0.2\,\%$ $\quad (- 2.5\,\%)$
1st lead-lag	$+ 1.1\,\%$	$- 7.7\,\%$ $\quad (- 8.7\,\%)$
2nd flap	$+ 2.8\,\%$	$+ 3.2\,\%$ $\quad (+ 0.5\,\%)$
2nd lead-lag	$+ 6.1\,\%$	$- 0.7\,\%$ $\quad (- 6.4\,\%)$

Table 4.6: *Comparison of eigenfrequencies determined from the displacement measurements performed by the Stevin Laboratory of Delft University of Technology (SL-DUT) to the ones resulting from the modal analysis performed by TNO (left) and comparison of the eigenfrequencies calculated by MARC relative to both the TNO and SL-DUT measurements (right) [123].*
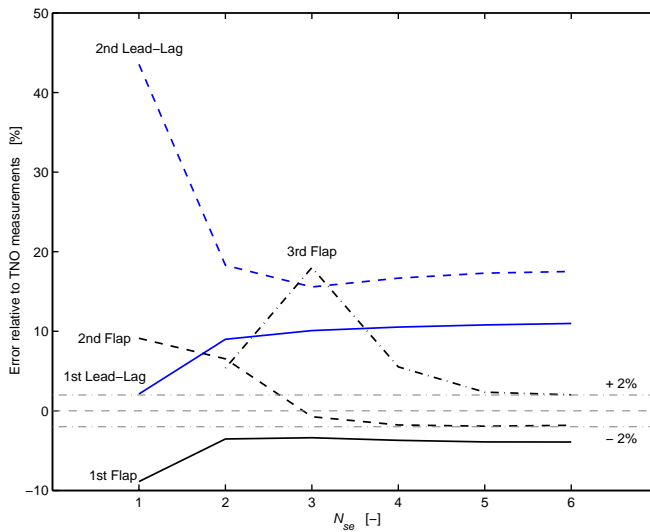
The errors for the first two flap and first two lead-lag eigenfrequencies of the RB-51 rotor blade are plotted relative to the TNO measurements as function of the number of superelements in Fig. 4.10. The most striking characteristic of this plot is that the final bias is already reached with only three superelements. For $N_{se} = 6$, the biases of the first mode in flap and lead-lag direction are $1.1\,\%$ and $-1.3\,\%$ respectively, while the biases of the second modes in flap and lead-lag direction are $8.1\,\%$ and $8.0\,\%$ respectively.

4.2.5 Case 5: RB-70 rotor blade (validation)

The RB-70 rotor blade has been developed by Polymarin for wind turbines measuring 70 m in diameter with a rated power of 1.5 MW. The tested blade, however, has a length of 28.75 m since a part of the tip has been removed [28]. The natural frequencies of this rotor blade have been determined from hand-excited displacement measurements carried out by the Stevin Laboratory (SL-DUT), as well as by a modal
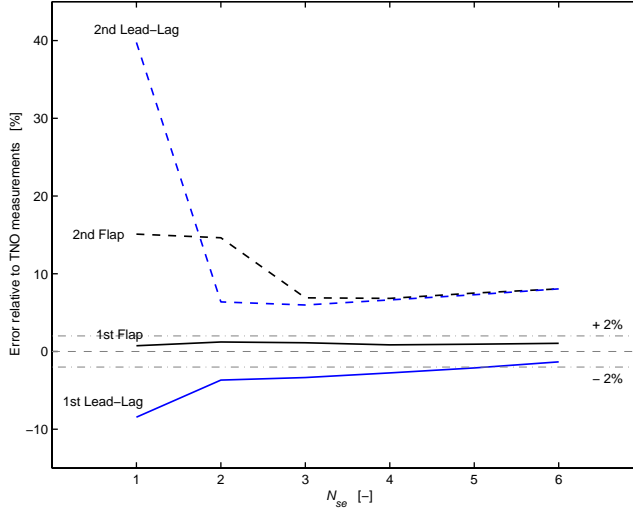
Figure 4.10: *The relative errors for the first three flap and first two lead-lag eigenfrequencies of the RB-51 rotor blade as function of the number of superelements N_{se}. Dashed-dotted horizontal lines: + 2% and - 2% error bound respectively.*

analysis carried out by TNO under contract of Delft University of Technology [124]. In the first column of Table 4.6 the resulting differences between the two methods are listed. It can be concluded that the differences are small. The right column shows the comparison of the eigenfrequencies calculated by MARC relative to both the TNO and SL-DUT measurements. The prediction in flap direction is worse than the prediction in lead-lag direction.

RB-70 rotor blade		
Mode	Difference SL-DUT w.r.t. TNO measurements	Difference MARC w.r.t. TNO (SL-DUT) measurements
1st flap	$-1.4\,\%$	$+6.2\,\%$ $(+7.7\,\%)$
1st lead-lag	$+1.2\,\%$	$-4.3\,\%$ $(-5.5\,\%)$
2nd flap	$+0.2\,\%$	$+12.5\,\%$ $(+12.3\,\%)$
2nd lead-lag	$+0.6\,\%$	$-1.5\,\%$ $(-2.1\,\%)$

Table 4.7: *Comparison of eigenfrequencies determined from the displacement measurements performed by the Stevin Laboratory of Delft University of Technology (SL-DUT) to the ones resulting from the modal analysis performed by TNO (left) and comparison of the eigenfrequencies calculated by MARC relative to both the TNO and SL-DUT measurements (right) [124].*

The errors for the first three flap and first two lead-lag eigenfrequencies of the RB-70 rotor blade are plotted relative to the TNO measurements as function of the number of superelements in Fig. 4.11. The first flap mode is predicted very accurately. For $N_{se} = 6$, the bias of the first, second and third mode in flap and lead-lag direction are $-0.1\,\%$, $6.2\,\%$ and $7.8\,\%$ respectively, while the bias of the first and second mode in lead-lag direction are $9.3\,\%$ and $12.3\,\%$ respectively.
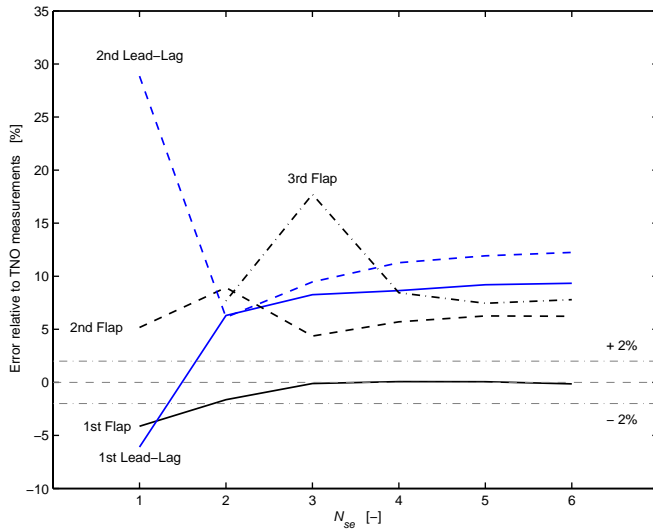

Figure 4.11: *The relative errors for the first three flap and first two lead-lag eigenfrequencies of the RB-70 rotor blade as function of the number of superelements N_{se}. Dashed-dotted horizontal lines: + 2% and - 2% error bound respectively.*

4.2.6   Discussion

In the previous subsections four different rotor blades have been examined in order to justify the use of the proposed systematic structural modeling procedure and the resulting models for both model based control design and design optimization purposes. Measured non-rotating eigenfrequencies obtained via either hand-excited displacement measurements or a modal analysis are compared with those from both a finite element and the superelement approximation. The following observations can be made:

- The effect of violating the modeling assumptions is negligible since the detailed finite element models do produce biases of the same order;

- The superelement models are very useful to approximate the first bending modes with only a few superelements. In general, it can be stated that the number of superelements required is equal to the number of modes the model needs to describe accurately plus one;

- The difference between the hand-lay-up (APX-45) and resin-infusion moulding (RIM) manufacturing technique (APX-70) could not be detected since the supplied mass distribution was already modified to diminish the difference between the measured and simulated mass and center of gravity location;

- The model accuracy is strongly limited by the quality of the supplied input data.

To stress the importance of the latter observation, we have used measured displacement information of static tests applied to both the APX-70 and the RB-70 rotor blade to modify the torsional spring constants accordingly. The displacement is measured using a LVDT located at a radial position of $r = 26.75$ m (APX-70) and $r = 26.2$ m (RB-70). The torsional springs of the APX-70 blade in flap direction are increased with 8.6% and in lead-lag direction reduced with 24.4%, while the the torsional springs of the RB-70 blade are reduced in flap direction with 0.6% and in lead-lag direction reduced with 18.5%. The results are plotted in Fig. 4.12 for $N_{se} = 1, \cdots, 6$, while for $N_{se} = 6$ the numerical values are listed in Table 4.8. The upper figure shows the relative frequency errors of the APX-70 blade, while the lower figure shows the errors of the RB-70 blade.
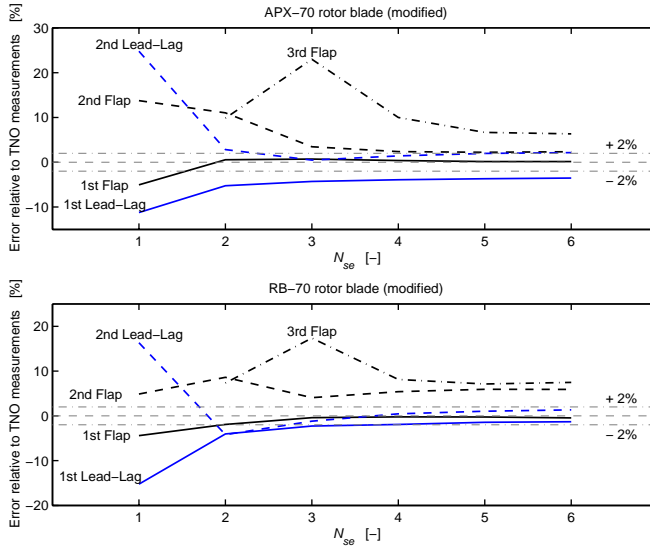
Figure 4.12: *The relative errors for the first three flap and first two lead-lag eigen-frequencies of the APX-70 rotor blade (upper plot) and RB-70 rotor blade (lower plot) as function of the number of superelements N_{se}. Displacement information of static tests has been used to modify the torsional spring constants accordingly. Dashed-dotted horizontal lines: + 2% and - 2% error bound respectively.*

It can be concluded by comparing the modified and original frequency error values for $N_{se} = 6$ listed in Table 4.8 that adding measured displacement information (even

at only one location) significantly reduces the absolute frequency error value. The mean value of the absolute frequency error is reduced from 7.2% to 2.9% in the APX-70 case, while for the RB-70 blade this value is reduced from 7.1% to 3.3%. It is expected that an even higher accuracy can be obtained if displacement (or acceleration) information is available at more radial positions. After all, this offers the possibility to tune the torsional spring constants individually using the procedure treated in Chapter 5.

Modified APX-70 and RB-70 rotor blade		
Mode	Difference $N_{se} = 6$ w.r.t. TNO measurements	Difference $N_{se} = 6$ w.r.t. TNO measurements
1st flap	$+0.1\%$ (-3.9%)	-0.4% (-0.1%)
1st lead-lag	-3.5% $(+11.0\%)$	-1.3% $(+9.3\%)$
2nd flap	$+2.3\%$ (-1.8%)	$+5.9\%$ $(+6.2\%)$
2nd lead-lag	$+2.2\%$ $(+17.5\%)$	$+1.3\%$ $(+12.3\%)$
3rd flap	$+6.3\%$ $(+2.0\%)$	$+7.5\%$ $(+7.8\%)$

Table 4.8: *Comparison of APX-70 and RB-70 rotor blade non-rotating eigenfrequencies calculated using the superelement approximation with modified (original) torsional spring constants for $N_{se} = 6$ to the ones resulting from the modal analysis performed by TNO.*

In the previous six cases the validity of the proposed systematic structural modeling procedure has been examined. We felt that it was important first to verify the proposed systematic structural modeling procedure using a test case, and subsequently to validate the approach using individual modal tests carried out on a number of rotor blades before applying it to a complete flexible wind turbine.

The test case shows that the superelement modeling method represents a consistent approximation to the Euler-Bernouilli beam with an approximation accuracy that increases with an increasing number of superelements. Furthermore, we found a good agreement between the measured non-rotating eigenfrequencies of various wind turbine rotor blades and those calculated using the superelement approximation. This means that the mass and stiffness properties of the rotor blade models are appropriate.

The aforementioned results demonstrate that it is, in principle, possible to derive limited order multibody models suited for time-domain simulation, analysis of dynamic loads, and model based control design directly from physical rotor blade design data using the proposed systematic structural modeling procedure. Depending on the intended model use, tuning of torsional spring constants using either static test data or experimental modal test data is required to reach the desired accuracy. We will now continue the validation using data acquired from a full-scale modal test applied to the Lagerwey LW-50/750 wind turbine.

4.2.7   Case 6: Lagerwey LW-50/750 wind turbine

The Lagerwey LW-50/750 wind turbine is located near Nieuwe-Tonge, Province of Zuid-Holland, The Netherlands. Fig. 4.13 shows a schematic of the measurement set-up of the full-scale modal test. The turbine was parked (*i.e.* non-rotating) during all testing. This implies that the bilateral coupling of the mechanical module to the electrical module, *see* Fig. 3.14 on page 69, can be omitted since the mechanical speed ω_m is equal to zero. Furthermore, the input from the aerodynamic module, F_{aero}, is replaced by a static load applied to the tower top (hereby assuming that the structural response caused by wind excitation on the rotor blades, nacelle and tower is negligible).
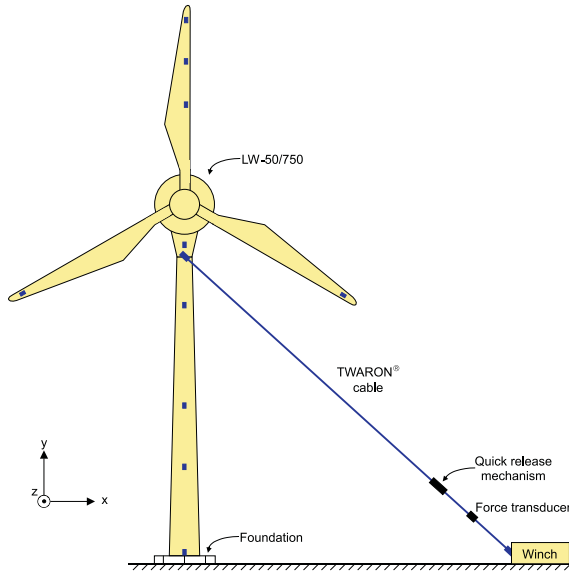

Figure 4.13: *Schematic of the measurement set-up of the full-scale modal test performed on the Lagerwey LW-50/750 wind turbine. Sensor locations are marked with a ▪. The rotor was yawed −90 degrees about the y-axis during the experiments.*

The mechanical structure is excited by applying the aforementioned static load to the tower top of the Lagerwey LW-50/750 wind turbine, and suddenly releasing this load via a quick release mechanism. The structure was instrumented with one force transducer in-line with the cable to measure the applied load, and 19 accelerometers on both the tower and the three rotor blades to measure the resulting response. The accelerometer mounting locations are marked with a ▪ in Fig. 4.13. Observe that the mounting and removing of the accelerometers from the rotor blades require a crane due to the size of the wind turbine ($D = 50.5$ m and $H = 46.165$ m).

The goal of this test is to validate the DAWIDUM model(s) of this wind turbine by comparing measured and simulated natural frequencies as well as time-domain simulations to measured responses. When the correlation with the modal test data

is not satisfactory, the time domain data can be used to update (some of) the model parameters following the approach that will be presented in Chapter 5. In the next paragraphs the applied excitation technique, the performed pre-test analysis as well as the results will be discussed in detail.

Excitation using step-relaxation

In principle two main ways to excite a structure, *viz.* ambient excitation and externally forced excitation:

- **Ambient excitation**. Ambient excitation implies that the structure is tested *in situ*, using the operational vibrations as the excitation source. Examples are traffic in the case of bridges or wind in the case of wind turbines. Ambient excitation is frequently used to excite large structures where externally forced excitation becomes difficult, inconvenient and/or expensive. For example, wind excitation has been applied to extract the modal parameters of the 110-m-tall EOLE vertical-axis wind turbine [40] and has been used to validate an ADAMS/WT model of the Cannon Wind Eagle 300 downwind horizontal-axis wind turbine [134, 319];

- **Externally forced excitation**. In this case both the input force and the resulting responses are measured. The input forces may be generated in several ways (*i.e.* electromagnetic or hydraulic shaker, instrumented hammer, human excitation or step relaxation).

The preferred exciter is often the electromagnetic shaker which has the ability, when properly sized, to provide a flexible way of specifying sufficiently exciting inputs. Conversely, for parked wind turbine testing, human excitation, step relaxation, and wind excitation are the most useful [152]. Human excitation, however, is limited to moderately sized wind turbines, because small turbines have natural frequencies too high to be excited manually, while larger turbines may be too massive to excite. Step relaxation as well as wind excitation have been reported to work extremely well on vertical-axis wind turbines [40, 151, 152]. Of the two excitation techniques, step relaxation is the most time-consuming. However, the frequency content of the step function makes it ideal for testing large, flexible structures since a large amount of strain energy can be input to the structure. In addition, it has been observed that structural damping is difficult to estimate accurately from the measurements using wind excitation.

We have decided to use the step-relaxation method to excite the parked Lagerwey LW-50/750 wind turbine because its ability to estimate the damping and the fact that it is mechanically straightforward to implement. This method of structural excitation involves applying a static load to the structure by a cable anchored to the ground or to a deadweight, and then suddenly releasing this load via a quick release mechanism. The static load was transmitted by a 225 meter long TWARON® cable. TWARON is a lightweight, superstrong synthetic fibre made from the aramid polymer. It is preferred to steel because it is five times lighter at the same strength (the cable has a tensile strength of 170 kN and a total mass of 82.5 kg). The interested

reader is referred to Appendix F.1 for a more detailed technical specification of the cable. Consequently, the mass loading is minimized. The only disadvantage is the lower modulus of elasticity, which is about half that of steel [47]. The cable has been secured to the tower at 40.5 m above the ground level using a cargo strap. A cargo strap was preferred to a fixture because mass loading is negligible and no special fixturing is required.

We have used a 20-ton truck as deadweight and used its hydraulic powered winch for loading the cable to the specified 40 kN. The tension in the cable is released by a firm pull on a nylon cord that activates the lever switch of the quick release mechanism. The cable is restrained at both ends by a chain preventing secondary hits or random banging after being released.

The left photograph in Figure 4.14 shows the initial position of the TWARON® cable, quick release mechanism, nylon cord, chain, force transducer, and the winch cable. The middle and right photograph show two successive frames of an actual release recorded with a Mini DV camera.

Figure 4.14: *Step-relaxation hardware and recorded release. Left photograph: position of the TWARON cable, quick release mechanism, nylon cord, chain, force transducer, and winch cable at $T = 0.0$ s, middle photograph: position at $T = 0.08$ s, and right photograph: position at $T = 0.16$ s.*

Pre-test analysis

Pre-test analysis was performed on two DAWIDUM models, notably SDLW1: an 18-DOF model, and SDLW2: a 34-DOF model. Both models describe the structural dynamics of the complete Lagerwey LW-50/750 wind turbine (*see* Appendix I.2.3 for more details). The analysis results have been used to determine the frequency range of interest, the required input force magnitude, the driving point on the tower, and the accelerometer locations:

- **Frequency range of interest**. From a dynamic analysis performed on the aforementioned DAWIDUM models it can be concluded that the dynamic response of the Lagerwey LW-50/750 wind turbine is dominated by the first few bending modes. These modes are in the frequency range of 0.5 to 40 Hz. Because of this low frequency range combined with light damping, each time record requires a duration of at least one minute. We selected a cutoff frequency of 160 Hz for the antialiasing filters and a sample frequency of 500

Hz for the measured signals. This choice is based on the above mentioned frequency range of interest, the requirement to be able to accurately estimate structural damping, and the fact that the number of data points of the used data acquisition system (SCADAS II of Leuven Measurement Systems), is limited to 32768 points. The interested reader is referred to Appendix F.2 where detailed specifications of the SCADAS II can be found;

- **Input force**. Obviously, the applied input force must cause no damage to the Lagerwey LW-50/750 wind turbine. Conversely, the input force should be sufficiently exciting to ensure that the responses contain sufficient information in the frequency range of interest. On the basis of simulations performed on the SDLW1 model it turned out that a 40 kN force should be adequate.

  A force transducer was placed in-line with the cable between the quick release mechanism and the winch truck to measure the input force. Although it is important for the force transducer to be close to the turbine so that it senses the force actually being applied to the structure [151], we have decided to place the force transducer close to the winch truck to avoid collision of the transducer with the tower;

- **Accelerometer locations**. Uniaxial accelerometers were used to measure the response at a number of locations on the tower as well as rotor blades. The accelerometers were placed on the blades so that they measured either purely lead-lag or flap deformations. The accelerometer mounting locations were selected on the basis of simulations performed on the SDLW1 module in order to avoid that an accelerometer is placed at a node for a frequency of interest. During instrumentation, however, it turned out that the crane was not able to reach the required working height of 75 meter. Consequently, we were forced to slightly adapt both the instrumentation procedure and the accelerometer mounting locations. In Appendix F.4 the final mounting locations as well as the technical specifications of the accelerometers are listed.

  It can be concluded that the mass of the accelerometers (28 grams (rotor blade) and 46 grams (tower) respectively) is negligible compared to the blade and tower mass. Prior to mounting the accelerometers, both the tower and rotor blade surface were cleaned. The accelerometers mounted on the blades are bond in place with hot glue for easy attachment and removal. The tower accelerometers are mounted using double-back tape. Response measurements were made normal to the blade and tower.

  Because this turbine has low natural frequencies, the acceleration response will be low. Also the transducer cables were quite long (ranging from 10 to 85 meter), making noise a special consideration. To address this problem, very high ly sensitive accelerometers with low-noise cables were used. All signals were low-pass filtered using analogue filters to avoid aliasing.

134

Experiments

Prior to the experiments, the results from the pre-test analysis are checked by performing an initial test which has not been recorded. This test has also been used to obtain adequate accelerometer response levels to minimize the quantisation errors as well as to determine an appropriate total experiment time / sample frequency combination. The input force was applied under an angle α of 10.1 degrees with the horizontal (*see* Figure 4.14). That is, the component of the force in positive x-direction is equal to $F_x = F_{cable} \cdot \cos \alpha$, and the component of the force in negative y-direction is equal to $F_y = F_{cable} \cdot \sin \alpha$.

The main specifications of the recorded experiments are listed in Table 4.9. All measurements have been preceded by a pre-trigger time of at least 0.240 s (the pre-trigger time varies with the quickness of response of the quick release mechanism operator). It should be stressed that all testing was done in very low winds (less than 3 m/s at the tower top).

Pitch angle position	Sample frequency	Duration	Pre-trigger time	No. samples	Filename
Work	1000 Hz	32.768 s	0.240 s	32768	M1
Work	500 Hz	65.536 s	0.488 s	32768	M2 & M3
Vane	500 Hz	65.536 s	> 0.28 s	32768	M4-M10

Table 4.9: *Modal analysis measurement overview: main specifications of the recorded experiments.*

The signals of the first measurement (*i.e.* M1) are sampled with a sample frequency of 1000 Hz, while the signals of measurements M2-M10 are sampled with a sample frequency of 500 Hz. The cutoff frequency of the ETD (equal time delay) anti-aliasing filter was set to 330 and 160 Hz respectively. From the Bode diagram of this filter (*see* Fig. F.3 on page 249) it can be concluded that the measured responses are undistorted up to and including $0.15 \cdot f_{co}$. This implies that if useful information is contained in frequencies above 24 Hz (measurement M1) or 49.5 Hz (measurements M2-M10) it might be distorted and should be handled with care. However, since the anti-aliasing filter is known, it can be included as a known part of the model and let the simulated acceleration responses pass through this filter before being compared to the measured responses.

It should be mentioned that we had planned more experiments than listed in Table 4.9 (including an experiment with a 180° yawed rotor position, and one where the pitch angles of all three rotor blades are set to 45°). However, the adapted instrumentation procedure took up a lot more time than planned and we were forced to limit ourselves to the most important experiments. The planned and the actual duration of the instrumentation, measurements and removal are compared in Table 4.10. The parked modal test of the Lagerwey LW-50/750 wind turbine required the effort of at least 8 people in one day.

Task	Planned duration	Actual duration
Instrumentation	5 hours	9 hours
Measurements	6 hours	4 hours
Removal	2 hours	3 hours

Table 4.10: *Time schedule full-scale modal test performed on the Lagerwey LW-50/750 wind turbine.*

Time series analysis

Figure 4.15 shows a typical tower top acceleration response in x-direction (*i.e.* sensor A-05) from a parked modal test. Obviously, the stepwise change in the force applied to the tower top excites a wide range of natural frequencies. The relative high frequencies at the beginning of the response are damped out quickly, leaving eventually the single frequency associated with the lowest system mode of vibration. This mode is in literature often denoted with the misleading term "first tower bending mode". The main reason for the domination of the response by the lowest system mode of vibration is that the total mass of the generator, chassis and rotor is relatively large with respect to the tower mass.
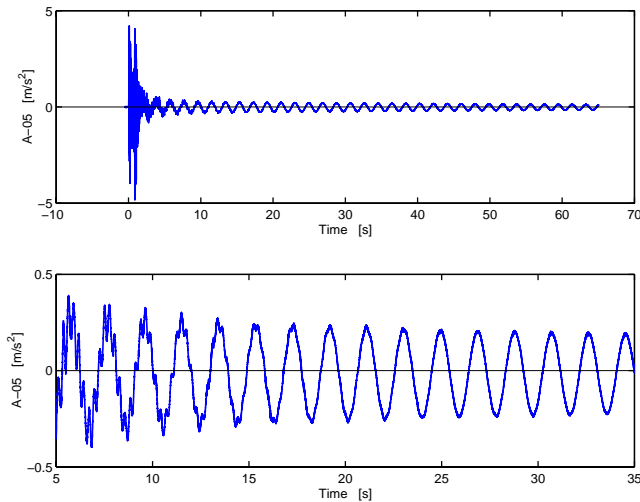

Figure 4.15: *Measured tower top acceleration (sensor A-05) from measurement M2. Upper figure: complete signal, and lower figure: zoom from 5 to 35 seconds.*

The response in Figure 4.15 also shows that the record length is not long enough to capture the complete response history. When the truncated time-domain response is transformed into the frequency domain using the Fast Fourier Transform (FFT)

136

this may result in so-called leakage errors. In this case the distortion due to leakage is negligible because the truncated response contains only one mode and this mode is truly periodic in time.

The corresponding periodogram estimate of the power spectral density (PSD) is depicted in Fig. 4.16. It shows how the average power of the tower top acceleration response in x-direction is distributed with frequency. The PSD estimate is computed via the Thomson multitaper method, and has a frequency resolution of $500/32768 = 0.0153$ Hz. Prior to the computation of the PSD, the acceleration record was pre-processed by filtering the data without phase distortion with an eighth order lowpass digital Butterworth filter with a cutoff frequency of 125 Hz, and subsequently removing the linear trend. It is clear that noise is not the primary problem since the individual peaks indicating the modes are clearly discernible in the plot.

Integrating the total area under the curve reveals that 99 % of the average power is located below 102.7 Hz (73.6 % of the average power is contained in the first system mode of vibration, 5.2 % in the fourth system mode, and 0.7 % in the fifth system mode). This average power distribution confirms the domination of the first system mode of vibration in the time-domain response.
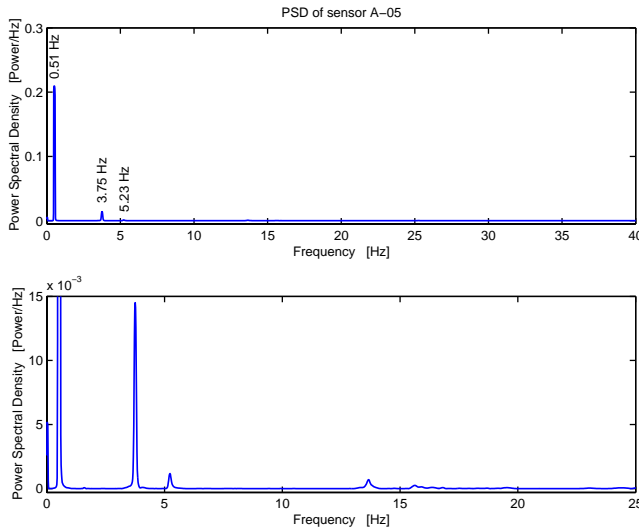

Figure 4.16: *Periodogram estimate of the power spectral density (PSD) of the tower top acceleration (sensor A-05) from measurement M2. Upper figure: signal in the frequency range of 0 to 40 Hz, and lower figure: zoomed in on the second bending mode and higher.*

The periodogram estimate of the PSD of both sensor A-03 and A-16, depicted in upper and lower part of Fig. 4.17 respectively, show a completely different picture. The top figure reveals that both the first and the fourth system mode in x-direction

(second and third mode are not present in this response) dominate the response of sensor A-03 (located about halfway between the tower bottom and top, *see* Table F.1 on page 251). Integrating the total area under the curve reveals that 22.6 % of the average power is contained in the first system mode, 29.7 % in the fourth system mode, and 12.3 % in the fifth system mode. The bottom figure reveals that the response of sensor A-16 is dominated by the fourth system mode of vibration in x-direction (the third system mode is not present in this response). Integrating the total area under the curve reveals that 4.3 % of the average power is contained in the first system mode, 7.6 % in the second system mode, 0.5 % in the third system mode, 66.1 % in the fourth system mode, and 27.8 % in the fifth system mode.
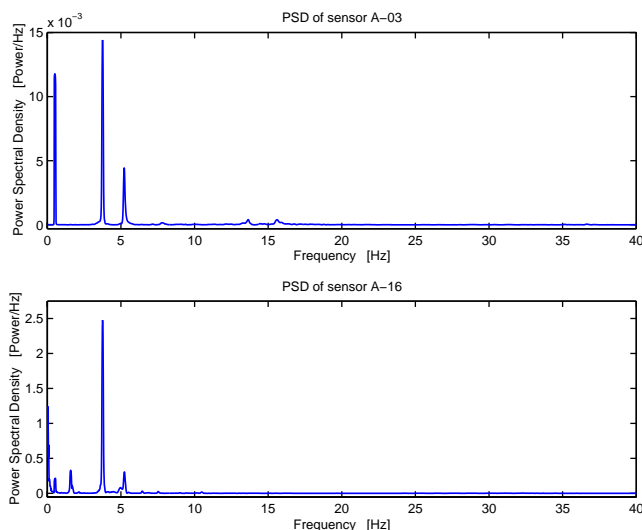

Figure 4.17: *Periodogram estimate of the power spectral density (PSD) of sensor A-03 (upper figure) and A-16 (lower figure) from measurement M2.*

Fig. 4.18 shows the periodogram estimates of the PSD of the responses in x-direction as a function of the sensor position with respect to the ground level. This three-dimensional plot reveals how the average power distribution changes with the sensor location. It shows that the modes of the Lagerwey LW-50/750 wind turbine in x-direction are not closely spaced, and not heavily damped. This implies that the modes are lightly coupled. Consequently, the turbine behaves at resonance predominantly as a single-degree-of-freedom (SDOF) system: the structural response at a natural frequency is (almost) completely determined by that mode.

Fig. 4.19 shows a two-dimensional view of Fig. 4.18. The viewpoint is set along the x-axis thereby disregarding the accelerometer position information. This figure clearly reveals that the dynamic response of the Lagerwey LW-50/750 wind turbine in x-direction is dominated by the first five bending modes. It should be stressed that the geometrical complexity of the mode shapes, rather than the number of modes observed, determines the number of degrees of freedom.

138

Natural frequencies

The SDLW1 model of the Lagerwey LW-50/750 wind turbine is linearized and subsequently the matrix eigenvalue problem is solved producing the simulated natural frequencies. The first five measured and simulated natural frequencies are compared in Table 4.11. It must be noted that the foundation spring stiffness of the SDLW1 model has been tuned (35 % lower than the value provided by Lagerwey) to ensure that the simulated initial tower top deflection equals the measured one. From this table it can be concluded that the differences in natural frequency are small.

LW-50/750 turbine	
Mode	Difference SDLW1 w.r.t. measurements
1st	0.0 %
2nd	+ 5.7 %
3rd	0.0 %
4th	+ 5.3 %
5th	+ 5.9 %

Table 4.11: *Comparison of simulated natural frequencies (SDLW1 model) to the ones resulting from the modal analysis applied to the Lagerwey LW-50/750.*

Time-domain responses

In Fig. 4.20 and 4.21 the measured and simulated tower top acceleration response in x-direction are compared. To ensure that the simulation starts in steady-state, the equilibrium point has been determined, and the corresponding state vector has been saved. This state vector is used as initial condition in the performed simulation. From the figures it is clear that the SDLW1 model accurately describes the real response. Note that the time-domain response depends on the unknown (viscous) damper constants. These constants have been estimated from the measured response and are used to generate the presented time histories. To achieve (even) better correlation with the measured response, all model parameters can be updated using the approach presented in Molenaar [191].
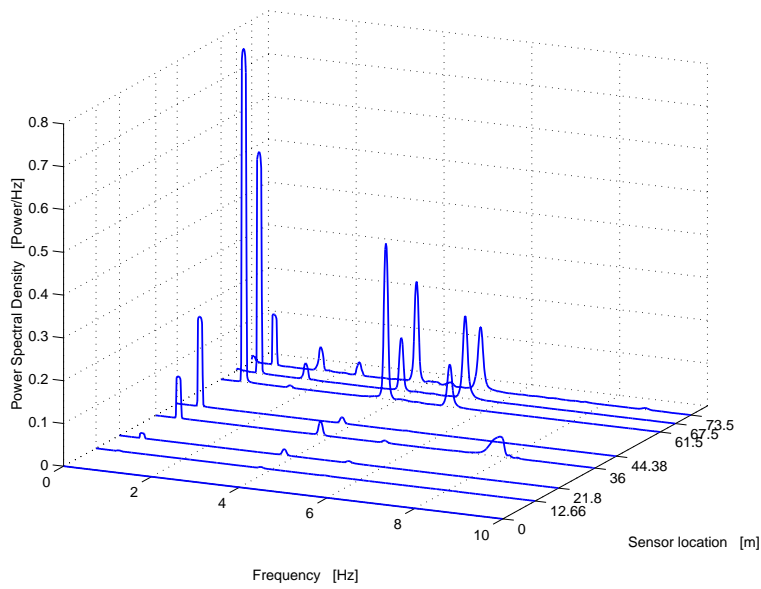
Figure 4.18: *Collection of periodogram estimates of the power spectral density (PSD) of the responses in x-direction (sensor A-01 to A-05, A-07, A-09 and A-11 respectively) from measurement M2.*
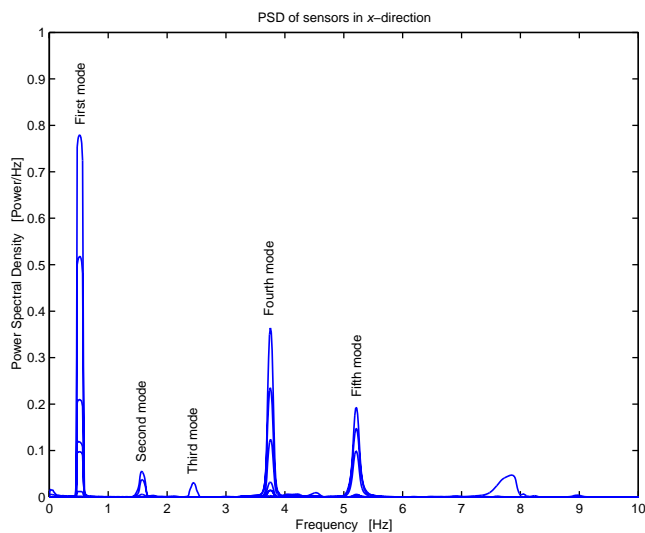
Figure 4.19: *Two-dimensional view of Fig. 4.18. The viewpoint set along the x-axis (thereby disrecarding the accelerometer position information).*
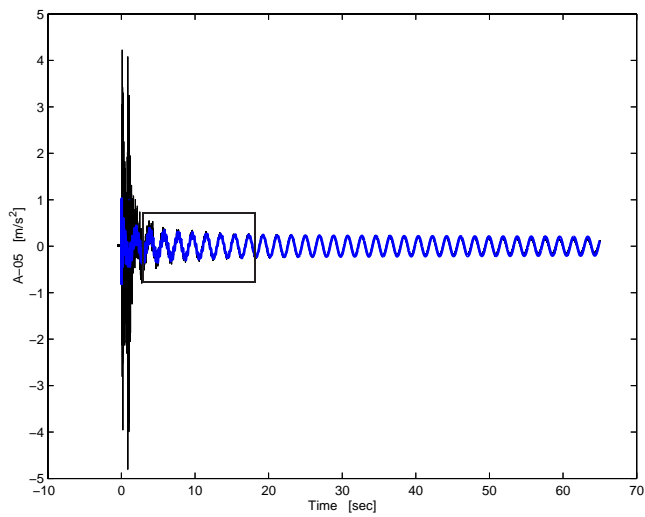
Figure 4.20: *Measured versus simulated tower top acceleration response from measurement M2. Thin line: measured response and thick line: simulated response.*

Figure 4.21: *Measured versus simulated tower top acceleration response from measurement M2 (zoom of box in Fig. 4.20). Thin line: measured response and thick line: simulated response.*

141

4.3 Electrical module verification and validation

In this section the electrical module will be validated to justify the use of this model for model based control design purposes. First, a brief review of the existing literature on synchronous machine i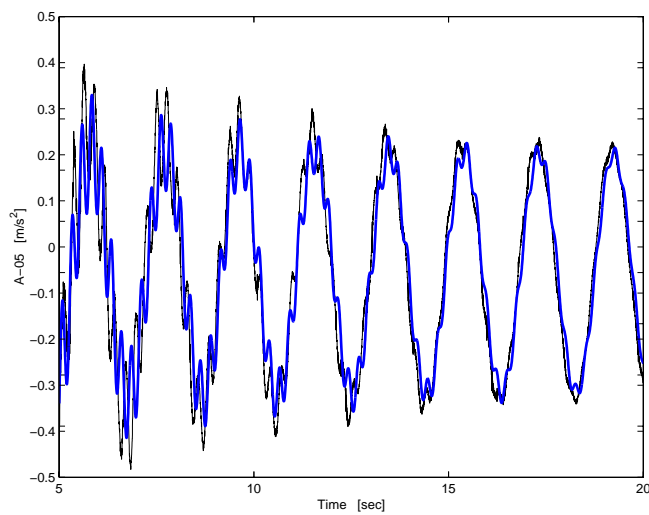dentification and parameter determination is given. Next, a new procedure is developed (using ideas from Touhami *et al.* [291]) for identifying the transfer functions of Park's *dq*-axis model of a synchronous generator from time-domain standstill step-response data. This procedure is applied to the synchronous generator implemented in the Lagerwey LW-50/750 wind turbine. The validity of the theoretical model will been verified by comparing time-domain simulations with measurements taken from the Lagerwey LW-50/750 generator.

4.3.1 Literature review

The design of a robust frequency converter controller for high dynamic performance requires that the (synchronous) generator model parameters are known accurately. In principle, synchronous machine parameters may be determined either from design calculations or from measurements acquired at the factory or on site. For high dynamic performance control, however, the former approach is inadequate. A primary goal of this section is to address the latter issue.

Many papers have been published on synchronous machine parameter identification (*see e.g.* [18, 136, 153, 248, 291, 294] and references therein). Most papers address standstill frequency response (SSFR) methods following the protocols of IEEE Standard 115-1995 [111]. This standard focusses on identifying equivalent circuit parameters rather than on transfer functions. Two papers address methods for identifying the parameters from time-domain data. In both cases, the parameter estimation process generally consists of two parts. First, the time constants are extracted by applying a curve-fitting procedure to measured data. Next, the equivalent circuit parameters are determined by solving a set of non-linear equations through numerical optimization. The weakness of this approach is that the order of the model must be known *a priori* and that numerical optimization is a process fraught with numerical difficulties [104].

4.3.2 Synchronous generator parameter identification

Synchronous machine identification and parameter determination can be performed either during normal operation (*i.e.* on-line), or during specially designed identification experiments (*i.e.* off-line) [90]. Each approach has advantages as well as disadvantages. For example, in the on-line case the measured input-output data reflect the actual operating conditions. A disadvantage is that it is not possible to manipulate the input signals arbitrarily in order to obtain the best identification results. This implies that the influence of the operating conditions on the (accuracy of the) identified parameters has to be carefully analysed. Off-line tests, on the other hand, require that the machine under test has to be taken out of regular operation, an action that might be inappropriate or even impossible.

Off-line identification experiments have been used for decades to identify electrical machine parameters. Two concepts are commonly used: running machine, or standstill. Standstill tests are very attractive from a practical viewpoint - if it is permissible to take the machine out of operation - because driving the machine often creates serious complications of the measurement set-up [301]. Furthermore, the measured signals will have good signal-to-noise ratios due to the absence of disturbance signals (electromagnetic interference). All standstill tests reported in literature are variations on the same concept, they mainly differ in the kind of excitation signal applied (*i.e.* step, ramp, sinusoidal, or random excitation).

The standstill test concept is preferred because there is no interaction between the direct- and the quadrature axis. Observe that the block diagram of Fig. 3.26 reduces to that of Fig. 4.22 for the standstill case (*i.e.* $\omega_m = 0$). Using this observation, it can be concluded that the parameter identification for both axes may be carried out separately. In practice, zero generator speed can be enforced by mechanically locking the rotor during the experiments.
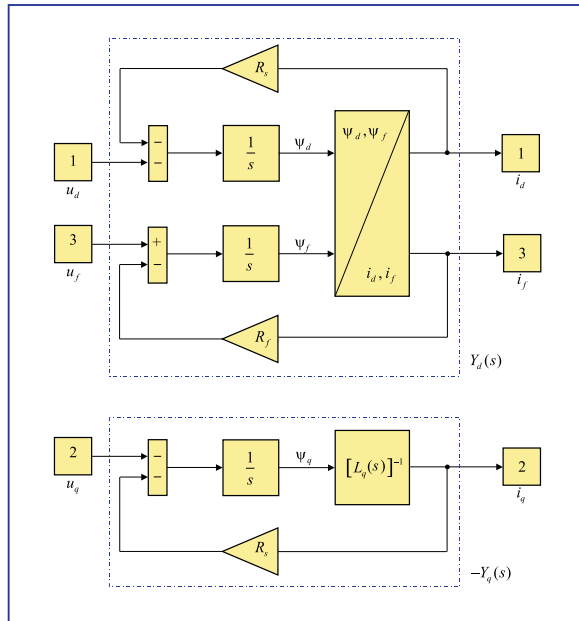
Figure 4.22: *Block diagram of an ideal synchronous machine at standstill.*

In addition, there are a few important practical demands in selecting a technique for the identification and parameter determination of the Lagerwey LW-50/750 generator considering the fact that the generator has already been installed in the nacelle at about 50 meter above the ground level. First of all, the measurements should have low power consumption. Secondly, the test equipment should be compact, and finally, the measurement time should be limited (*i.e.* < 1 day).

Before selecting the most appropriate standstill test, we will first highlight the most important aspects of both the quadrature-axis and the direct-axis identification.

Quadrature-axis identification

The dynamic behavior of the quadrature-axis of an ideal synchronous generator is fully described by the transfer function $Y_q(s)$ in Fig. 4.22. From the block diagram it directly follows that

$$Y_q(s) = -\frac{I_q(s)}{U_q(s)} = \frac{1}{R_s + s \cdot L_q(s)} \tag{4.10}$$

For the identification of $Y_q(s)$ knowledge of the quadrature-axis voltage $u_q(t)$ and current $i_q(t)$ is thus both necessary and sufficient. It will be shown below that these quantities can be easily derived from three measurable variables, *viz.* the stator voltages of the b and c phase ($u_b(t)$, and $u_c(t)$ respectively), and the stator current $i_c(t)$.

An appropriate rotor position for quadrature-axis identification is the one when the field winding axis is parallel to the a-phase winding (*i.e.* $\theta_e = p\,\theta_m = 0$, *see* Fig. 3.24 on page 87). In addition, if in this position the stator b-c terminals are excited while the a-terminal remains open (*i.e.* $i_a = 0$), it follows that $i_b = -i_c$. Furthermore, it can be concluded from symmetry considerations that $u_a = \frac{1}{2}\,(u_b + u_c)$.

Substituting the above results in the equations for the transformed stator voltages and currents

$$\begin{aligned} \mathbf{u_{0dq}} &= \mathbf{T}_{0dq} \cdot \mathbf{u}_s \\ \mathbf{i_{0dq}} &= \mathbf{T}_{0dq} \cdot \mathbf{i}_s \end{aligned}$$

where

$$\begin{aligned} \mathbf{u_{0dq}} &= \begin{bmatrix} u_0 & u_d & u_q \end{bmatrix}^T \\ \mathbf{u_s} &= \begin{bmatrix} u_a & u_b & u_c \end{bmatrix}^T \\ \mathbf{i_{0dq}} &= \begin{bmatrix} i_0 & i_d & i_q \end{bmatrix}^T \end{aligned}$$

and $\mathbf{T}_{0dq}$ the Park's power-invariant transformation matrix,

$$\mathbf{T}_{0dq} = \sqrt{\tfrac{2}{3}} \begin{bmatrix} \frac{1}{\sqrt{2}} & \frac{1}{\sqrt{2}} & \frac{1}{\sqrt{2}} \\ \cos(p\,\theta_m) & \cos(p\,\theta_m - \tfrac{2}{3}\pi) & \cos(p\,\theta_m + \tfrac{2}{3}\pi) \\ \sin(p\,\theta_m) & \sin(p\,\theta_m - \tfrac{2}{3}\pi) & \sin(p\,\theta_m + \tfrac{2}{3}\pi) \end{bmatrix}$$

gives

$$\begin{aligned} u_q &= \tfrac{1}{2}\sqrt{2}\,(u_c - u_b) & u_d &= 0 \\ i_q &= \sqrt{2}\,i_c & i_d &= 0 \end{aligned} \tag{4.11}$$

Finally, the q-axis parameters (*i.e.* $L_q(s)$ and R_s) are deduced algebraically from the transfer function $Y_q(s)$.

Direct-axis identification

The dynamic behavior of the direct-axis of an ideal synchronous generator is fully described by the transfer function matrix $Y_d(s)$ between u_d, u_f and i_d, i_f in Fig. 4.22. In this case, an appropriate rotor position is the one when the field winding axis is perpendicular to the a-phase winding (*i.e.* $\theta_e = \frac{1}{2}\pi$, *see* Fig. 3.24). After all, it can be easily shown that for $\theta_e = \frac{1}{2}\pi$ it follows that

$$
\begin{aligned}
u_d &= -\tfrac{1}{2}\sqrt{2}\,(u_c - u_b) & u_q &= 0 \\
i_d &= -\sqrt{2}\,i_c & i_q &= 0
\end{aligned}
\tag{4.12}
$$

In principle, the elements of Eq. (3.107), *viz.* $L_{fo}(s)$, $L_{fdo}(s)$ and $L_{do}(s)$, can be identified using data acquired from two independent measurements, namely one with excitation of the direct-axis voltage while the field winding is left open and one when the field winding is short-circuited [301]. Combining the resulting transfer functions gives the required 2×2 transfer function matrix. Due to the finite-precision arithmetic of a computer, however, this will result in an ill-conditioned matrix.

One way to overcome this problem is to identify the MIMO (multiple-input-multiple-output) transfer function between the fluxes ψ_d, ψ_f and the currents i_d, i_f assuming that both R_s and R_f are known. Recall that the stator winding resistance is known from the quadrature-axis identification. One possible way to determine the field winding resistance is by a stepwise excitation of u_f and measuring i_f. Subsequently, dividing the steady-state value of u_f by the steady-state value of i_f gives R_f.

Neither the direct-axis winding flux ψ_d, nor the field winding flux ψ_f, however, can be measured in practice. Conversely, these variables can be generated by integration of Eq. (3.104) with the u_d, u_f, i_d, and i_f acting as input. Analogous to the quadrature-axis identification, the latter variables can be deduced from the three measurable variables u_b, u_c, and i_c.

Standstill test (excitation signal) selection

The character of the input signal that is applied during the experiment determines the amount of relevant information that is present in the data. For example, applying a constant input signal $u(t) = c$, $t \in (-\infty, \cdots, +\infty)$ (c a constant) to the generator will not result in an output signal that contains any information on the dynamics of the system. Observe that in this case only static behavior can be uniquely determined. Consequently, in order to extract sufficient information from measured data concerning the dynamics, conditions have to be imposed on the character of the input signal.

In the derivation of Eqs. (3.103) and (3.105) a linear magnetic circuit was assumed. Due to hysteresis and saturation, however, the relationship between the current i and flux ψ is non-linear. As a result, the kind of excitation signal as well as the values of the currents during the measurements influence the identified slope of the hysteresis loop [185]. Fig. 4.23 shows two exaggerated hysteresis loops. The minor loop, which is symmetric with respect to the origin and has a smaller overall

slope than the full loop, is traveled by small sinusoidal (as in the SSFR test) and random excitation signals. The only way to force the slope of the minor loop to approximate that of the full loop is to use large excitation signal amplitudes. Obviously, this requires special test equipment which is in conflict with our practical demands.
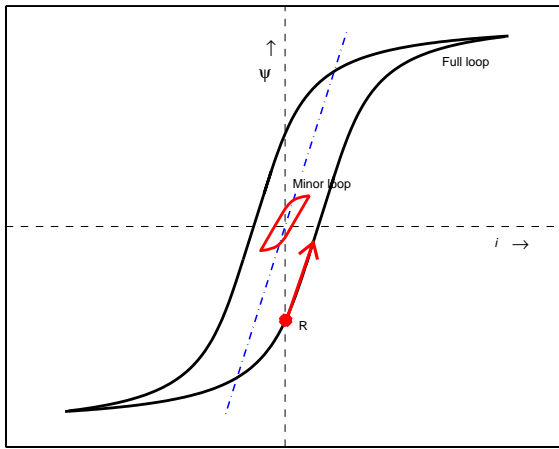

Figure 4.23: *Full and minor hysteresis loop (width of loop is exaggerated) with approximate slope (dashed-dotted line) and R: initial magnetic state.*

The slope of step or ramp excitation signals with the initial magnetic state fixed on the low boundary of the hysteresis loop (location R in Fig. 4.23) by preliminary magnetisation of the magnetic circuit, on the other hand, coincides with the full loop slope. In addition, while a complete SSFR test requires a long period of time, the step- or ramp-response test can be performed in a very short time period [136]. Consequently, step or ramp excitation signals are preferred over small sinusoidal and random excitation signals for our intended model use. The step excitation signal can be easily generated by switching on a a low-power DC voltage source (*e.g.* an ordinary car battery). That is, it has the advantage of not requiring any special test equipment. Consequently step-response testing may be more practical for obtaining parameters for installed synchronous machines. Summarising, based on both the excitation requirements and the practical demands, a step-response test seems the most appropriate test among the standstill tests for the identification and parameter determination of the Lagerwey LW-50/750 generator.

Step-response tests are proposed by *e.g.* Boije *et al.* [18], by Keyhani *et al.* [136] and by Vleeshouwers [301]. The measurement set-up as well as the experimental procedures are similar in the aforementioned step-response tests. In all cases, a sudden DC voltage is applied across two of the stator terminals with the rotor positioned in the d or q axis. In contrast, the way the parameters are identified is quite distinct. For example, Keyhani *et al.* obtain initial values for the maximum-likelihood estimation by first applying a curve-fitting procedure to measured data. Subsequently, the

maximum-likelihood estimation algorithm is used to identify the d and q axis transfer function model parameters. Vleeshouwers, on the other hand, transforms the measured time-domain data first to the frequency domain and after that identifies the transfer function model parameters using a maximum-likelihood (ML) estimator. We have decided to follow the well-documented procedures of Vleeshouwers' "modified step-response test" (MSR) to generate the time-domain data. For identifying the transfer functions, however, we developed a new, straightforward procedure.

4.3.3 MSR test applied to the LW-50/750 generator

In the previous section the modified step-response (MSR) test turned out to be most appropriate for synchronous machine identification and parameter determination. In this section the MSR-test will be used to identify the transfer function $Y_q(s)$, the MIMO transfer function between the fluxes ψ_d, ψ_f, the currents i_d, i_f, and the resistances R_s and R_f of the Lagerwey LW-50/750 generator. This generator is a 750 kW, directly driven (or low-speed), salient-pole rotor synchronous generator. The power is generated in two star connected three-phase systems. A rectifier at the tower base converts the three-phase alternating currents to the 1100 V DC of the DC-bus. Adjacent to the rectifier, is an inverter, which converts the DC to 690 V AC of the utility grid (50 Hz).

Measurement set-up

Fig. 4.24 shows a schematic of the measurement set-up, while in Appendix H the technical specifications of measurement equipment are listed. The whole set-up has been installed in the nacelle at about 50 meter above the ground level. The step-like excitation signal is generated by switching on a low-power DC voltage source (*i.e.* a 12 V battery). The battery is connected to the b and c stator terminals of the synchronous generator (SG). A thyristor is used for the switching. A thyristor is preferred over a mechanical switch because it eliminates the problem of bouncing [301]. Furthermore, the machine parameters are identified at ambient temperature (20°).

The data-acquisition system consists of three main parts, *viz.* an input-output (I/O) board, a digital signal processor (DSP) board from dSPACE® [53] with a TMS320C40 processor from Texas Instruments®, and a personal computer (PC) connected to the processor board. The automated data-acquisition process is started by switching on the (mechanical) switch and subsequently triggering the thyristor. Depending on the measurement type, a combination of the following signals is measured: i_c (stator current), u_{bc} (stator voltage), u_f (field winding voltage), and i_f (field winding current).

Data-acquisition and identification procedure

The modified step-response test consists of three successive measurements:

1. **Q-measurement**. Rotor positioned such that the quadrature axis is excited;
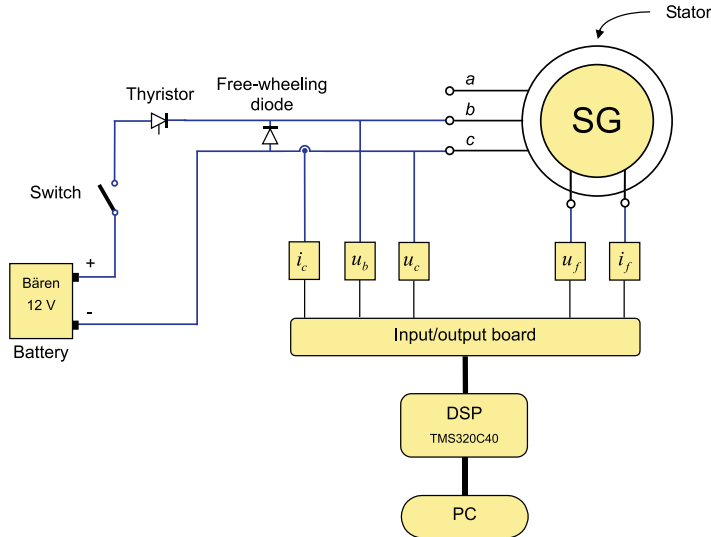
Figure 4.24: *Scheme of the measurement set-up of the modified step-response test as used for the identification of the machine parameters of the synchronous generator (SG) of the Lagerwey LW-50/750 wind turbine.*

2. **D-measurement**. Rotor positioned such that the direct axis is excited, while the field winding is short-circuited;

3. R_f-**measurement**. Stepwise excitation of u_f and measuring i_f;

The "D" and "Q"- measurements have been preceded by remagnetising the system by either a large negative or positive current depending on the direction of the step in order to fix the initial magnetic state on the low boundary of the hysteresis loop (location R in Fig. 4.23).

It should be noted that none of the measurements incorporated anti-aliasing filters. The "Q"-measurement data were collected with a sample rate of 5 kHz and have a 3.1 second measurement period. Both the "D" and "R_f"-measurement data were collected with a sample rate of 1 kHz and a 10.1 second measurement period. Each measurement is repeated at least three times. Example input output data of the "Q"-measurement is shown in Fig. 4.25. Notice that the measured voltage appears to be a modified step instead of an exact step due to the battery's internal voltage drop. This drop, in turn, is caused by the significant current taken from the battery.

Parameter estimation procedure   System identification or parameter estimation deals with constructing mathematical models of dynamical systems from experimental data. The parameter estimation procedure picks out the "best" model within the chosen model structure according to the measured input and output sequences
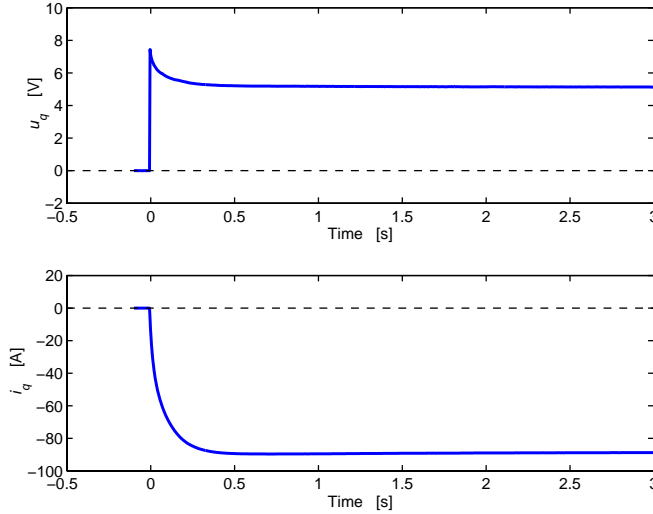
148

Figure 4.25: *Time-domain MSR input-output signals for estimation of transfer function $Y_q(s)$ (excitation u_q and response i_q).*

and some identification criterion. A common and general method of estimating the parameters in system identification is the prediction-error method [166]. In this method, the parameters of the model are chosen so that the difference between the model's (predicted) output and the measured output is minimized.

Black-box model structures In the system identification approach [166], it is assumed that the "true" system description is given in the following form

$$y(k) = G_0(q)u(k) + v(k) \tag{4.13}$$

where $y(k)$ is the (measured) output signal, $G_0(q)$ is a proper, rational, stable transfer function, q the shift operator, $u(k)$ the (measured) input signal, and $v(k)$ the disturbance signal. The disturbance $v(k)$ is modeled as a filtered sequence of zero-mean, identically distributed, independent random variables (*i.e.* white noise $e(k)$)

$$v(k) = H_0(q)e(k) \tag{4.14}$$

The transfer function $H_0(q)$ is restricted to be monic ($H_0(0) = 1$) and minimum phase (*i.e.* $H_0^{-1}(q)$ has a stable inverse). The whole system specification is thus given by specifying the two transfer functions (or filters) $G_0(q)$ and $H_0(q)$.

Analogous to the true system description given by Eq. (4.13), the model is determined by the relation

$$y(k, \theta) = G(q, \theta)u(k) + H(q, \theta)e(k) \tag{4.15}$$

A particular model corresponds thus to the specification of $G(q, \theta)$ and $H(q, \theta)$. One way to parametrize the transfer functions $G(q, \theta)$ and $H(q, \theta)$ is to represent them

149

as rational functions and let the parameters be the numerator and denominator coefficients. These coefficients are collected in the parameter vector θ, which is to be estimated.

For single-input, single-output systems, the general linear, time invariant, black-box model structure is given by

$$A(q)y(k) = q^{-n_k} \frac{B(q)}{F(q)} u(k) + \frac{C(q)}{D(q)} e(k) \tag{4.16}$$

where A, B, C, D, and F are polynomials in the delay operator q^{-1}

$$
\begin{aligned}
A(q) &= 1 + a_1 q^{-1} + \cdots + a_{n_a} q^{-n_a} \\
B(q) &= b_0 + b_1 q^{-1} + \cdots + b_{n_b} q^{-n_b} \\
C(q) &= 1 + c_1 q^{-1} + \cdots + c_{n_c} q^{-n_c} \\
D(q) &= 1 + d_1 q^{-1} + \cdots + d_{n_d} q^{-n_d} \\
F(q) &= 1 + f_1 q^{-1} + \cdots + f_{n_f} q^{-n_f}
\end{aligned}
$$

The numbers n_a, n_b, n_c, n_d, and n_f are the orders of the respective polynomials. The number n_k is the pure time delay (the dead-time) from input to output. Notice that for a sampled data system, n_k is equal to 1 if there is no dead-time.

Within the structure of Eq. (4.16) all the usual linear black-box model structures are obtained as special cases. For example, the ARX (Autoregressive with external input) model structure is obtained for $n_c = n_d = n_f = 0$.

One-step-ahead prediction error A model obtained by identification can be used in many ways, depending on the intended use of the model. For both simulation as well as control design purposes, it is valuable to know at time $(k-1)$ what the output of the system is likely to be at time k in order to determine the input at time $(k-1)$. Therefore, the parameter estimate θ is usually determined so that the one-step-ahead prediction error

$$\epsilon(k, \theta) \equiv y(k) - \hat{y}(k|k-1, \theta) \qquad k = 1, \cdots, N \tag{4.17}$$

is small for every time instant. In Eq. (4.17) $\hat{y}(k|k-1, \theta)$ denotes the one-step-ahead prediction of $y(k)$ given the data up to and including time $(k-1)$ based on the parameter vector θ. Observe that the prediction error can only be calculated a posteriori, when measurement $y(k)$ has become available. In Ljung [166] it is shown that the one-step-ahead prediction of $y(k)$ is given by

$$
\begin{aligned}
\hat{y}(k|k-1, \theta) &= H^{-1}(q, \theta) G(q, \theta) u(k) \\
&+ \left[1 - H^{-1}(q, \theta) \right] y(k) \qquad k = 1, \cdots, N
\end{aligned}
\tag{4.18}
$$

Recall that $H^{-1}(0, \theta) = 1$, which means that the predictor depends only on previous output values. Substituting Eq. (4.18) in Eq. (4.17), the prediction error becomes

$$\epsilon(k, \theta) = H^{-1}(q, \theta) \left[y(k) - G(q, \theta) u(k) \right] \tag{4.19}$$

The prediction error is thus exactly that component of $y(k)$ that could not have been predicted at time instant $(k-1)$. Obviously, in case of a consistent model estimate (*i.e.* if the estimated model $G(q,\theta)$, $H(q,\theta)$ is equal to the true system $G_0(q)$, $H_0(q)$), then the prediction error becomes a white noise signal ($\epsilon(k) = e(k)$).

Identification criterion The most simple and most frequently applied identification criterion is a quadratic function on $\epsilon(k,\theta)$, denoted as

$$V_N(\theta, Z_N) = \frac{1}{N} \sum_{k=1}^{N} \epsilon^2(k,\theta) \tag{4.20}$$

where $Z_N := \{y(1), u(1), y(2), u(2), \cdots, y(N), z(N)\}$.

The estimated parameter vector $\hat{\theta}_N$ is now defined as the minimizing element of the criterion Eq. (4.20), *i.e.*

$$\hat{\theta}_N = \arg\min_\theta V_N(\theta, Z_N) \tag{4.21}$$

This criterion is known as the "least squares criterion".

For the FIR (finite impulse response; $n_a = n_c = n_d = n_f = 0$) and the ARX model structure, the one-step-ahead prediction $\hat{y}(k|k-1)$ is a linear function of the polynomial coefficients that constitute the parameter vector θ (the so-called linear-in-the-parameters property). A consequence of this linearity is that a least squares identification criterion defined on the prediction errors $\epsilon(k)$ is a quadratic function in θ. As a result, there will be an analytical expression for the optimal parameter $\hat{\theta}$ that minimizes the quadratic criterion. For all other model structures, on the other hand, the parameter estimation involves an iterative, numerical search for the best fit.

The developed identification procedure consists of three successive steps:

- **Step 1: Pretreatment of data**. In general, when the data have been collected from the identification experiment, they have to be pretreated to avoid problems during the parameter identification. The necessary pretreatment of the time-domain data, however, is limited since the MSR-test results in relatively clean signals. This is mainly because the machine has been taken out of operation. The only pretreatment of the data that is required is compensating for the (slight) static non-linearity of the sensors and removal of the offset;

- **Step 2: Model structure and order selection**. It is trivial that a bad model structure cannot offer a good, low order model, regardless the amount and quality of the available data. The measured input-output data is imported into SITB (graphical user interface to the System Identification Toolbox) [287]. First, an initial model order estimate is made by estimating 1100 ARX-models.

  Recall that a linear regression estimate ARX is generally the most simple model to start with, particularly because of its computationally simplicity [166]. If the resulting model, however, produces an unsatisfactory simulation error and/or

if the input is correlated with the residual, the model is rejected and another model structure (or order) is selected. This continues until the model produces a satisfactory simulation error and results in zero cross-covariance between residual and past inputs. In that case it can be concluded that a consistent model estimate has been obtained;

- **Step 3: Model validation**. Model validation is highly important when applying system identification. The parameter estimation procedure picks out the "best" model within the chosen model structure. The crucial question is whether this "best" model is "good enough" for the intended application: time-domain simulation, analysis of dynamic loads, or control design purposes. To this end, the identified models should be confronted with as much information about the process as practical. Here, the outputs of the identified model are compared to the measured ones on a data set that was not used for the fit (the so-called "validation data set").

Model validation

As mentioned above, the outputs of the identified model are compared to the measured ones from a validation data set to (in)validate the model. The percentage of the output variations that is reproduced by the model is chosen as measure of the "goodness" of fit. The precise definition is:

$$
M_{gof} = \left[1 - \frac{\sqrt{\sum_{t=-0.1}^{10} \left(y(t) - y_{sim}(t) \right)^2}}{\sqrt{\sum_{t=-0.1}^{10} |y(t) - \bar{y}|^2}} \right] \cdot 100
$$

with $0 \leq M_{gof} \leq 100$ %, y is the measured output, y_{sim} is the simulated model output, and $\bar{y}$ the average value.

Results

The q-axis transfer function $Y_q(s)$ of the electromagnetic part of the Lagerwey LW-50/750 generator has been identified using an ARX model structure. A third order model turns out to be sufficient. The q-axis parameters (*i.e.* $L_q(s)$ and R_s) of measurement M^1 are deduced algebraically from $Y_q(s)$ using Eq. (4.10). From this equation it can be observed that the stator-winding resistance R_s is equal to the DC gain of the inverse of the quadrature-axis transfer function Y_q. The resulting value of R_s is

$$
R_s = 57.90 \qquad [\mathrm{m}\Omega]
$$

Determining the values for R_s of the other two measurements gives similar results. The resulting mean value of R_s is 57.92 mΩ with a standard deviation of 0.02 mΩ. In addition, it can be concluded that the stator-winding temperature has not changed significantly during the experiments. It must be noted that, during normal operation, the temperature of the copper windings will increase from about 20° (temperature at which the MSR-measurements are performed) to about 100°. As a

consequence, the stator-winding resistance will increase from 57.9 mΩ to about 77.8 mΩ using the temperature resistance coefficient of copper: $\alpha_{cu} = 4.3 \cdot 10^{-3}$ K^{-1}. Interestingly, the value of the stator-winding resistance calculated from the machine design is equal to 81.8 mΩ [224]. Consequently, for time-domain simulation of the Lagerwey LW-50/750 generator, the estimated value of R_s have to be corrected for the differences in temperature between measurement and actual operation.

Finally, the resulting quadrature-axis synchronous inductance is given by

$$L_q = \frac{0.002756 \cdot s^2 + 0.5421 \cdot s + 17.45}{s^2 + 157.3 \cdot s + 2766}$$

with the following roots

$$s_1 = -20.1708$$
$$s_2 = -137.1292$$

and DC-gain

$$L_q^{DC} = 6.3095 \qquad [\text{mH}]$$

Calculated was a value of 7.7 mH [224].

The structure of the symmetric d-axis transfer function matrix (*i.e.* common denominator) and the high signal-to-noise ratio calls for a MIMO ARX model structure. Numerical difficulties in deducing the d-axis parameters from the estimated transfer functions, however, forced us to use the following three-step approach:

- **Step 1:** Use the modified step-response test data to determine the stator-winding resistance R_s and the field winding resistance R_f;

- **Step 2:** Generate the direct-axis stator flux ψ_d and direct-axis field winding flux ψ_f by running a simulation with the measured u_d, u_f, i_d, and i_f acting as input. The generated flux signals as well as the measured currents of measurement M^{18} are shown in Fig. 4.26;

- **Step 3:** Import the generated flux signals into SITB and identify the MIMO (multiple-input-multiple-output) ARX transfer function between the fluxes ψ_d, ψ_f and the currents i_d, i_f (*see* Eq. (3.107)).

It should be noted that converting the individual transfer functions in Eq. (3.107 to state-space prior to combining the transfer functions did not solve the problem. Recall that the state-space representation is best suited for numerical computations.

For both inputs i_d and i_f, the percentage of the variations in the fluxes ψ_d, ψ_f that is reproduced by the (fourth order) model is larger than 99.5 % (identification data set). The common denominator of the MIMO transfer function between the fluxes ψ_d, ψ_f and the currents i_d, i_f is given by

$$L_{do}(s) \cdot L_{fo}(s) - L_{fdo}^2(s) = s^4 + 672 \cdot s^3 + 756.9 \cdot s^2 + 1795.1 \cdot s + 1197.4$$
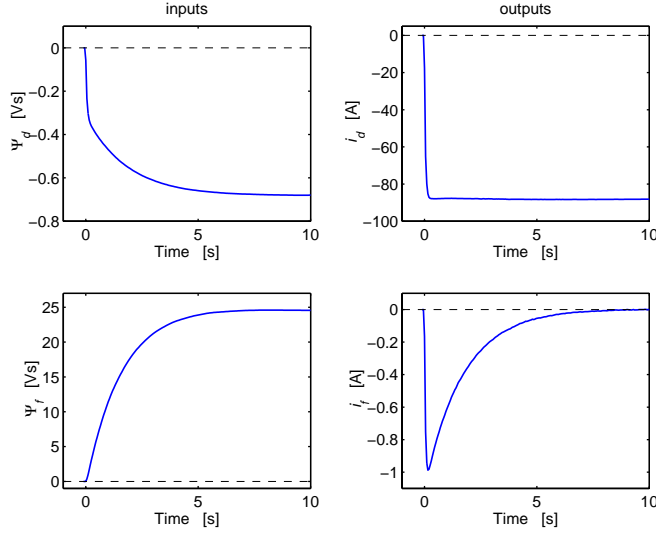
Figure 4.26: *Left figures: simulated inputs ψ_d and ψ_f as function of time. Right figures: Measured outputs i_d and i_f as function of time from measurement* M^{18}.

with the following roots

$$
\begin{aligned}
s_1 &= -1.2878 \\
s_2 &= -1.6416 \\
s_3 &= -10.5381 \\
s_4 &= -53.7496
\end{aligned}
$$

The aforementioned q-axis parameters and d-axis transfer function matrix, as well as the field-winding resistance, are implemented in the block diagram shown in Fig. 4.22. The resulting inputs and outputs of the model are shown in Fig. 4.27 for a validation data set. Obviously, the simulated data matches the measured data very well. Observe that u_f is not equal to zero because the short-circuit is not perfect due to the slip-rings. Fig. 4.28 shows the outputs once again, but now on a reduced time scale. The percentage of the output variations that is reproduced by the model is, in the case of the identification data set, 99.74 %, 99.47 %, and 99.89 % for i_d, i_f, and i_q respectively. For the validation data set the percentage is 99.16 %, 92.78 %, and 99.76 % for i_d, i_f, and i_q respectively. In addition, the quality of the model is also checked by examining the cross correlation function between inputs and output residuals. In both cases an almost zero cross-covariance exists.
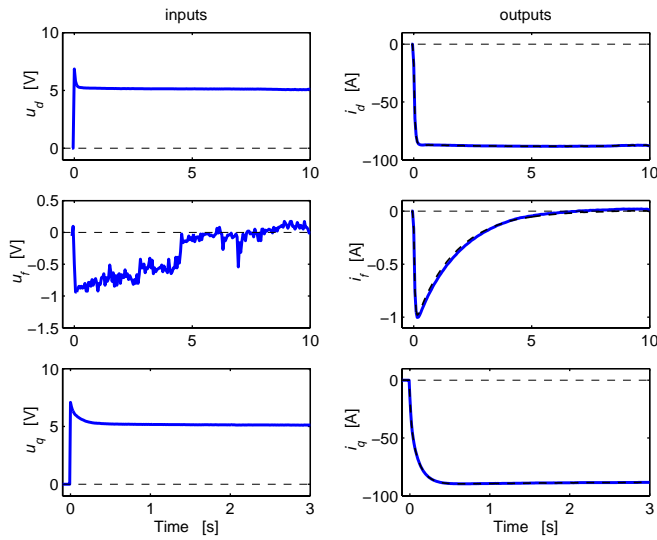
Figure 4.27: *Left figures: measured inputs u_d, u_f and u_q as function of time. Right figures: outputs i_d, i_f and i_q as function of time. Solid lines: measured data (validation data set), and dashed-lines: simulated data.*
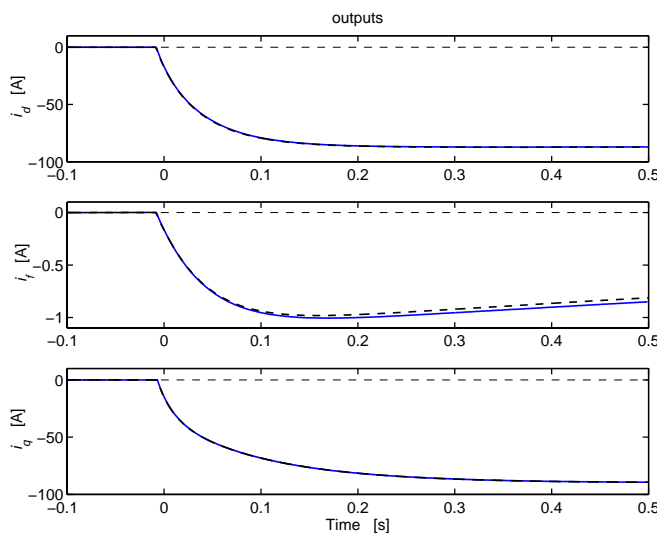

Figure 4.28: *Outputs i_d, i_f and i_q as function of time (zoom of right figures in Fig. 4.27). Solid lines: measured data (validation data set), and dashed-lines: simulated data.*

4.4 Conclusions

In this chapter the first verification as well as experimental validation results of DAWIDUM's wind turbine module library have been presented. The validation has been subdivided into three distinct parts, *viz.* mechanical module, electrical module, and complete wind turbine model in order to meet the accuracy demanded by the intended model use. It should be stressed that only the first two validation parts are treated in this thesis. The interested reader is referred to Van Baars [6] for a detailed and systematic treatment of the validation of a complete wind turbine model through open field identification experiments.

In the first place the verification and validation of DAWIDUM's automated systematic structural modeling procedure has been examined by considering six cases. In the first case the procedure has been verified by comparing the exact rotating as well as non-rotating solutions to the frequency equation for transverse vibration of an Euler-Bernouilli beam to the ones from the superelement approximation. In the second till the fifth case measured non-rotating eigenfrequencies of different rotor blades have been compared to those of the superelement approximation. Finally, in the sixth case, natural frequencies, mode shapes and time-domain responses acquired from a modal test applied to the Lagerwey LW-50/750 wind turbine and the ones from a DAWIDUM wind turbine model are compared. The following conclusions can be drawn:

- DAWIDUM's automated systematic structural modeling procedure approximates the dynamics effectively as a collection of rigid and flexible bodies;

- The resulting models are suited for both model based control design and design optimization purposes since the first bending modes are approximated with only a few superelements;

- The model accuracy is strongly limited by the quality of the supplied input data. This implies that, depending on the intended model use and quality of the supplied data, tuning of the torsional spring constants using experimental modal test data might be required to reach the required model accuracy.

Secondly, the validity of DAWIDUM's procedure for identifying the transfer functions of Park's *dq*-axis model describing the electromagnetic part of a synchronous generator has been examined by comparing time-domain simulations with measurements taken from the Lagerwey LW-50/750 generator. The required input-output data is obtained from the modified step-response test. The following conclusions can be drawn:

- The parameters of Park's *dq*-axis model describing the electromagnetic part of a synchronous generator can be easily and accurately identified following the developed procedure on the basis of modified step-response data;

- It is justified to use this model for model based control design purposes. The ultimate validation of the method and its impact on variable speed wind turbine performance can be proved only after the implementation of the designed frequency converter controller in the Lagerwey LW-50/750 wind turbine.

In Chapter 6 the validated model will be used to develop a new, but preliminary rectifier frequency converter controller to achieve the required high dynamic performance of the Lagerwey LW-50/750 wind turbine direct-drive synchronous generator.

Chapter 5

Model parameter updating using time-domain data

Assessing design changes in wind turbines from simulation results requires both accurate dynamic models and accurate values for the (physical) model parameters. For various reasons, however, the theoretical predictions do often not fully correspond with the experimental measurements. Consequently, the model parameters need to be tuned or updated so as to achieve better correlation with the test data. This should be done in a physically meaningful way, because only in that way it is possible to give direct feedback to the wind turbine designers.

This chapter addresses the subject of updating the physical parameters of the structural models derived in Section 3.4 using input-output data acquired from experimental tests. Section 5.1 gives a short introduction to model parameter updating and its relation to system identification. The problem of parameter identifiability is treated in Section 5.2. The developed model parameter optimization procedure is presented in Section 5.3. In Section 5.4 this procedure is verified using simulated data.

5.1 Introduction

Model parameter updating or model parameter tuning can be defined as a model-based methodology for the reconciliation of measured and simulated data. In other words, the goal of model parameter updating is to improve the accuracy of mathematical models by adjusting the tunable parameters so that the differences between simulated and measured dynamic properties vanish. A question that can be asked is: "What is the relationship between model parameter updating and system identification?"

Recall that system identification deals with constructing mathematical models of dynamical systems from experimental data. Basically, there are three types of identification, *viz.* black-box, grey-box, and white-box identification. Black-box

identification deals with the situation where a model is identified purely on the basis of measured data and a given "universal" model class. The models within this class can be either linear, such as the common ARX (Autoregressive with external input) structure, or non-linear, such as Hammerstein models or neural networks [17]. As a consequence of the model being identified purely on the basis of measured data rather than reflecting the physical structure, the parameters and states in a black-box model might not have any physical interpretation. Grey-box identification corresponds to the case where physical laws are applied to arrive at the model, but where (some of) the physical parameters are unknown (or are not exactly known) and should be estimated (or updated) from measured input and output data. In grey-box identification both prior information and experimental data are used. Because of the fact that the estimated parameters have physical meanings it is possible to compare the estimated values with information from other sources, such as likely ranges and values in the literature. Furthermore, a model reflecting the physical structure will produce models with a wider validity range than black-box models. As a consequence, a grey-box model may require fewer parameters to be updated to achieve the same quality as its black-box counterpart. White-box identification, on the other hand, deals with pure physical modeling (*i.e.* first principles modeling). That is, the modeling is performed without the use of experimental data. White and black-box identification can thus be viewed as extreme cases.

In essence, model parameter updating is thus not different from grey-box identification. The term "grey-box identification" is common in control system analysis, while the term "model parameter updating" is used in the field of structural dynamics. Similar to black-box identification, model parameter updating requires selection of the input-output data, a criterion (or objective function), and a model class. In this thesis the model class is defined by the physical model structure presented in Section 3.4. It is thus assumed that structural dynamics of a flexible wind turbine can be approximated adequately by a superelement model. Consequently, the model structure is known *a priori*.

The main two advantages of model parameter updating are that the model structure reflects that of the physical system and that the tunable parameters have a clear physical interpretation since they are directly related to the geometry and material properties. The former advantage allows the calculation of an initial parameter estimate that is close to the real parameters. The latter advantage offers the possibility to establish a bilateral coupling between the design of a new wind turbine and the design of its control system. The main disadvantage is that the objective function is generally a non-linear (and non-quadratic) function in the (user-selected) tunable parameters. Consequently, no analytic solution exists and minimization of the objective function can only be obtained through methods of iterative search (*i.e.* numerical optimization). After all, trial and error becomes impractical for more than three or four parameters. Such a minimization can cause difficulty and/or failure to calculate the desired optimal solution [54]. In addition to this it should be mentioned that the computational cost of numerical optimization is very high. Fortunately, in case of updating the physical parameters of a structural wind turbine model, the optimization has to be done only once. However, before the model parameter up-

dating can take place, we have to examine whether the tunable parameters can be uniquely (globally or locally) identified from measured input-output data.

5.2 Identifiability of model parameters

This section considers the identifiability of dynamical systems from input-output data. Identifiability is concerned with the question whether or not the tunable parameters of a certain model can be uniquely (globally or locally) identified from input-output observations of the system. In other words: are the identified parameters unique or does there exist more than one distinct solution that satisfy the measured input-output data. Obviously, this is an important question that has to be answered before the model parameter updating can take place (to stress that the analysis can and should be done before an experiment is carried out, the term *a priori* identifiability is often used in literature). In addition, the terms "structural identifiability" and "deterministic identifiability" also have been proposed.

The first question is whether we can in principle, given perfect (*i.e.* noise-free) input-output data, extract the correct parameter values. There are three possible outcomes, *viz.* the system is:

- **Globally identifiable**. A system is globally identifiable if and only if its parameters can be uniquely determined from measured input-output data for all possible initial estimates of the parameter vector;

- **Locally identifiable**. A system is locally identifiable when its parameters can only be uniquely determined from measured input-output data when the initial parameter estimate is constrained to a small enough neighbourhood of the real parameter vector θ_0;

- **Unidentifiable**. A system is unidentifiable if at least one of its parameters in the parameter vector cannot be estimated uniquely from the measured input-output data. That is, there are a finite (but more than one) number of solutions (*i.e.* different parameter values) that give identical responses to the same input(s). Thus the values found for the tunable parameters after applying any parameter updating procedure are highly questionable, if not meaningless. After all, the demand that a bidirectional communication between the wind turbine design and the controller design has to be established requires that the tunable physical parameters must be uniquely (globally or locally) identifiable in order to be able to quantify them.

Obviously, the outcome is dependent on both the order of excitation of the input signal and the model parametrization. Both aspects will be discussed in detail in the next two subsections.

The identifiability question in the presence of real (*i.e.* noise contaminated) data is in literature referred to as numerically identifiability, or *a posteriori* identifiability. Numerically unidentifiable implies thus that the parameters, although uniquely (globally or locally) identifiable, can not be extracted from the data due to limited parameter estimation accuracy [86].

5.2.1 Persistence of excitation

It is straightforward to understand that the character of the input signal that is applied during an experiment highly determines the amount of relevant information that is present in the data. For example, applying a constant input signal $u(t) = c$, $t \in [0, \cdots, t_f]$ (c a constant, and t_f the final time) to the system will not result in an output signal that contains any information on the dynamics of the system. Observe that in this case only static behavior can be uniquely determined. Consequently, in order to extract sufficient information from measured data concerning the dynamics, conditions have to be imposed on the character of the input signal.

In order to characterize the so-called "order of excitation", a distinction have to be made between quasi-stationary signals (*e.g.* white noise) and transient signals (*e.g.* step or pulse) as will be shown below.

Definition 5.1 (Persistence of excitation of quasi-stationary signals) *Consider a quasi-stationary signal $u(t)$, and let the $n \times n$ matrix $\mathbf{R_n}$ be defined as the symmetric Toeplitz matrix*

$$\mathbf{R_n} = \begin{bmatrix} R_u(0) & R_u(1) & \cdots & R_u(n-1) \\ R_u(1) & R_u(0) & \cdots & R_u(n-2) \\ \vdots & \ddots & \ddots & \vdots \\ R_u(n-1) & \cdots & R_u(1) & R_u(0) \end{bmatrix} \quad (5.1)$$

with $R_u(i) \equiv Eu(t)u(t-i)$, then $u(t)$ is persistently exciting of order n if and only if $\mathbf{R_n}$ is nonsingular. □

Note that a sequence of zero mean, independent random variables (*i.e.* white noise) is persistently exciting of any finite order, since for these signals $\mathbf{R_n} = \mathbf{I_n}$ for all $1 \leq n \in \mathbb{N}$. Conversely, when applying the above definition to transient signals, it appears that these signals are persistently exciting of order 0. This is inconsistent with the fact that the dynamics of a linear, time invariant (LTI) system are completely characterized with their pulse or step response (modulo initial conditions). This implies that Definition 5.1 is not suitable for application of transient signals.

It is a general rule of thumb that, to identify a model of n independent parameters, the system has to be excited with an input that is persistently exciting of order n. The simplest way to achieve this is by ensuring that the input signal is a sum of $n/2$ distinct frequency sinusoids. After all, a sinusoid in principle exhibits two degrees of freedom: an amplitude an a phase. This implies that by exciting a dynamic system with one sinusoid we can identify precisely two parameters (*i.e.* a sinusoid is persistently exciting of order 2).

In the sequel it is assumed that the experiment has been designed such that the measured input-output data is "informative enough". Meaning that the data can distinguish between nonequal models. The next question is whether different values of the parameter vector can give equal models. This problem concerns the invertibility of the model structure (*i.e.* model parametrization).

5.2.2 Model parametrization

The way in which the parameters enter into the model is determined by the parametrization. Formally, a parametrization Π is a surjective mapping that maps the parameter vector θ onto a specific model $M(\theta)$ of a model class $\mathcal{M}$ as follows:

$$\Pi : \theta \to M(\theta) \qquad \theta \in \Theta \quad M \in \mathcal{M}$$

Clearly, different values of θ produce different models. There are many different ways of parametrizing sets of models as meant above. For example, in black-box system identification the most common model set is described in terms of fractions of polynomials (*e.g.* ARX). An important property that a parametrization may exhibit is identifiability. A formal definition of identifiability is adopted from Ljung [166] and is listed below.

Definition 5.2 (Global identifiability) *The parametrization Π is locally identifiable at $\theta^\star$ if*

$$\Pi(\theta) = \Pi(\theta^\star) \quad \Rightarrow \quad \theta = \theta^\star \qquad \forall \theta \in \Theta \tag{5.2}$$

Subsequently, the parametrization Π is globally identifiable if it is locally identifiable at almost all $\theta^\star \in \Theta$.

Thus a model parametrization is globally identifiable if the mapping Π is injective (and therefore bijective). Therefore, identifiability of a parametrization can be considered as a property of finding a unique value of a parameter vector θ when applying an identification procedure to find an estimate $\hat{\theta}$. That is, when a parametrization is globally identifiable the solution set contains only one element: the real parameter vector θ_0. However, it is practically impossible (except in a view particular cases) to prove mathematically that the mapping Π is injective [46]. Thus Definition 5.2 is more a theoretical than a practical tool of investigating identifiability. Consequently, global identifiability is difficult to deal with in general terms [167, 256]. In the next two paragraphs, we shall only briefly discuss identifiability of black-box and grey-box model structures.

Black-box model structures

For single-input, single-output (SISO) systems, the general linear, time invariant (LTI), black-box model structure is given by

$$A(q)y(t) = q^{-n_k} \frac{B(q)}{F(q)} u(t) + \frac{C(q)}{D(q)} e(t) \tag{5.3}$$

where $u(t)$ the input signal, $y(t)$ the output signal, $e(t)$ a white noise signal, A, B, C, D, and F are polynomials in the delay operator q^{-1}

$$
\begin{aligned}
A(q) &= 1 + a_1 q^{-1} + \cdots + a_{n_a} q^{-n_a} \\
B(q) &= b_0 + b_1 q^{-1} + \cdots + b_{n_b} q^{-n_b} \\
C(q) &= 1 + c_1 q^{-1} + \cdots + c_{n_c} q^{-n_c} \\
D(q) &= 1 + d_1 q^{-1} + \cdots + d_{n_d} q^{-n_d} \\
F(q) &= 1 + f_1 q^{-1} + \cdots + f_{n_f} q^{-n_f}
\end{aligned}
$$

163

The numbers n_a, n_b, n_c, n_d, and n_f are the orders of the respective polynomials. The number n_k is the pure time delay (the dead-time) from input to output. Notice that for a sampled data system, n_k is equal to 1 if there is no dead-time. The variance of the white noise is assumed to be λ. The coefficients of the polynomials are collected in the parameter vector θ

$$\theta = \begin{bmatrix} f_1 & f_2 & \cdots & f_{n_f} & d_1 & \cdots & a_1 & \cdots & a_{n_a} \end{bmatrix}^T \tag{5.4}$$

It has been shown in Ljung [166] that the above mentioned black-box model structure is globally identifiable provided that the polynomials do not all have a common factor (*i.e.* the model can not be represented using a smaller order of the polynomials).

Grey-box model structures

For grey-box model structures or model structures with physical parameters the situation is much more complex. Except for special structures, there are no general techniques available to test for unique identifiability [166]. Intuitively, one would expect a relationship between controllability/observability on the one hand and identifiability on the other hand. Unfortunately, in Walter [303] it has been shown that controllability and observability are neither necessary nor sufficient conditions for the model to be uniquely (globally or locally) identifiable. Consequently, checking the observability and controllability of a given structure does not able us to conclude whether or not the tunable parameters of this structure are identifiable. Note that local identifiability is a necessary conditon for global identifiability.

We limit ourselves to the model class defined by the lumped-parameter model describing the structural dynamics of a flexible wind turbine. This model class has been presented in Section 3.4 and is here referred to as: $\mathcal{M}_m^{wt}$. That is, we have to examine whether the tunable parameters in $\mathcal{M}_m^{wt}$ are uniquely (globally or locally) identifiable from measured input-output data. We use the following definition

Definition 5.3 (Global identifiability of $\mathcal{M}_m^{wt}$) *The model class $\mathcal{M}_m^{wt}$ is globally identifiable at $\theta^\star$ if*

$$y_{meas}(t, \theta^\star) \equiv y_{sim}(t, \theta) \qquad implies \qquad \theta = \theta^\star \qquad \forall\, t \in \mathbb{R}^+ \tag{5.5}$$

where y_{meas} the actually measured output and y_{sim} the model output as a function of the parameter vector θ and time t for a fixed initial condition. The model class is locally identifiable at $\theta^\star$ when Eq. (5.5) results when θ is confined to a small neighbourhood of $\theta^\star$. Note that the size of the neighbourhood of $\theta^\star$ is, in general, not easily found.

Most techniques used to test identifiability, however, rely on the availability of an analytic expression for the observed outputs as function of the tunable parameters. In Appendix G it has been shown that for the model class $\mathcal{M}_m^{wt}$ it is difficult and cumbersome to obtain such an expression. Consequently, we have decided to check the identifiability of the model class $\mathcal{M}_m^{wt}$ through simulation. Before the identifiability can be checked, however, a parameter optimization procedure has to be developed. This is the subject of the next section.

5.3 Off-line parameter optimization procedure

In this section the developed off-line, model parameter optimization procedure is presented. In Section 5.1 it has been explained that model parameter updating implies numerical optimization. In general, optimization concerns the minimization (or maximization) of a user-specified objective function of several parameters, possibly subject to restrictions on the values of the parameters defined by a set of constraints (*e.g.* lower and/or upper bounds on the parameters). In literature it has been shown that most optimization problems benefit from good initial guesses for the values of the model parameters [7]. This improves the execution efficiency and can help locate the global minimum instead of a local minimum. For this reason, the model parameters of the first principles models of Section 3.4 are used as a starting point.

Solution of optimization problems by a single, all-purpose, method is cumbersome and inefficient. Optimization problems are therefore classified into particular categories, where each category is defined by the properties of the objective and constraint functions. Typical objective functions to be minimized are the sum of squares and weighted sum of squares. Constraint functions often arise from prior information concerning the parameter values. The presence of constraint functions, particularly in the form of upper and lower bounds on each parameter, often exerts a beneficial influence on the convergence of an optimization algorithm [7]. Moré and Wright [194] presented an overview of algorithms for different classes of optimization problems as well as information on some of the most widely used optimization software. In this section, the possibilities and limitations of both unconstrained and constrained optimization will be discussed briefly in order to be able to select the most suitable method for updating the physical parameters of a structural wind turbine model.

5.3.1 Unconstrained optimization

The unconstrained optimization problem is central to the development of optimization software since constrained optimization algorithms are often extensions of unconstrained algorithms, while the non-linear least-squares algorithm tend to be a specialization. In many algorithms, the objective function is modified in constrained algorithms in such a way that it increases drastically as (one of) the parameter values approaches a constraint. To accomplish this, penalty functions are assigned to each of the constraints. Although many methods exists for unconstrained optimization, they can be categorized into two general classes: direct and indirect search methods.

Direct search methods were the earliest methods used for unconstrained optimization and use only function evaluations in determining the search direction. Indirect search methods, on the other hand, require the use of (numerical or analytic) gradient information [54]. The indirect search methods (or "gradient-based search methods") are generally more efficient when the function to be minimized is continuous in its first derivative. Direct search methods, which are often also referred to as "function comparison methods", are claimed to be more robust for problems that are very non-linear, have a number of discontinuities or where the function values are noisy [181]. In contrast, Gill *et al.* [79] state that "a method using function

comparison should be used only when there is no other suitable alternative method available" (*e.g.* non-smooth objective functions). This statement is confirmed by Bard [7]. Direct methods are, however, popular in practice, since they require the user to supply only function values, not information about the slope of the objective function. However, if a user decides to use a direct method only because of its simplicity, a severe price may be paid in speed and reliability (*i.e.* only a few guarantees can be made concerning convergence) [79].

Indirect methods

The class of indirect optimization methods is dominated by three basic approaches, *viz.* Modified Newton methods, Quasi-Newton methods, and Conjugate-Gradient methods. The distinctions among the three methods arise primarily from the need to use varying levels of information about the derivatives of the objective function in defining the search direction.

The Modified Newton methods use the Hessian matrix (*i.e.* matrix of second partial derivatives with respect to the tunable parameters), or a finite difference approximation of it (in order to avoid analytic differentiation of the objective function) to compute search directions. Quasi-Newton or variable metric methods approximate the Hessian by a matrix which is built up from iteration to iteration (*e.g.* fminu uses either the Broyden-Fletcher-Goldfarb-Shanno (BFGS) or the Davidon-Fletcher-Powell (DFP) update formula). This method can be used when the Hessian matrix is difficult or time-consuming to evaluate [194]. Conjugate-Gradient algorithms are ideally suited for large-scale optimization, since they do not require the storage of a large matrix in generating the direction of search. The interested reader is referred to Gill *et al.* [79] for a full description of the aforementioned methods.

The problem of minimizing a user-specified objective function of several parameters using gradient information can be stated mathematically as follows

$$\min_{\theta} F_{obj}(\theta)$$

where F_{obj} is the objective function and the θ the physical parameter vector ($\theta \in \mathbb{R}^n$, that is $\theta = (\theta_1, \theta_2, \cdots, \theta_n)$ with n the number of tunable parameters).

The necessary condition for minimizing the objective function $F_{obj}(\theta)$ is obtained by setting the derivative of F_{obj} with respect to the parameters to zero, *i.e.*

$$\frac{\partial F_{obj}}{\partial \theta_i} = 0 \qquad i = 1, 2, \cdots, n$$

or

$$\nabla F_{obj} = 0$$

where

$$\nabla F_{obj} = \left[\frac{\partial F_{obj}}{\partial \theta_1}, \frac{\partial F_{obj}}{\partial \theta_2}, \cdots, \frac{\partial F_{obj}}{\partial \theta_n} \right]^T$$

which is known as the gradient vector. The terms associated with second derivatives is given by

$$H = \nabla^2 F_{obj}$$

166

The above equation results in a symmetric matrix called the Hessian matrix of the function. Once the derivative of F_{obj} vanishes at local extrema $(\hat{\theta}_1, \hat{\theta}_2, \cdots, \hat{\theta}_n)$, for F_{obj} to have a relative minimum, the Hessian matrix evaluated at $(\hat{\theta}_1, \hat{\theta}_2, \cdots, \hat{\theta}_n)$ must be a positive definite matrix. This condition requires that all eigenvalues of the Hessian matrix evaluated at $(\hat{\theta}_1, \hat{\theta}_2, \cdots, \hat{\theta}_n)$ be positive.

In summary, the unconstrained minimum of a function is found by setting its partial derivatives (with respect to the tunable parameters) equal to zero and solving for the parameter values. Among the sets of parameter values obtained, those at which the matrix of second partial derivatives of the cost function is positive definite are local minima. If there is a single local minimum, it is also the global minimum; otherwise, the cost function must be evaluated at each of the minima to determine which one is the global minimum.

Direct methods

The three most widely used direct search methods are the Hooke and Jeeves pattern search method [110], the Nelder and Mead Simplex method [199], and Powell's conjugate gradient method [210]. In the sequel we discuss in detail only the most efficient and accurate one: the Nelder-Mead Simplex method (*see* Onwubiko [204] for a comparison).

The Nelder-Mead Simplex method is based on the "Sequential Simplex" method formulated by Spendley, Hext, and Himsworth in 1962 [278]. To understand the Nelder-Mead method, we need to briefly consider the sequential simplex method.

A simplex in $\mathbb{R}^n$ is a set of $n+1$ points $(x_0, x_1, \cdots, x_n)$ which form a polyhedron. In the case of $\mathbb{R}^2$ a simplex is simply a (equilateral) triangle, while in three dimensions it becomes a tetrahedron. At each iteration, to minimize the user-specified objective function, the function values are determined at each of the $n+1$ vertices. After that, the vertex with the highest function value is mirrored (reflected) in the centroid of the other n vertices as illustrated in Fig. 5.1, with the result that a new simplex is created. The objective function is then evaluated at the new vertex, and the process is repeated. Observe that the search direction points away from the vertex having the largest function value.

During the iterations after the first one it might be that the newest vertex still has the largest function value in the new simplex, and reflecting this vertex would cause oscillation. To prevent this, the largest function value other than that at the newest vertex is subsequently used to decide which vertex to reflect. As the optimum is approached, the last vertex will straddle the optimum point or be within a distance of the order of its own size from the optimum. In the latter case, the procedure cannot get closer to the optimum without reducing the simplex size. The simplex size is reduced ("contracted") by replacing the other vertices by new ones half way the last vertex. When the resulting simplex size is smaller than a prescribed tolerance, the iteration is stopped. Thus the optimum parameter vector is determined to within a tolerance influenced by the size of the simplex.

The typical progress of the iteration is illustrated in Fig. 5.2 using a function of two parameters [64]. Vertices 1,2 and 3 form the initial simplex, and increasing
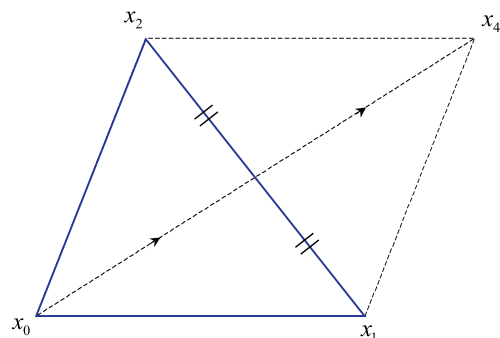
Figure 5.1: *Reflection to a new point in the Simplex method. Vertices x_0 (with largest function value), x_1, and x_2 form the initial simplex. The next point (vertex) is x_4.*

numbers indicate the new vertices added to each iteration. Note that vertex 7 has the largest function value for the simplex (4,6,7) but is not reflected immediately since it is the newest vertex in that simplex. When simplex (6,9,10) is reached, the procedure cannot get closer to the optimum without reducing the simplex size to (6,11,12). The iteration continues again from this simplex until the simplex is smaller than a prescribed tolerance. The interested reader is referred to Buchanan *et al.* [35] and Walters *et al.* [304] for detailed information (including applications) about the Simplex search method.
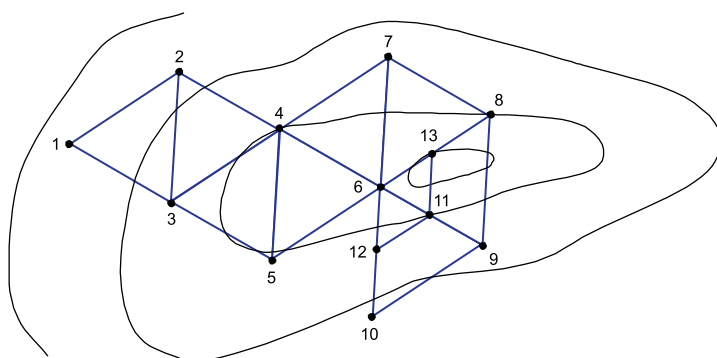

Figure 5.2: *Illustration of the iteration progress of the Simplex method in two parameters (n = 2). Vertices (1,2,3) form the initial simplex. Succeeding new vertices are numbered starting with 4 and continuing to 10 at which a cycle starts to repeat. Consequently the simplex is contracted to the new simplex (6,11,12). After that the procedure is continued.*

The problem with the method thus far is that the use of regular simplices slows down the rate of acceleration of the search. It would be more efficient to allow the simplex to adapt to the local contours of the objective function [181]. Because of this, Nelder and Mead introduced the use of nonregular simplices. However, it is known that the Nelder-Mead method frequently fails to converge to a local minimum. Furthermore, this method is slow and can be applied only to problems in which n is small [194]. In spite of this, it is enormously popular in practice. The main reasons are twofold. First, it typically produces significant improvement in the first few iterations. Second, the Nelder-Mead method uses a small number of function evaluations per iteration. The interested reader is referred to Lagarias *et al.* [148] were convergence properties of this method are discussed.

5.3.2 Constrained optimization

The constrained optimization problem differs from the unconstrained minimization problem in that at least one of the variables is subject to a restriction on its value. The general constrained optimization problem can be defined as to minimize a non-linear function subjected to non-linear constraints. This situation is encountered often in engineering practice because design problems are typically constrained by several factors (*e.g.* prior information concerning a parameter value limits the domain within the estimate is to be found). The introduction of constraints, however, may create difficulties with regard to obtaining solutions.

The simplest approach to constrained optimization is to transform a constrained problem into a single function by adding the constraints to the objective function and use one of the aforementioned direct search methods [204]. This approach is convenient because the direct search methods do not require the determination of the derivatives of the objective function or constraints. Consequently, this approach is generally applicable because it can be used for functions whose differentiation is difficult and even for functions whose derivatives are discontinuous. In spite of these advantages, direct search methods are often criticized because they are not rooted in any mathematical basis. Criticism not withstanding, direct search methods are often more practical because of the previously stated reasons.

The main indirect search methods that have been proposed for solving constrained optimization problems are reduced-gradient methods, sequential linear and quadratic programming methods, and exact penalty functions [194].

The interested reader is referred to the books of Fletcher [64] and Gill *et al.* [79] for a detailed treatment of constrained optimization theory.

5.3.3 Selecting a method

Based on an investigation of the main properties of both the unconstrained and constrained optimization methods, the most suitable method for updating the physical parameters of a structural wind turbine model must be selected. The first step is to investigate the smoothness of the objective function. After all, most algorithms exclude all problems for which the objective function is not smooth. This arises when finding best solutions to over-determined systems ($m > n$, where m number

of data points and n number of tunable variables) as in data fitting applications. In general, non-smooth (*i.e.* non-differentiable) objective functions are more difficult to minimize than smooth (*i.e.* at least twice continuously differentiable) objective functions.

The general rule in selecting a method for optimization of smooth objective functions is to make use of as much of derivative information as possible [79]. In our situation it is impossible to analytically determine the gradient vector of F_{obj}, since the function is the result of a simulation. Consequently, either the values of the derivatives are to be approximated by a finite difference method or a direct method must be used. Finite difference methods use the first term of the Taylor series expansion to compute the gradient vector.

Non-smooth problems are generally solved by direct methods, since indirect optimization routines assume that the objective function has continuous first and second derivatives. However, if the objective function has just a "few" discontinuities in its first derivative, and these discontinuities do not occur in the neighbourhood of the solution, methods designed for smooth problems are likely to be more efficient [79].

It is decided to use a time-domain model parameter updating technique. Fig. 5.3 shows a schematic of the implemented model parameter updating procedure. Measured input (force) and output (accelerations) data of a modal test are used as reference. The optimization performs successive simulations on a DAWIDUM model and changes the tunable parameters in an attempt to minimize the error between the measured (y_{meas}) and the simulated (y_{sim}) response (*i.e.* output error). That is, the parameters are determined in such a way that the objective function

$$F_{obj}(\theta) = \sum_{t=0}^{T} \| \underbrace{y_{meas}(t, \theta_0) - y_{sim}(t, \theta)}_{e_{oe}} \|^{2}$$

is minimal. $\| \cdot \|$ denotes the Euclidian norm and θ the physical parameter vector ($\theta \in \mathbb{R}^n$ with n the number of tunable parameters). Note that for the situation that the system is present in the model set and assuming noise-free data, the output error will be zero for the true parameter values (*i.e.* $F_{obj}(\theta_0) = 0$).

The procedure uses either the Nelder-Mead simplex method or a combined Gauss-Newton and modified Newton algorithm. Both algorithms require function values only. Both objective functions are defined in a MATLAB® M-file (ObjFun.m and lsfun1.m respectively). The optimization routine (either fmins [91] or e04fdf [197]) is invoked in NMstart.m/LSstart.m. Examples of these files can be found in Molenaar [191].

In the sequel it is assumed that the mass, inertia and length of the rigid bodies within the superelements are estimated fairly accurately at the design stage, but that calculation of the stiffness and damping parameters may be difficult. Consequently, the tunable parameters are the torsional spring and damper constants. When the uncertainties in mass, inertia or length can not be neglected, however, SD/FAST® offers the possibility of leaving systems parameters unspecified in the System Description file (using a "?" instead of a number). In addition, a default numerical value can be specified immediately before the question mark. For example, the en-
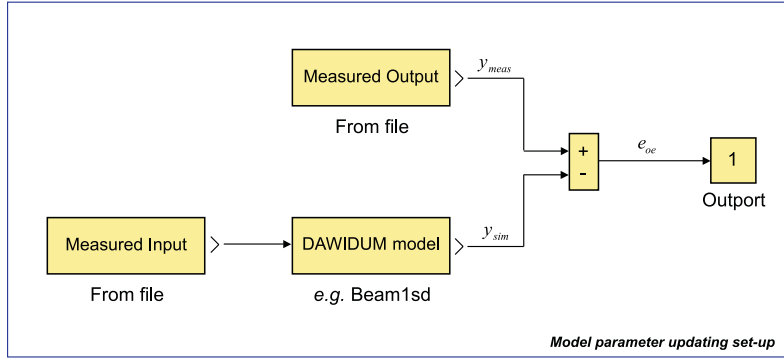
Figure 5.3: *Schematic of the time domain model parameter updating procedure, with y_{meas} the measured output, y_{sim} the simulated output and e_{oe} the output error.*

try: `mass = 500?` indicates that the initial mass is equal to 500 kg. but that its value can be changed at run time. Thus mass properties and system geometry can also be treated as variable.

5.4 Verification using simulated data

In this section the identifiability of the model class $\mathcal{M}_m^{wt}$ will be checked using simulation. Furthermore, the proposed parameter optimization procedure will be verified using simulated data before applying it to real data. The optimization performs successive simulations on different models from the DAWIDUM mechanical module library and changes the tunable parameters in an attempt to minimize the error between "measured" and simulated response.

In this way the most suitable optimization method for updating the physical parameters of a structural wind turbine model can be selected in a systematic way. Two cases are considered. In the first subsection the one superelement approximation of an Euler-Bernoulli beam is used to generate the "measured" data. In the second subsection the mechanical model SDLW1 has been used to generate the "measured" data. This section concludes with a discussion.

5.4.1 Beam1sd

In this subsection the one superelement approximation of an Euler-Bernoulli beam is used to generate the "measured" data. This model is referred to as Beam1sd and is depicted in Fig. 5.4. The Euler-Bernoulli beam considered has length $L = 50$ m, modulus of elasticity $E = 21 \cdot 10^{10}$ N/m^2, area of beam cross-section (circular) $A = \pi$ m^2, mass density $\rho = 7850$ kg/m^3, and area moment of inertia $I = \frac{1}{4}\pi$ m^4. The beam is built in at the base.
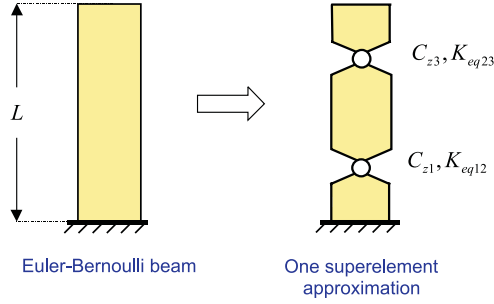
Figure 5.4: *One superelement approximation of an Euler-Bernoulli beam.*

The torsional spring constants for the superelement can be derived directly from the data mentioned above using the automated structural modeling procedure outlined in Section 3.4. The resulting constants are

$$
\begin{aligned}
C_{z1} &= 6.5973 \cdot 10^9 \qquad [\text{Nm/rad}] \\
C_{z3} &= 6.5973 \cdot 10^9 \qquad [\text{Nm/rad}]
\end{aligned}
$$

Viscous damping, sufficient to produce a damping ratio of 1%, has been added to the model by specifying the following coefficients of viscous damping

$$
\begin{aligned}
K_{eq12} &= 3.70 \cdot 10^7 \qquad [\text{kg/s}] \\
K_{eq23} &= 3.25 \cdot 10^6 \qquad [\text{kg/s}]
\end{aligned}
$$

It is assumed that the mass, inertia and length of the rigid bodies within the superelement are estimated fairly accurately, but that calculation of the stiffness and damping parameters may be difficult. Consequently, C_{z1}, K_{eq12}, C_{z3}, and K_{eq23} are the tunable parameters. The aforementioned values of the spring and damper constants form the real parameter vector θ_0. Thus in this case

$$
\theta = \begin{bmatrix} C_{z1} & K_{eq12} & C_{z3} & K_{eq23} \end{bmatrix}^T
$$

and consequently

$$
\theta_0 = \begin{bmatrix} 6.5973 \cdot 10^9 & 3.70 \cdot 10^7 & 6.5973 \cdot 10^9 & 3.25 \cdot 10^6 \end{bmatrix}^T
$$

The input is a stepwise change in the force at the beam top (step time 0 s, initial value of zero and final value of 80000 N) producing a maximum deflection of 0.04 m. The output is the acceleration of the beam top. Time histories of 301 points are generated using the Runge-Kutta fourth order (RK-45) method to numerically integrate the differential equations with a fixed step size of 0.05 s. The step size is selected such that at there are least three points within the smallest oscillation period. Furthermore, it has been checked that halving the step size has no effect on the results.

The objective function is defined as the sum of squares of the difference between the measured and simulated output. The objective is depicted in Fig. 5.5 as a function of the percentage of variation in the parameter vector θ (*i.e.* $100\% = \theta_0$, and 110% means that the numerical values of all four tunable parameters are set to 110% of their real values). Observe the two local minima around 75% and 125% of the real parameter vector.
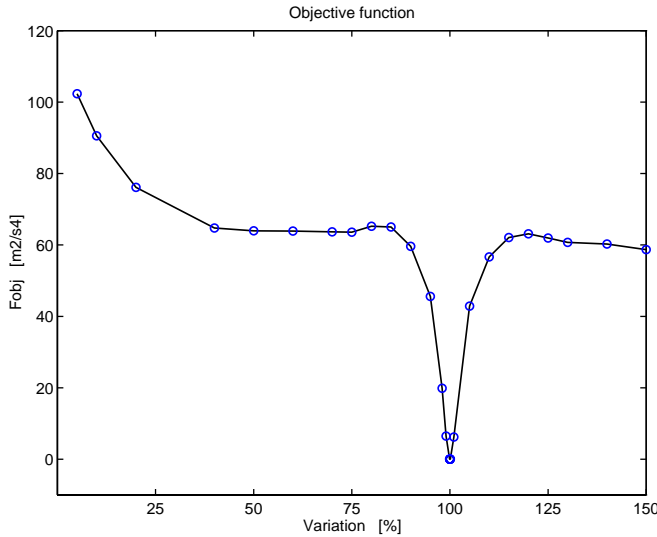

Figure 5.5: *Objective function F_{obj} of **Beam1sd** with ∘ calculated values.*

It is now interesting to determine which parameter variations around the real values of C_{z1}, K_{eq12}, C_{z3}, and K_{eq23} can be allowed such that the estimated parameter vector $\hat{\theta}$ still converges to the real parameter vector θ_0. That is, determine

$$max\{\Delta\theta_0\} \quad s.t. \quad \hat{\theta} \to \theta_0$$

Two noise-free cases and one where a white-noise signal has been added to represent measurement noise are considered in the sequel. The first and third case use the Nelder-Mead simplex method implemented by the fmins function in the Optimization Toolbox of MATLAB®. The second uses a combined Gauss-Newton and modified Newton algorithm to minimize the unconstrained sum of squares. The algorithm is the so-called e04fdf routine from the Numerical Algorithms Group (NAG) Toolbox [197]. Both algorithms use function values only.

Case 1: Nelder-Mead (noise-free)

Table 5.1 summarizes the obtained results of the noise-free simulations performed on the DAWIDUM model Beam1sd using the Nelder-Mead simplex method. The first

column indicates the run number. The second till the fifth column specify the initial values of the tunable parameters. For example, $C_{z1} = 135\,\%$ means that the initial value of the torsional spring constant between the first and the second rigid body is set to $135\,\%$ of the real value (*i.e.* $6.5973 \cdot 10^9$). The sixth column shows the number of iterations it took to converge to a local or to the global minimum. Notice that in this simulation example it is possible to make a distinction between a local and the global minimum since the real parameter vector is known.

Run	Noise-free simulations: "Beam1sd"					
	ΔC_{z1}	ΔK_{eq12}	ΔC_{z3}	ΔK_{eq23}	N_{iter}	Minimum
NM 0	65 %	65 %	65 %	65 %	1691	local
NM 1	70 %	70 %	70 %	70 %	1314	global
NM 2	90 %	90 %	90 %	90 %	699	global
NM 3	100 %	100 %	100 %	100 %	257	global
NM 4	110 %	110 %	110 %	110 %	701	global
NM 5	125 %	125 %	125 %	125 %	789	global
NM 6	135 %	135 %	135 %	135 %	611	global
NM 7	140 %	140 %	140 %	140 %	> 3700	local
NM 8	135 %	65 %	65 %	135 %	1113	global

Table 5.1: *Model updating results for* **Beam1sd**. *Case 1: Nelder-Mead (noise-free).*

As expected, the optimization takes many iterations to converge. To illustrate, Fig. 5.6 shows the convergence of the parameters for run **NM 6**. Observe that the number of iterations increases as the initial values of the tunable parameters are further away from the real values. Moreover, when the initial values of the tunable parameters differ more than $-30\,\%$ or more than $+35\,\%$ of their real values, the method fails to converge. Consequently, good *a priori* parameters are essential for the error between measured and simulated response to vanish.

Case 2: Least-squares (noise-free)

Table 5.2 summarizes the obtained results of the noise-free simulations performed on the DAWIDUM model **Beam1sd** using a least-squares method. The first column indicates the run number. The second till the fifth column specify the initial values of the tunable parameters. For example, $C_{z1} = 135\,\%$ means that the initial value of the torsional spring constant between the first and the second rigid body is set to $135\,\%$ of the real value (*i.e.* $6.5973 \cdot 10^9$). The sixth column shows the number of iterations it took to converge to to a local or to the global minimum. Again it is possible to make a distinction between a local and the global minimum since the real parameter vector is known.

It can be concluded that in this case the least-squares method greatly reduces the number of iterations. Consequently, the amount of time it takes to perform an optimization is decreased, since the majority of the optimization time is spent conducting simulations. Furthermore, the region of convergence is increased from $-30\,\% \leq \Delta\theta_0 \leq +35\,\%$ to $-40\,\% \leq \Delta\theta_0 \leq +45\,\%$.
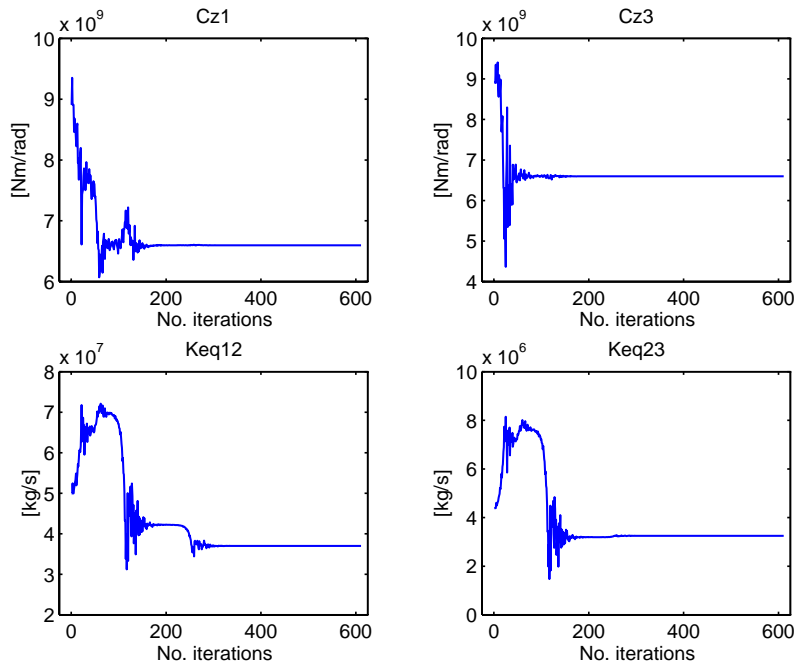
Figure 5.6: *Convergence of the parameters for* **run NM 6** *(noise-free simulations performed on* **Beam1sd** *using Nelder-Mead simplex method; initial values of the tunable parameters:* $C_{z1} = C_{z3} = 8.9064 \cdot 10^9$, $K_{eq12} = 4.995 \cdot 10^7$, *and* $K_{eq23} = 4.3875 \cdot 10^6$*).*

Run	Noise-free simulations: "Beam1sd"					
	ΔC_{z1}	ΔK_{eq12}	ΔC_{z3}	ΔK_{eq23}	N_{iter}	Minimum
LS 0	55 %	55 %	55 %	55 %	62	local
LS 1	60 %	60 %	60 %	60 %	195	global
LS 2	75 %	75 %	75 %	75 %	165	global
LS 3	90 %	90 %	90 %	90 %	106	global
LS 4	100 %	100 %	100 %	100 %	37	global
LS 5	110 %	110 %	110 %	110 %	128	global
LS 6	125 %	125 %	125 %	125 %	95	global
LS 7	145 %	145 %	145 %	145 %	186	global
LS 8	150 %	150 %	150 %	150 %	99	local
LS 9	135 %	65 %	65 %	135 %	122	global

Table 5.2: *Model updating results for* **Beam1sd**. *Case 2: least-squares (noise-free).*

Case 3: Nelder-Mead (additive noise)

In practice, the measured input and output signals are contaminated with noise. To make the simulation more realistic, a white-noise signal has been added to the "measured" output to represent measurement noise. The variance of the normally distributed noise was varied to analyse the effect of the signal-to-noise ratio on the optimization. Table 5.3 summarizes the obtained results for the various signal-to-noise ratios. The first column indicates the run number. The second column shows the signal-to-noise ratio. The signal-to-noise ratio is defined as follows:

$$\text{S/N-ratio} = 20 \log_{10} \left(\frac{\text{std(noise-free output)}}{\text{std(noise)}} \right) \qquad [\text{dB}]$$

The third till the sixth column show the deviation of the four parameters from their real values after optimization. The deviation is defined as

$$\Delta = \frac{\text{real parameter - optimized parameter}}{\text{real parameter}} \qquad [\%]$$

The seventh column shows the number of iterations it took to converge to a local or to the global minimum. Finally, the eighth column displays the final value of the objective function F_{obj}.

Run	Additive noise simulations: "Beam1sd"						
	S/N-ratio [dB]	ΔC_{z1} [%]	ΔK_{eq12} [%]	ΔC_{z3} [%]	ΔK_{eq23} [%]	N_{iter} [-]	F_{obj} [-]
1	∞	0.00	0.00	0.00	0.00	293	$8.54 \cdot 10^{-28}$
2	50.1	0.00	-0.01	0.00	0.01	663	$3.183 \cdot 10^{-4}$
3	30.1	-0.01	-0.14	0.00	0.08	554	$3.183 \cdot 10^{-2}$
4	10.1	-0.06	-1.43	0.04	0.75	586	3.183
5	-3.87	-0.29	-6.73	0.20	2.68	665	79.585
6	-9.89	-0.52	-12.59	0.39	2.38	587	318.39

Table 5.3: *Model updating results for Beam1sd. Case 3: Nelder-Mead (additive noise).*

It can be concluded that noise causes the optimization to converge more slowly (compare run 1 with run 2-6), or even fails to converge to the real values. Especially the damping parameters K_{eq12} and K_{eq23} are hard to estimate from noise contaminated data. The deviations from the real values are acceptable up to a signal-to-noise ratio of 30 dB.

The previous three cases have shown the ability of the proposed model parameter updating procedure to reproduce the known parameter values from simulated data. This observation gives confidence in its application to data generated by more complex models.

As a next step in the verification of the model parameter updating procedure, the mechanical model SDLW1 describing the structural dynamics of the complete

Lagerwey LW-50/750 wind turbine is used to generate the "measured" data. In addition, the results will be used to determine the required magnitude of input force and the excitation/observation point(s) on the Lagerwey LW-50/750 wind turbine that would excite all modes of interest and result in adequate response levels.

5.4.2 SDLW1

In this subsection the mechanical model SDLW1 is used to generate "measured" data. This 18-DOF model (exclusive pitch and azimuth) describes the structural dynamics of the complete Lagerwey LW-50/750 wind turbine. Both the tower and rotor blades are approximated by one superelement. A schematic of this module is depicted in Fig. 5.7. Additional information can be found in Appendix I.2.3.
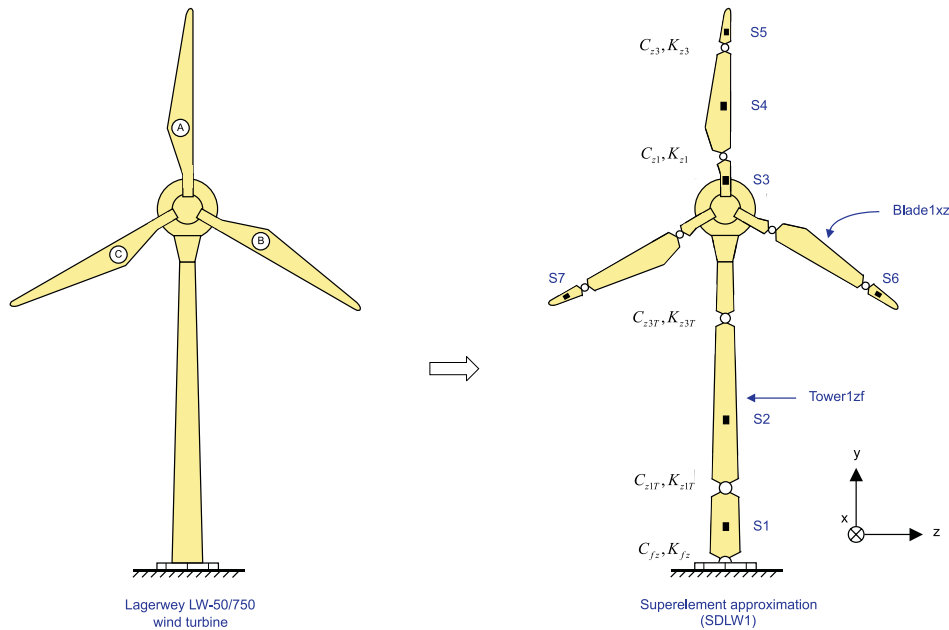

Figure 5.7: *Superelement approximation of the Lagerwey LW-50/750 wind turbine. Both the tower and rotor blades are approximated by one superelement (Tower1zf and Blade1xz respectively). The flexibility of the foundation is approximated by a torsional spring. Sensor locations S1 to S7 are marked with a* ■ *.*

Again it is assumed that the mass, inertia and length of the rigid bodies within the superelements are estimated fairly accurately, but that calculation of the stiffness and damping parameters may be difficult. Consequently, C_{fz}, K_{fz} (foundation spring and damper), C_{z1T}, K_{z1T}, C_{z3T}, K_{z3T} (tower springs and dampers), C_{z1}, K_{z1}, C_{z3}, K_{z3} (rotor blade springs and dampers) are the tunable parameters.

The input is a stepwise change in the force at the tower top in positive x-direction (step time 0 s, initial value of 40000 and final value of 0 N) producing an initial tower top deflection of 0.0405 m. To ensure that the simulation starts in steady-state, the equilibrium point has been determined using the SIMULINK$^{\circledR}$ function trim and the resulting state vector has been saved in a MAT-file. This state vector is used as initial condition in the performed simulations. The outputs are the accelerations measured at 7 locations on the structure (marked with a ■ in Fig. 5.7).

The objective function is defined as the sum of squares of the difference between the measured and simulated outputs. Because the measured accelerations have strongly different orders of magnitude, they are scaled to ensure that no information contained in the signals will be lost. Time histories of 1001 points are generated and the stiff solver Linsim is used to numerically integrate the differential equations with a fixed step size of 0.01 s.

It is assumed that flexibility of the foundation can be approximated by a torsional spring. The spring constant is experimentally determined by Jacobs [116] and is equal to

$$C_{fz} \quad = \quad 1.94000 \cdot 10^{10} \quad \text{[Nm/rad]}$$

Both the tower and the rotor blades of the Lagerwey LW-50/750 wind turbine are approximated by one superelement. The torsional spring constants for the superelements can be derived directly from the physical data supplied by the manufacturer using the automated structural modeling procedure outlined in Section 3.4. The resulting tower torsional spring constants are

$$
\begin{aligned}
C_{z1T} &= 1.72901 \cdot 10^9 && \text{[Nm/rad]} \\
C_{z3T} &= 6.95511 \cdot 10^8 && \text{[Nm/rad]}
\end{aligned}
$$

and the rotor blade torsional spring constants are

$$
\begin{aligned}
C_{z1} &= 1.75912 \cdot 10^7 && \text{[Nm/rad]} \\
C_{z3} &= 1.19998 \cdot 10^6 && \text{[Nm/rad]}
\end{aligned}
$$

Viscous damping, sufficient to produce a damping ratio of about 1 %, has been added to the model by specifying the following coefficients of viscous damping

$$
\begin{aligned}
K_{fz} &= 5 \cdot 10^7 && \text{[kg/s]} \\
K_{z1T} &= 1 \cdot 10^7 && \text{[kg/s]} \\
K_{z3T} &= 1 \cdot 10^6 && \text{[kg/s]} \\
K_{z1} &= 9 \cdot 10^3 && \text{[kg/s]} \\
K_{z3} &= 1 \cdot 10^3 && \text{[kg/s]}
\end{aligned}
$$

The above mentioned constants are used to generate the "measured" response. In the sequel, these constants will be referred to as "real values". The objective is depicted in Fig. 5.8 as a function of the percentage of variation in the parameter vector θ (*i.e.* 100 % = θ_0, and 110 % means that the numerical values of all ten tunable

parameters are set to 110 % of their real values). Obviously, both the Nelder-Mead method and the least-squares method should be able to locate the global minimum without much difficulty.
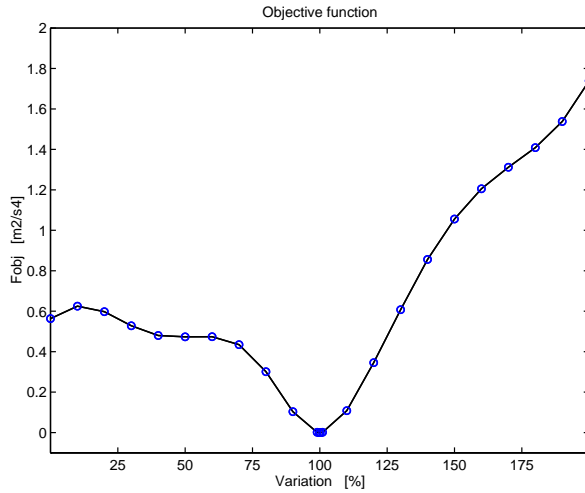

Figure 5.8: *Objective function F_{obj} of SDLW1 with ○ calculated values.*

The optimization is started by invoking NMstart.m which sets the initial values of the tunable parameters a certain percentage of their real values and subsequently performs successive simulations on SDLW1. The Nelder-Mead algorithm changes the tunable parameters in an attempt to minimize the error between "measured" and simulated response. In this case, the optimization time can be reduced from 10 to 1 second by multiplying the objective function by the time vector t. The explanation is as follows: because t is small in the early stages of the response, it weights early errors less heavily than late errors allowing a reduction of the simulation time.

The numerical results are given in Table 5.4. The first column indicates the run number. The second till the sixth column specify the initial values of the tunable parameters. For example, $C_{z1T} = 110\%$ means that the initial value of the torsional spring constant between the first and the second rigid body of the tower is set to 110 % of the real value (*i.e.* $1.72901 \cdot 10^9$). The seventh column shows the number of iterations it took to converge to a local or to the global minimum. It can be concluded that the torsional spring and damper constants can be identified uniquely using perfect data provided that the initial guess is sufficiently close to the real values.

The region of convergence can be increased substantially by first applying the aforementioned least-squares method and subsequently finetuning the results by using the Nelder-Mead direct search method. The results of this case are summarized in Table 5.5.

Run	Noise-free simulations: "SDLW1"						
	C_{fz},K_{fz}	C_{z1T},K_{z1T}	C_{z3T},K_{z3T}	C_{z1},K_{z1}	C_{z3},K_{z3}	N_{iter}	Minimum
NM 0	60 %	60 %	60 %	60 %	60 %	7199	local
NM 1	65 %	65 %	65 %	65 %	65 %	6795	global
NM 2	80 %	80 %	80 %	80 %	80 %	6301	global
NM 3	90 %	90 %	90 %	90 %	90 %	3297	global
NM 4	100 %	100 %	100 %	100 %	100 %	579	global
NM 5	110 %	110 %	110 %	110 %	110 %	3259	global
NM 6	120 %	120 %	120 %	120 %	120 %	3368	global
NM 7	125 %	125 %	125 %	125 %	125 %	4026	local
NM 8	120 %	80 %	120 %	80 %	120 %	3683	global

Table 5.4: *Model updating results for **SDLW1**. Case 1: Nelder-Mead (noise-free)*

Run	Noise-free simulations: "SDLW1"						
	C_{fz},K_{fz}	C_{z1T},K_{z1T}	C_{z3T},K_{z3T}	C_{z1},K_{z1}	C_{z3},K_{z3}	N_{iter}	Minimum
LS-NM 0	15 %	185 %	15 %	185 %	15 %	2681	local
LS-NM 1	20 %	180 %	20 %	180 %	20 %	4333	global
LS-NM 2	25 %	25 %	25 %	25 %	25 %	6445	local
LS-NM 3	30 %	30 %	30 %	30 %	30 %	2592	global
LS-NM 4	40 %	40 %	40 %	40 %	40 %	3544	global
LS 5	60 %	60 %	60 %	60 %	60 %	4038	global
LS-NM 6	80 %	80 %	80 %	80 %	80 %	1520	global
LS 7	100 %	100 %	100 %	100 %	100 %	236	global
LS-NM 8	120 %	120 %	120 %	120 %	120 %	2883	global
LS-NM 9	140 %	140 %	140 %	140 %	140 %	3527	global
LS-NM 10	145 %	145 %	145 %	145 %	145 %	3110	local
LS 11	125 %	75 %	125 %	75 %	125 %	1985	global
LS-NM 12	130 %	70 %	130 %	70 %	130 %	3680	local

Table 5.5: *Model updating results for **SDLW1**. Case 2: least-squares and Nelder-Mead (noise-free).*

The ability of the presented off-line model parameter updating procedure to reproduce the known parameter values gives confidence for its application to field data obtained from a modal test.

5.5   Discussion

The purpose of this section is to briefly revisit the obtained results. In this chapter an off-line, time-domain model parameter updating procedure is presented for the identification of wind turbine stiffness and damping parameters under the assumption that the model structure is known *a priori*. The procedure tries to produce an

updated model which replicates the simulated time-domain data exactly. The procedure uses either the Nelder-Mead simplex method or a combined Gauss-Newton and modified Newton algorithm. Both algorithms require function values only (*i.e.* no numerical or analytic gradient information required). This implies that they are well suited for optimizing objective functions that are noisy or are discontinuous at the solution.

The parameter optimization procedure has been verified using simulated data. The optimization performs successive simulations on a model from DAWIDUM's mechanical module library and changes the tunable parameters in an attempt to minimize the error between "measured" and simulated response. Two cases were considered: 1) the one superelement approximation of an Euler-Bernoulli beam has been used to generate the "measured" data, and 2) the mechanical model SDLW1 has been used to generate the "measured" data. In both cases global optimization can be achieved provided that the initial guess is close enough to the real parameter values. Otherwise, a local minimum will be found.

Having established a validated mathematical model of a flexible wind turbine that provides a base for better overall design and control synthesis, we proceed with developing a tool to design a control strategy that reduces the price of the produced electrical energy.

Part III:

Model based control design

Chapter 6

Frequency converter controller design

In the introduction it is stated that to reach economic viability, the design and operation of the complete wind turbine has to be optimized with respect to both cost and performance. Reduction of fatigue loads can significantly contribute to achieve this goal. The bandwidth of the active-pitch system, however, is in general too small to be able to achieve fatigue load reduction. As a result, pitch control should be used to follow minute-to-minute fluctuations in aerodynamic power, while the electromechanical torque control will focus on fatigue load reduction.

Obviously, fatigue load reduction requires almost instantaneous torque control which can only be achieved with a high bandwidth frequency converter controller. In this chapter such a controller will be developed for electromechanical torque control of the direct-drive synchronous generator of the Lagerwey LW-50/750 wind turbine. Section 6.1 motivates the need for an improved frequency converter controller. In Section 6.3 a possible controller configuration is presented after listing the main controller objectives in Section 6.2. A new rectifier frequency converter controller will be designed on the basis of an identified model of the electromagnetic part of the Lagerwey LW-50/750 synchronous generator in Section 6.4. Finally, the conclusions are presented in Section 6.5.

6.1   Introduction

Modern vector control techniques enable the torque of alternating current (AC) generators to be controlled with a rapid dynamic response. Unfortunately, investigation has shown that the bandwidth of the frequency converter controller implemented in the Lagerwey LW-50/750 wind turbine is too small to utilize the potential benefits of model based control. Consequently, we have decided to develop a new frequency converter controller for the direct-drive synchronous generator of the Lagerwey LW-50/750 wind turbine.

The frequency converter of the Lagerwey LW-50/750 wind turbine consists of a rectifier, DC bus with a smoothing capacitor, and an inverter as illustrated in Fig. 6.1. The frequency converter is located at the tower base. The DC bus capacitor is used to make the DC input appear as a DC voltage source with a very small internal impedance at the switching frequency. The rectifier and inverter are connected back-to-back via the DC bus. The rectifier converts the three-phase alternating currents to 1100 V DC by connecting each of the three stator phases to the positive or negative side of the DC link voltage. The inverter in turn converts the DC to 690 V AC 50 Hz of the utility grid. Because all power is rectified to DC and then inverted to AC the generator is decoupled from the utility grid allowing variable speed operation.

Both the inverter and rectifier are composed of six power semiconductor devices or power switches. Each switch consists of an insulated gate bipolar transistor (IGBT) with a reverse diode in antiparallel. The antiparallel diodes provide paths for the current independent of the switching state of the IGBT's.
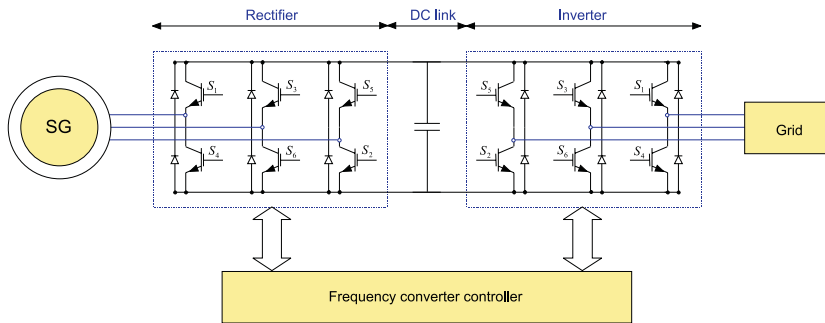

Figure 6.1: *Schematic of back-to-back converter, with SG: synchronous generator, and S_i: switch i.*

The frequency converter controller in Fig. 6.1 actually consists of two controllers, *viz.* a rectifier controller and an inverter controller. The rectifier controller forces the electromechanical torque to equal the torque set-point specified by the wind turbine controller. The power quality requirements (*e.g.* power factor) are controlled by the inverter (the power factor is often set to unity to obtain zero reactive power). Both goals can be achieved independently of each other by the capacitor decoupling between the rectifier and inverter.

6.2   Frequency converter controller objectives

Before we can design a new frequency converter controller we first need to specify the controller objectives for both the rectifier and inverter controller. The rectifier controller objectives can be summarized as:

- Controllable electromechanical torque with a closed-loop bandwidth of at least 200 Hz;

- Minimize total losses (*i.e.* stator copper losses, iron losses, converter losses, rotor copper losses, switching losses, and cable losses);

- Reduce the effect of disturbances (including model uncertainties) on the controlled torque output of the system.

The main inverter controller objective is to match to grid operator requirements (including power quality issues as: controllable power factor (active/reactive power) and low harmonic disturbances). In the next section a possible controller configuration is presented.

6.3 Frequency converter controller configuration

The input to both the rectifier and inverter will be assumed to be a DC voltage source, as was already assumed in Section 6.1. Such rectifiers and inverters are in literature referred to as voltage-source converters (VSC). The VSC makes it possible to connect each of the three generator phases to the positive or negative side of the DC link voltage U_{dc}. Although the shown VSC consists of six IGBT's with $2^6 = 64$ different switching states, it is important to realize that the VSC must be operated so that none of its phases is short-circuiting the link voltage U_{dc} [159]. Hence only one of the two switches in each phase can be conductive (*e.g.* when S_1 is turned on, S_4 must be turned off).

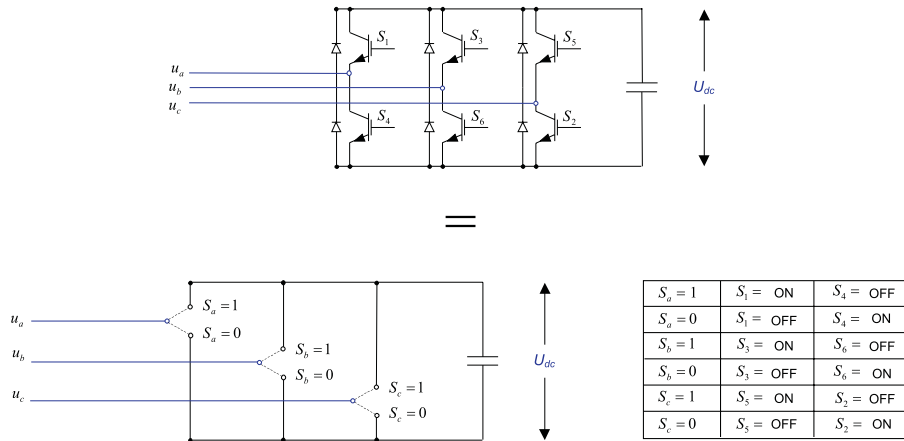| $S_a = 1$	$S_1 =$ ON	$S_4 =$ OFF
$S_a = 0$	$S_1 =$ OFF	$S_4 =$ ON
$S_b = 1$	$S_3 =$ ON	$S_6 =$ OFF
$S_b = 0$	$S_3 =$ OFF	$S_6 =$ ON
$S_c = 1$	$S_5 =$ ON	$S_2 =$ OFF
$S_c = 0$	$S_5 =$ OFF	$S_2 =$ ON

Figure 6.2: *Schematic of a VSC consisting of six IGBT's and its 2-way switch representation with the appropriate switch positions.*

It is common practice to represent each stator phase as an ideal 2-way switch as shown in Fig. 6.2. This implies that there are $2^3 = 8$ different switching states

possible. Six of these states yield active vectors (*i.e.* $[S_a\ S_b\ S_c] = [1\,0\,0]$, $[1\,1\,0]$, $[0\,1\,0]$, $[0\,1\,1]$, $[0\,0\,1]$, and $[1\,0\,1]$) for the terminal stator voltages, and two states yield zero vectors (*i.e.* $[1\,1\,1]$, and $[0\,0\,0]$). In the latter two cases the generator is short-circuited because each of the three-phases is connected to either the positive ($[S_a\ S_b\ S_c] = [1\,1\,1]$) or negative ($[S_a\ S_b\ S_c] = [0\,0\,0]$) side of the DC link.

The required switching states can be determined in various ways using either the measured three-phase stator currents or the measured three-phase stator voltages. When the current is used to determine the state of the switches, the VSC is referred to as a current-controlled VSC, otherwise as a voltage controlled VSC. The current-controlled VSC, however, is preferred to the voltage-controlled VSC [26]. The main reason for the selection of the current as the controlled variable is the same as for the DC machine: the stator dynamics (stator resistance, stator inductance, and induced stator voltages or EMF) are eliminated. Consequently, the complexity of the controller can be significantly reduced.

There are two ways of implementing current controllers: as AC or as DC current controllers. From a control perspective, DC current controllers are preferred since the steady-state currents represented in the rotating dq reference frame are DC currents [19]. This implies that any current controller with integral action (*e.g.* a PI-controller) will result in zero steady-state error.

Current controllers for AC machines are, however, more complex than for DC machines because an AC current controller must control both the amplitude and phase of the three-phase stator currents.

6.3.1 Rectifier controller

A possible rectifier controller configuration that meets the objectives listed in the previous section is shown in Fig. 6.3. Three main parts can be distinguished:

- **Part 1:** Frequency converter controller

- **Part 2:** Voltage-source converter (VSC)

- **Part 3:** Synchronous generator

The synchronous generator is controlled along the dq model in rotor coordinates which corresponds to DC for steady-state. The reference dq currents are transformed into stator coordinates using Park's transformation to be then realized by the vector modulator in the VSC (in rectifier mode). It is assumed that both torque and mechanical speed set-points are calculated by the wind turbine controller such that the cost price of electricity generated by the wind turbine is minimal. It should be stressed that all variables used for the control of the synchronous generator are lower-bounded and/or upper-bounded by physical constraints. For example, the currents are limited to the maximum value that the power electronic components can hold to avoid overheating, and the mechanical speed ω_m is limited by the mechanical constraints. The aforementioned parts will be treated in detail in the next three subsubsections.
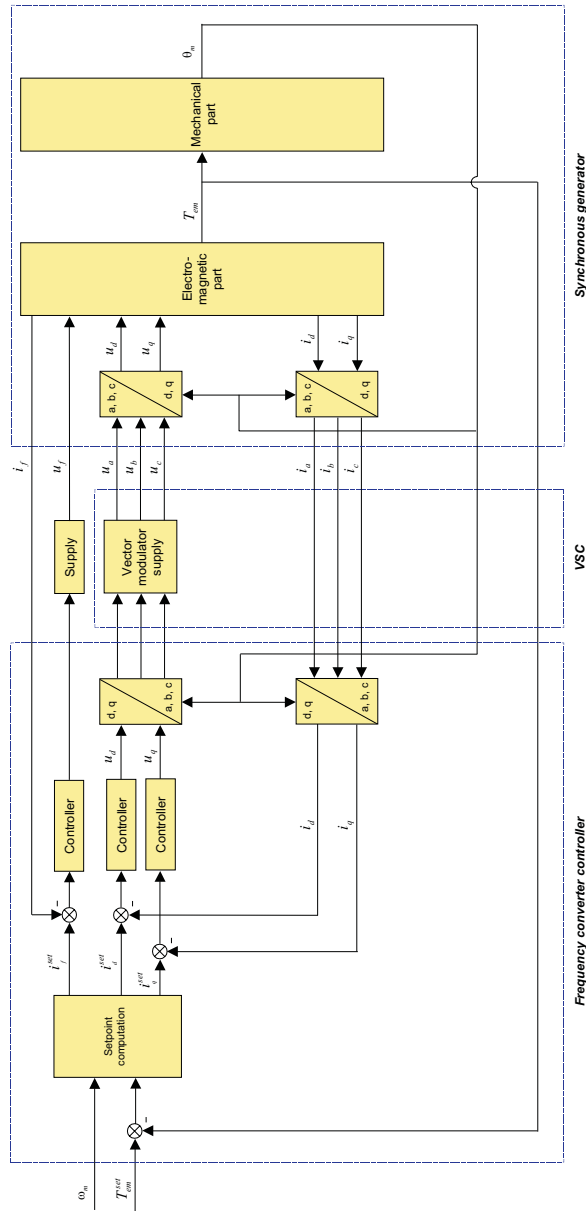
Figure 6.3: *Control of direct-drive synchronous generator of the Lagerwey LW-50/750 wind turbine in rotating dq-reference frame, with VSC: voltage source converter (in rectifier mode).*

Part 1: Frequency converter controller

The frequency converter controller calculates the desired three-phase voltages that must be delivered by the power converter to the generator terminals. The mechanical speed ω_m and the torque set-point T_{em}^{set} specified by the wind turbine controller are the inputs to the frequency converter controller. Comparison of set-point of the electromechanical torque and its actual value T_{em} gives an error which serves as input to the Set-point computation block. The outputs of this block are the reference values of the field current i_f^{set}, the direct-axis stator current i_d^{set}, and the quadrature-axis stator current i_q^{set}.

The reference value of the field current and its actual value are compared, and their difference serves as input to the field current controller (*e.g.* a PI controller). The output of the field current controller is used to supply a field winding voltage u_f to the rotor terminals of the synchronous generator. Similarly, the direct-axis and quadrature-axis stator current set-points are compared with their actual values and the differences are fed to current controllers. The voltage outputs (in the synchronously rotating reference frame) of these controllers, on the other hand, are first transformed into the stator reference frame by application of the Park transformation. The abc/dq block contains the power-invariant Park transformation (Eq. (3.82)), while the dq/abc block contains the its inverse.

In the block diagram of Fig. 6.3, it is assumed that the stator currents i_a, i_b, and i_c are measured. Notice that, when the generator is star connected, only two stator current measurements are necessary to compute both i_d and i_q [220]. After all, in that specific case one of the currents is redundant because, due to the isolated neutral,

$$i_a + i_b + i_c = 0$$

is valid at any instant. Furthermore, exact knowledge of the mechanical rotor angle θ is needed to transform the AC quantities in the stator reference frame to DC quantities in the synchronously rotating reference frame and *vice verse*. In the sequel of this section it is assumed that θ is measured using a position sensor and that the electromechanical torque T_{em} is also available (either measured or estimated using an observer).

Part 2: Voltage-source converter

The VSC contains a vector modulator. The vector modulator forces the three-phase stator voltages to equal their reference voltages. The rectifier switch control signals are determined using a prestored table of optimal gate switching. It is assumed that the three-phase stator voltages equal the reference values within the elapsed time between two switching instants. This assumption is justified if the desired closed-loop bandwidth is small compared to the switching frequency. Provided that this assumption holds, the vector modulator can be modeled as a dead time of length

$$T_{switch} = \frac{1}{f_{switch}}$$

with f_{switch} the switching frequency.

Observe that if the VSC was ideal such that the actual three-phase stator voltages were instantaneously equal to their reference voltages, the block diagram could be simplified by omitting all Park's transformation blocks (hereby assuming that θ as well as the machine model is ideal). However, it is preferred that the physical system structure is maintained.

Part 3: Synchronous generator

The mathematical model of a synchronous generator consists of two main parts, *viz.* an electromagnetic and a mechanical part. The electromagnetic part contains the voltage and flux equations of the synchronous generator as described in Section 3.5. This model has been identified, verified and validated in Section 4.3 using experimental data. The mechanical part is not a separate model but is contained in the model describing the structural dynamics of the complete turbines as derived in Section 3.4 and validated in Section 4.2.

6.3.2   Inverter controller

The VSC connected to the grid is set to control the voltage level of the DC link independent of the operating point of the generator-rectifier subsystem. The main goal is to set the reactive power demand to zero to obtain unity power factor. But, if the grid is weak (*i.e.* has a non-negligible, short-circuit impedance), the reactive power can be used to control the voltage level of the grid. In the sequel it is assumed that the grid can be modeled as an infinite bus (*i.e.* voltage source of constant voltage and frequency). Furthermore, it is assumed that the inverter control loop is fast enough to maintain the DC link voltage at its reference value. Hence, its operation does not affect the wind turbine dynamics.

6.4   Rectifier frequency converter controller design

In this section a new, but preliminary rectifier frequency converter controller will be designed on the basis of the validated model of the electromagnetic part of the Lagerwey LW-50/750 synchronous generator. The adjective "preliminary" is used to stress that we will focus on the first controller objective only. As a consequence, no attention will be paid to minimize the total losses and disturbance rejection (second and third controller objective).

6.4.1   Open-loop analysis

First an open-loop analysis is performed on the identified, verified and validated model of the Lagerwey LW-50/750 synchronous generator to determine possible control strategies. Consider the (open-loop) Bode magnitude diagram from inputs u_d, u_f, and u_q to outputs i_d, i_f, and i_q shown in Fig. 6.4 (be aware of the different scales of the y-axes). The solid lines correspond to the standstill case; the dashed lines to the case in which the synchronous generator is rotating at rated speed (*i.e.*

$\omega_m \approx 2.82$ [rad/s], *see* Table A.4 on page 226). The Bode magnitude plot is created by selecting the appropriate inputs and outputs from the identified synchronous generator model, and subsequently linearizing it about the aforementioned operating points. As the plots reveal, the synchronous generator dynamics strongly depend on the mechanical rotational speed ω_m. As expected, there is no interaction between the direct-axis and the quadrature-axis at standstill.
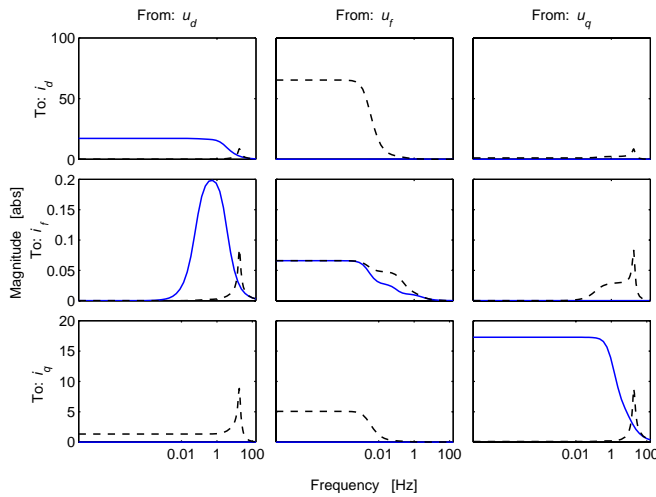

Figure 6.4: *Open-loop Bode magnitude diagram from inputs u_d, u_f and u_q to outputs i_d, i_f and i_q. Solid lines: standstill case, and dashed lines: synchronous generator rotating at rated speed ($\omega_m \approx 2.82$ [rad/s])*

6.4.2   Set-point computation and controller design

The design of a robust frequency converter controller is based on two tasks: determining the structure of the controller and adjusting the controller's parameters to achieve an "optimal" controlled synchronous generator behavior. Our main controller design objective is that the electromechanical torque should exactly and instantaneously reproduce its set-point with a bandwidth of at least 200 Hz. That is, the system's closed-loop transfer function should be as flat and as close as possible to unity up to 200 Hz for the identified synchronous generator model and designed controller combination. Another important goal is to minimize power losses (*i.e.* maximum efficiency) and to reduce the effect of disturbances on the output of the system. Recall that the stator copper losses, converter losses, and cable losses are proportial to the stator current squared, the rotor copper losses are proportial to the field current squared, and the iron losses to the square of the voltage (*see* Eq. (3.112) to Eq. (3.119) on page 101-102).

Set-point computation

From Eq. (3.114) and the set of equations Eqs. (3.105) it is evident that we need more information to select for each value of the reference electromechanical torque T_{em}^{set} unique values of i_d^{set}, i_q^{set}, and i_f^{set}. This additional information may be obtained through an optimization criterion such as: maximum torque per current, maximum torque per flux, maximum efficiency etc. In the sequel it is assumed for simplicity that:

1. The field winding current i_f is kept constant for achieving maximum torque per ampere (except when field weakening would be required to meet the objectives);

2. The reference value of the direct-axis current i_d^{set} is set to zero. The main reason is that the time constant of the dominating pole associated with the d-axis is about fifteen times larger than that of the q-axis (compare the numerical value of s_1 on page 153 with the one on page 154). This implies that i_q is preferred to i_d as the controlled variable for fast torque response.

This implies that the electromechanical torque is proportional to the quadrature-axis current according to:

$$T_{em} \overset{(3.114)}{=} p\left(\psi_d \cdot i_q - \underbrace{\psi_q \cdot i_d}_{=0}\right) \qquad \Rightarrow \qquad i_q^{set} = \frac{T_{em}^{set}}{p\,\psi_d}$$

with p the number of pole-pairs, ψ_d, ψ_q and i_d, i_q the direct- and quadrature-axis stator flux linkages and currents, respectively. The result being that the torque can be adjusted as accurately and as rapidly as the quadrature-axis current can be adjusted and controlled.

Controller design

Recall that there are several options to control the torque of AC machines via the currents. We have decided to use synchronous frame PI or DC current control since it allows a fixed switching frequency (unlike hysteresis control), and yields zero control error at steady-state (unlike stator-frame or AC current control). The controller blocks in Fig. 6.3 thus contain (parallel) PI controllers. The parallel PI controller is described by the following transfer function

$$
\begin{aligned}
G_{pi}(s) &= P + \frac{I}{s} \\
&= \frac{P\,s + I}{s} \\
&= \frac{P(s + \frac{I}{P})}{s}
\end{aligned}
$$

with P the proportional gain, and I the integral constant. Obviously, the zero of the above transfer function is given by

$$z = -\frac{I}{P}$$

Therefore a PI controller introduces a transfer function with one pole at the origin and one zero that can be located anywhere in the (left-hand) s-plane. The objective is thus to choose the parameters P and I to meet the performance specifications and have desirable robustness properties. Unfortunately, it is not immediately clear how to choose the parameters in the PI controllers to obtain certain performance and robustness characteristics. The controller parameters P and I are determined by trial and error such that the desired performance is achieved without violating the following current and voltage limits:

$$0 \leq \sqrt{i_d^2 + i_q^2} \leq 340A$$
$$0 \leq \sqrt{u_d^2 + u_q^2} \leq 690V$$

The performance of the resulting closed-loop system is treated in the next subsection.

6.4.3   Closed-loop analysis

The simulated closed-loop response of the electromechanical torque of the Lagerwey LW-50/750 synchronous generator to a number of stepwise changes in its reference value for $\omega_m = 2.0$ rad/s is shown in Fig 6.5. Observe that the response has been normalized with respect to the nominal electromechanical torque. For convenience, Fig. 6.6 shows a zoom of the response after the second stepwise change. It can be concluded that electromechanical torque can considered to be instantaneously controlled considerably over 200 Hz due to the high bandwidth of the designed current controllers. Consequently, for wind turbine time-domain simulation purposes, it suffices to use a first order model of the generator plus frequency converter. The time constant can be derived from the torque response time.

It must be noted that when the electromechanical torque set-point T_{em}^{set} changes (and thus the set-point for i_q), a transient error in i_d results, since the PI current controllers work in two single loops. To combat this, more advanced MIMO current controllers are required.

6.5   Conclusions

In this chapter a preliminary frequency converter controller has been developed for the validated model of the Lagerwey LW-50/750 synchronous generator. It has been shown that, under the assumptions made, the generator plus conversion system can be viewed as an (almost) instantaneous torque source within the specified bandwidth using single loop PI current controllers. No effort has been put in to either minimize the power losses or to reduce the effect of disturbances. It is expected that the performance can be even further improved (or harmonic content can be reduced) by designing more advanced controllers (*e.g.* MIMO current controllers) that exploit the interaction which exists between the d and q components of the stator voltage and current.
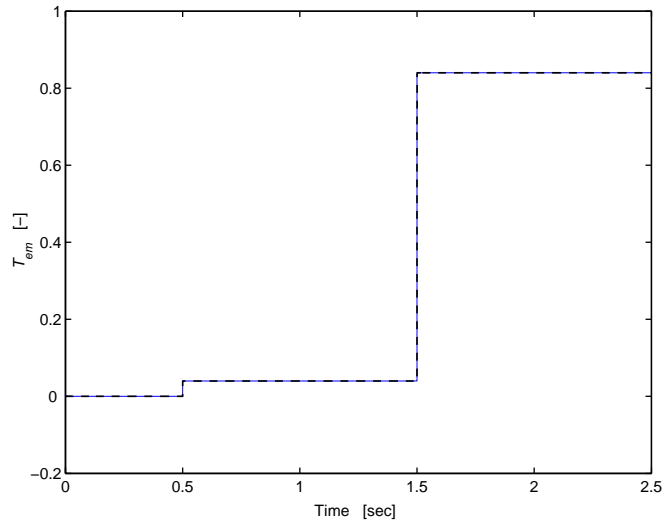
Figure 6.5: *Normalized electromechanical torque response of PI-controlled Lagerwey LW-50/750 synchronous generator to a number of stepwise changes in the torque set-point T_{em}^{set}.*
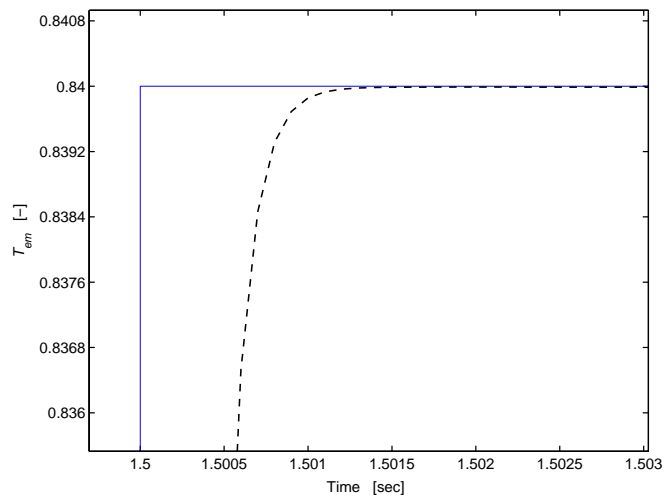

Figure 6.6: *Zoom around the second stepwise changes.*

Chapter 7

Economic control design

In this chapter the first steps towards the development of a wind turbine control system design methodology with an economic objective function will be made by presenting some design guidelines. Eventually, we will arrive at a methodology that translates the manufacturer's specifications as well as site-specific data automatically in a purpose-made controller. Together with the systematic approach developed in Part I and verified and (partly) validated in Part II, this will lead to an integrated and optimal wind turbine design. Consequently, this may help to close the gap that exists between the control engineering and the wind engineering community.

In Section 7.2 following the introduction, closed-loop wind turbine control issues will be discussed. In Section 7.3 a breakdown of cost of generating electricity using wind turbines as well as ways to reduce the cost will be presented. Finally, in Section 7.4 design guidelines are presented.

7.1 Introduction

The previous chapters have discussed the modeling of the wind input as well as the modeling and coupling of the aerodynamic, mechanical and electrical module of a flexible, variable speed onshore wind turbine. To successfully extract electrical power from the wind, a wind turbine also needs a control system that ties the operation of the aforementioned modules together. In general, a wind turbine control system has to carry out following two functions:

- Supervisory control

- Closed-loop control

The supervisory control system manages and monitors the switching between the various wind turbine modes of operation (*see* Appendix E for an overview of the main modes) and performs the reporting to the turbine operator(s). The main goal of the closed-loop control system is to enhance the overall performance aiming at both cost reduction and performance increase. It must be noted that the supervisory

control system is capable of overriding the closed-loop controller in order to provide for a safe shutdown if a serious malfunction has been detected. The design of such event-driven systems is not yet provided by DAWIDUM, but can be done by using the event-driven capabilities of SIMULINK® or by adding Stateflow diagrams to the models. In the sequel of this chapter only closed-loop control issues will be discussed.

7.2 Closed-loop wind turbine control

In this section the history of windmill and wind turbine control as well as the state-of-the-art of variable speed wind turbine control will be quickly reviewed.

7.2.1 History of windmill and wind turbine control

Wind turbine control has a long history which was probably initiated by the regulation of the rotational speed of the Persian windmills in the tenth century A.D using a series of shutters. Another early example of a windmill regulation device is the mill-hopper which was used to regulate the flow of grain in a mill depending on the speed of rotation of the millstone by about 1588.

The variability of the wind in both speed and direction was addressed and patented by the British blacksmith E. Lee in 1745 [154]. The drawing annexed by Lee's patent is depicted in Fig. 7.1. To compensate for wind speed variations, he invented a mechanism that pitched the blades as the wind speed increased and vice versa. The general principle of working of this device was that the force of the wind pitched the blades when the force magnitude exceeded that of the counterweight.
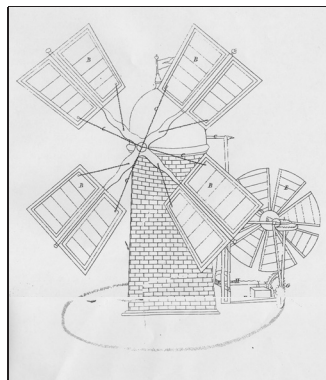

Figure 7.1: *Drawing annexed by Lee's patent titled "Self-regulating Wind Machine" with "A, the case of the Machine, B, the Sails, C, the Regulating Barr passing thro' the center of the originall axis, D, the Chains from the Barr to the Sails, E, the Back Sails which keep the machine constantly in the wind, F, the weight which regulates the Sails according to the winds force, G, the Traveling wheel which moves on planks round the machine, H, the Regulator to which the weight is Fixed."*

In addition, for keeping windmills pointed into the wind he developed the fantail: an auxiliary set of blades located behind and oriented perpendicular to the rotor. This yaw mechanism turned the cap of a tower mill automatically into the wind, thereby eliminating the need for manual changes in the windmill's orientation. The fantail thus had the ability to follow the changes in wind direction and is one of the earliest applications of feedback control.

Proportional feedback in the form of a centrifugal or fly-ball governor was used to regulate the speed of grain grinding windmills by controlling the force between the millstones around 1750 [5]. It must be noted that, in 1788, James Watt used a similar system for speed control of steam engines. The fly-ball governor and linkage kept the millstones apart, allowing the rotor to run unloaded up to a specified rotational speed. At this speed, the fly-balls rose up and allowed the millstones to move together and absorb torque. As the wind ramped up, the miller increased the flow rate of grain to absorb more torque. If the wind increased even more, it was necessary to turn the rotor out of the wind and stop it. Next, the sheets of canvas that were stretched over the wooden framework of the sails were reefed in order to reduce the swept area, and the milling process could be restarted. The spring sail, invented by the Scottish millwright A. Meikle in 1772, replaced the sheets of canvas with a series of wooden shutters. The openings of the shutters could be adapted manually by pulling on a chain or rope attached to a system of levers to "spill" the wind. One difficulty with both methods was that the windmill had to be stopped in order to adjust the settings in case the strength of the wind altered. This problem was resolved in 1807 by W. Cubit who introduced the patent sail. In this design all the shutters of all the sails were controlled automatically by a counterweight suspended outside the windmill.

In the windmill era there was, in principle, thus no need to closely control the rotational speed. In fact, allowing the windmills to operate at variable speed was highly advantageous as it increased the total energy extracted from the wind. The same holds true for the turbines that harnessed the wind for battery charging at the start of the electric era. The majority of these turbines were equipped with a DC generator, had blades with a fixed pitch angle and were operated at variable speed. In the early to mid-1970's, the need for supplying AC power to the grid changed the demands on wind turbine control because of the the fixed relationship between the speed of the AC generators and the fixed utility grid frequency. Consequently, the majority of the machines were operated at constant speed and had pitchable blades to level off excess power.

The control of the constant speed of commercial turbines has been done predominantly using PI-controllers with additional lead-lag and notch filters, while in simulation studies more advanced control strategies were proposed and explored (including optimal control [93, 179, 205] and gain-scheduled controllers [158]). The majority of the simulation studies followed a format of applying (advanced) control system design to not yet validated and often over-simplified turbine models, followed by simulation based performance comparisons. These performance comparisons are almost invariably based on measures of pitch angle, shaft speed and power variations. Fair comparisons between the industry standard control system and more

advanced controllers, however, are scarce. Knudsen *et al.* [138] compared a robust controller with the existing PI-type controller of a 400 kW commercial wind turbine. The robust controller, designed on the basis of an identified turbine model, achieved a reduction of pitch activity and some potential for fatigue load reduction compared to the existing controller. The comparison confirmed that improvement in performance can be achieved by proper control. The interested reader is referred to La Salle *et al.* [245] for a more thorough review of constant speed pitch controlled wind turbines as late as the 1990's.

The majority of the wind turbines now in operation are three-bladed, stall regulated constant speed turbines [1][172]. It must be stressed that in this case the blade pitch angle is fixed and, as a consequence, no control possibilities exist at all. Recall that stall utilizes the inherent aerodynamic properties of a rotor blade to limit the aerodynamic power. In the sequel, however, we will focus our attention on the closed-loop control of grid-connected, variable speed pitch-regulated turbines since this configuration has the highest potential to reach cost-effectiveness in the (near) future.

7.2.2 State-of-the-art variable speed wind turbine control

In a variable speed wind turbine, the rotor and the generator are decoupled from the grid by the power electronics implying that the rotor may rotate at (almost) any speed. Consequently, variable speed operation offers more control possibilities than constant rotational speed does. Variable speed operation has two main advantages over constant speed operation: i) additional energy capture at partial load and ii) potential reduction of fatigue loads on the structure by absorbing torque fluctuations in the rotor momentum. Other benefits that have been claimed are enhanced utility grid system compatibility, controllable power factor, reduction of acoustic noise at low wind speeds, adaptation to local conditions or compensating for changing conditions, and avoidance of stall over most the operating range [186].

In the context of maximum power extraction in partial load, the effect of variable speed is easily described. The kinetic energy content of the wind passing through the rotor varies with the cube of the wind velocity as illustrated in Fig. 7.2. Only a fraction of this energy can be extracted by the rotor (and subsequently converted into electrical power) as explained in Section 3.3. This fraction is denoted by the power coefficient C_p, which is a function of the tip-speed ratio λ (*i.e.* the ratio of rotor circumferential speed to wind velocity) and the blade pitch angle θ. Usually, the power coefficient has one distinct maximum at the optimal tip-speed ratio and blade pitch angle. Practically achievable maximum values are in the range of $0.40 < C_p < 0.50$, while common optimum values of the tip-speed ratio lie between 5 and 10 depending on the aerodynamic properties of the wind turbine configuration under investigation.

It is thus desirable to let the wind turbine rotational speed vary over a wide range, since maximum energy is extracted if the turbine operates constantly at or

---

[1]Most megawatt sized wind turbine models that are installed recently and the ones under development are, however, of the pitch controlled variable speed type
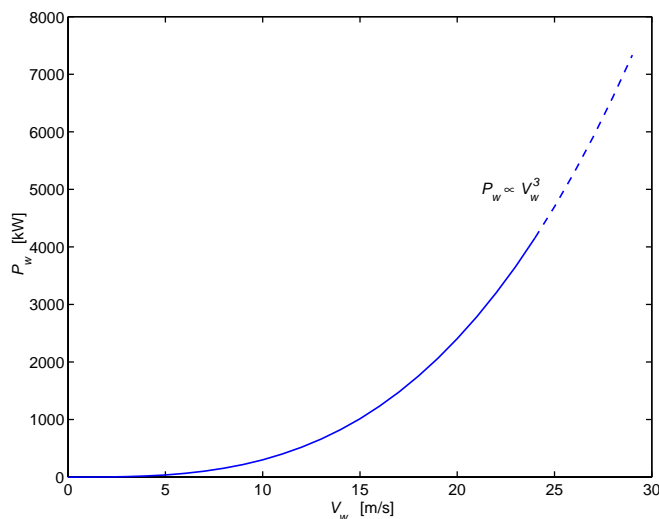
Figure 7.2: *Total power in the wind passing through a 25-meter diameter rotor as function of the wind velocity.*

near its optimum tip-speed ratio. Observe that variable speed operation is not possible in case that the generator is directly connected to the utility grid. To allow the generator rotational speed to vary to extract the maximum amount of power, a power electronic interface is thus needed. In such an interface the three-phase generator output is rectified into DC and subsequently interfaced with the three-phase utility source by means of a power electronic converter as outlined in Section 3.5. In general, a rectifier at the generator side as well as an inverter at the utility grid site is required to provide both control and power quality requirements (including power factor).

The control problem of pitch-regulated, variable speed wind turbines significantly differs from that of constant speed wind turbines using pitch regulation. The latter presents a SISO control problem, while variable speed using pitch regulation presents a MIMO control problem as the electromechanical torque control loop is added to the existing pitch control loop. This opens the possibility to exploit the interactions between the inputs and outputs in the system to reduce dynamic loads as well as maintaining a desired amount of energy production. The current control strategy is to use the fast electromechanical torque control to respond to transients, and a slower pitch control loop to follow minute-to-minute fluctuations in wind speed. Both loops, however, often carry out their tasks independently by PID-type controllers [30, 283]. Probably, a more cost-effective strategy is couple the two control loops and make them to interfere constructively. Finally, it must be stressed that in order to make fair comparisons between the industry standard closed-loop controller and more advanced ones, it is necessary to i) establish the best possible PID controller, and ii) define criteria by which the performance can be evaluated.

The control objectives of the variable speed turbine depend on the operating regime. Below rated wind speed (or partial load) a common objective is to operate the turbine at optimum tip-speed ratio until a speed, power or torque limit is reached [245]. Above the rated wind velocity (or full load), power limitation is the main goal. In literature, various controllers are proposed for the aforementioned operating regimes. Multivariable controllers are successfully applied in simulation studies by Steinbuch [281] (at full load only, results based on a rather coarse wind turbine model that has not been confronted with measured data), Bongers [21] (achieved significant fatigue load reduction of both rotor shaft torque and blade root bending moments in one full load operating condition), and Stol [283] (reduced cyclic blade root bending moments by periodic control of the pitch angles). Molenaar [188] examined the effect of a simple filter controller on the fatigue loads on a model of a 2-bladed 500 kW variable speed turbine. It has been shown by comparison of the areas enclosed by the rainflow counts of in total 26 load cases (including power production with or without the occurrence of fault, startups and stops at normal wind conditions and parking cases as prescribed by the IEC-1400-1 standard [112]) that filtering the generator speed before computing a new torque set-point significantly reduces the fatigue loads on blade root (flap direction only), drive-train and tower.

In several other publications (*see e.g.* [39, 51, 95, 96, 135, 238, 276]) additional promising simulation results are shown. Various control design methodologies have been applied to models of different variable speed wind turbines in order to meet the aforementioned control objectives. However, all studies are performed with fairly basic wind turbine models (either the aerodynamics are approximated by a (static) model stored in a look-up table, or the structural flexibility is neglected). Sensor and actuator dynamics as well as disturbance issues are, in general, not addressed. As a consequence, the obtained results should be handled with care.

At the application side, however, still (too) little convincing results are reported in literature. Bongers applied robust control to a small experimental test-rig and demonstrated, in only one operating point, that a robust controller is capable to reduce fatigue loading while simultaneously maintaining a desired amount of energy production. De Boer and Mortier [16] presented experimental results of the application of static optimal output feedback on a 300 kW wind turbine. They showed by comparing time-series that, at full load, the direct current fluctuations can be reduced with almost a factor three with respect to the existing SISO controller. It is concluded from this that the fatigue loads are reduced as well, although no rainflow countings or load spectra are shown to illustrate the effect on the fatigue life. Krüger *et al.* [41, 42, 142] demonstrated the potential of advanced control on an experimental 33 kW wind turbine. They showed, by comparing load spectra of the blade root bending moments, that i) variable speed operation is capable of reducing mechanical loads when compared to constant speed operation, and ii) advanced control can significantly reduce rotor blade fatigue loads (although at the expense of a slight reduction in the annual electricity yield).

The quick review of the history and state-of-the-art of (closed-loop) wind turbine control shows that:

- The industry standard closed-loop controller is (still) of the PID-type. It is

202

unkown how the PID controller parameters are determined and to what extent they are optimized;

- Simulation studies are often performed with fairly basic wind turbine models, while the proposed control strategies are elaborate and, in general, do not address the real issue: cost-effective control of the whole operating envelope;

- There is a lack of literature reporting on practical field experience obtained with control systems. Many of the applications reported are restricted in the scope to only one operating point;

- For variable speed to become the norm and not the exception in the (near) future, the added cost of power electronics required by most variable-speed designs must be clearly offset by the increased electricity yield, reduction in fatigue loads and other systems costs, impact on the wind turbine design, and the added benefit of providing power conditioning for utilities.

As a consequence, significant improvements are still possible to reach the desired economic viability of wind power. The first step is to show on a simulation level that the competitive position of wind power can be significantly improved by advanced control. The models used in these studies need to be validated against data acquired from experimental tests. Next, the achieved benefits need to be demonstrated in practice on a (prototype of a) commercial wind turbine.

The main question is how these controllers can be designed. The controller design must, in principle, encompass all aspects of both performance and cost, ranging from energy production, quality of power, lifetime and safety, through cost-effectiveness, acoustic noise and reliability. Notice that the relative importance of these aspects may vary from site to site. For example, a key objective for the design of cost-effective offshore wind turbines will be that the operation and maintenance requirements are reduced to a minimum, possibly at the expense of a somewhat higher wind turbine capital cost or lower electricity yield. The challenge for the control system designer is thus to specify an economic control design objective that reveals the financial impact of a proper controlled wind turbine. Before we can develop such an objective, we first have to determine what makes up the cost of generating electricity using wind.

7.3 The cost of generating electricity using wind

In the introduction it was stated that the capital cost accounts for 70%, and the O&M cost for $6-29\%$ of the cost per kilowatt-hour. The cost of capital include the purchase price, cost of transporting, assembling, and erecting a wind turbine on site, as well as connecting it to the grid, cost of installing grid lines, and transformers. The O&M cost, on the other hand, include all troubleshooting, inspections, adjustments, retrofits, preventive as well as unscheduled maintenance performed on wind turbines, and the downtime that accumulates while waiting for parts, instructions, or outside services that are not available on site but are required to bring the turbine back in operation.

Thus wind energy is a highly capital-intensive technology, and consequently the economics of wind power are highly sensitive to both the size of the capital investment and the interest rate charged on that capital. This in turn means that the cost can be effectively reduced by reducing the capital cost (hereby assuming a given, constant capital interest rate). Besides capital and O&M cost reduction, the competitive position of wind power can also be improved by ensuring that the turbine is operating continuously at the best possible performance as well as by minimizing the difference between the technical and economic lifetime.

Now that we know roughly the breakdown of the cost of generating electricity from wind, the question is how can we reduce these cost in order to make it competitive with all other electricity sources. From the preceding it can be concluded that either the cost (both capital and O&M) can be reduced or the performance of the turbine can be increased. Both aspects will be discussed in more detail in the next two subsections.

7.3.1   Performance increase

It is important to realize that the wind turbine performance is achieved to a large extent during normal operation. The cost, on the other hand, are generated during all operational modes (including power generation cases with the occurrence of fault, parking at storm, and idling). The energy capture of a variable speed wind turbine depends for the greater part on its ability to successfully operate at the peak of the $C_p(\lambda, \theta)$-curve in partial load. After all, maximum aerodynamic efficiency is achieved at the optimum tip-speed ratio $\lambda = \lambda_{opt}$ at which the power coefficient C_p has its maximum value: $C_{p,max}$. This implies that the electromechanical torque T_{em} must be adapted in proportion to the wind velocity V_w squared (or rotor speed squared since $V_w = \omega_r R/\lambda$) to maintain the optimum tip-speed ratio. In steady-state, the electromechanical torque balances the aerodynamical torque reduced by the amount of any mechanical torque loss in the drive-train. This fact is used in the commonly used "omega-squared" control law which is given by:

$$T_{em}^{set} = \frac{\rho \pi R^5 C_{p,max}}{2\lambda_{opt}^3} \cdot \omega_r^2 - T_{loss} \tag{7.1}$$

where T_{em}^{set} is the set-point for the electromechanical torque, ρ is the air density, R is the rotor radius, $C_{p,max}$ is the power coefficient at the optimum tip-speed ratio λ_{opt}, ω_r the rotor rotational speed, and T_{loss} the mechanical torque loss (which may itself be a function of the rotational speed and torque). Although this relationship is valid only in steady-state, it is also used dynamically to control the electromechanical torque demand of variable speed turbines as a function of the measured rotor (or generator speed since, in steady-state, $\omega_g = i_{tr} \omega_r$ with i_{tr} the transmission ratio) speed. The measured rotational speed is often filtered using a first order low pass filter to avoid rapid electromechanical torque set-point changes. This way of controlling the electromechanical torque below rated wind speed may work satisfactory on relatively rigid turbines located on sites with uniform wind fields. More flexible

variable speed turbines exposed to more turbulent wind conditions, however, will require a dynamic control law taking also the phase information into account.

Fingersh and Carlin [61] applied the "omega-squared" control law to the NREL Variable Speed Test Bed turbine and showed that this resulted in an overall energy capture loss of over 5% when compared with the idealized variable speed operation. Modification of the law indicates a preliminary energy capture improvement of between 0.3% and 3%. It can be concluded that the losses associated with variable speed turbines running off the optimal point can be reduced by applying more advanced control algorithms to track the optimal tip-speed ratio in partial load.

7.3.2 Cost reduction

From the aforementioned two cost items we need to identify the most important cost driver(s). In the introduction it has been mentioned that fatigue loads on the wind turbine structure are the main cause of failure in the present onshore wind turbine design. This implies that the current design of the main wind turbine components (*i.e.* rotor blades, support structure, and drive-train) is driven by fatigue loads. As a consequence, fatigue loads are an important cost driver. It must be noted that already from the very beginning wind turbines have experienced fatigue problems [285]. The early wind turbines were mainly designed using static and quasi-static analysis. At best, these rather simple analysis led to over-designed wind turbines, and at worst, to premature field failures. The latter is exemplified by the fact that almost all rotor blades have been repaired or replaced in the early California wind farms [284]. Wind turbines installed more recently have demonstrated a substantial improvement in availability due to the fact that the designers used the gain in wisdom of thousands of hours operating experience. However, with the trend towards increasingly lightweight and larger wind turbines operating at variable speed the fatigue problems are not yet solved.

The most fatigue critical wind turbine parts are the rotor blades and their connection to the hub [180]. The latter, the so-called blade root, is an area of critical importance as it transmits the entire blade load through a relatively small space envelope. The unique combination of steady and fatigue loading on a rotor blade makes this a challenging part of the design. In a design life-time of 20 years a rotor blade must withstand at least 10^8 to 10^9 cycles of variable amplitude due to gusts, atmospheric turbulence, wind shear, gravity, startup and (emergency) shutdown procedures. Very few data are available in this high cycle fatigue range for the materials and components used in wind turbines, especially in combination with the fact that rotor blades are exposed to a hostile environment throughout their life-time. Such effects include: temperature fluctuations, rain, thunderstorms, formation of ice, hailstones, and erosion from sand particles. Other important parts to be considered are the rotor shaft torque, rotor thrust, tower foot bending moment and internal stresses at critical points on the structure (*e.g.* the nodes on a tripod foundation).

Fatigue loads are characterized by lightly damped structural modes. Adding damping of the structural modes can significantly reduce the impact of fatigue loads.

Both rotor and electromechanical torque control can be used for fatigue load reduction. Active rotor control includes full-span (collective) pitch control (low frequencies only), cyclic control, aileron control, and individual blade control [78, 175]. It must be stressed that in order to investigate the cost-effectiveness of the aforementioned options the availability of a validated model is essential.

7.4 Closed-loop control design methodology: design guidelines

Various design procedures exist for control design and may therefore also be applied to a wind turbine. They range from "classical" design techniques such as root locus and Bode analysis, via optimal control to techniques based on the minimization of an objective function through numerical optimization. The proper formulation of the objective function in the latter procedure is one of the crucial steps in achieving the desired closed-loop performance. After all, a poorly formulated criterion will simply yield a controller that optimally implements the poor design. In general, it is difficult to translate a verbal statement (*e.g.* minimum fatigue loads) or a concept of the desired objective into mathematical terms. Our controller objective is to arrive at cost-effective design and operation of flexible, variable speed wind turbines. That is, we have to minimize the cost per kilowatt-hour. The economic control design objective should at least include a measure of the (annual) electricity yield, fatigue (representative selection of loads). The exact translation of the performance and cost related to wind turbine construction and operation into an economic model is, however, beyond the scope of this thesis. We will conclude this chapter with presenting the five main steps in designing cost-effective wind turbines on the basis of a mathematical model:

- **Step 1:** Develop a mathematical model using design data from the wind turbine manufacturer describing the relevant dynamics of the turbine under investigation

- **Step 2:** Validate the model using experimental data obtained from the turbine under investigation

- **Step 3:** Translate the manufacturer's specifications to an economic objective function that can be solved through numerical optimization

- **Step 4:** Design a controller on the basis of the validated model by minimizing a specified objective function

- **Step 5:** Implement the controller and evaluate the closed-loop performance

The aforementioned steps imply the need for a close co-operation between the wind turbine designer and the control engineers in order to identify those design parameters for which the economic objective function is most sensitive.

Part IV:

Conclusions and recommendations

Chapter 8

Conclusions

This chapter presents the conclusions of this thesis. In the past decades, the wind industry has grown from a niche business serving the environmental aware into one that has established itself as the most competitive form of renewable energy. Wind has the potential to play an important role in the future world electricity supply provided that the cost per kilowatt-hour are further reduced. The cost of wind-generated electricity can be effectively reduced by steady improvements in both wind turbine design and operation since wind is a highly capital-intensive and maintenance-demanding technology.

The challenge of wind energy research lies in developing wind turbines that are optimized with respect to both cost and performance. A prerequisite for the cost-effective design of such turbines is the availability of a systematic methodology that generates accurate and reliable dynamic models of the complete system within the design phase with low modeling effort. The main conclusion of this thesis is that such a methodology has been developed for flexible, variable speed, grid connected, horizontal-axis wind turbines that are equipped with a direct-drive synchronous generator and are located on land. The solution to the main thesis problem has been achieved by the successive solution of the following of sub-problems:

- Sub-problem 1.2.1: Modeling of flexible wind turbines

- Sub-problem 1.2.2: Model validation

- Sub-problem 1.2.3: Model based control design

These sub-problems and their respective solutions will be discussed in detail below. We would like to emphasize that the presented solutions must not be regarded as the one and only ones, although they have proven to be sufficient to solve the main thesis problem. New demands resulting from, for example, cost developments in both conventional and renewable electricity sources may call for other solutions in the (near) future to maintain at least the current share of wind power in the global electricity mix.

Sub-problem 1.2.1: Modeling of flexible wind turbines

The wind turbine modeling sub-problem has been addressed in Part I (comprising Chapter 2 and Chapter 3). In Chapter 2 an inventory of the state-of-the-art of wind turbine design codes has been made. From this inventory it can be concluded that most of the design codes have been developed specially to deal with wind turbine design calculations and time-domain simulations, but are not suited to solve the main thesis problem. The main reasons are: i) the absence of the indispensable bilateral coupling between the design of a new wind turbine and the design and implementation of its control system, ii) model validation has not received the attention required for obtaining economic viability of wind power, and iii) the modeling of the electromagnetic part of the generator plus conversion system has received too little attention.

In Chapter 3 the development of a new software tool called DAWIDUM was described that overcomes the aforementioned shortcomings. It must be stressed that DAWIDUM continues and combines the work that has already been done in the aforementioned design codes. Within DAWIDUM any wind turbine is modeled as a set of four bilaterally coupled modules (*i.e.* aerodynamic, mechanical, electrical and controller) and one input module (*i.e.* wind). The main conclusions are grouped per module.

- **Wind module**. Realistic modeling is essential for wind turbine design and evaluation purposes (since the wind drives the system and at the same time also acts as the main disturbance). DAWIDUM is coupled to SWING-4 (a 3-D wind field simulation code) to generate stochastic wind field velocity components. Alternatively, measured time-varying winds can also be used as input. In addition, some effort is made in modeling the deterministic part of the undisturbed wind velocity.

- **Aerodynamic module**. The implementation of the rotor aerodynamics in DAWIDUM is based on Glauert's BEM theory plus the corrections that are common to be applied to the quasi-steady momentum theory.

- **Mechanical module**. Much effort has been put in developing tools that would establish a bilateral coupling between the wind turbine design and its control system. The main conclusions are:

  – DAWIDUM's mechanical module is equipped with a systematic procedure for modeling the structural dynamics of flexible wind turbines. The structural dynamics are modeled as a collection of rigid and flexible bodies. Flexible body dynamics are approximated using superelements. The systematic procedure allows both structural designers and control engineers to rapidly and easily build dynamic wind turbine models. Both the model configuration and complexity can be easily adapted by the user;

  – An off-line, time-domain model parameter updating procedure has been developed for updating the (user-selected) tunable parameters of the structural model when measured (modal test) data is available.

- **Electrical module**. The electrical module contains a dynamic model of the electromagnetic part of an ideal synchronous generator. This model is obtained by rewriting Park's dq-axis model equations such that the model parameters retain their physically meaningful interpretation. In addition, the parameters of the reformulated equations can be easily obtained from measured data.

Sub-problem 1.2.2: Model validation

Model verification and validation issues have been addressed in Part II (comprising Chapter 4 and Chapter 5). In Chapter 4 the verification as well as experimental validation of DAWIDUM's wind turbine mechanical and electrical module have been given, while in Chapter 5 the verification of the parameter updating procedure has been addressed. The main conclusions regarding model validation issues are grouped below per module.

- **Mechanical module**. The main conclusions are:

  - The systematic modeling procedure has, after being verified using a test case, been used to generate the equations of motion of 4 different rotor blades as well as to generate a dynamic structural model of the complete Lagerwey LW-50/750 wind turbine. Based on thorough comparison of the system's natural frequencies, mode shapes and time-domain responses it can be concluded that the superelement models are suited to solve the modeling sub-problem;

  - The parameter updating procedure has been verified using simulated data. It has been made plausible that global optimization is likely to be achieved provided that the initial parameter guess is close enough to the real parameter values.

- **Electrical module**. The validity of DAWIDUM's procedure for identifying the transfer functions of Park's dq-axis model describing the electromagnetic part of a synchronous generator has been examined by comparing time-domain simulations with measurements taken from the Lagerwey LW-50/750 generator. The required input-output data is obtained from the modified step-response test. The following conclusions can be drawn:

  - The parameters of Park's dq-axis model describing the electromagnetic part of a synchronous generator can be easily and accurately identified following the developed procedure on the basis of modified step-response data;

  - It is justified to use this model for model based control design purposes. The ultimate validation of the method and its impact on variable speed wind turbine performance can be proved only after the implementation of the designed frequency converter controller in the Lagerwey LW-50/750 wind turbine.

Sub-problem 1.2.3: Model based control design

The wind turbine control design sub-problem has been treated in Part III (comprising Chapter 6 and Chapter 7). Two main conclusions are grouped below:

- **Electrical module**. A preliminary frequency converter controller has been developed for the validated model of the Lagerwey LW-50/750 synchronous generator. It has been shown that the PI-controlled generator plus conversion system can be viewed as an (almost) instantaneous torque source within the specified bandwidth;

- **Economic control design**. The first steps towards the systematic synthesis of model based controllers aiming at cost-effectiveness have been taken. The penalty for poor closed-loop control is a less cost-effective wind turbine.

Chapter 9

Recommendations for future research

This chapter presents the main recommendations for future research. The recommendations originate from the fact that not all ideas gained or questions raised during the project term have been explored or answered. The main reason for this is that priority has been given to first solve the questions that initially seemed the most important ones. The numerous issues that deserve future research are sorted by the three sub-problem as listed in Section 1.2 and will be discussed below.

Sub-problem 1.2.1: Modeling of flexible wind turbines

First of all, given the fact that considerable effort has been put in the development of DAWIDUM, a warm recommendation is given to fully exploit the potential of this new wind turbine design code. This requires the joint effort of all DUWIND members to develop and implement new models as well as wind turbine specific analysis and (control) design tools. In addition, the code must be extended with a wave and hydrodynamic module required to compute the water wave forces acting on the support structure of wind turbines located offshore. The latter extension is essential, since the future of wind energy will be in large-scale offshore wind farms.

The gained modeling experience has lead, for most modules, to several recommendations for future research. The recommendations are grouped per module.

- **Aerodynamic module**. The following suggestions can be given to improve the quality of DAWIDUM's aerodynamic module:

    - An area of great importance and significant uncertainty that deserves attention is that of modeling of skewed wake effects (also referred to as yawed flow, yaw misalignment or oblique flow). From the practical point of view, yaw misalignment is a fact of life, and is of paramount importance since an important part of fatigue lifetime consumption of rotor

blades can be attributed to these conditions. In addition, it is of importance to the load spectra of yaw bearing, tower, and rotor shaft. Hence, corrections must be made to the blade element momentum theory when the rotor operates at a yaw angle. Although considerable progress has been made, the results are not yet sufficiently accurate when compared with measurements;

– It is recommended to develop an optimization procedure that calculates the optimal number of blade elements (independently of the number of superelements) for a given wind turbine configuration.

- **Mechanical module**. The following suggestions can be given to improve the quality of the models within DAWIDUM's mechanical module:

  – At present, the superelement method used to model the flexible wind turbine part considers bending deformation only. It must be noted that both axial deflection and torsion (or twist) can be included easily by subdividing the middle body into two bodies and connecting them using a joint with one translational and one rotational degree of freedom. The equations for the computation of the axial and torsional spring stiffness are given in Molenaar [189]. It is strongly recommended that the torsion degree of freedom is included when investigating (unknown) aero-elastic instabilities (*e.g.* pitch-flap flutter) of especially large rotor blades;

  – It is assumed that either the blade designer or the blade manufacturer supplies the mass and the flexural rigidity in the two principal bending direction as function of the length of the wind turbines parts that are treated as flexible. These values are used to compute the required simulation parameters (including the torsional spring constants in bending direction). At present, the off-diagonal terms of the rotor blade inertia matrices (*i.e.* the products of inertia) and blade twist are neglected. It is strongly recommended to add this information when available.

- **Electrical module**. The following suggestions can be given to either improve the model quality or to increase the model scope:

  – In subsection 4.3.3 a MIMO ARX model has been estimated without using the fact that the off-diagonal terms of Eq. (3.107) on page 99 are identical. It is recommended to include such linear constraints in an ARX model structure while preserving the linear in the parameters property (*e.g.* by modifying the standard routines in SITB);

  – Large-scale application of wind energy implies large-scale penetration of the utility grid. Careful consideration of the interaction wind turbine and grid is thus required in order to meet the grid operator requirements. To date, this problem has been addressed in only a very superficial way.

Besides the aforementioned suggestions to improve DAWIDUM's model quality, effort must be put in the development of accurate pitch and yaw actuator models.

Sub-problem 1.2.2: Model validation

The following suggestions can be given to improve the validation of DAWIDUM's module library. The recommendations are sorted per module.

- **Aerodynamic module**. In this thesis the aerodynamic module has not been confronted with measured data. It is strongly recommended to perform validation experiments in the near future since considerable uncertainty exist about the validity of the commonly used 2-D BEM theory and its (semi-empirical) corrections to describe the 3-D rotor aerodynamics.

- **Mechanical module**. The following recommendations can be given to improve the quality of the models available in the mechanical module library:

  - In this thesis the models within DAWIDUM's mechanical module have been verified for both the non-rotating and the rotating case, but have only been validated for the non-rotating situation. It is recommended to also examine the validity as function of the rotational speed, since substantial damping is created due to aero-elastic interaction during normal operation;

  - It has been shown that the quality of the rotor blade models can be significantly improved by tuning the torsional springs using displacement information. The displacement, resulting from a static load, has been measured at only one location near the blade tip. It is recommended to equip the blades with a larger number of displacement sensors to accurately determine the bending stiffness and torsion distribution, preferably for several load cases. This information can be used to further improve the FAROB models and reduce the observed bias.

    In addition, it is recommended that the acceleration responses from modal tests are stored on disk so that they can be used to compare mode shapes as well as to tune/update the torsional spring constants and/or damper constants using the developed off-line procedure. This will further improve the model quality, yet after being manufactured.

- **Electrical module**. The synchronous machine model parameters have been determined using time-domain standstill test data. In the time of the experiments, the equations had not yet evolved to the final simulation scheme shown in Fig. 3.26 on page 100. In the Lagerwey LW-50/750 case, the excitation of the field winding voltage was sufficient because the short-circuit was not perfect due to the slip-rings. Next time, however, it is recommended to stepwise change both the stator *bc*-terminals and the field winding voltage at the same time to enforce proper excitation.

It must be stressed that additional full-scale measurements are, without doubt, required for designing cost-effective wind turbines using DAWIDUM. Not only for validation purposes, but also to convince investors of the reliability and cost-effectiveness of newly developed (control) techniques. It is thus strongly recommended to perform

in the near future full-scale validation experiments on variable speed, commercial (offshore) wind turbines.

Sub-problem 1.2.3: Model based control design

The model based control design sub-problem has been addressed only briefly. The main aspects that seem to be worthwhile to be investigated in more detail are listed below:

- **Electrical module**. The robustness (of for example different values of the rotational speed) of the developed PI current controllers need to be assessed. In addition, attention must be paid to the minimization of power losses;

- **Economic control design**. More effort must be put in the design of an economic control design criterion that can be minimized through numerical optimization. In this way the effect of (more) advanced control design on the reduction of the cost per kWh can be quantified.

To demonstrate the cost-effectiveness of controlled wind turbines in practice, it is essential that the opportunity is given to implement the presented ideas and resulting control strategies in a flexible, variable speed wind turbine. Furthermore, it is recommended that effort is put in to include the constraints imposed by the safety system. How quickly the aforementioned technical improvements can be introduced in commercial wind turbines depends on their cost relative to the price of electricity.

Epilogue

Where do we go from here? First of all, the "special position" that wind energy takes now must be changed. To become an accepted source of electricity, it is essential that wind is looked at from an economical business perspective and not only from an environmental point of view. I would like to stress that without subsidies and a consistent policy of the government, the (Dutch) wind industry would disappear [137]. In this respect it is thus of utmost importance that the fiscal instruments used to allocate the (significant) subsidies must be gradually amended in the near future to ensure that (most of) the money involved will be invested in research and development aiming at achieving economic viability of wind power (*see* Subsection 1.1.2 for a list of main topics that need to be addressed first).

An important question is how to continue and to organize the required research and development. At present, the missing link in the realization of cost-effective wind turbines is the absence of a representative experimental facility. Such a facility is a necessity to validate design tools like DAWIDUM as well as to demonstrate the cost-effectiveness of controlled wind turbines in practice (preferably by direct comparison of a standard controlled wind turbine with an identical turbine equipped with an advanced controller at the same location). This implies that access to a (small) wind farm (consisting of at least two fully instrumented state-of-the-art wind turbines) is indispensable to demonstrate that the cost per kilowatt-hour can be effectively reduced by means of technological advancements.

Part V:

Appendices

Appendix A

Main features Lagerwey LW-50/750 wind turbine

In this appendix we will list the main technical data of the Lagerwey LW-50/750 wind turbine that is located is near Nieuwe-Tonge (Province of Zuid-Holland, The Netherlands). In Section A.2 the main technical data of the rotor is listed after presenting some general information in Section A.1. Section A.3 presents the main technical data of the support structure, while in Section A.4 the main technical data of the generator is listed.

A.1   The Lagerwey LW-50/750 wind turbine

The Lagerwey LW-50/750 wind turbine is a 750 kW, variable speed wind turbine with an upwind rotor of 50.5-meter diameter. A picture of this turbine is shown in Fig. A.1. The "LW-50/750" is located near Nieuwe-Tonge (Province of Zuid-Holland, The Netherlands). The rotor consists of 3 blades that can be actively and individually pitched over the full span. The pitch control is used for power control at full load, and to stop the turbine if the safe operating limits are exceeded. The turbine is equipped with a gearless (or direct-drive) synchronous ring-generator, which converts the mechanical power into electrical power at variable frequency. Subsequently, an insulated gate bipolar transistor (IGBT) based frequency converter is used to convert the electrical energy of varying frequency to the utility grid with a fixed 50-Hz frequency. The generator torque will follow an external set-point signal, which is calculated by the control computer. The support structure consists of a 46.165-meter conical tower with a circular cross section, and a foundation. The tower is made of tubular steel.

The Lagerwey LW-50/750 belongs to a new generation of wind turbines which are more flexible than the majority of the turbines currently on the market. It has soft characteristics realized in all subsystems in order to reduce internal stresses, and thereby to make lighter, and hence less costly components possible. The explanation

Figure A.1: *Lagerwey LW-50/750 wind turbine, located near Nieuwe-Tonge (Province of Zuid-Holland, The Netherlands).*

for this is that in a stiff system concept the transient air loadings go into the structural components as physical strains, and (sooner or later) induce fatigue damage. In a soft system concept, on the other hand, these air loadings are reacted primarily by the subsystem masses with little strain energy involvement. In other words: the subsystems bend under the transient air loading by which internal stresses will be reduced. Hence, there is low tendency for fatigue failure in a dynamically soft system.

A.2 Rotor

The rotor of the LW-50/750 wind turbine consists of 3 extended APX-45 rotor blades (in the sequel referred to as APX-48 rotor blades) that can be actively and individually pitched over the full span. The blades are bolted on spacers to increase the rotor diameter from 48.0 m to 50.52 m. The spacers are, in turn, bolted directly on the pitch bearings located on rotor hub. The rotor consists thus of three main parts, notably:

- Rotor blades;
- Spacer;
- Rotor hub.

These three parts will be discussed in detail below.

a:) Rotor blades

The rotor blades of the Lagerwey LW-50/750 - APX48/750 - are designed by the Stevin Laboratory of Delft University of Technology, The Netherlands [242], and manufactured by Aerpac Special Products B.V., Hengelo, The Netherlands [241]. The rotor blades are designed for both (full-span) pitch-controlled and (active) stall regulated 3-bladed wind turbines.

The APX-45/APX-48 rotor blade consists of two main parts: a 3.75 m long non-aerodynamic part where the cylindrical contour is transformed into an aerodynamic shaped root aerofoil, and an 18 m long aerodynamic part. The length of both blades is 21.75 m (the APX-45 blade is extended at the root to achieve an APX-48 blade). The primary aerofoils were selected to suit a stall controlled wind turbine (*i.e.* non-optimal for variable speed wind turbines like the Lagerwey LW-50/750). The optimum tip speed ratio is set to 7 with a maximum blade tip speed of 60 meters per second.

The blades are mainly made of glass fibre reinforced epoxy (GRE). A 12° twist is built in to keep the angle of attack constant over the length of the blade. The main technical data of these rotor blades is summarized in Table A.1 [155].

<div style="border:1px solid">

Main technical data rotor blades

Geometry:

Length	
APX-45 (L_{apx45})	21.75 m (from root separation plane to tip)
APX-48 (L_{apx48})	21.75 m (from root separation plane to tip)
Length spacer (L_{sp})	2.060 m
Twist	12°
Chord length	
minimum	492 mm @ the blade tip
maximum	2104 mm @ $r = 3.75$ m (from root separation plane, *see* Fig. A.2)
Center of gravity	7310 mm [*)] (from root separation plane)

Aerodynamic profiles: (*see* Fig. A.4)

$3.75 \leq r < 10.75$ m	DU-97-W-300
$r = 10.75$ m	DU-91-W2-250
$10.75 < r < 16.75$ m	Linear interpolation according to t/c
$r = 16.75$ m	FFA-W3-211
$16.75 < r \leq 20.25$ m	Linear interpolation according to t/c
$20.25 < r \leq 21.75$ m	NACA-63-218

Material:

Glass fibre reinforced epoxy (GRE)

Masses:

Blade mass (M_{apx45})	1522 kg.[*)]
Cylindrical T-bolt nuts of pitch bearing	32 kg.
Spacer mass (M_{sp})	1110 kg.

</div>

Table A.1: *Main technical data of the Lagerwey LW-50/750 rotor blades, with* [*)]: *measured.*

Fig. A.2 shows the chord length, the chord thickness, and chord ratio (which is defined as the chord thickness divided by the chord length) of the APX-45/APX-48 rotor blade as function of the radial position along the blade. Detailed aerodynamic design of the APX-45 and APX-48 rotor can be found in Van Rooij and Timmer [242].
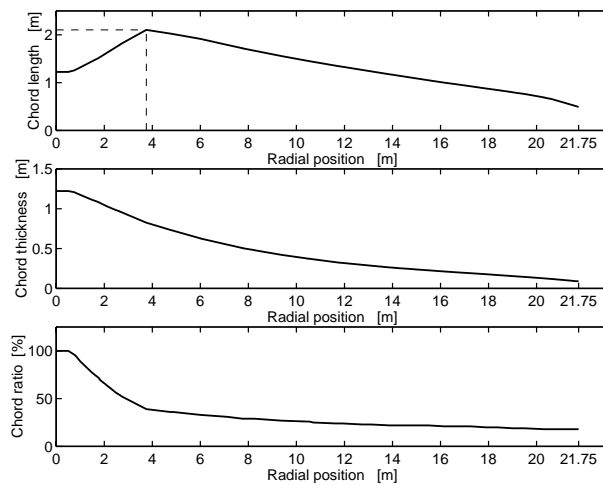

Figure A.2: *Chord of the APX-45/APX-48 rotor blade as function of the radial position along the blade. Upper figure: chord length with dashed lines indicating the maximum length of* 2.104 *at* $r = 3.75$ *m, middle figure: Chord thickness, and lower figure: chord ratio.*

For the purpose of illustration, Fig. A.3 shows a 3-D impression of the APX-45/APX-48 rotor blade.
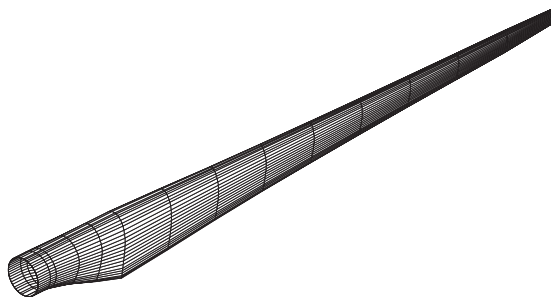
Figure A.3: *A 3-D impression of the APX-45/APX-48 rotor blade. By courtesy of R. van Rooij, Delft University of Technology, The Netherlands.*

The contours of the primary aerofoils (*i.e.* shape of a cross-section of a rotor blade) of the APX-45/APX-48 rotor blade are shown in Fig. A.4. Observe that the relative thickness decreases from root to tip. Thicker aerofoils near the blade root provide greater strength, and can do so without seriously degrading the overall performance of the blade.

NACA 63-218

FFA-W3-211

DU 91-W2-250

DU 97-W-300
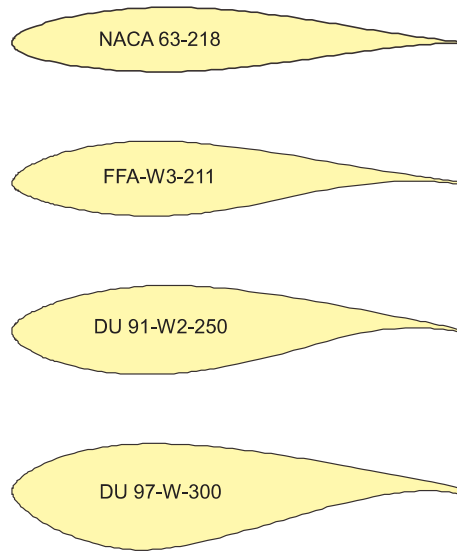
Figure A.4: *The contours of the primary aerofoils of the APX-45/APX-48 rotor blade. The relative thicknesses are from top to bottom* 18.0%, 21.1%, 25.0%, *and* 30.3% *respectively.*

The eigenfrequencies obtained from the full-scale modal test performed by the Stevin Laboratory of Delft University of Technology [156, 241] are listed in Table A.2.

Mode	[rad/s]
1st flap	11.69
1st lead-lag	17.34
2nd flap	33.62
2nd lead-lag	51.33
1st torsional	122.5

Table A.2: *Rotor blade non-rotating eigenfrequencies from a full-scale modal test performed by the Stevin Laboratory of Delft University of Technology.*

The figures indicate that the blades are torsionally rigid. Friedman [67] states that this is typical for wind turbines.

b:) Spacer

The spacers, with a length $L_{sp} = 2.060$ m (*see* Table A.1), are made of steel. The centroidal mass moment of inertia as well as the location of the center of gravity of the spacer is determined from CAD-drawings supplied by Lagerwey.

c:) Rotor hub

The rotor hub is a welded construction made of steel. The total mass (including the three pitch bearings, pitch motors, and gearboxes) of the rotor hub equals 10500 kg. Again, the centroidal mass moment of inertia as well as the location of the center of gravity of the rotor hub is determined from CAD-drawings supplied by Lagerwey.

A.3 Support structure

The support structure of the Lagerwey LW-50/750 wind turbine consists of three main parts, notably

- Tower;

- Foundation;

- Nacelle.

The main technical data of the support structure is summarized in Table A.3. The three support structure parts will be discussed in more detail below.

a:) Tower

The Lagerwey LW-50/750 tower is a a 46.165-meter conical tower with a circular cross section made of steel.

b:) Foundation

The reinforced concrete foundation is described in detail in Jacobs [116].

c:) Nacelle

The nacelle is that part of a turbine that connects the rotor hub to the tower. The nacelle contains the stationary part of the generator (or: stator), and the ground plate at which the yaw mechanism has been placed. The nacelle mass M_n equals the sum of the mass of the chassis M_c and the stator mass M_g^s. The centroidal mass moment of inertia of both the chassis and the stationary part of the generator as well as the locations of the center of gravity w.r.t the tower center at the top

are determined from CAD-drawings supplied by Lagerwey. For the Lagerwey LW-50/750, the nacelle increases the hub height from 46.165 to 50 m. This is necessary to be able to assemble the large synchronous ring generator to the nacelle.

Main technical data support structure

Tower:
  Geometry:
    Height (L_t)   46.165 m
    Shape   conical
    Wall thickness (t)   20 mm ($0.0 \leq h \leq 2.8$), 18 mm ($2.8 < h \leq 5.5$),
         16 mm ($5.5 < h \leq 8.3$), 14 mm ($8.3 < h \leq 11.0$),
         12 mm ($11.0 < h \leq 28.58$), 10 mm ($28.58 < h \leq 46.165$)
    Diameter
      D_{top} 1.92 m @ tower top
      D_{bottom} 3.60 m @ tower bottom
  Material:
    Tubular steel   Fe 360
      E 21e10 N/m^2
      ρ_{st} 7850 kg
      ν 0.286

Foundation:
  Spring stiffness C_f $19.4 \cdot 10^9$ Nm/rad

Nacelle:
  Mass stator M_g^s 8910 kg
  Mass chassis M_c 7350 kg (including yaw motor and bearing, flanges ed.)

Table A.3: *Main technical data Lagerwey LW-50/750 support structure.*

A.4   Generator

The Lagerwey LW-50/750 belongs to a new generation of wind turbines in which the conventional rotor-gearbox-generator drive train is abandoned. The three bladed rotor is directly connected to the (synchronous) generator. This has the major advantage of not having a gearbox and therefore avoiding extensive, and expensive gearbox maintenance. Besides that, the noise level is reduced since the gearbox is a relatively noisy system component.

The Lagerwey LW-50/750 generator is a 750 kW, directly driven (or low-speed), synchronous ring-generator. The power is generated in two star connected three-phase systems. A rectifier at the tower base converts the three-phase alternating currents to 1100 V DC. The DC-bus is very short and, adjacent to the rectifier, is an inverter, which converts the DC to 690 V AC 50-Hz of the utility grid. Insulated gate bipolar transistors IGBT are used as switching elements. Such converters are able to generate almost perfect sine waves with low harmonic distortion (THD $\leq 3\,\%$). This is due to the fact that by switching the IGBT's properly, only the high-frequency harmonics remain. The applied switching frequeny is 2 kHz. Because all power is

rectified to DC and then inverted to AC the generator is decoupled from the utility grid, which allows operation at a wide range of speeds [223]. This configuration thus unites the advantages of variable speed (additional energy capture at partial load and potential reduction of fatigue loads on rotor and drive-train) with those of a grid supply having substatially lower harmonic feedback. The main features are summarized in Table A.4.

Main technical data generator	
General:	
Rated power (P_r^{elec})	750 kW
Rotor speed	
Minimum (n_{min})	19 r.p.m.
Rated (n_r)	27 r.p.m.
Maximum (n_{max})	36 r.p.m.
Number of pole-pairs (p)	42
Number of phases	6
Voltage	690 V
Rated efficiency (η_{conv}^r)	0.97
Geometry:	
Diameter	
Stator	5.50 m.
Rotor	4.90 m.
Airgap between rotor and stator	$5^{\pm 0.5}$ mm.
Mass:	
Rotorwheel	14000 kg

Table A.4: *Main technical data Lagerwey LW-50/750 generator.*

Appendix B

Flow states of a wind turbine rotor

In the previous chapters, a wind turbine is assumed to be operating in its intended state in which kinetic energy is extracted from the wind. The rotor converts the extracted energy into mechanical energy thereby producing a downwind force while slowing down the free-stream wind velocity accordingly. This operating state requires that the axial induction factor lies between zero and unity. This operating state comprises two so-called rotor flow states, notably the windmill and the turbulent wake state. Besides these two flow states, a number of other flow states can be distincted. The axial induction factor a, or equivalently the thrust coefficient C_{dax}, can be used to characterise these different flow states. The following flow states may occur:

- **Propellor**

- **Windmill**

- **Turbulent wake**

- **Vortex ring**

- **Propellor brake**

Fig. B.1 indicates these five rotor flow states in the C_{dax}-a diagram.

Wind turbines normally operate in the *windmill state*, with $0 \leq a \leq 0.5$. Glauerts well-known, and well established blade element momentum theory is generally recommended for use in this flow state, resulting in the following relationship between the thrust coefficient and the axial induction factor:

$$C_{dax} = 4a(1 - a) \qquad \text{(B.1)}$$

This relationship can also be applied for negative axial induction factors (*i.e.* $a < 0$). In this so-called *propellor state* energy is added to the wake thereby producing an upwind force (*i.e.* $C_{dax} < 0$).
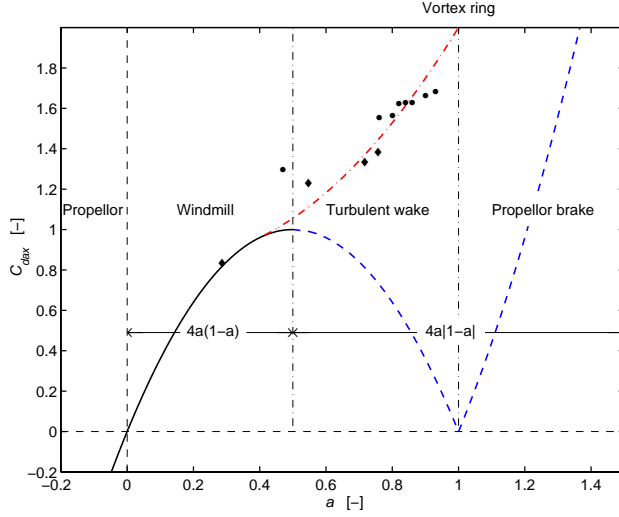
Figure B.1: *Thrust coefficient as function of the axial induction factor and corresponding rotor flow states. Solid curve: momentum theory, dashed curve: momentum theory not valid, dashed-dotted curve: Glauert empirical relation, and ♦, •: measured data [282].*

In the *turbulent wake state* the relationship between the axial induction factor and the thrust coefficient according to the actuator disk/momentum theory has to be replaced by an empirical relation. The explanation for this is that the momentum theory predicts a decreasing thrust coefficient with an increasing axial induction factor, while data obtained from wind turbines show an increasing thrust coefficient [279] (*see* Figure B.1). Thus, the momentum theory is considered to be invalid for axial induction factors larger than 0.5. A number of empirical relations have been derived in order to improve agreement between theory and experiment. These empirical relations are compared in Fig. 2.1 on page 25 for perpendicular flow. Here Glauert's empirical model is depicted in order to illustrate that the C_{dax}-a curve from actuator disk/momentum theory fails to describe to measured results for $0.5 < a < 1.0$. This is consistent with the fact that the (flow streamline) assumptions on which this theory is based are violated in this region.

Wilson and Lissaman extended Eq. (B.1) (knowing that the assumptions are violated) to the region $a > 0.5$ in order to understand the observed differences between momentum theory and experimental results. The resulting equation for the thrust coefficient as function of the axial induction factor is as follows:

$$C_{dax} = 4a|1 - a| \quad \text{for} \quad a > 0.5 \tag{B.2}$$

When the induction factor is somewhat over unity, the rotor flow state is called the *vortex ring state*. For axial induction factors greater than unity, where the rotor reverses the direction of the flow, the state is termed the *propellor brake state*. The

interested reader is referred to Stoddard [282] for a more comprehensive survey.

Appendix C

Comparison of the finite element, lumped-mass and superelement method

In this appendix we will compare exact eigenfrequencies of an Euler-Bernoulli beam with those of the finite element, lumped-mass and superelement method. In Section C.1 the exact eigenfrequencies of an Euler-Bernoulli beam are computed. Section C.2 computes the eigenfrequencies of the finite element approximation. The eigenfrequencies of the lumped-mass approximation are computed in Section C.3, while those of the superelement approximation are computed in Section C.4. The approaches are compared in Section C.5.

C.1 Exact eigenfrequencies

The exact analytical eigenfrequencies are obtained by solving the following frequency equation (*see* Section 4.2):

$$\cos(k_i L) \cosh(k_i L) = -1 \qquad \text{for} \qquad i = 1, 2, 3, \cdots, \infty$$

The first four non-zero positive roots of this equation are:

$$
\begin{aligned}
k_1 * L &= 1.875104069 \\
k_2 * L &= 4.694091133 \\
k_3 * L &= 7.854757438 \\
k_4 * L &= 10.99554073
\end{aligned}
$$

The eigenfrequencies in radians per second corresponding to these values of k_i are obtained as

$$\omega_i = k_i^2 \cdot \sqrt{\frac{EI}{\rho A}} \tag{C.1}$$

where E the modulus of elasticity, I the area moment of inertia, ρ the mass density of the material, and A the cross-sectional area of the beam. Hence, the frequency of vibration of any mode is inversely proportional to square of the length, and proportional to the radius of gyration of the cross-section (*i.e.* $\sqrt{I/A}$). Thus for geometrically similar beams of the same material, the eigenfrequencies vary in direct proportion to the dimensions.

The Euler-Bernoulli beam considered has length $L = 50$ m, modulus of elasticity $E = 21 \cdot 10^{10}$ N/m^2, area of beam cross-section $A = \pi$ m^2, mass density $\rho = 7850$ kg/m^3, and area moment of inertia $I = \frac{1}{4}\pi$ m^4. The first four exact frequencies are listed in Table C.1, and will serve as reference solution.

Mode	Exact eigenfrequencies
1	3.637
2	22.79
3	63.82
4	125.1

Table C.1: *The first four exact eigenfrequencies in radians per second of an Euler-Bernoulli beam with length $L = 50$ m, a constant flexural rigidity EI of $1.6493 \cdot 10^{11}$, a uniformly distributed mass density of 7850 kg/m^3, and a cross-sectional area of π.*

C.2 Finite Element approximation

In this case, the Euler-Bernoulli beam has been modeled using an increasing number of finite elements. The elements are 2-noded, elastic straight 3-D beam elements with 6 degrees of freedom at each node (MARC element type 98). The beam is built in at the base. The eigenfrequencies were calculated using the Lanczos eigenvalue extraction algorithm. The first four eigenfrequencies are listed in Table C.2.

Mode	Number of finite elements					
	3	6	9	12	15	18
1	3.715	3.655	3.644	3.640	3.638	3.637
2	26.81	23.58	23.08	22.91	22.84	22.79
3	-	69.34	65.78	64.62	64.10	63.82
4	-	146.5	132.3	128.0	126.1	125.1
Singularity ratio (10^{-4})	11.534	5.2742	3.4614	2.5820	2.0604	1.7147

Table C.2: *The first four eigenfrequencies in radians per second of the Finite Element approximation as function of the number of finite elements. The singularity ratio is a measure of the reliability of the results. Reliable results are obtained if the ratio is larger than 10^{-4} and smaller than 1.*

From this table it can be concluded that the first four modes are represented very accurately by 18 finite elements. This model has 36 degrees of freedom (actually 216, but in all fairness we do not count the unused degrees of freedom). The singularity ratio (a measure of the reliability of the results; reliable results are obtained if the ratio is larger than 10^{-4} and smaller than 1) indicates that the maximum number of elements has been reached. Increasing this number any further will result in singular equations (*i.e* unreliable results), since the cross sectional area - length of element ratio becomes out of proportion.

C.3   Lumped-mass approximation

In this case, the Euler-Bernoulli beam has been modeled by discretizing it in n equally spaced particles (*i.e.* lumped-masses) connected by joints with springs. In Fig. C.1 this is schematically depicted. Again, the beam is built in at the base. The mass of the lumped-masses has been determined by identifying a portion of the beam such that the inertia effects are modeled by the discrete beam [133].
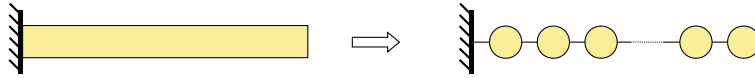
Figure C.1: *Fixed-free Euler-Bernoulli beam discretized with n equally spaced particles (lumped-masses).*

The resulting eigenfrequencies of the lumped-mass approximation as function of the number of lumped-masses can be found in Kelly [133]. We use only the first four eigenfrequencies which are repeated in Table C.3. The pattern is clear: dividing the Euler-Bernoulli beam into more lumped-masses produces more eigenfrequencies, and improves the accuracy. The limiting case being an infinite number of lumped-masses of which the eigenfrequencies equal to those of the exact solution.

Mode	Number of lumped-masses					
	2	3	4	5	6	7
1	3.265	3.461	3.536	3.572	3.591	3.603
2	16.82	19.54	20.78	21.45	21.84	22.08
3	-	48.65	55.03	57.88	59.54	60.60
4	-	-	95.9	108.0	113.3	116.3

Table C.3: *The first four eigenfrequencies in radians per second of the lumped-mass approximation as function of the number of lumped masses.*

C.4 Superelement approximation

In this case, the Euler-Bernoulli beam has been modeled using a number of superelements. Each superelement consists of a series of three rigid bodies connected by springs C_{z1} and C_{z3} as depicted in Fig. C.2. Again, the beam is built in at the base. The torsional spring constants for each superelement are determined as follows:

$$c_{z1} = c_{z3} = \frac{2EI_z}{L_{se}} \qquad [\text{Nm/rad}]$$

with E the modulus of elasticity, I_z the area moment of inertia, and L_{se} the length of the superelement which is, in turn, defined as

$$L_{se} = \frac{L}{N_{se}}$$

with L the length of the Euler-Bernoulli beam and N_{se} the number of superelements the beam is subdivided in (*see* Fig 3.15 on page 72). The most important difference with the lumped-mass method is that rigid bodies within a superelement are not of equal length.
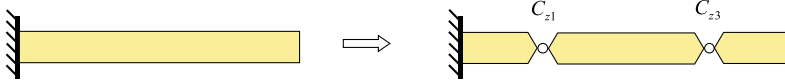
Figure C.2: *Fixed-free Euler-Bernoulli beam discretized with one superelement, with ○: 1 degree of freedom rotational joints.*

The first four eigenfrequencies of the superelement approximation as function of the number of elements are listed in Table C.4. The pattern is clear: dividing the beam into more superelements produces more eigenfrequencies (of which only the first four are shown), and improves the accuracy. The limiting case being an infinite number of superelements of which the eigenfrequencies equal to those of the exact solution. In addition, the mode shapes become better defined with an increasing number of superelements, since information on more locations along the beam is available (*see* Fig. 4.4 on page 119).

C.5 Comparison

The exact analytical solution of Section C.1 is used to evaluate the three approximations. In order to do so, the relative frequency errors are computed. This error is defined as:

$$\text{Relative error} = \frac{\text{Approximated eigenfrequency}}{\text{Exact eigenfrequency}} \cdot 100 - 100 \qquad [\%]$$

Mode	Number of superelements N_{se}, with $k = \frac{1}{2}(1 - \frac{1}{\sqrt{3}})$				
	1	2	3	4	5
1	3.599	3.636	3.636	3.636	3.636
2	36.86	22.12	22.70	22.75	22.75
3	-	73.88	60.90	63.18	63.46
4	-	159.7	140.0	117.8	122.9

Table C.4: *The first four eigenfrequencies in radians per second of the superelement approximation as function of the number of superelements.*

The relative errors for the first four eigenfrequencies of both the finite element and superelement approximation are plotted as function of the number of degrees of freedom in Fig. C.3. Notice that the number of degrees of freedom N_{dof} are related to the number of superelements N_{se} as follows:

$$N_{dof} = 2N_{se}$$
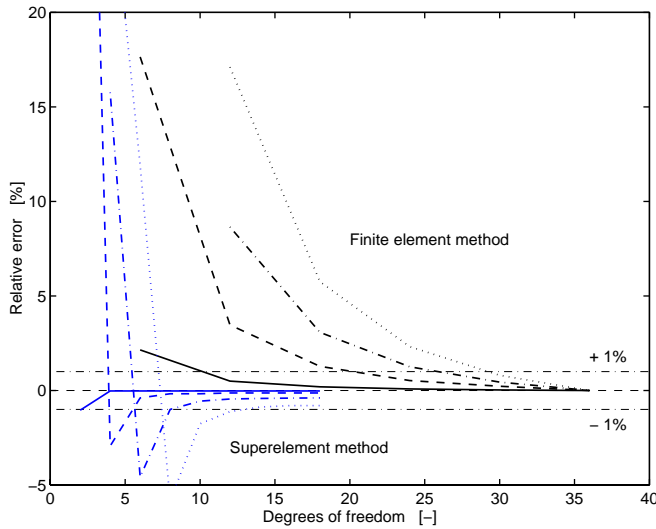
Figure C.3: *The relative errors for the first four eigenfrequencies of the finite element and superelement approximation as function of the number of degrees of freedom. Solid line: first mode, dashed line: second mode, dashed-dotted line: third mode, dotted line: fourth mode, and dashed-dotted horizontal lines: + 1 % and - 1 % error bound respectively.*

The finite element errors are all positive (*i.e.* the eigenfrequencies are overestimated by the finite element model implying that the model is stiffer than the real system), and decrease monotonically with an increasing number of finite elements.

In the superelement approximation, some eigenfrequencies are smaller, and some are larger than in reality, while the errors reach the indicated 1 % error bound rather fast.

The relative errors for the first four eigenfrequencies of the both the lumped-mass and superelement approximation are plotted as function of the number of degrees of freedom in Fig. C.4. Note that, of course, each lumped-mass has one degree of freedom.
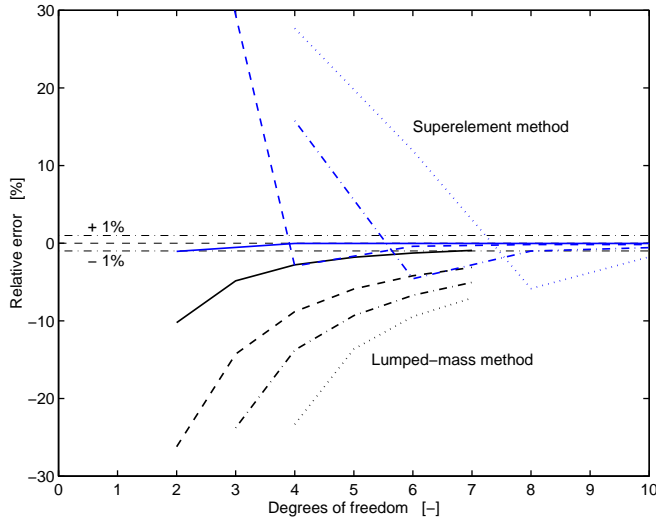
Figure C.4: *The relative errors for the first four eigenfrequencies of the lumped-mass and superelement approximation as function of the number of degrees of freedom. Solid line: first mode, dashed line: second mode, dashed-dotted line: third mode, dotted line: fourth mode, and dashed-dotted horizontal lines: + 1 % and - 1 % error bound respectively.*

Figure C.4 shows that for an Euler-Bernoulli beam both the lumped-mass and the superelement modeling approach represent a consistent approximation to the continuum model (in the sense that it represents a discretization of the continuum model with an approximation accuracy that increases with an increasing number of lumped-masses/superelements).

It can be concluded that the superelement approach is particularly useful for approximating the first number of eigenfrequencies with a limited number of superelements (*i.e.* degrees of freedom). In general, these lowest frequency modes have the largest amplitude and are the most important to be approximated well both for time-domain simulation and control system design.

Appendix D

Proofs of Section 3.5

This appendix contains the proofs of the elimination of the non measurable variables in the stator flux equations of Section 3.5. In Section D.1 both Eq. (3.99) and Eq. (3.100) are proven. In Section D.2 Eq. (3.101) is proven.

D.1 Direct-axis

The equation for the field winding voltage, and the equation for the voltage across the direct-axis damper are given by

$$U_f = R_f I_f + s\Psi_f \tag{D.1}$$
$$0 = -R_{1d}I_{1d} - s\Psi_{1d} \tag{D.2}$$

and the flux linkage equations on the direct-axis are given by

$$\Psi_d = L_d I_d + kM_f I_f + kM_{1d}I_{1d} \tag{D.3}$$
$$\Psi_f = kM_f I_d + L_f I_f + M_r I_{1d} \tag{D.4}$$
$$\Psi_{1d} = kM_{1d}I_d + M_r I_f + L_{1d}I_{1d} \tag{D.5}$$

Substituting Eq. (D.5) in Eq. (D.2) gives

$$0 = -R_{1d}I_{1d} - s\left\{kM_{1d}I_d + M_r I_f + L_{1d}I_{1d}\right\}$$

Rearranging leads to

$$I_{1d}\left(1 + \tau_{1d}\,s\right) = -s\left(\frac{kM_{1d}}{R_{1d}}\right)I_d - s\left(\frac{M_r}{R_{1d}}\right)I_f \tag{D.6}$$

with

$$\tau_{1d} = \frac{L_{1d}}{R_{1d}}$$

the rotor time constant for the direct-axis.

Substituting this result in Eq. (D.3) gives

$$\Psi_d = L_d I_d + k M_f I_f + \frac{k M_{1d}}{(1 + \tau_{1d} s)} \left\{ -s \left(\frac{k M_{1d}}{R_{1d}} \right) I_d - s \left(\frac{M_r}{R_{1d}} \right) I_f \right\}$$

Rearranging leads to

$$
\begin{aligned}
\Psi_d &= \left(L_d - \frac{k^2 M_{1d}^2}{R_{1d}} \frac{s}{(1 + \tau_{1d} s)} \right) I_d + \left(k M_f - \frac{k M_{1d}}{(1 + \tau_{1d} s)} \frac{M_r}{R_{1d}} s \right) I_f \\
&= \underbrace{\left(\frac{(1 + \tau_{1d} \sigma_{1d} s)}{(1 + \tau_{1d} s)} L_d \right)}_{L_{do}(s)} I_d + \underbrace{\left(\frac{(1 + \tau_{1d} \mu_{1d} s)}{(1 + \tau_{1d} s)} k M_f R_{1d} \right)}_{L_{dfo}(s)} I_f \qquad \text{(D.7)}
\end{aligned}
$$

with

$$\tau_{1d} = \frac{L_{1d}}{R_{1d}} \qquad \sigma_{1d} = 1 - \frac{k^2 M_{1d}^2}{L_d L_{1d}}$$

and

$$\mu_{1d} = 1 - \frac{M_{1d} M_r}{L_{1d} M_f}$$

Analogously, substituting Eq. (D.6) in Eq. (D.4) gives

$$\Psi_f = k M_f I_d + L_f I_f + \frac{M_r}{(1 + \tau_{1d} s)} \left\{ -s \left(\frac{k M_{1d}}{R_{1d}} \right) I_d - s \left(\frac{M_r}{R_{1d}} \right) I_f \right\}$$

and rearranging leads to

$$
\begin{aligned}
\Psi_f &= \left(k M_f - \frac{k M_{1d}}{(1 + \tau_{1d} s)} \frac{M_r}{R_{1d}} s \right) I_d + \left(L_f - \frac{M_r^2}{R_{1d}} \frac{s}{(1 + \tau_{1d} s)} \right) I_f \\
&= \underbrace{\left(\frac{(1 + \tau_{1d} \mu_{1d} s)}{(1 + \tau_{1d} s)} k M_f R_{1d} \right)}_{L_{fdo}(s)} I_d + \underbrace{\left(\frac{(1 + \tau_{1d} \sigma_r s)}{(1 + \tau_{1d} s)} L_f \right)}_{L_{fo}(s)} I_f \qquad \text{(D.8)}
\end{aligned}
$$

with

$$\tau_{1d} = \frac{L_{1d}}{R_{1d}} \qquad \mu_{1d} = 1 - \frac{M_{1d} M_r}{L_{1d} M_f}$$

and

$$\sigma_r = 1 - \frac{M_r^2}{L_f L_{1d}}$$

In matrix form

$$
\begin{aligned}
\begin{bmatrix} \Psi_d \\ \Psi_f \end{bmatrix} &= \begin{bmatrix} L_{do}(s) & L_{dfo}(s) \\ L_{fdo}(s) & L_{fo}(s) \end{bmatrix} \cdot \begin{bmatrix} I_d \\ I_f \end{bmatrix} \\
&= \frac{1}{(1 + \tau_{1d} s)} \begin{bmatrix} (1 + \tau_{1d} \sigma_{1d} s) L_d & (1 + \tau_{1d} \mu_{1d} s) k M_f R_{1d} \\ (1 + \tau_{1d} \mu_{1d} s) k M_f R_{1d} & (1 + \tau_{1d} \sigma_r s) L_f \end{bmatrix} \cdot \begin{bmatrix} I_d \\ I_f \end{bmatrix}
\end{aligned}
$$

A few observations can be made. The most important one is that the denominators of $L_{do}(s)$, $L_{dfo}(s)$, $L_{fdo}(s)$, and $L_{fo}(s)$ are all the same. In addition, the nominators of $L_{dfo}(s)$ and $L_{fdo}(s)$ are identical. Consequently,

$$L_{dfo}(s) = L_{fdo}(s) \tag{D.9}$$

with a DC-gain of $kM_f R_{1d}$. In this thesis this DC-gain is referred to as L_{fdo}^{DC} (or L_{dfo}^{DC}). Furthermore, the DC-gain of $L_{do}(s)$ is equal to that of $L_d(s)$ and is referred to as L_d^{DC}. Finally, the DC-gain of $L_{fo}(s)$ is equal to L_f and is referred to as L_{fo}^{DC}.

The aforementioned conclusion that the denominators of $L_{do}(s)$, $L_{dfo}(s)$, $L_{fdo}(s)$, and $L_{fo}(s)$ are identical is valid only for the case that one damper winding is located on the direct-axis. Below we will show that this conclusion can be generalized for n damper windings. Consider the n equations for the voltage across the direct-axis dampers:

$$
\begin{aligned}
0 &= -R_{1d}I_{1d} - s\Psi_{1d} \\
0 &= -R_{2d}I_{2d} - s\Psi_{2d} \\
\vdots\ &= \quad\vdots\qquad\vdots \\
0 &= -R_{nd}I_{nd} - s\Psi_{nd}
\end{aligned}
$$

In matrix form

$$
\begin{bmatrix} 0 \\ 0 \\ 0 \\ \vdots \\ 0 \end{bmatrix} = -
\begin{bmatrix}
R_{1d} & 0 & 0 & \cdots & 0 \\
0 & R_{2d} & 0 & \cdots & 0 \\
0 & 0 & R_{3d} & \cdots & 0 \\
\vdots & \vdots & \vdots & \ddots & \vdots \\
0 & 0 & 0 & \cdots & R_{nd}
\end{bmatrix}
\cdot
\begin{bmatrix} I_{1d} \\ I_{2d} \\ I_{3d} \\ \vdots \\ I_{nd} \end{bmatrix}
-
\begin{bmatrix}
s & 0 & 0 & \cdots & 0 \\
0 & s & 0 & \cdots & 0 \\
0 & 0 & s & \cdots & 0 \\
\vdots & \vdots & \vdots & \ddots & \vdots \\
0 & 0 & 0 & \cdots & s
\end{bmatrix}
\cdot
\begin{bmatrix} \Psi_{1d} \\ \Psi_{2d} \\ \Psi_{3d} \\ \vdots \\ \Psi_{nd} \end{bmatrix}
$$

The corresponding direct-axis and field winding flux linkage equations are given by

$$
\begin{aligned}
\Psi_d &= L_d I_d + kM_f I_f + kM_{1d}I_{1d} + kM_{2d}I_{2d} + \cdots + kM_{nd}I_{nd} \\
\Psi_f &= kM_f I_d + L_f I_f + M_{1r}I_{1d} + M_{2r}I_{2d} + \cdots + M_{nr}I_{nd}
\end{aligned}
$$

while the damper winding flux linkage equations are given by

$$
\begin{aligned}
\Psi_{1d} &= kM_{1d}I_d + M_{1r}I_f + L_{1d}I_{1d} + M_{1d2d}I_{2d} + \cdots + M_{1dnd}I_{nd} \\
\Psi_{2d} &= kM_{2d}I_d + M_{2r}I_f + L_{2d}I_{2d} + M_{2d1d}I_{1d} + \cdots + M_{2dnd}I_{nd} \\
\vdots\ &= \quad\vdots\qquad\quad\vdots\qquad\quad\vdots\qquad\quad\vdots\qquad\quad\vdots\qquad\quad\vdots \\
\Psi_{nd} &= kM_{nd}I_d + M_{nr}I_f + L_{nd}I_{nd} + M_{nd1d}I_{1d} + \cdots + M_{ndnd-1}I_{nd-1}
\end{aligned}
$$

with

$$M_{idjd} = M_{jdid} \qquad \text{for} \quad i \neq j$$

239

In matrix form

$$
\begin{bmatrix} \Psi_{1d} \\ \Psi_{2d} \\ \Psi_{3d} \\ \vdots \\ \Psi_{nd} \end{bmatrix} = \left[\begin{array}{cc|cccccc} k\,M_{1d} & M_{1r} & L_{1d} & M_{1d2d} & M_{1d3d} & \cdots & M_{1dnd} \\ k\,M_{2d} & M_{2r} & M_{1d2d} & L_{2d} & M_{2d3d} & \cdots & M_{2dnd} \\ k\,M_{3d} & M_{3r} & M_{1d3d} & M_{2d3d} & L_{3d} & \cdots & M_{3dnd} \\ \vdots & \vdots & \vdots & \vdots & \vdots & \ddots & \vdots \\ k\,M_{nd} & M_{nr} & M_{1dnd} & M_{2dnd} & M_{3dnd} & \cdots & L_{nd} \end{array} \right] \cdot \begin{bmatrix} I_d \\ I_f \\ \hline I_{1d} \\ I_{2d} \\ I_{3d} \\ \vdots \\ I_{nd} \end{bmatrix}
$$

The derivation of $\Psi_d = f(I_d, I_f)$ and $\Psi_f = f(I_d, I_f)$ via substitution and rearranging of the aforementioned equations is very time-consuming with pen and paper. Therefore, we have decided to use the mathematical manipulation package MAPLE V [45] to symbolically determine the aforementioned expressions. Next, the I_f and I_d components are extracted from $\Psi_d = f(I_d, I_f)$ and $\Psi_f = f(I_d, I_f)$. Subsequently, the numerators and denominators of both $L_{do}(s)/L_{fdo}(s)$ and $L_{dfo}(s)/L_{fo}(s)$ are determined. Finally, the four denominators and the numerators of $L_{fdo}(s)$ and $L_{dfo}(s)$ are compared in order to check the general conclusion.

For example, consider the case where two damper windings are located on the d-axis (*i.e.* $n = 2$):

```
%
% Maple V input:
%

%
% Psid:
%

eq1:= -R1d*I1d-s*Psi1d=0:
eq2:= -R2d*I2d-s*Psi2d=0:
eq3:= k*M1d*Id+M1r*If+L1d*I1d+M1d2d*I2d=Psi1d:
eq4:= k*M2d*Id+M2r*If+L2d*I2d+M1d2d*I1d=Psi2d:
eq5d:= Ld*Id+k*Mf*If+k*M1d*I1d+k*M2d*I2d=Psid:

%

SolutionSetPsid:=solve({eq1,eq2,eq3,eq4,eq5d},{Psi1d,I1d,Psi2d,I2d,Psid});

%
% Select Psid from SolutionSet:
%
% --> Psid = (Ld*Id*R1d*R2d+Ld*Id*R1d*s*L2d+ ...
%             +k*M2d*s^2*M1r*If*M1d2d) / ...
%             (R1d*R2d+R1d*s*L2d+s*L1d*R2d+s^2*L1d*L2d-s^2*M1d2d^2)
%

op(3,SolutionSetPsid);

%
% --> Psid = ...
%
```

```
Psid:=(...);
Psid:=collect(Psid,[Id,If]);

%
% Extract Ldo(s)*Id and Ldfo(s)*If from expression:
%

Ldo:=op(1,Psid);
Ldfo:=op(2,Psid);

%
% Compute numerators and denominators:
%

num_LdoId:=numer(Ldo);
nops_LdoId:=nops(num_LdoId);
%
% --> nops_LdoId:= 2
%
num_Ldo:=op(nops(num_LdoId)-1,num_LdoId);
den_Ldo:=denom(Ldo);

num_LdfoIf:=numer(Ldfo);
nops_LdfoIf:=nops(num_LdfoIf);
%
% --> nops_LdfoIf:= 3
%
num_Ldfo:=op(nops_LdfoIf-1,num_LdfoIf)*op(nops_LdfoIf-2,num_LdfoIf);
den_Ldfo:=denom(Ldfo);

%
%
%

%
% Psif:
%

eq5f:= k*Mf*Id+Lf*If+M1r*I1d+M2r*I2d=Psif:

%

SolutionSetPsif:=solve({eq1,eq2,eq3,eq4,eq5f},{Psi1d,I1d,Psi2d,I2d,Psif});

%
% Select Psif from SolutionSet:
%

op(3,SolutionSetPsif);

%
% --> Psif = ...
%

Psif:=(...);
Psif:=collect(Psif,[Id,If]);
```

```
%
% Extract Lfdo(s)*Id and Lfo(s)*If from expression:
%

Lfdo:=op(1,Psif);
Lfo:=op(2,Psif);

%
% Compute numerators and denominators:
%

num_LfdoId:=numer(Lfdo);
nops_LfdoId:=nops(num_LfdoId);
%
% --> nops_LfdoId:= 3
%
num_Lfdo:=op(nops(num_LfdoId)-2,num_LfdoId)*op(nops(num_LfdoId)-1,num_LfdoId);
den_Lfdo:=denom(Lfdo);

num_LfoIf:=numer(Lfo);
nops_LfoIf:=nops(num_LfoIf);
%
% --> nops_LfoIf:= 2
%
num_Lfo:=op(nops(num_LfoIf)-1,num_LfoIf);
den_Lfo:=denom(Lfo);

%
% Check whether denominators and numerators are identical:
%

(den_Ldo-den_Ldfo)-(den_Lfdo-den_Lfo);
(num_Ldfo-num_Lfdo);

%
%
%
```

Investigation has shown that the four denominators as well as the numerators of L_{dfo} and L_{fdo} are identical at least till 4 damper windings. Due to similarity, it is expected that this conclusion holds for a finite number of damper windings.

D.2 Quadrature-axis

The equation for the voltage across the quadrature-axis damper is given by

$$0 = -R_{1q}I_{1q} - s\Psi_{1q} \tag{D.10}$$

and the flux linkage equations on the quadrature-axis are given by

$$\Psi_q = L_q I_q + kM_{1q}I_{1q} \tag{D.11}$$
$$\Psi_{1q} = kM_{1q}I_q + L_{1q}I_{1q} \tag{D.12}$$

Rearranging Eq. (D.11) gives

$$I_{1q} = \frac{\Psi_q - L_q I_q}{k M_{1q}} \tag{D.13}$$

Substituting this result in Eq. (D.12) gives

$$\Psi_{1q} = k M_{1q} I_q + L_{1q} \left\{ \frac{\Psi_q - L_q I_q}{k M_{1q}} \right\} \tag{D.14}$$

Substituting Eq. (D.13) and Eq. (D.14) in Eq. (D.10) gives

$$0 = -R_{1q} \left\{ \frac{\Psi_q - L_q I_q}{k M_{1q}} \right\} - s \left\{ k M_{1q} I_q + L_{1q} \left(\frac{\Psi_q - L_q I_q}{k M_{1q}} \right) \right\} \tag{D.15}$$

Rearranging Eq. (D.15) gives

$$
\begin{aligned}
\Psi_q \left\{ \frac{R_{1q}}{k M_{1q}} + \frac{s L_{1q}}{k M_{1q}} \right\} &= \left\{ \frac{R_{1q} L_q}{k M_{1q}} \right\} I_q - \{ s k M_{1q} \} I_q + \left\{ \frac{s L_{1q} L_q}{k M_{1q}} \right\} I_q \\
\Psi_q \left\{ 1 + \frac{L_{1q}}{R_{1q}} \cdot s \right\} &= \left\{ L_q - \frac{s \, k^2 M_{1q}^2}{R_{1q}} + \frac{s L_{1q} L_q}{R_{1q}} \right\} I_q \\
&= L_q I_q \left\{ 1 + \frac{L_{1q}}{R_{1q}} \cdot s - \frac{k^2 M_{1q}^2}{R_{1q}} \frac{1}{L_q} \cdot s \right\} \\
&= L_q I_q \left\{ 1 + \underbrace{\frac{L_{1q}}{R_{1q}}}_{\tau_{1q}} \underbrace{\left(1 - \frac{k^2 M_{1q}^2}{L_q L_{1q}} \right)}_{\sigma_{1q}} \cdot s \right\} \tag{D.16}
\end{aligned}
$$

with τ_{1q} the rotor time constant for the quadrature-axis and σ_{1q} the leakage factor. Rearranging the above equation leads to

$$
\begin{aligned}
\Psi_q &= L_q I_q \frac{1 + \tau_{1q} \sigma_{1q} \cdot s}{1 + \tau_{1q} \cdot s} \\
&= \underbrace{\left(L_q \frac{1 + \tau_{1q} \sigma_{1q} \cdot s}{1 + \tau_{1q} \cdot s} \right)}_{L_q(s)} \cdot I_q
\end{aligned}
$$

$\square$

Appendix E

Main wind turbine modes of operation

In this chapter the main wind turbine modes of operation will be discussed. In general, the following modes of operation can be distinguished [179]:

- **Startup**

- **Power generation**

- **Shutdown**

- **Emergency**

In the startup mode the rotor of the wind turbine is accelerated, and the generator is connected to the utility grid.

In the power generation mode, power is extracted from the wind and converted to electricity. In this mode the wind velocity ranges from the cut-in wind velocity V_{ci}, via the rated velocity V_r to the cut-out wind velocity V_{co} as illustrated in Fig. E.1 for a fictive variable rotational speed wind turbine. For the purpose of illustration, the values for V_{ci}, V_r and V_{co} are 3.0, 12.5 and 25.0 m/s respectively for the Lagerwey LW-50/750. In the power generating mode, two different operating areas can be distinguished, *viz.* partial load ($V_{ci} < V_w \leq V_r$) and full load ($V_r \leq V_w < V_{co}$) [36]. In partial load, the aerodynamic (or rotor) power is proportional to the cubic wind velocity. In this operating area maximum energy capture can be achieved by tracking the optimum tip-speed ratio curve (*i.e.* the λ_{opt}-curve). Above the rated wind velocity the aerodynamic power P (and by that the rated generator power) is kept at a constant level: P_r. This is a given fact from generator design, in what, among other things, the wind regime, heat rise and loads acting on the construction are considered. This can be achieved either by stall or, in case of adjustable blades, by pitching the rotor blades towards a smaller (*i.e.* feathering control) or larger angle of attack (active stall control). In Molenaar [188] it has been concluded that i) adjustable blades are preferred to blades with a fixed pitch angle (despite the

higher initial costs), and ii) pitching the blades towards a smaller angle of attack is preferred to active stall control.
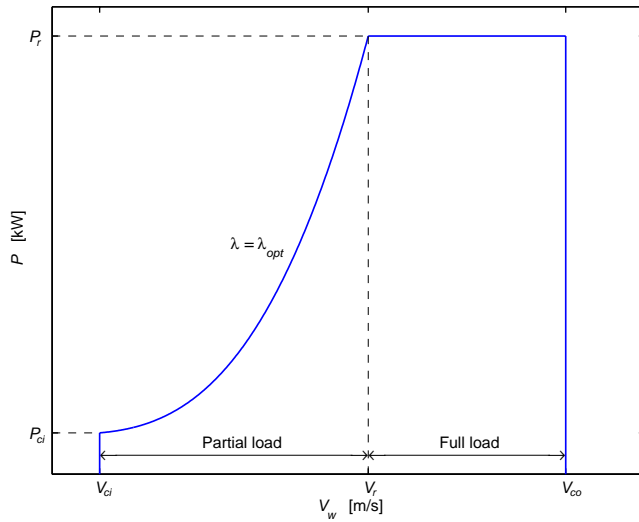
Figure E.1: *Rotor power (P) as a function of the undisturbed wind velocity (V_w) of a fictive variable rotational speed wind turbine, with V_{ci}: cut-in wind velocity, V_r: rated wind velocity, V_{co}: cut-out wind velocity, P_{ci}: start power, P_r: rated aerodynamic power, and λ: tip-speed ratio.*

In the shutdown mode the generator is disconnected and the turbine is decelerated. The system is in an emergency mode if a serious malfunction has been detected (*e.g.* failed pitch mechanism). If happens, the backup systems are invoked by the supervisory control system to provide for a safe shutdown.

Appendix F

Modal analysis measurement equipment

This appendix describes the measurement equipment used in the "modal analysis". Section F.1 lists the main specifications of the cable used to excite the Lagerwey LW-50/750 wind turbine. The main features of the data acquisition system are presented Section F.2. Section F.3 lists the main specifications of the force transducer. Finally, Section F.4 presents the specifications as well as locations of the accelerometers used.

F.1 Cable

The static load is applied to the tower by a 225 meter long TWARON® cable anchored a 20-ton winch truck using a pin joint (*see* Fig. F.1). TWARON® is a lightweight, superstrong synthetic fiber made from the aramid polymer. The cable has a tensile strength of 170 kN and a total mass of 82.5 kg (*i.e.* including pin joints). The interested reader is referred to the homepage of Twaron Products V.o.F. (www.twaron.com) for detailed information about TWARON®.

Figure F.1: *Detail of the TWARON cable and pin joint.*

F.2 Data acquisition system

Two supervisory control and data acquisition systems (SCADAS II) of Leuven Measurement Systems (LMS) with each 24 channels are used to store the time-domain as well as frequency domain data [249]. The name plate data of both SCADAS are listed in Fig. F.2.

<table>
<tr><td colspan="2">LMS-DIFA SCADAS II Data Acquisition Systems</td></tr>
<tr>
<td>
LMS-DIFA Measuring Systems
• Type: SC 212-1
• 24 channels
• Block size: 32768
• PDFA modules
• Serial number: 81904002
• 09/2000 – 09/2001
</td>
<td>
LMS-DIFA Measuring Systems
• Type: SC 212-1
• 24 channels
• Block size: 32768
• PDFA modules
• Serial number: 81904003
• 09/2000 – 09/2001
</td>
</tr>
</table>

Figure F.2: *Name plate data of LMS-DIFA SCADAS II data acquisition system.*

The programmable dual filter amplifier (PDFA) module in the LMS-DIFA SCADAS II is a universal signal conditioning module providing two identical, but each independently programmable differential amplifiers and analogue anti-aliasing filters. The PDFA includes a current source to provide power to integrated circuit piezoelectric transducers.

Five commonly used types of analogue filters are Butterworth, Elliptic, Chebyshev (Type I and II), and Bessel. These so-called infinite impulse response (IIR) filters all approximate the ideal filter in different ways. Note that an ideal low-pass filter would have no attenuation in the pass band (*i.e.* $0 < f < f_{co}$), infinite attenuation in the stopband (*i.e.* $f > f_{co}$), and a zero phase characteristic. In practice, a linear phase characteristic is often regarded as "ideal". After all, a linear phase characteristic introduces a time shift but preserves the wave shapes. Of the five mentioned filter types, elliptic filters usually meet a given set of filter performance specifications with the lowest filter order.

The PDFA anti-aliasing filters are eighth-order elliptic filters. They are built up by cascading four identical second order filter stages to approximate the ideal filter. Three filter characteristics are available, *viz.* PDFA-ETD (Equal Time Delay), PDFA-ELL (Elliptical), and PDFA-US (Ultra Sharp). We have used the PDFA-ETD anti-aliasing filter. The cutoff frequency f_{co} of this filter can be varied from 10 Hz to 10.23 kHz in 10 Hz steps to meet the sample frequency and frequency range of interest requirements. The ETD filter uses 8 poles and 8 zeros to approximate the ideal filter. The result is a linear phase response within $2.2°$ while the stopband attenuation of 70 dB is reached at $3.7 \cdot f_{co}$. The Bode diagram of this filter is depicted in Fig. F.3.

The sampling and quantisation is carried out by a 16-bit A/D converter. The accuracy of the sampling and quantisation process depends on the number of quantisation levels available in the A/D converter (an n-bit converter has 2^n quantisation levels). In practice, the measured signal should occupy as much of the range of the

248
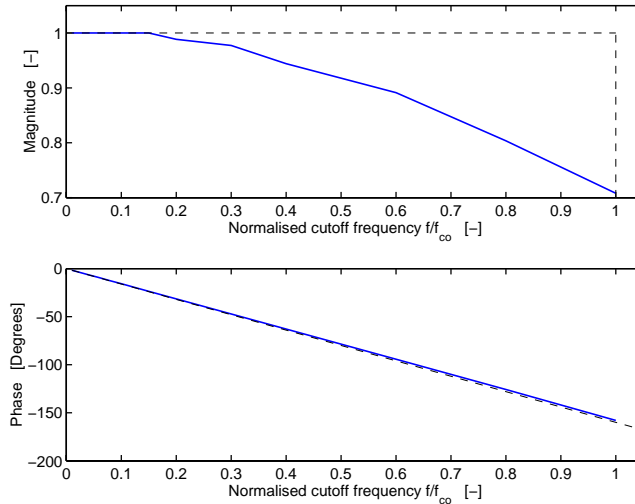
Figure F.3: *Amplitude and phase characteristic of the Equal Time Delay anti-aliasing filter as a function of the normalised cutoff frequency f/f_{co}. Dashed line: ideal low-pass filter with phase proportional to f/f_{co}.*

A/D converter as possible. Provided that is done, quantisation errors are normally insignificant [170, 265]. The data were collected with a sample rate of 1000 Hz (measurement M1) and 500 Hz (measurement M2-M10), and with the cutoff frequency of the ETD low-pass filter set to 330 and 160 Hz respectively.

F.3 Force transducer

The magnitude of the input force is measured in-line with the cable between the quick release mechanism and the winch truck using a force transducer. The name plate data of the force transducer is listed in Fig. F.4.

Figure F.4: *Name plate data of the force transducer.*

F.4 Accelerometers

Three types of accelerometers are used, *viz.* Endevco model 2262A-25, Endevco model 2262A-200, and Sundstrand model QA-700. The Endevco accelerometers are rugged, fluid damped transducers of the piezoresistive type. The output range of model 2262A-25 is ± 25 g, and of model 2262A-200 ± 200 g. Both models are light weight (28 gram), high-sensitivity (20 mV/g and 2.5 mV/g respectively at 100 Hz). The static acceleration limit is 250 g for model 2262A-25 and 1000 g for model 2262A-200. The frequency range of model 2262A-25 is from 0 to 650 Hz and of model 2262A-200 from 0 to 1800 Hz. Detailed technical data can be found at www.endevco.com.

The integral electronics in the Sundstrand accelerometers develop an acceleration-proportional output current providing both static and dynamic acceleration measurements. They have an output range of ± 30 g and a maximum bias of $8 \cdot 10^{-3}$ g. The static acceleration limit is 250 g. The Sundstrand accelerometers weigh 46 grams. Detailed technical data can be found at www.inertialsensor.com.

The high-sensitivity of both the Endevco and Sundstrand accelerometers is ideal for obtaining good signal-to-noise ratio even when the response amplitudes are low.

F.4.1 Accelerometer mounting

For an accelerometer to generate accurate and useful data, it must be properly coupled to the system under investigation. This means that the mounting must be rigid over the frequency range of interest to avoid distortion of the frequency response of the measurement. The natural frequency of an accelerometer, when mounted, is dependent on the stiffness of the coupling method. This requires a proper selection of the accelerometer mounting technique to be applied as well as thorough surface preparation. The following mounting methods are commonly used:

- **Threaded studs**;

- **Adhesives** (*e.g.* hot glue, double-back tape, and cyanoacrylate);

- **Magnetic adapters**.

The key question is which mounting method is most suited for the intended purpose. The recommended mounting method is that used for calibration [177]. Issues that must be considered include: weight of the accelerometer, required bandwidth of the measurement, amplitude anticipated, type of mounting surface, and whether or not a mounting surface may be altered.

When possible, the best method is to mount an accelerometer with a stud since no adhesive is as stiff as a mounting stud. Cyanoacrylate instant adhesives have the widest frequency range and the broadest temperature limits of the adhesive-mount options for accelerometers weighing less than 10 grams, but attachment on rough surfaces is difficult and removal is time consuming [178]. Double back tape and hot glue are viable alternatives when removal time is an important issue. Hot glue is the preferred method of attachment for systems having hard to reach areas. Magnetic

mounting is convenient and easily accomplished for accelerometers weighing over 50 grams. This method, however, reduces the usable bandwidth.

In our case it was not allowed to tap holes into the tower and rotor blades for a stud mount. We have decided to mount the accelerometers on the blades with hot glue (for easy attachment and removal) and to mount the accelerometers on the tower with double-back tape.

F.4.2 Accelerometer positions

The accelerometer positions are listed in Table F.1. The tower postions are measured with respect to the ground level, the blade postions are measured with respect to the blade tips.

Accelerometers				
Tag	Position	Tower/Blade	Orientation	Type
A-01	0.00	Tower	$-$ (x)	QA-700
A-02	12.66	Tower	$-$ (x)	QA-700
A-03	21.80	Tower	$-$ (x)	QA-700
A-04	36.00	Tower	$-$ (x)	QA-700
A-05	44.38	Tower	$-$ (x)	QA-700
A-06	13.75	Blade A	L1 (z)	2262A-25
A-07	13.75	Blade A	D1 (x)	2262A-25
A-08	7.75	Blade A	L1 (z)	2262A-200
A-09	7.75	Blade A	D1 (x)	2262A-200
A-10	7.75	Blade A	D2 (x)	2262A-200
A-11	1.75	Blade A	L1 (z)	2262A-200
A-12	1.75	Blade A	D1 (x)	2262A-200
A-13	1.75	Blade A	D2 (x)	2262A-200
A-14	1.75	Blade B	L1 (z)	2262A-200
A-15	1.75	Blade B	D1 (x)	2262A-200
A-16	1.75	Blade B	D2 (x)	2262A-200
A-17	1.75	Blade C	L1 (z)	2262A-200
A-18	1.75	Blade C	D1 (x)	2262A-25
A-19	1.75	Blade C	D2 (x)	2262A-25

Table F.1: *Accelerometer positions on both the tower (w.r.t. ground level) and the rotor blades (w.r.t. blade tip). During the parked modal test, blade A is pointing upwards (i.e. at 12 o'clock position) while blade B and C are numbered anti-clockwise (rotation about x-axis).*

The orientation of the rotor blade accelerometers is shown in Fig. F.5. The "L1" accelerometers are placed at the rotor blade nose. The "D1" accelerometers

are placed on the rib, while the "D2" accelerometers are placed midway the "D1" accelerometers and the tail.
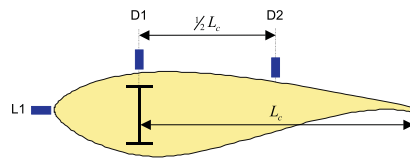
Figure F.5: *Orientation of the accelerometers mounted on the rotor blades.*

Appendix G

Frequency response functions

This appendix gives a brief review of the main properties of frequency response functions. Section G.1 treats a single degree of freedom system, while Section G.2 treats a two degrees of freedom system.

G.1 Single degree of freedom

Consider the single degree of freedom (SDOF) system shown in Fig. G.1. The system consists of a rigid body of length L that is free to rotate about the axis of rotation and that is connected to the ground through a torsional spring. Damping is completely neglected. For a rigid body in pure rotation about a fixed axis, Newton's second law of motion states that the sum off all torques about a given axis is equal to the product of the mass moment of inertia of a body about that axis and its angular acceleration. Consequently, the equation of motion for the above system can be written as

$$J_O \, \ddot{\theta} = M_O \tag{G.1}$$

where J_O, θ, and M_O are, respectively, the mass moment of inertia about point O, the angle of rotation, and the external moment about O.
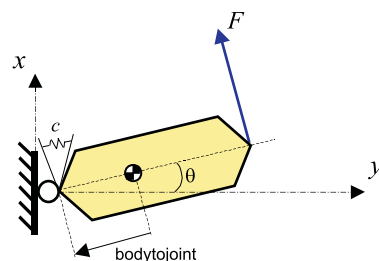
Figure G.1: *Single degree of freedom system consisting of a rigid body of length L connected to the ground by means of a pin joint.*

According to the parallel-axis theorem, the mass moment of inertia about point O is related to the mass moment of inertia about its center of mass, J_{C_g}, as follows

$$J_O = J_{C_g} + m(y_{b2j})^2 \qquad \text{(G.2)}$$

where m the mass of the rigid body, and y_{b2j} is the distance from the center of mass to point O (the so-called bodytojoint vector in SD/FAST$^\circledR$'s system description file).

Substituting the expression for the bending moment in Eq. (G.1) gives

$$J_O \ddot{\theta} = FL - c\theta \qquad \text{(G.3)}$$

where L the length of the rigid body, and c the torsional spring stiffness. Taking the Laplace transform on each side of Eq. (G.3), and assuming zero initial conditions results in the following equation

$$
\begin{aligned}
J_O s^2 \theta(s) &= F(s)L - c\theta(s) \\
\Rightarrow \quad \left(J_O s^2 + c\right)\theta(s) &= F(s)L
\end{aligned}
\qquad \text{(G.4)}
$$

The ratio of transformed response $\theta(s)L$ (output) to the transformed excitation $F(s)$ (input) can be expressed as

$$H(s) = \frac{\theta(s)L}{F(s)} = \frac{L^2/J_O}{s^2 + c/J_O} \qquad \text{(G.5)}$$

which is known as the system transfer function. The transfer function describes the system under analysis in terms of poles and residues, and gives the dynamic response of a system under any type of excitation, including periodic and harmonic ones. Evaluating the transfer function only in the frequency domain, *i.e.* along the imaginary axis, gives

$$H(\omega) = H(s)\Big|_{s=j\omega} = \frac{L^2/J_O}{c/J_O - \omega^2} \qquad \text{(G.6)}$$

which is called the system's frequency response function (FRF). Notice that the FRF is just a particular case of the transfer function, and that it gives the dynamic response of a system under sinusoidal excitation only. In practice, however, it may replace the transfer function without loss of useful information [126].

Notice that Eq. (G.3) is an ordinary second order mass-spring equation. This means that we need two state variables to transform this differential equation to state-space form. We choose θ and $\dot{\theta}$ as state variables, or define

$$
\begin{aligned}
\theta_1 &= \theta \\
\theta_2 &= \dot{\theta}
\end{aligned}
$$

Then we obtain

$$
\begin{aligned}
\dot{\theta}_1 &= \theta_2 \\
\dot{\theta}_2 &= -\left(\frac{c}{J_0}\right)\theta_1 + \left(\frac{L}{J_0}\right)F
\end{aligned}
\qquad \text{(G.7)}
$$

The output equation is

$$y = L\,\theta_1 \tag{G.8}$$

In vector-matrix form, Eq. (G.7) and (G.8) can be written as

$$\begin{bmatrix} \dot{\theta}_1 \\ \dot{\theta}_2 \end{bmatrix} = \begin{bmatrix} 0 & 1 \\ -\frac{c}{J_0} & 0 \end{bmatrix} \begin{bmatrix} \theta_1 \\ \theta_2 \end{bmatrix} + \begin{bmatrix} 0 \\ \frac{L}{J_0} \end{bmatrix} F \tag{G.9}$$

$$y = \begin{bmatrix} L & 0 \end{bmatrix} \begin{bmatrix} \theta_1 \\ \theta_2 \end{bmatrix} \tag{G.10}$$

The above equation is in standard state-space form

$$\begin{aligned} \dot{\mathbf{x}} &= \mathbf{A}\mathbf{x} + \mathbf{B}u \\ y &= \mathbf{C}\mathbf{x} + Du \end{aligned}$$

where

$$\mathbf{A} = \begin{bmatrix} 0 & 1 \\ -\frac{c}{J_0} & 0 \end{bmatrix}, \quad \mathbf{B} = \begin{bmatrix} 0 \\ \frac{L}{J_0} \end{bmatrix}, \quad \mathbf{C} = \begin{bmatrix} L & 0 \end{bmatrix}, \quad D = 0$$

In structural and control engineering, the frequency response function is graphically plotted as $\log|H(s)|$ and $\arg(H(s))$ against $\log(\omega)$, which is called the Bode diagram or Bode plot.

A few observations can be made. Examination of Eq. (G.5) reveals that the natural frequency of a SDOF system with input and output configuration as selected, is equal to

$$\omega_n = \sqrt{\frac{c}{J_O}} = \sqrt{\frac{c}{J_{C_g} + m(y_{b2j})^2}} \tag{G.11}$$

Furthermore, it is clear from Eq. (G.6) that the DC-gain ($\omega = 0$) is equal to L^2/c, while for high frequencies ($\omega \gg \omega_n$) the asymptote has a slope of -2 on a log-log plot.

Consider a SDOF system consisting of a rigid body with length $L = 9$ m, distance from the center of mass to point O $y_{b2j} = 5$ m, mass $m = 1000$ kg, centroidal mass moment of inertia $J_{C_g} = 50000$ kgm^2, and torsional spring stiffness $c = 250000$ N/m. The receptance, mobility and inertance (or accelerance) Bode plot of this system are shown in Fig. G.2. The receptance plot displays the ratio between a harmonic displacement response and the harmonic input force, the mobility plot displays the ratio between the velocity response and input force, while the inertance (or accelerance) plot displays the ratio of acceleration response and input force.

The low-frequency asymptote (indicated by the dashed horizontal line in the receptance plot) intersects the high-frequency asymptote (indicated by the dashed line with a slope of -2 in the receptance plot) at a point corresponding to the natural frequency of the system. This is to be expected if we recall that spring force and inertia force cancel when the system is oscillating at its natural frequency ($\omega = \omega_n$). From this figure it can be concluded that the inertia and stiffness properties always appear as straight lines in a Bode plot. In addition, the mobility plot is symmetrical about a vertical line passing through the resonance frequency (this is approximately true for lightly damped SDOF systems).
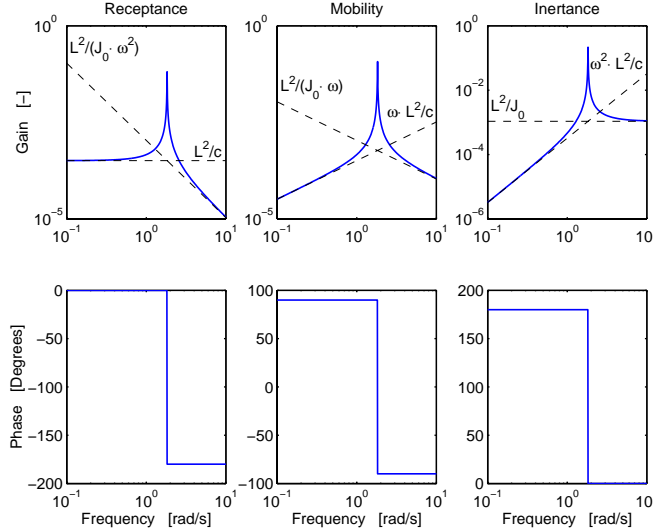
Figure G.2: *Bode diagrams (receptance, mobility and inertance) of an undamped, single degree of freedom system (example rigid body with length $L = 9$ m, distance from the center of mass to point O $y_{b2j} = 5$ m, mass $m = 1000$ [kg], centroidal mass moment of inertia $J_{C_g} = 50000$ [kgm^2], and torsional spring stiffness $c = 250000$ [N/m].)*

Hence, if Fig. G.2 represented a Bode diagram of experimental data, it would be possible to derive the torsional spring constant (provided that the length is known), and the mass moment of inertia about O of a SDOF model for the system under analysis. Damping characteristics can be obtained as well, as will be explained further on. This reasoning forms the basis of grey-box system identification techniques which aim at deriving the dynamic characteristics from experimental data using a physical model structure.

If we add a viscous damper to the SDOF system at the pin joint (by specifying a coefficient k of viscous damping), the system transfer function from force to displacement becomes

$$H(s) = \frac{\theta(s)L}{F(s)} = \frac{L^2/J_O}{s^2 + k/J_O\, s + c/J_O} \tag{G.12}$$

and the receptance FRF becomes

$$H(\omega) = H(s)\Big|_{s=j\omega} = \frac{L^2/J_O}{c/J_O + k/J_O\, j\omega - \omega^2} \tag{G.13}$$

$$= \frac{L^2/J_O}{\omega_n^2 + k/J_O\, j\omega - \omega^2} \tag{G.14}$$

Observe that the receptance FRF is now (as opposed to the undamped case) a complex valued function, containing both phase and frequency information.

The real and imaginary parts of the receptance, mobility and inertance FRF of the viscously damped SDOF system are shown in Fig. G.3. The coefficient k is selected such that the system has a damping ratio of 1% (*i.e.* lightly damped). It is interesting to note that the phase change trough the resonance region is characterized by a sign change in one part accompanied by a peak (either a minimum or a maximum) in the other part. From this figure it can be concluded that the receptance and inertance frequency response function are, at resonance, purely imaginary, while the mobility FRF is at resonance purely real. This fact can be used to check the viscously damped assumption for lightly damped systems.
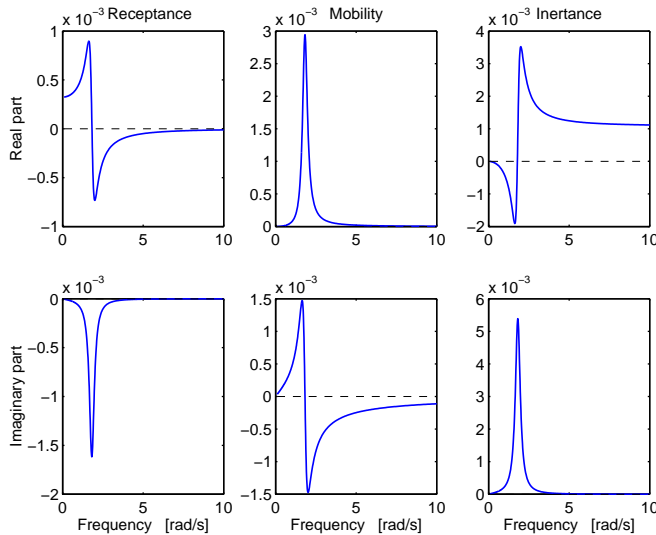
Figure G.3: *Plots of real and imaginary parts of the frequency response functions of a viscously damped, single degree of freedom system (example rigid body with length $L = 9$ m, distance from the center of mass to point O $y_{b2j} = 5$ m, mass $m = 1000$ [kg], centroidal mass moment of inertia $J_{C_g} = 50000$ [kgm^2], torsional spring stiffness $c = 250000$ [N/m] and damping $k = 27500$ [kg/s].)*

G.2 Two degrees of freedom

Consider the two degrees of freedom (2-DOF) system shown in Fig. G.4. The system consists of three rigid bodies connected by two ideal torsional springs C_{z1} and C_{z3} that model the elastic properties in bending direction. The damping is modeled by two viscous dampers, K_{eq12} and K_{eq23} respectively. The input is the force F and the output is the displacement of the point action of F. Gravity is completely neglected.

The equations of motion of the above (2-DOF) system can be solved more easily using Lagrange's equations than using Newton's law directly as in Section G.1. The
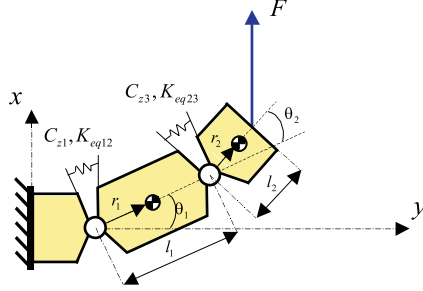
Figure G.4: *Two degrees of freedom system (superelement) of length L_{se} consisting of three rigid bodies with lengths $\frac{1}{2}(1 - \frac{1}{\sqrt{3}}) \cdot L_{se}$, $\frac{1}{\sqrt{3}} \cdot L_{se}$, and $\frac{1}{2}(1 - \frac{1}{\sqrt{3}}) \cdot L_{se}$.*

Lagrange formulation states that the equations of motion can be derived from

$$\frac{d}{dt}\left(\frac{\partial T}{\partial \dot{q}_i}\right) - \left(\frac{\partial T}{\partial q_i}\right) + \left(\frac{\partial U}{\partial q_i}\right) = Q_i \qquad i = 1, 2, \cdots, n \qquad \text{(G.15)}$$

where $\dot{q}_i = \partial q_i / \partial t$ is the generalized velocity, T is the kinetic energy of the system, U the potential energy of the system, an Q_i represents all the nonconservative forces corresponding to q_i. Here $\partial / \partial q_i$ denotes the partial derivative with respect to the coordinate q_i. For conservative systems, $Q_i = 0$ and Eq. (G.15) reduces to

$$\frac{d}{dt}\left(\frac{\partial T}{\partial \dot{q}_i}\right) - \left(\frac{\partial T}{\partial q_i}\right) + \left(\frac{\partial U}{\partial q_i}\right) = 0 \qquad i = 1, 2, \cdots, n \qquad \text{(G.16)}$$

Equations (G.15) and (G.16) represent one equation for each generalized coordinate. These equations can be rewritten in a slightly simplified form by defining the Lagrangian, L, to be $L = T - U$, the difference between the kinetic and potential energies. Then if $\partial U / \dot{q}_i = 0$, the Lagrangian equation becomes

$$\frac{d}{dt}\left(\frac{\partial L}{\partial \dot{q}_i}\right) - \left(\frac{\partial L}{\partial q_i}\right) = 0 \qquad i = 1, 2, \cdots, n \qquad \text{(G.17)}$$

Notice that Eq. (G.17) is just a restatement of Newton's law in generalized coordinates ($\frac{d}{dt}(\text{momentum}) = \text{applied force}$).

The equations of motion of the two degrees of freedom system in Fig. G.4 can be described by the two independent coordinates θ_1 and θ_2, so a good choice of the generalized coordinates is $q_1(t) = \theta_1(t)$ and $q_2(t) = \theta_2(t)$. Letting r_1 and r_2 be the distance from the joints to the center of mass and l_1 and l_2 the length for each rigid body, as shown in the figure, we have for rigid body 1

$$\begin{aligned} x_1 &= r_1 \sin q_1 \\ y_1 &= r_1 \cos q_1 \\ \dot{x}_1 &= r_1 \dot{q}_1 \cos q_1 \\ \dot{y}_1 &= -r_1 \dot{q}_1 \sin q_1 \end{aligned}$$

258

and for rigid body 2 we have

$$
\begin{aligned}
x_2 &= l_1 \sin q_1 + r_2 \sin(q_1 + q_2) \\
y_2 &= l_1 \cos q_1 + r_2 \cos(q_1 + q_2) \\
\dot{x}_2 &= l_1 \dot{q}_1 \cos q_1 + r_2(\dot{q}_1 + \dot{q}_2) \cos(q_1 + q_2) \\
\dot{y}_2 &= -l_1 \dot{q}_1 \sin q_1 - r_2(\dot{q}_1 + \dot{q}_2) \sin(q_1 + q_2)
\end{aligned}
$$

For rigid body 1 the kinetic and potential energy becomes

$$
\begin{aligned}
T_1 &= \tfrac{1}{2}m_1(\dot{x}_1^2 + \dot{y}_1^2) + \tfrac{1}{2}J_1\dot{q}_1^2 \\
&= \tfrac{1}{2}m_1 r_1^2 \dot{q}_1^2 + \tfrac{1}{2}J_1 \dot{q}_1^2 \\
U_1 &= \tfrac{1}{2}C_{z1}q_1^2
\end{aligned}
$$

where m_1 the mass, and J_1 the mass moment of inertia about the center of mass of rigid body 1. The velocity squared of the center of gravity of rigid body 2 is

$$
\dot{x}_2^2 + \dot{y}_2^2 = l_1^2 \dot{q}_1^2 + r_2^2(\dot{q}_1 + \dot{q}_2)^2 + 2l_1 r_2(\dot{q}_1^2 + \dot{q}_1 \dot{q}_2) \cos q_2
$$

Therefore the expression for kinetic energy for rigid body 2 is

$$
\begin{aligned}
T_2 &= \tfrac{1}{2}m_2(\dot{x}_2^2 + \dot{y}_2^2) + \tfrac{1}{2}J_2(\dot{q}_1 + \dot{q}_2)^2 \\
&= \tfrac{1}{2}m_2 l_1^2 \dot{q}_1^2 + \tfrac{1}{2}m_2 r_2^2(\dot{q}_1 + \dot{q}_2)^2 + m_2 l_1 r_2(\dot{q}_1^2 + \dot{q}_1 \dot{q}_2) \cos q_2 + \tfrac{1}{2}J_2(\dot{q}_1 + \dot{q}_2)^2
\end{aligned}
$$

The potential energy is

$$
U_2 = \tfrac{1}{2}C_{z3}q_2^2
$$

The Lagrangian for the complete system expressed in the generalized coordinates q_1 and q_2 is

$$
\begin{aligned}
L &= T - U = T_1 + T_2 - U_1 - U_2 \\
&= \tfrac{1}{2}m_1 r_1^2 \dot{q}_1^2 + \tfrac{1}{2}J_1 \dot{q}_1^2 + \tfrac{1}{2}m_2 l_1^2 \dot{q}_1^2 + \tfrac{1}{2}m_2 r_2^2(\dot{q}_1 + \dot{q}_2)^2 + m_2 l_1 r_2(\dot{q}_1^2 + \dot{q}_1 \dot{q}_2) \cos q_2 \\
&\quad + \tfrac{1}{2}J_2(\dot{q}_1 + \dot{q}_2)^2 - \tfrac{1}{2}C_{z1}q_1^2 - \tfrac{1}{2}C_{z3}q_2^2
\end{aligned}
$$

Substituting L into Lagrange's equations and calculating the derivatives gives for $i = 1$

$$
\begin{aligned}
\frac{\partial L}{\partial \dot{q}_1} &= m_1 r_1^2 \dot{q}_1 + J_1 \dot{q}_1 + m_2 l_1^2 \dot{q}_1 + m_2 r_2^2(\dot{q}_1 + \dot{q}_2) + m_2 l_1 r_2(2\dot{q}_1 + \dot{q}_2) \cos q_2 \\
&\quad + J_2(\dot{q}_1 + \dot{q}_2) \\
\frac{d}{dt}\frac{\partial L}{\partial \dot{q}_1} &= \left[m_1 r_1^2 + J_1 + m_2 l_1^2 + m_2 r_2^2 + 2m_2 l_1 r_2 \cos q_2 + J_2\right] \ddot{q}_1 \\
&\quad - \left[m_2 l_1 r_2 2\dot{q}_2 \sin q_2\right] \dot{q}_1 \\
&\quad + \left[m_2 r_2^2 + m_2 l_1 r_2 \cos q_2 + J_2\right] \ddot{q}_2 - \left[m_2 l_1 r_2 \dot{q}_2 \sin q_2\right] \dot{q}_2 \\
\frac{\partial L}{\partial q_1} &= C_{z1}q_1
\end{aligned}
$$

and for $i = 2$

$$\frac{\partial L}{\partial \dot{q}_2} = m_2 r_2^2 (\dot{q}_1 + \dot{q}_2) + m_2 l_1 r_2 (\dot{q}_1) \cos q_2 + J_2 (\dot{q}_1 + \dot{q}_2)$$

$$\frac{d}{dt} \frac{\partial L}{\partial \dot{q}_2} = \left[m_2 r_2^2 + m_2 l_1 r_2 \cos q_2 + J_2 \right] \ddot{q}_1 + \left[m_2 r_2^2 + J_2 \right] \ddot{q}_2 - m_2 l_1 r_2 \dot{q}_1 \dot{q}_2 \sin q_2$$

$$\frac{\partial L}{\partial q_2} = -m_2 l_1 r_2 (\dot{q}_1^2 + \dot{q}_1 \dot{q}_2) \sin q_2 + C_{z3} q_2$$

Combining the expression for $i = 1$ and $i = 2$ into one vector equation in the generalized vector $[\ q_1 \quad q_2 \ ]^T = [\ \theta_1 \quad \theta_2 \ ]^T$ yields

$$\underbrace{\left[\begin{array}{cc} J_{j1} + m_2 l_1^2 + J_{j2} + 2 l_1 m_2 r_2 \cos q_2 & J_{j2} + l_1 m_2 r_2 \cos q_2 \\ J_{j2} + l_1 m_2 r_2 \cos q_2 & J_{j2} \end{array} \right]}_{\mathbf{M}} \underbrace{\left[\begin{array}{c} \ddot{q}_1 \\ \ddot{q}_2 \end{array} \right]}_{\ddot{\mathbf{q}}} +$$

$$+ \left[\begin{array}{c} -l_1 m_2 r_2 (2\dot{q}_1 + \dot{q}_2) \dot{q}_2 \sin q_2 \\ l_1 m_2 r_2 \dot{q}_1^2 \sin q_2 \end{array} \right] + \underbrace{\left[\begin{array}{cc} C_{z1} & 0 \\ 0 & C_{z3} \end{array} \right]}_{\mathbf{C}} \underbrace{\left[\begin{array}{c} q_1 \\ q_2 \end{array} \right]}_{\mathbf{q}} = \left[\begin{array}{c} F \\ 0 \end{array} \right] \qquad \text{(G.18)}$$

where $J_{j1} = J_1 + m_1 r_1^2$, and $J_{j2} = J_2 + m_2 r_2^2$ are the mass moments of inertia about joint 1 and 2 respectively. This is a set of coupled non-linear differential equations (the generalized inertia matrix is not diagonal, implying that the two equations of motion are coupled through the inertia terms) which describe the motion q given the input force F. Furthermore, the generalized inertia matrix $\mathbf{M}$ has as determinant $J_{j2} J_{j1} + J_{j2} m_2 l_1^2 - l_1^2 m_2^2 r_2^2 \cos^2 q_2$, which is positive for all q_2. The result being that the inverse of $\mathbf{M}$ exists. Observe that the above equations of motion is in the standard form:

$$M(q, t) \cdot \ddot{q}(t) + [K(q, \dot{q}, t) \cdot \dot{q}(t)] \cdot \dot{q}(t) + C(q, t) \cdot q(t) + f(q, t) = 0$$

with $q(t), \dot{q}(t)$ denoting the generalized coordinates and generalized speeds, respectively, $M(q, t)$ denoting the (positive definite, symmetric) generalized inertia matrix, possibly dependent on q, and t, $K(q, \dot{q}, t)$ denoting the three-dimensional generalized coriolis/centripetal array, $C(q, t)$ denoting the generalized stiffness matrix, and $f(q, t)$ denoting the vector of externally applied force fields.

The matrix equation Eq. (G.18) is linearized by using the small-angle, small motion approximation (i.e. $\sin \theta \to 0$, $\cos \theta \to 1$, and $\dot{\theta}^2 \to 0$). In matrix form this becomes

$$\underbrace{\left[\begin{array}{cc} J_{j1} + m_2 l_1^2 + J_{j2} + 2 l_1 m_2 r_2 & J_{j2} + l_1 m_2 r_2 \\ J_{j2} + l_1 m_2 r_2 & J_{j2} \end{array} \right]}_{\mathbf{M}} \underbrace{\left[\begin{array}{c} \ddot{q}_1 \\ \ddot{q}_2 \end{array} \right]}_{\ddot{\mathbf{q}}} + \underbrace{\left[\begin{array}{cc} C_{z1} & 0 \\ 0 & C_{z3} \end{array} \right]}_{\mathbf{C}} \underbrace{\left[\begin{array}{c} q_1 \\ q_2 \end{array} \right]}_{\mathbf{q}}$$

$$= \underbrace{\left[\begin{array}{c} F \\ 0 \end{array} \right]}_{\mathbf{F}}$$

or

$$\mathbf{M}\ddot{\mathbf{q}} + \mathbf{C}\mathbf{q} = \mathbf{F} \qquad \text{(G.19)}$$

Note that this linearization occurs after the equations of motion have been derived.

Up to now, the effect of viscous damping has been neglected. Since the damping is a local effect, the term

$$\mathbf{K}\dot{\mathbf{q}} = \begin{bmatrix} K_{eq12} & 0 \\ 0 & K_{eq23} \end{bmatrix} \begin{bmatrix} \dot{q}_1 \\ \dot{q}_2 \end{bmatrix} \qquad \text{(G.20)}$$

can simply be added to Eq. (G.19) resulting in

$$\mathbf{M}\ddot{\mathbf{q}} + \mathbf{K}\dot{\mathbf{q}} + \mathbf{C}\mathbf{q} = \mathbf{F} \qquad \text{(G.21)}$$

It is useful to rewrite Eq. (G.21) in the following first-order or linear state-space form

$$\begin{aligned} \dot{\mathbf{x}} &= \mathbf{A}^{\mathrm{ss}}\mathbf{x} + \mathbf{B}^{\mathrm{ss}}u \\ y &= \mathbf{C}^{\mathrm{ss}}\mathbf{x} + D^{ss}u \end{aligned}$$

with x the state vector which constitute the generalized coordinates and the generalized velocities, u the input vector representing the externally applied forces, y the output vector, and $\mathbf{A}^{\mathrm{ss}}$ the state, $\mathbf{B}^{\mathrm{ss}}$ the input, $\mathbf{C}^{\mathrm{ss}}$ the output, and $\mathbf{D}^{\mathrm{ss}}$ the direct feedthrough matrix.

This can be done by defining the two $n \times 1$ vectors $\mathbf{x_1} = \mathbf{q}$ and $\mathbf{x_2} = \dot{\mathbf{q}}$. Note that $\mathbf{x_1}$ is the vector of displacements and $\mathbf{x_2}$ is the vector of velocities. Differentiating these two vector yields

$$\begin{aligned} \dot{\mathbf{x}}_1 &= \dot{\mathbf{q}} = \mathbf{x_2} \\ \dot{\mathbf{x}}_2 &= \ddot{\mathbf{q}} = \mathbf{M}^{-1}\mathbf{F} - \mathbf{M}^{-1}\mathbf{K}\dot{\mathbf{q}} - \mathbf{M}^{-1}\mathbf{C}\mathbf{q} \end{aligned}$$

Obviously, this transformation requires (symbolic) inversion of the generalized inertia matrix. In our case, $\mathbf{q} = [\ q_1 \quad q_2\ ]^T$, and $\dot{\mathbf{q}} = [\ \dot{q}_1 \quad \dot{q}_2\ ]^T$ yields for the state vector $\mathbf{x} = [\ \mathbf{x_1} \quad \mathbf{x_2}\ ]^T = [\ q_1 \quad q_2 \quad \dot{q}_1 \quad \dot{q}_2\ ]^T$. With the result that the state matrix $\mathbf{A}^{\mathrm{ss}}$ can be partitioned as follows

$$\mathbf{A}^{\mathrm{ss}} = \begin{bmatrix} \mathbf{0} & \mathbf{I} \\ -\mathbf{M}^{-1}\mathbf{C} & -\mathbf{M}^{-1}\mathbf{K} \end{bmatrix}$$

with the terms

$$\mathbf{I} = \begin{bmatrix} 0 & 1 \\ 1 & 0 \end{bmatrix}$$

$$-\mathbf{M}^{-1}\mathbf{C} = \begin{bmatrix} \dfrac{J_{j2}C_{z1}}{-J_{j2}J_{j1}-J_{j2}m_2l_1^2+l_1^2m_2^2r_2^2} & -\dfrac{(J_{j2}+l_1m_2r_2)C_{z3}}{-J_{j2}J_{j1}-J_{j2}m_2l_1^2+l_1^2m_2^2r_2^2} \\ -\dfrac{(J_{j2}+l_1m_2r_2)C_{z1}}{-J_{j2}J_{j1}-J_{j2}m_2l_1^2+l_1^2m_2^2r_2^2} & \dfrac{(J_{j1}+m_2l_1^2+J_{j2}+2l_1m_2r_2)C_{z3}}{-J_{j2}J_{j1}-J_{j2}m_2l_1^2+l_1^2m_2^2r_2^2} \end{bmatrix}$$

$$-\mathbf{M}^{-1}\mathbf{K} = \begin{bmatrix} \dfrac{J_{j2}K_{eq12}}{-J_{j2}J_{j1}-J_{j2}m_2l_1^2+l_1^2m_2^2r_2^2} & -\dfrac{(J_{j2}+l_1m_2r_2)K_{eq23}}{-J_{j2}J_{j1}-J_{j2}m_2l_1^2+l_1^2m_2^2r_2^2} \\ -\dfrac{(J_{j2}+l_1m_2r_2)K_{eq12}}{-J_{j2}J_{j1}-J_{j2}m_2l_1^2+l_1^2m_2^2r_2^2} & \dfrac{(J_{j1}+m_2l_1^2+J_{j2}+2l_1m_2r_2)K_{eq23}}{-J_{j2}J_{j1}-J_{j2}m_2l_1^2+l_1^2m_2^2r_2^2} \end{bmatrix}$$

The output and direct feedthrough matrix are given by

$$\mathbf{C^{ss}} = \begin{bmatrix} -(l_1 + l_2) & -l_2 & 0 & 0 \end{bmatrix}$$
$$D^{ss} = 0$$

while the input matrix is given by

$$\mathbf{B^{ss}} = \begin{bmatrix} 0 \\ 0 \\ \dfrac{J_{j2}(l_1+l_2)}{-J_{j2}J_{j1}-J_{j2}m_2l_1^2+l_1^2m_2^2r_2^2} - \dfrac{(J_{j2}+l_1m_2r_2)l_2}{-J_{j2}J_{j1}-J_{j2}m_2l_1^2+l_1^2m_2^2r_2^2} \\ -\dfrac{(J_{j2}+l_1m_2r_2)(l_1+l_2)}{-J_{j2}J_{j1}-J_{j2}m_2l_1^2+l_1^2m_2^2r_2^2} + \dfrac{(J_{j1}+m_2l_1^2+J_{j2}+2l_1m_2r_2)l_2}{-J_{j2}J_{j1}-J_{j2}m_2l_1^2+l_1^2m_2^2r_2^2} \end{bmatrix}$$

Appendix H

Modified step-response test measurement equipment

This appendix describes the equipment used in the "Modified step-response test" as proposed by Vleeshouwers [301] for the identification and parameter determination of the Lagerwey LW-50/750 generator. Section H.1 lists the main specifications of the generator under test. The name plate data of the shunt used to short-circuit the field winding is given in Section H.2. Section H.3 lists the specifications of the applied DC voltage source. Section H.4 addresses the thyristor used for switching. Finally, Section H.5 presents the main features of the data-acquisition system.

H.1   Generator

A 750 kW synchronous generator has been used. The rated data of the machine can been found on the name plate of the machine, and is listed in Fig. H.1.

LW-50/750 Generator

Type:	Synchronous ring
Rated power:	750 kW
Voltage:	690 V

Figure H.1: *Name plate data of generator.*

H.2 Transfoshunt

The field winding is during the "D-measurement" short-circuited by a shunt. The name plate data of the used shunt is listed in Fig. H.2.

<div style="border:1px solid black; background:#f5e79e; padding:1em;">

LEM 100 A Labo

Current nominal 100 A   Rapport des courants 1:1000
Plage de measure 0 - 300 A   Isolation 5 kV – 60s
Tension de measure 10 V à 100 A   Resistance interne: R_s = 25 Ω
No. 7088   Alimentation 220 V – 50 Hz.

LEM sa CH 1212 Geneve

</div>

Figure H.2: *Name plate data of transfoshunt.*

H.3 Low power DC voltage source

An ordinary car-battery has been used to generate the required step-like excitation. The name plate data of the used battery is listed in Fig. H.3.

<div style="border:1px solid black; background:#f5e79e; padding:1em;">

Bären 12 V

Hochleistungsbatterie

554 27
12V 54Ah 300A

</div>

Figure H.3: *Name plate data of battery.*

H.4 Thyristor

For the switching, a thyristor has been used.

H.5 Data-acquisition system

The data-acquisition system can be divided into three parts, input-output (I/O) boards, a digital signal processor (DSP) board from dSPACE® with a TMS320C40 processor from Texas Instruments®, and a personal computer (PC) connected to the processor board.

H.5.1 Input-output boards

Two high-resolution A/D boards are used to convert the measured analogue signals into digital signals. The main specifications are listed in Fig. H.4.

DS2001 High-Speed AD Board

5 parallel A/D channels (single-ended)
Simultaneous sample & hold
Sample & hold tracking or hold mode (programmable)
4, 8, 12 or 16 bit resolution (programmable)
± 5 V or ±10 V input voltage range (programmable)
1 MΩ input impedance
80 dB signal-to-noise ratio

Sample time (all channels): 6.2 µs (16 bit)
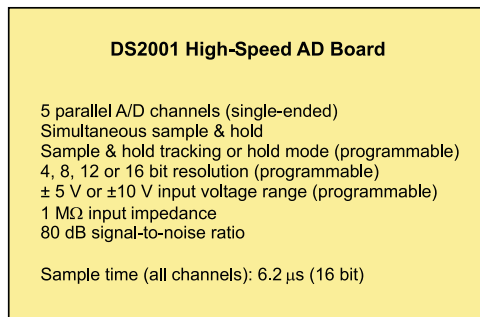
Figure H.4: *Main specifications of I/O Board.*

H.5.2 Digital Signal Processor (DSP) board

A Digital Signal Processor (DSP) board is used to perform the actual data-acquisition. The main specifications are listed in Fig. H.5.

DS1003 DSP Board

Texas Instruments TMS320C40 60 MHz processor with
- 2 KWords on-chip RAM
- 6-channel DMA controller
- 6 parallel communication ports at 20 MByte/s
- Two timers

PHS-Bus Interface with:
- 32-bit synchronous I/O-bus
- 20 Mbyte/s transfer speed
- 256 32-bit memory mapped I/O channels
- Eight PHS-bus interrupt lines, expansible to 64 interrupts
- Synchronization lines for parallel sampling and update for all I/O boards

Figure H.5: *Main specifications of Digital Signal Processing Board.*

H.5.3   Personal computer

The main specifications of the used personal computer are listed in Fig. H.6.

Personal Computer

Processor type:	486 DX4-S 100
Hard disk drive:	500 Mb
System memory:	16 Mb
Dimensions:	430 x 430 x 175 mm
Weight:	5 kg.

Figure H.6: *Name plate data of PC.*

Appendix I

DAWIDUM: a new wind turbine design code

In this appendix a new MATLAB®/SIMULINK® Toolbox will been presented. In section I.1 the software requirements are specified for DAWIDUM to run properly. It also contains information how to start-up DAWIDUM. The options that are available on the main window are discussed in the ensuing sections.

I.1 Introduction

The DAWIDUM toolbox has been purpose-made to provide wind turbine designers and control engineers with a design tool that enables them to rapidly and easily build accurate dynamic models of wind turbines. The resulting non-linear dynamic models can be used to objectively compare and optimize different controllers to achieve improved performance and robustness. Because the models are fully parametric with physical meaningful parameters, the models can also be used to obtain an optimized wind turbine design. Through simulations, wind turbine designers can explore how the wind turbine would perform under extreme conditions and evaluate different wind turbine configurations.

DAWIDUM has been developed in the MATLAB®/SIMULINK® environment. Consequently, both programs are required for DAWIDUM to run properly. The DAWIDUM toolbox is equipped with a Graphical User Interface (GUI) offering a systematic, rapid method of determining these optimal solutions. This will lead to better wind turbine designs with improved system performance and will reduce dependence on prototypes and testing. The former will reduce the cost price of electricity by capturing maximum energy at minimum fatigue loads, while the latter will shorten the design cycle and reduce development cost.

If the installation of DAWIDUM has been completed successfully, MATLAB® should be (re)invoked. If MATLAB® is running, and the matlabpath has been properly set, the command

```
>> Dawidum
```

typed in the command window will start up DAWIDUM. Alternatively, DAWIDUM can also be invoked by double-clicking on the shortcut icon located on the desktop. In both cases, the window depicted in Fig. I.1 will appear. A click on the Info-button will yield some more information about DAWIDUM, while a click on the Abort-button directly aborts the program. Finally, by a click on the Continue-button the main window of DAWIDUM will be opened.
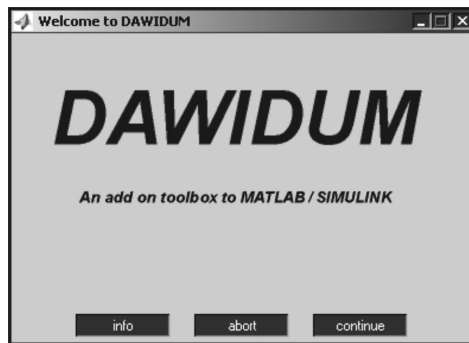
Figure I.1: *Welcome window of DAWIDUM.*

After starting up DAWIDUM, and subsequently pressing the Continue-button in the "Welcome to DAWIDUM" window, the main window is opened. This window is depicted in Fig. I.2. The main window has been divided into three parts:

- **Menu bar**. At the top of the window you will find the menu bar. Via the options on the menu bar you can either create a new or modify an existing a wind turbine model, optimize model parameters using measured data, start a simulation, analyse the results, design a controller, or visualize the obtained results. Once a model has been loaded or saved, the name of the model is placed between the brackets in the title of the main DAWIDUM window;

- **Main board**. The main board is used to display useful information. For example, by choosing Modeling and subsequently Create new model, both the developed wind turbine module library and a new SIMULINK® window called "Untitled" will be opened and displayed in the main board as illustrated in Fig. I.2;

- **Status line**. The status line is located at the bottom of the window. It is used to display all kinds of messages to the user. Moreover, the user is guided by the messages through the operations involved with creating, optimizing, analysing, simulating and animating the non-linear dynamic wind turbine models.

A more detailed discussion of the options that are available on the menu bar can be found in the ensuing sections.
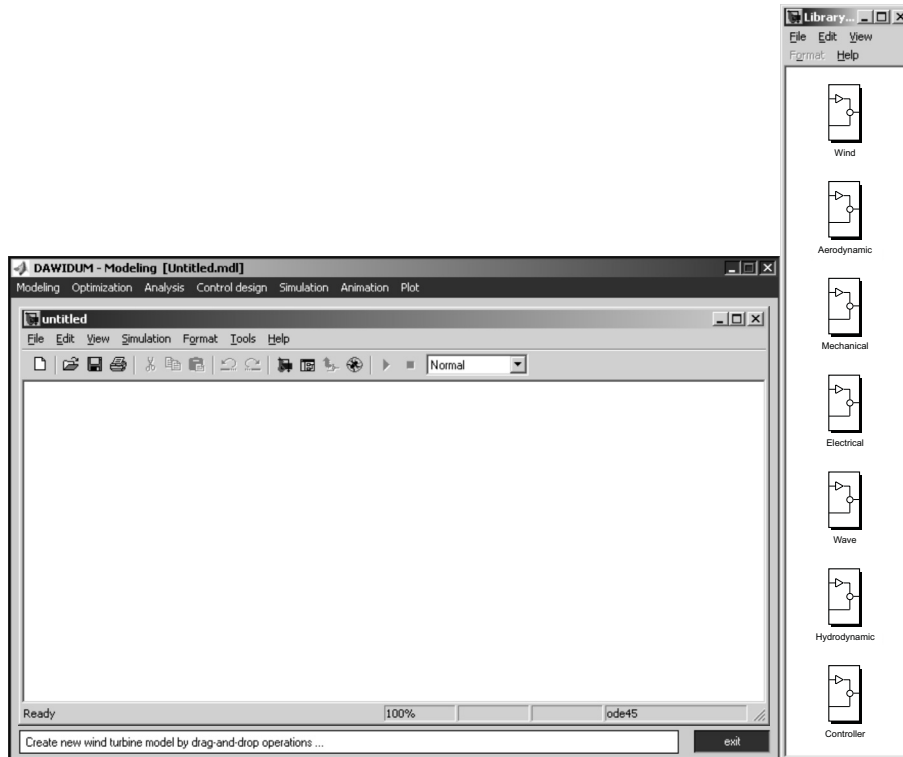
Figure I.2: *Main window of DAWIDUM with the WTML library and an untitled SIMULINK window openend.*

Remark

Once DAWIDUM is running, you must be careful when using the functions `clear` and `clear global`, as they tend to break the link between the global variables used by the graphical user interface and the variables local to your workspace. If you have such a problem, re-executing DAWIDUM will usually solve it.

I.2 Modeling

In this section the main modeling options are discussed. We will start with the wind module library.

I.2.1 Wind module library

DAWIDUM's wind module consists of two submodules, *viz.*: "deterministic" and "stochastic" as illustrated in Fig. I.3. The deterministic submodule allows the following undisturbed wind inputs to be specified: a uniform wind field (*i.e.* V_w is

constant both in space and time), a sequence of upward and downward stepwise changes in the wind velocity, and the undisturbed wind velocity can be read from a user specified WindData.mat file.
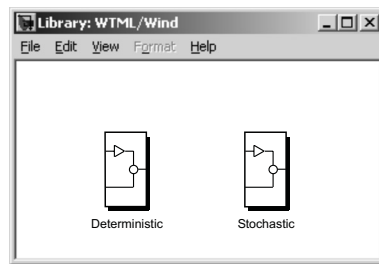
Figure I.3: *Wind module library consisting of two submodules: deterministic and stochastic. The stochastic submodule is able to read the output generated by the wind field generator SWING-4.*

The stochastic submodule is able to read the output generated by SWING-4. This stochastic wind generator calculates the Fourier coefficients (for each radial position and for each time step specified in the input file) expressed in the harmonics of the azimuth. The interested reader is referred to Bierbooms [11, 13] for detailed information about SWING-4.

The SWING-4 interface converts the aforementioned coefficients during simulation into the required stochastic wind velocity components U (longitudinal) and V (tangential) for each rotor blade N_b and blade section (or blade element) N_s. The user must ensure that the radial positions for which the SWING-4 output is generated are identical to the blade element positions at which the aerodynamic forces are to be calculated. In addition, the azimuth Ψ of blade 1 (pointing upwards at $t = 0$) needs to be available during simulation. The interface is coded as an M-File S-Function named Swing consisting of the following two files: SwingInit.m, and SwingCalc.m.

The file SwingInit loads the output of a SWING-4 simulation and initializes the data to be used in SwingCalc. In the latter file the actual calculation takes place. The S-Function is shown in Fig. I.4. The number of rotor blade is specified in the "S-Function parameters" field.

The size of the output vector is $2\,N_b N_s$, with N_b number of rotor blades and N_s number of blade elements. It is checked in SwingCalc if the specified simulation stop time of DAWIDUM exceeds that of the SWING-4 output (and if that is the case an error is displayed). It is preferable that the step size of the integration routine used for time-domain simulation equals that of the one used to generate the SWING output, although a linear interpolation scheme is included in SwingCalc.

270
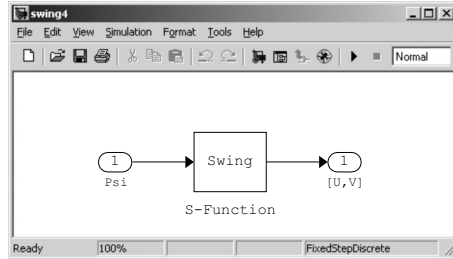
Figure I.4: *SWING-4 interface in DAWIDUM. Input: Ψ, and outputs: $U = [U_1(1 : N_s), \cdots, U_{N_b}(1 : N_s)]$ and $V = [V_1(1 : N_s), \cdots, V_{N_b}(1 : N_s)]$ for each blade element N_s and rotor blade N_b.*

I.2.2   Aerodynamic module library

The aerodynamic module is coded as an M-File S-Function named BEM. The S-Function is shown in Fig. I.5 and is built up out of the following two files: AeroInit.m, and AeroCalc.m. The file AeroInit provides an initial guess for both the axial and tangential induction factor, and loads the specified turbulent wake state model. This model is specified in the "S-Function parameters" field. In AeroCalc.m deterministic effects as wind shear, tower shadow and the ten-minute average wind speed at hub height are added to the zero-mean stochastic components of SWING-4 before the aerodynamic forces are computed.
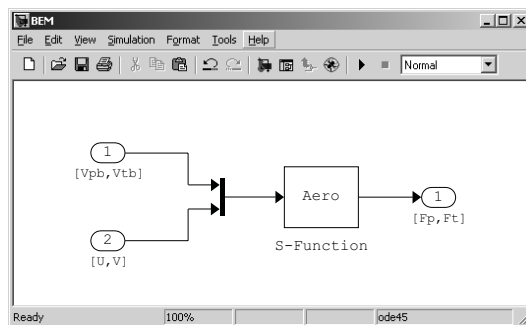
Figure I.5: *Aerodynamic module in DAWIDUM. Inputs: $[V_{pb}, V_{tb}]$: blade element velocities $\dot{x}$, and $[U, V]$: SWING-4 output. Outputs: $[F_p, F_t] = [F_{p,1}(1 : N_s) \ F_{t,1}(1 : N_s) \cdots F_{p,N_b}(1 : N_s) \ F_{t,N_b}(1 : N_s)]$ the aerodynamic forces F_{aero} with N_s the number of blade elements and N_b the number of rotor blades).*

271

I.2.3 Mechanical module library

The mechanical module library contains four submodules describing the structural dynamics at different level of complexity: Rotor blade, Rotor (3-bladed), Tower (plus foundation), and Wind turbine (3-bladed) (*see* Fig. I.6). These modules form the basis of all different developed (and those to be developed) mechanical models of (flexible) wind turbines. All submodules can be opened by double-clicking, and each submodule contains several models. The model complexity ranges from rigid models that have no effect on the system dynamics to flexible models consisting of a collection of superelements. The selection of number of superelements depends on the stiffness of the wind turbine under investigation. The library can be modified by dragging new modules or models onto it and saving the resulting system.
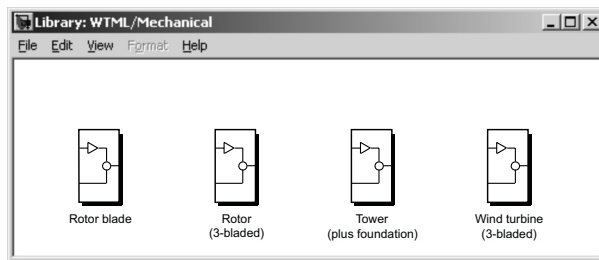
Figure I.6: *Mechanical module library.*

Automated structural modeling procedure: performance

The performance of the automated structural modeling procedure implemented in DAWIDUM can be best illustrated by considering the following two situations:

- Create a new structural model from scratch;

- Modify an existing structural model from the mechanical module library. In this case we have to make a distinction between:

  - Model configuration and/or complexity changes;
  - Parameter changes.

Obviously, to create a new wind turbine model from scratch will be more time-consuming than changing the model configuration (*e.g.* two or three rotor blades), model complexity (*i.e.* number of degrees of freedom) or adapting some model parameters (*e.g.* replacing the rotor blades by another type). The latter change requires only a few minutes, while changing the model configuration and/or complexity will take a few hours. The time to develop a new model from scratch will range from a couple of hours to a few days depending on the wind turbine configuration under investigation.

To emphasize that the time needed to generate the equations of motion is negligible with respect to the time to make the aforementioned changes, consider the CPU times required to generate the equation of motion of several DAWIDUM models listed in Table I.1. These timings demonstrate that the formulation of one set of equations (even for the most complex structural models) takes only a few seconds.

Timing comparisons		
DAWIDUM model	CPU time	Complexity
Beam1sd	0.10 s	2
Beam3sd	1.25 s	6
Beam6sd	1.57 s	12
Beam9sd	1.90 s	18
SDLW1	2.38 s	20
SDLW2	3.77 s	36
SDLW3	5.13 s	52

Table I.1: *Overview of the CPU time used to generate the equations of motion of several DAWIDUM models on a PC with a 700 MHz Pentium II processor running Windows-2K with 384 MB RAM. The total number of degrees of freedom (including fictitious ones) has been used as a measure of complexity.*

Rotor blade

The equations implemented in BladePM to compute the centroidal mass moments of inertia, and center of gravity of all rigid bodies within each superelement will now be presented. Recall that the mass as well as the flexural rigidity in the two principal bending directions need to be supplied by either the blade designer or the blade manufacturer. The center of gravity of each rigid body with respect to its base is determined as follows:

$$C_g = \sum_{r=0}^{L_{rb}} m(r) \cdot (R(r) - R(0))/M_{rb}$$

with $m(r)$ the mass as function of the local radius r, and M_{rb} the mass of the rigid body under consideration which is, in turn, defined as:

$$M_{rb} = \sum_{r=0}^{L_{rb}} m(r)$$

Subsequently, the centroidal mass moment of inertia is determined as

$$J_x = \sum_{r=0}^{L_{rb}} m(r) \cdot \{(R(r) - R(0)) - C_g\}^2$$

273

Note that J_z equals to J_x due to the point mass assumption. The torsional spring constants for each superelement are determined as follows:

$$c_{x1} = \frac{2}{L_{se}} \cdot \text{mean}\left[EI_x(0 \le r \le \tfrac{1}{2}L_{se})\right]$$

$$c_{x3} = \frac{2}{L_{se}} \cdot \text{mean}\left[EI_x(\tfrac{1}{2}L_{se} < r \le L_{se})\right]$$

with $EI_x(r)$ the flexural rigidity in the principal bending x-direction as function of the local radius r, and L_{se} the length of the superelement which is, in turn, defined as

$$L_{se} = \frac{R}{N_{se}}$$

with R the length of the rotor blade and N_{se} the number of superelements the blade is subdivided in. The torsional spring constants in z-direction are determined analogously.

Using the presented modeling approach a number of rotor blade models with different levels of complexity have been developed. The main features are listed in Table I.2. The integer appended to the basename "Blade" represents the number of superelements each blade has been subdivided in, while the characters xz indicate that the blade has a bending degree of freedom in both the global x and z-direction.

Rotor blade model features overview					
Model name	Bending	Torsion	N_{dof}	N_{se}	N_{rb}
Blade1xz	fl + ll	–	4	1	3
Blade2xz	fl + ll	–	8	2	5
Blade3xz	fl + ll	–	12	3	7
Blade4xz	fl + ll	–	16	4	9
Blade5xz	fl + ll	–	20	5	11
Blade6xz	fl + ll	–	24	6	13

Table I.2: *Overview rotor blade models, with fl flap, ll lead-lag, N_{dof} number of degrees of freedom per blade, N_{se} number of superelements per blade, N_{rb} number of rigid bodies per blade, and –: not implemented in the model.*

Rotor (3-bladed)

In general, a wind turbine rotor consists of one, two or three rotor blades. The blades are bolted on spacers, which are, in turn, bolted directly on the pitch bearings located on rotor hub. The modeling of the rotor consists thus of three parts

- Rotor blade

- Spacer

- Rotor hub

The main features of the different developed DAWIDUM rotor models are listed in Table I.3. The integer appended to the basename "Rotor" represents the number of superelements each blade has been subdivided in, while the p indicates that each blade has a pitch degree of freedom. The rigid rotor model, *i.e.* Rotor0p, has been specially added for checking out the aerodynamics.

Wind turbine rotor model features overview							
Model name	N_b	Pitching	Bending	Torsion	N_{dof}	N_{se}	N_{rb}
Rotor0p	3	●	–	–	0	0	1
Rotor1p	3	●	fl + ll	–	12	1	3
Rotor2p	3	●	fl + ll	–	24	2	5
Rotor3p	3	●	fl + ll	–	36	3	7
Rotor4p	3	●	fl + ll	–	48	4	9
Rotor5p	3	●	fl + ll	–	60	5	11

Table I.3: *Overview rotor models, with N_b number of blades, fl flap, ll lead-lag, N_{dof} total number of degrees of freedom (exclusive pitch, and azimuth), N_{se} number of superelements per blade, N_{rb} number of rigid bodies per blade, –: not implemented in the module, and ●: implemented in the model.*

Tower (plus foundation)

The equations implemented in TowerPM to compute the mass, inertia (mass moments as well as area moments), and center of gravity of the tapered, hollow tower sections are derived given below. The torsional spring constants for each superelement are determined as follows:

$$c_{x1T} = \frac{2E_t}{L_{se}} \cdot \text{mean} \left[I_x(0 \leq h \leq \tfrac{1}{2}L_{se}) \right]$$

$$c_{x3T} = \frac{2E_t}{L_{se}} \cdot \text{mean} \left[I_x(\tfrac{1}{2}L_{se} < h \leq L_{se}) \right]$$

with E_t the modulus of elasticity, $I_x(h)$ the area moment of inertia as function of the local tower height h, and L_{se} the length of the superelement which is, in turn,

defined as

$$L_{se} = \frac{L_t}{N_{se}}$$

with L_t the length of the tower and N_{se} the number of superelements the tower is subdivided in. Because of symmetry, the torsional spring constants in x-direction are equal to those in z-direction (*i.e.* $c_{x1T} = c_{z1T}$, and $c_{x3T} = c_{z3T}$).

The main features of the models available within tower submodule are listed in Table I.4. The filename convention used in this table is depicted in Fig. I.7. The name "Tower" might sound confusing, since "support structure" is actually meant. However, since file names were limited to eight characters within the 1.3c version of SIMULINK$^{\circledR}$, and a suffix like "1" (used for indicating the number of superelements) already uses one of them, we have chosen to use the model name "Tower".
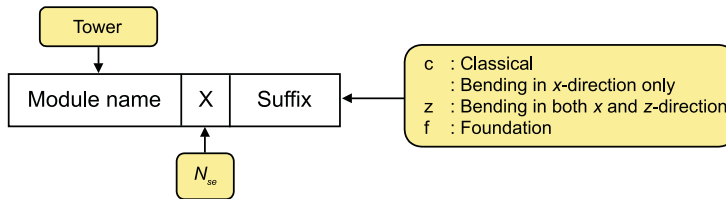
Figure I.7: *File name convention used in the "Wind turbine tower model features overview" table, with N_{se}: number of superelements the tower is subdivided in.*

Complete wind turbine

Each spacer is connected to a rotor blade using a weld joint. This has the advantage in terms of uniform treatment within the presented approach. However, a weld joint adds 6 constraints, so this method is computationally more expensive. Each spacer has been modeled as one single rigid body. The blades are attached to the rotating hub with a pin joint in order to allow pitch control.

We have introduced fictitious degrees of freedom in order to be able to specify the rotor blade inertia, and geometry in a reference frame unrelated to the hub reference frame. In other words, this allows us to specify three identical rotor blades in the system description file, while the pins are set to the proper angle (*i.e.* $\frac{2}{3}\pi$, and $\frac{4}{3}\pi$ respectively) at runtime, and subsequently prescribed to fix the blade in the specified position. The rotor hub has been modeled as one single rigid body.

Here it is assumed that flexibility of the support structure can be approximated by a torsional spring. The nacelle has been modeled as one single rigid body.

Wind turbine tower model features overview						
Model name	Bending	Torsion	N_{dof}	N_{se}	N_{rb}	Foundation
Tower0c	x	–	1	0	1	–
Tower0	x	–	1	0	1	–
Tower1	x	–	2	1	4	–
Tower2	x	–	4	2	6	–
Tower3	x	–	6	3	8	–
Tower4	x	–	8	4	10	–
Tower5	x	–	10	5	12	–
Tower6	x	–	12	6	14	–
Tower7	x	–	14	7	16	–
Tower8	x	–	16	8	18	–
Tower9	x	–	18	9	20	–
Tower1z	x + z	–	4	1	4	–
Tower2z	x + z	–	8	2	6	–
Tower3z	x + z	–	12	3	8	–
Tower4z	x + z	–	16	4	10	–
Tower5z	x + z	–	20	5	12	–
Tower1f	x	–	3	1	4	●
Tower2f	x	–	5	2	6	●
Tower3f	x	–	7	3	8	●
Tower4f	x	–	9	4	10	●
Tower5f	x	–	11	5	12	●
Tower1zf	x + z	–	6	1	4	●
Tower2zf	x + z	–	10	2	6	●
Tower3zf	x + z	–	14	3	8	●
Tower4zf	x + z	–	18	4	10	●
Tower5zf	x + z	–	22	5	12	●

Table I.4: *Overview tower models, with N_{dof} number of degrees of freedom, N_{se} number of superelements, N_{rb} number of rigid bodies (including nacelle), –: not implemented in the module, and ●: implemented in the model.*

I.2.4 Electrical module library

The electrical module library contains two modules, *i.e.* Elec0, and Elec2, describing the dynamics of the electromagnetic part of a synchronous generator plus AC-DC-AC conversion system at different levels of complexity.

Elec0 module

The Elec0 module contains the simplest model. It is assumed that vector control has been successfully applied to the synchronous generator in question, implying that the synchronous generator can be viewed as an instantaneous torque source. Such a controlled generator can be modeled as a first order system with a time constant $\tau_{T_{em}}$ derived from the torque response time. The time constant comprises thus both the power converter and the electromagnetic dynamics of a synchronous generator. The value of the constant is dependent on the switching frequency of the converter and the sampling rate of the torque controller. For example, the torque response time of the controlled Elec2 module can be used to derive the time constant $\tau_{T_{em}}$ required for simulation of Elec0.

Elec2 module

The Elec2 module contains the most complex generator model in the library. The electromagnetic part contains the voltage and flux equations of the synchronous generator as described in Section 3.5. This model has been identified, verified and validated in Section 4.3 using experimental data acquired from the Lagerwey LW-50/750 synchronous generator. The block diagram of this module is depicted in Fig. 3.26 on page 100.

Main features overview

The main features of the two modules are listed in Table I.5. The Elec2 module is most-suited for designing a frequency converter controller on the basis of a validated synchronous generator model, while the Elec0 module is most suited for time-domain wind turbine simulations.

Electrical modules features overview			
Module name	Order	Time-domain simulation	Frequency converter control design
Elec0	1	++	−
Elec2	$\geq 8^{\dagger}$	−	++

Table I.5: *Overview electrical modules, with †: depends on synchronous generator under investigation, ++ suited, − not suited.*

Bibliography

[1] ABB Reinosa, S.A. Dpto. de Calidad, Ensayos Electricos, *Test record LW50/750, 810 KVA, 690 V, 27 R/min.* Generator No. 51210-001, Reinosa, 4 Agosto de 1998.

[2] M.B. Anderson, "A vortex-wake analysis of a horizontal axis wind turbine and a comparison with modified blade element theory." In *Proceedings of 3rd International Symposium on Wind Energy Systems, Copenhagen, BHRA Fluid Engineering*, pp. 357–374, 1980.

[3] P.M. Anderson, and A.A. Fouad, *Power System Control and Stability.* The Iowa State University Press, Ames, Iowa, U.S.A., 464p., 1977.

[4] Anon, *Adams User's Guide*, Mechanical Dynmics Inc., 3055 Plymouth Rd., Ann Arbor, Michigan, 1987.

[5] K.J. Åström, and T. Hägglund, *PID Controllers: Theory, Design and Tuning.* Instrument Society of America, Research Triangle Parc, NC, USA, 1995.

[6] G.E. van Baars, *Validation of flexible wind turbine dynamic models through open field identification experiments.* PhD. Thesis, Delft University of Technology, Mechanical Engineering Systems and Control group, (to appear).

[7] Y. Bard, *Nonlinear Parameter Estimation.* Acdemic Press, New York, 341p., 1974.

[8] N.D.P. Barltrop, and A.J. Adams, *Dynamics of fixed marine structures.* Butterworth-Heinemann Ltd, Linacre House, Jordan Hill, Oxford, Great-Britain, 764p., 1991.

[9] W.A.A.M. Bierbooms, *A dynamic model of a flexible rotor - Part 1: Description of the mathematical model.* Delft University of Technology, Institute for Wind Energy, IW 89.034R, 82p., May 1990.

[10] W.A.A.M. Bierbooms, *Modellering van Dynamic Stall met behulp van de Onera Methode.* Delft University of Technology, Institute for Wind Energy, IW 91.044m, 30p., July 1991.

[11] W.A.A.M. Bierbooms, *Swing4 User Guide.* Delft University of Technology, Institute for Wind Energy, IvW-98133 R, 22p., February 1998.

[12] W.A.A.M. Bierbooms, P.M.M. Bongers, and M. Steinbuch, *An integrated dynamic model of a wind turbine.* Delft University of Technology, Institute for Wind Energy, IW 87.011 R, 73p., May 1987.

[13] W.A.A.M Bierbooms, and J.B. Dragt (Institute for Wind Energy), "SWING 4: A stochastic 3D wind field generator for design calculations." In *Proceedings of European Union Wind Energy Conference, EUWEC 1996*, Göteborg, Sweden, pp. 942–945, May 20–24, 1996.

[14] A. Björck, and S-E. Thor (FFA, The Aeronautical Institute of Sweden), "Dynamic stall and 3D effects." In *Proceedings of European Union Wind Energy Conference, EUWEC 1996*, Göteborg, Sweden, pp. 683–686, May 20–24, 1996.

[15] J.K. de Boer, *FLEXLAST 3.0, Description of an analysis tool for the prediction of loads on wind turbines.* Stork Product Engineering, Amsterdam, The Netherlands, SPE report 94-040, September 1993.

[16] W.W. de Boer and M.W. Mortier (KEMA, The Netherlands), "Experimental results of optimal output feedback controlled wind turbines of the experimental wind farm." In *Proceedings of European Wind Energy Conference, EWEC 1994*, Thessaloniki, Macedonia, Greece, pp. 593–598, October 10–14 1994.

[17] T. Bohlin and S.F. Graebe, "Issues in nonlinear stochastic grey box identification." In *International Journal of Adaptive Control and Signal Processing.* Volume 9, pp. 465–490, 1995.

[18] E.S. Boije, J.C. Balda, R.G. Harley, and R.C. Beck, "Time-domain identification of synchronous machine parameters from standstill tests.", In *IEEE Transactions on Energy Conversion*, Volume 5, No. 1, pp. 164–175, 1990.

[19] I. Boldea, and S.A. Nasar, *Electric drives.* CRC Press, Inc., Boca Raton, Florida, 411p., 1999.

[20] P.M.M. Bongers, *DUWECS Reference guide V2.0, Delft University Wind Energy Converter Simulation Package.* Delft University of Technology, The Netherlands, DUT-MEMT 26, 1993.

[21] P.M.M. Bongers, *Modeling and Identification of Flexible Wind Turbines and a Factorizational Approach to Robust Control.* PhD. Thesis, Delft University of Technology, Faculty of Mechanical Engineering and Marine Technology, Measurement and Control group, June 1994.

[22] P.M.M. Bongers, G.E. van Baars, Sj. Dijkstra and O.H. Bosgra, *Dynamic models for wind turbines.* Delft University of Technology, Faculty of Mechanical Engineering and Marine Technology, Measurement and Control group, memt-28, 115p., 1993.

[23] P.M.M. Bongers, W. Bierbooms, Sj. Dijkstra, and T. van Holten, *An integrated dynamic model of a flexible wind turbine.* Delft University of Technology, Faculty of Mechanical Engineering and Marine Technology, Measurement and Control group, memt-6, 106p., 1990.

[24] P.M.M. Bongers, Th. van Holten and Sj. Dijkstra, "Control of wind turbine systems for load reduction." In *Proceedings of Wind Energy: Technology and Implementation, EWEC 1991.* Amsterdam, The Netherlands, pp. 68–72, 1991.

[25] I. Bonnet, "Tegenwind voor windenergie." In *Delta*, No. 36, 23 November 2000.

[26] B.K. Bose, *Power Electronics and Variable Frequency Drives.* IEEE Press, 445 Hoes Lane, P.O. Box 1331, Piscataway, NJ, 640p., 1997.

[27] B. Bosman (TNO Bouw - Centrum voor Mechanische Constructies), "Trilvormen aan vleugelprofiel: APX-70", TNO Bouw Memorandum No. 2000-CMC-M288/BNB, 17p., 11 July 2000.

[28] B. Bosman (TNO Bouw - Centrum voor Mechanische Constructies), "Trilvormen aan een 29m blad", TNO Bouw Memorandum No. 2002-CMC-B89/BNB, 17p., 12 Maart 2002.

[29] E.A. Bossanyi (Garrad Hassan & Partners), *Bladed for Windows - Theory Manual.* Garrad Hassan & Partners Limited, Bristol, England, Document No. 282/BR/009, Issue No. 3, 54p., June 1997.

[30] E.A. Bossanyi (Garrad Hassan and Partners Ltd.), "Developments in closed loop controller design for wind turbines." In *Proceedings of the 2000 AIAA/ASME Wind Energy Symposium*, Reno, NV, pp. 64–74, January 10-13, 2000.

[31] A. Boxmeer, "Niemand wil een windmolen." In *Intermediair*, No. 31, pp. 27–29, 5 August 1999.

[32] A.J. Brand, H. Snel (Netherlands Energy Research Foundation ECN), G.E. van Baars, P.M.M. Bongers (Delft University of Technology), N.O.T. Hansen and G.A.M. van Kuik (Stork Product Engineering), *The Dutch contribution to the IEA UNIWEX project.* ECN-C-94-075, 61p., September 1994.

[33] BTM Consults ApS, *Ten Percent of the World's Electricity Consumption from Wind Energy! - Is that target achievable?* Main report for the Forum for Energy & Development (FED), BTM Consults ApS, I.C. Christensens Allé 1, DK-6950 Rinkøbing, Denmark, 55p., October 1998.

[34] BTM Consult ApS (www.btm.dk), *World Market Update 2001 - Forecast 2002-2006.* I.C. Christenses Allé 1, Rinkøbing, Denmark, 66p., March 2002.

[35] J.L. Buchanan, and P.R. Turner, *Numerical methods and analysis.* International series in pure and applied mathematics, McGraw-Hill, New York, 751 p., 1992.

[36] I.K. Buerings and L.L. Freris, "Control policies for wind energy conversion systems." In *Proceedings of the IEEE Conference on Control Applications*. Volume 128, 1981.

[37] T. Burton, D. Sharpe, N. Jenkins, and E. Bossanyi, *Wind Energy Handbook*, John Wiley & Sons, Ltd, Baffins Lane, Chichester, West Sussex PO19 1UD, England, 617p., 2001.

[38] T.R. Camp, E.A. Bossanyi, and D.C. Quarton (Garrad Hassan and Partners Limited), "Design loads for offshore wind turbines." `http://www.energyweb.net/articles/gh_design_loads.html,`4p, 1999.

[39] R. Cardenas-Dobson (Universidad de Magallanes, Punta Arenas Chile), and G.M. Asher (University of Nottingham, Electrical Engineering Department, United Kindom), "Power Limitation in Variable Speed Wind Turbines using Pitchh Control and a Mechanical Torque Observer." In *Wind Engineering*. Volume 20, No. 6, pp. 363–387, 1996.

[40] T.G. Carne, J.P. Lauffer, A.J. Gomez, and H. Benjannet (Sandia National Laboratories), *Modal Testing the EOLE*. Sandia Report SAND87-1506, 24p., April 1988.

[41] P. Caselitz, W. Kleinkauf, T. Krüger, J. Petschenka (Institut für Solare Energieversorgungstechnik e. V.), and K. Störzel (Fraunhofer-Institut für Betreibsfestigkeit), "Load reduction by multivariable control of wind energy convertors - simulations and experiments." In *Proceedings of European Union Wind Energy Conference, EUWEC 1996*, Göteborg, Sweden, pp. 821–824, May 20–24, 1996.

[42] P. Caselitz, W. Kleinkauf, T. Krüger, J. Petschenka, M. Reichardt (Institut für Solare Energieversorgungstechnik e. V.), and K. Störzel (Fraunhofer-Institut für Betreibsfestigkeit), "Reduction of fatigue loads on wind energy convertors by advanced control methods." In *Proceedings of European Wind Energy Conference, EWEC 1997*, Dublin, Ireland, pp. 555–558, October 6–9 1997.

[43] S.K. Chakrabarti, *Hydrodynamics of Offshore structures*. WIT Press, Computations Mechanical Publications, 440p., 1999.

[44] S.J. Chapman, *Electric Machinery Fundamentals*. Schaum's Outline Series in Electronics & Electrical Engineering, McGraw-Hill, Inc., New York, 716p., 1991.

[45] B.W. Char, K.O. Geddes, G.H. Gonnet, B.L. Leong, M.B. Monagan, and S.M. Watt, *Maple V Library Reference Manual*. Springer-Verlag, 698p., 1992.

[46] G. Chavent, "Identifiability of parameters in output least square formulation." In E. Walter (editor), *Identifiability of parametric models*, Pergamon Press, pp. 67–74, 1987.

[47] P.J. Cloos (Twaron Products V.o.F.), personal communication, November 3, 1998.

[48] T. Christensen, J. Pedersen, L.B. Plougmand, S. Mogensen, H. Sterndorf, "Flex5 for offshore environments." In *Proceedings of 2001 European Wind Energy Conference and Exhibition*, Bella Center, Copenhagen, Denmark July 2–6, 2001.

[49] T.H. Cockerill, R. Harrison, M. Kühn, and G.J.W. van Bussel, *Comparison of Cost of Offshore Wind Energy at European Sites*, Opti-OWECS Final Report, Volume 3, ISBN 90-76468-04-4, 1998.

[50] J.R. Connell (Pacific Northwest Laboratory, Richland, Washington), "A primer of turbulence at the wind turbine rotor." In *Windpower 1985*, San Fransisco, California, USA, pp. 57–66, 1985.

[51] A. Dadone, and L. Dambrosio, "Estimator based adaptive fuzzy logic control technique for a wind turbine-generator system." In *Energy Conversion & Management*, Volume 44, pp. 135–153, 2002.

[52] J. d'Alembert, *Traité de Dynamique*, Paris, 1743.

[53] dSPACE®: http://www.dspace.de/

[54] T.F. Edgar, and D.M. Himmelblau, *Optimization of chemical processes.* McGraw-Hill International Editions, Chemical Engineering Sciences, Singapore, 652p., 1989.

[55] D.M. Eggleston and F.S. Stoddard, *Wind turbine engineering design.* Van Nostrand Reinhold, New York, USA, 352p., 1987.

[56] A.S. Elliott (Mechanical Dynamics, Inc., Ann Arbor, Michigan), and A.D. Wright (National Renewable Energy Department, Golden, Collerado), *ADAMS/WT 1.0 User's Guide and Reference Manual.* Version 1.0, February 1994.

[57] A.S. Elliott (Mechanical Dynamics, Inc., Ann Arbor, Michigan), and A.D. Wright (National Renewable Energy Department, Golden, Collerado), *ADAMS/WT 2.0 User's Guide.* Version 2.0, December 1998.

[58] Energy Information Administration (EIA), International Energy Annual 1999, DOE/EIA-0219(99), Washington, DC, January 2001.

[59] L. Euler, "Nova methods motum corporum rigidarum determinandi." In *Novi Commentarii Academiæ Scientiarum Petropolitanæ*, 20, pp. 208–238, 1776.

[60] *Wind Energy - The Facts*, European Commission, Directorate-General for Energy, 1999.

[61] L.J. Fingersh, and P.W. Carlin (National Renewable Energy Laboratory, Golden, Colorado), "Results from the NREL variable-speed test bed." In *Proceedings of the 1998 ASME Wind Energy Symposium Technical Papers Presented at the 36th AIAA Aerospace Sciences Meeting and Exhibit*, Reno, NV, pp. 233–237, January 12-15, 1998.

[62] P. Fisette, and J.C. Samin (Department of Mechanical Engineering, Université catholique de Louvain, Belgium), "The modelling of complex mechanical systems in the Matlab/Simulink environment." In *Proceedings 1st Benelux Matlab Users Conference*, Amsterdam, The Netherlands, Chapter 4 pp. 1–11, October 27–28, 1997.

[63] A.E. Fitzgerald, C. Kingsley Jr., and S.D. Umans, *Electric Machinery*. MacGraw-Hill International (UK) Limited, 599p., 1992.

[64] R. Fletcher, *Practical Methods of Optimization*. John Wiley & Sons, Baffins Lane, Chichester, West Sussex PO19 1UD, England, 436p., 1987.

[65] L.L. Freris, *Wind energy conversion systems*. Prentice Hall International (U.K.) Ltd, University Press, Cambridge, 388 p., 1990.

[66] L.N. Freeman, and R.E. Wilson (Department of Mechanical Engineering, Oregon State University, Corvallis), "The FAST code." In *Proceedings of the 28th IEA Meeting of Experts "State of the Art of Aerolelastic Codes for Wind Turbine Calculations"*, Technical University of Denmark, Lyngby, pp. 37-56, 11–12 April 1996.

[67] P.P. Friedmann (Mechanics and Structures Department, University of California), "aero-elastic Modelling of Large Wind Turbines." In *Journal of American Helicopter Society*, Volume 21, No. 4, pp. 17–27, October 1976.

[68] R.E. Froude, "On the part played in propulsion by differences of fluid pressure." In *Transactions of the Institute of Naval Architects*, Volume 30, p. 390, 1889.

[69] H. Ganander (Teknikgruppen AB, Sollentuna, Sweden), "The Vidyn story." In *Proceedings of the 28th IEA Meeting of Experts "State of the Art of Aerolelastic Codes for Wind Turbine Calculations"*, Technical University of Denmark, Lyngby, pp. 77-90, 11–12 April 1996.

[70] H. Ganander, and B. Olsson (Teknikgruppen AB), *VIDYN - Time simulation program for wind turbines*. Version 6, 69p., 14 December 1994.

[71] G.H. Gaonkar and D.A. Peters, "Effectiveness of Current Dynamic-Inflow Models in Hover and Forward Flight." In *Journal of the American Helicopter Society*, Volume 31, No. 2, pp. 47–57, April 1986.

[72] G.H. Gaonkar and D.A. Peters, "Review of Dynamic Inflow Modeling for Rotorcraft Flight Dynamics." In *Vertica*, Volume 12, No. 3, pp. 213–242, 1988.

[73] A.D. Garrad, "Dynamics of wind turbines." In *IEEE Proceedings*, Volume 130, No. 9, pp. 523–530, December 1983.

[74] Bladed for Windows - A Design Tool for Wind Turbine Performance and Loading (Offshore Upgrade), http://www.garradhassan.com/bladed/index.htm, 2001.

[75] J. Geldermans, "Nut windmolens is te verwaarlozen.", In *Alkmaarse Courant*, 30 October 2000.

[76] J.M. Gere (Stanford University), and S.P. Timoshenko (Late of Stanford University), *Mechanics of Materials*. Van Nostrand Reinhold (International), Hong Kong, 762p., 1987.

[77] Germanischer Lloyd, *Rules & Guidelines 2000: IV Non-marine Technology - Regulations for the Certification of (Offshore) Wind Energy Conversion Systems*, 1999.

[78] M. Geyler, *Advanced Pitch Control for Wind Turbines - Literature survey and first considerations on the potential of pitch control to reduce structural vibrations and fatigue loads*. Duwind Report 2001.001, 68p., January 2001.

[79] P.E. Gill, W. Murray, and M.H. Wright, *Practical Optimization*. Academic Press Inc., London, 401p., 1981.

[80] P. Gipe, *Wind energy comes of age*. John Wiley & Sons, Inc., United States of Ameica, 536p., 1995.

[81] H. Glauert, "Airplane propellors." In *W.F. Durand (editor), Aerodynamic Theory*, Volume 4, pp. 169–360, Springer, Berlin, 1935.

[82] H. Glauert, *The Analysis of Experimental Results in Windmill Brake and Vortex Ring States of an Airscrew*. Reports and Memoranda, No. 1026, London: Aeronautical Research Committee, 1926.

[83] H. Glauert, *The elements of airfoil and airscrew theory (second edition)*. Cambridge University Press, 232p., 1959.

[84] Global Business Environment (PXG), *Energy Needs, Choices and Possibilities - Scenarios to 2050*, www.shell.com/scenarios, Exploring The Future, Shell International Limited, Shell Centre, London SE1 7NA, 60p., 2001.

[85] Global Business Environment (PXG), *People and Connections - Global Scenarios to 2020*, Public Summary (www.shell.com/scenarios), Exploring The Future, Shell International Limited, Shell Centre, London SE1 7NA, 2002.

[86] K.R. Godfrey, and J.J. DiStefano, III, "Identifiability of model parameters." In E. Walter (editor), *Identifiability of parametric models*, Pergamon Press, pp. 1–20, 1987.

[87] A. de Goederen, "Windenergie parasiteert op de conventionele centrales.", In *Het Parool*, 29 April 2000.

[88] S. Goldstein, "On the Vortex Theory of Screw Propellors". In *Roy. Soc. Proc. (A)*, 123, p. 440, 1929.

[89] R.E. Gormont, "A mathematical model of unsteady aerodynamics and radial flow for application to helicopter rotors." Final Report, D210-10492-1, The Boeing company, Vertol division, Philadelphia, PA, USA, 172p., May 1973.

[90] R.J.A. Gorter, *Grey-box Identification of Induction Machines: on-line and offline approaches*. PhD. Thesis, Eindhoven University of Technology, December 1997.

[91] A. Grace, *Optimization Toolbox*, The MathWorks, Inc., 21 Eliot Street, South Natick, MA, November 1990.

[92] A. Grauers, *Design of Direct-driven Permanent-magnet Generators for Wind Turbines*. Technical report No. 292, Department of Electric Power Engineering, Chalmers University of Technology, Göteborg, Sweden, 1996.

[93] M.J. Grimble, "Two and a Half Degrees of Freedom LQG Controller and Application to Wind Turbines." In *Proceedings IEEE transactions on automatic control*. Volume 39, No. 1, pp. 122–127, January 1994.

[94] "Haarscheurtjes in windmolens", In *De Telegraaf*, 14 October 1999.

[95] M.M. Hand, (National Wind Technology Center, NREL), and M.J. Balas (Department of Aerospace Engineering Sciences, University of Colorado at Boulder), "Systematic approach for PID controller design for pitch-regulated, variable speed wind turbines." In *Proceedings of the 1998 ASME Wind Energy Symposium Technical Papers Presented at the 36th AIAA Aerospace Sciences Meeting and Exhibit*, Reno, NV, pp. 84–94, January 12-15, 1998.

[96] M.M. Hand, (National Wind Technology Center, NREL), and M.J. Balas (Department of Aerospace Engineering Sciences, University of Colorado at Boulder), "Non-Linear and Linear Model Based Controller Design for Variable Speed Wind Turbines." In *Proceedings of the 3rd ASME/JSME Joint Fluids Engineering Conference*, San Francisco, California, pp. 1–6, July 18-23, 1999.

[97] A.C. Hansen (University of Utah, Salt Lake City, UT), *User's Guide to the Yaw Dynamics Computer Program YawDyn*. 32p., August 1993.

[98] A.C. Hansen (University of Utah, Salt Lake City, UT), *YawDyn / Aerodyn*. http://www.nrel.gov/wind/software/yawdyndesc.html, 2p., 1998.

[99] A.C. Hansen (University of Utah, Salt Lake City, UT), *Yaw dynamics of horizontal axis wind turbines*. Final Report, National Renewable Energy Laboratory, NREL/TP-442-4822, 73p., May 1992.

[100] A.C. Hansen (Mechanical Engineering Department, University of Utah) and C.P. Butterfield (National Renewable Energy Laboratory, Golden, Colorado), "Aerodynamics of horizontal-axis wind turbines." In *Annu. Rev. Fluid Mechanics*, Volume 25, pp. 115–149, 1993.

[101] L.H. Hansen, L. Helle, F. Blaabjerg, E. Ritchie, S. Munk-Nielsen, H. Bindner, P. Sørensen and B. Bak-Jensen, *Conceptual survey of Generators and Power Electronics for Wind Turbines*. Risø National Laboratory, Roskilde, Denmark, Risø-R-1205(EN), 105p., December 2001.

[102] A.C. Hansen, and D.L. Laino (University of Utah, Salt Lake City, UT), *User's Guide to the Wind Turbine Dynamics Computer Programs YawDyn and Aerodyn for Adams® - Version 11.0*. 79p., 31 August 1998.

[103] F.D. Harris, F.J. Tarzanin, and F.J. Fisher, "Rotor high speed performance - theory versus test." In *Journal American Helicopter Society*, Volume 17, 1972.

[104] S. Henschel, and H.W. Dommel, "Noniterative Synchronous Machine Parameter Identification from Frequency Response Tests.", In *IEEE Trans. on Power Systems*, Vol. 14, No. 2, pp. 553–560, 1999.

[105] R.L. Hills, *Power from wind - A history of windmill technology*. Cambridge University Press, 324p., 1994.

[106] E.N. Hinrichsen (Power Technologies, Inc., Schenectady, New York), "Variable rotor speed for wind turbines objectives and issues." In *Windpower 1985*, San Fransisco, California, USA, pp. 164–170, 1985.

[107] M.J. Hoeijmakers (Delft University of Technology), *Elektrische omzettingen*. Delftse Universitaire Pers, 198p., 18 Januari 1997.

[108] M.J. Hoeijmakers (Delft University of Technology), *Personal communication*. October 6, 1999.

[109] M.G. Hollars, D.E. Rosenthal, and M.A. Sherman, *SD/FAST User's Manual*. Symbolics Dynamics, Inc., Version B.2, September 1994.

[110] R. Hooke, and T.A. Jeeves, "Direct search solution of numerical and statistical problems." In *Journal of the Association for Computing Machinery*, Volume 8, pp. 221-229, 1961.

[111] IEEE Standard 115-1995: IEEE Guide: Test Procedures for Synchronous Machines Part I – Acceptance and Performance Testing and Part II – Test Procedures and Parameter Determination for Dynamic Analysis (revisions of IEEE Std 115-1983 and IEEE Std 115A-1987 *see* http://standards.ieee.org/catalog/olis/index.html), Institute of Electrical and Electronics Engineers, Inc. New York, NY, 216p., 1996.

[112] International Standard IEC 1400–1, *Wind turbine generator systems – Part 1: Safety requirements.* Bureau Central de la Commission Electrotechnique Internationale, 3 rue de la Varambé, Genève, Suisse, First edition, December 1994.

[113] International Energy Agency, *Needs for Renewables*, A Report on a Workshop of the Renewable Energy Working Party (REWP) of the International Energy Agency (IEA), Paris, France, October 11, 2000.

[114] International Energy Agency, *World Energy Outlook, 1999 Insights: Looking at Energy Subsidies: Getting the Prices Right.* International Energy Agency (IEA), Paris, France, 206 p., 1999.

[115] M.T. Iqbal, A.H. Coonick and L.L. Freris, "Dynamic control for variable speed wind turbines." In *Wind Engineering.* Volume 18, No. 1, pp. 1–12, 1994.

[116] A.R. Jacobs, *Rapport betreffende de funderingswijze van een LW 45/750 windturbine met een 50 m mast.* Rapport WTXF - 6091. ABT Adviesburau voor Bouwtechniek BV, Arnhemsestraat 358, 6881 NK Velp, 27 p., Oktober 1995.

[117] G.H. James III, T.G. Carne, and J.P. Lauffer (Sandia National Laboratories), *The Natural Excitation Technique (NExT) for Modal Parameter Extraction From Operating Wind Turbines.* Sandia Report SAND92-1666, 46p., February 1993.

[118] W. Johnson, *Helicopter Theory.* Princeton US, 1089p., 1980.

[119] C.N. Jones (Department of Mechanical Engineering, University of Queensland, Brisbane, Australia), "Blade Element Performance in Horizontal-Axis Wind-Turbine Rotors." In *Wind Engineering*, Volume 7, No. 3, pp. 129–137, 1983.

[120] I. de Jong (OJA-Services), and H. Bouwmeester. *Toepassing windenergie in Nederland. Het meerjarenprogramma windenergie 1996-2000 TWIN-2.* Novem, August 1996.

[121] J.B. Jonker, *Spacar User manual and System Description.* Report TM872, Delft University of Technology, Laboratory for Engineering Mechanics, 1988.

[122] P.A. Joosse, G.D. de Winkel, and C. Lindenburg, *Natural vibrations of the APX70 blade, measurements and calculations.* WMC group, Delft University of Technology, Report WMC 6-00-25, 17 July 2001.

[123] P.A. Joosse, G.D. de Winkel, and C. Lindenburg, *Natural vibrations of the RB51 blade, measurements and calculations.* WMC group, Delft University of Technology, Report WMC 2002-06, 14 May 2002.

[124] P.A. Joosse, G.D. de Winkel, and C. Lindenburg, *Natural vibrations of the RB70 blade, measurements and calculations.* WMC group, Delft University of Technology, Report WMC 2002-17, 14 May 2002.

[125] P.E.B. Jourdain, "Note on an analogue at Gauss' principle of least constraints". In *Quarterly Journal on Pure Applied Mathematics*, 40, pp. 153–197, 1909.

[126] J-N. Juang, *Applied System Identification*. Hall, Inc. Englewood Cliffs, New Jersey, USA, 394p., 1994.

[127] J.L. Junkins (Editor), *Mechanics and Control of Large Flexible Structures*. American Institute of Aeronautics and Astronautics, Washington, 705p., 1990.

[128] J.L. Junkins, and Y. Kim, *Introduction to Dynamics and Control of Flexible Structures*. American Institute of Aeronautics and Astronautics, Washington, 452p., 1993.

[129] T.R. Kane (Stanford University), and D.A. Levinson (Lockheed Martin Missiles and Space), *Dynamics OnLine: Theory and implementation with AUTOLEV*. OnLine Dynamics, Inc., Sunnyvale, CA, United States of America, 354p., 1996.

[130] T.R. Kane (Stanford University), and D.A. Levinson (Lockheed Palo Alto Research Laboratory), *Dynamics: Theory and Applications*. McGraw-Hill Series in Mechanical Engineering, McGraw-Hill Book Company, 379p., 1985.

[131] T.R. Kane and D.A. Levinson, "Formulations of Equations of Motion for Complex Spacecraft." In *Journal of Guidance and Control*, Volume 3, No. 2, pp. 99–112, March-April 1980.

[132] N.D. Kelley (National Renewable Energy Laboratory, Golden, Colorado), "Full vector (3-D) inflow simulation in natural and wind farm environments using an expanded version of the SNLWIND (Veers) turbulence code." http://www.nrel.gov/wind/library.html, 9p., 1997.

[133] S.G. Kelly, *Fundamentals of Mechanical Vibrations*. McGraw-Hill series in mechanical engineering, New York, 643p., 1993.

[134] N. Kelley, A. Wright, and R. Osgood (National Wind Technology Center NREL), "A Progress Report on the Characterization and Modeling of a Very Flexible Wind Turbine Design." In *Proceedings 1999 ASME Wind Energy Symposium AIAA/ASME*, Reno, Nevada, pp. 243–252, January 11–14 1999.

[135] L. Kendall, M.J. Balas, Y.J. Lee (Department of Aerospace Engineering Sciences, University of Colorado at Boulder), and L.J. Fingersh (Wind Technology Division, NREL, Colorado), "Application of Proportional-Integral and Disturbance Accomodating Control to Variable Speed Variable Pitch Horizontal Axis Wind Turbines." In *Wind Engineering*. Volume 21, No. 1, pp. 21–38, 1997.

[136] A. Keyhani, H. Tsai, and T. Leksan, "Maximum likelihood estimation of synchronous machine parameters from standstill time response data.", In *IEEE Transactions on Energy Conversion*, Volume 9, No. 1, pp. 98–114, 1994.

[137] KIVI, *Resultaten van een debat tussen voor- en tegenstanders van windenergie.* Report nummer An963057.R20, 31p., Juni 2002.

[138] T. Knudsen, P. Andersen, and S. Toffner-Clausen (Aalborg university, Institute of Electronic Systems, Department of Control Engineering), "Comparing PI and Robust pitch controllers on a 400 kW wind turbine by full scale tests." In *Proceedings of European Wind Energy Conference, EWEC 1997*, Dublin, Ireland, pp. 546–550, October 6–9 1997.

[139] G.A.M. van Kuik, *On the limitations of Froude's actuator disc concept.* PhD. Thesis, Eindhoven University of Technology, February 1991.

[140] E. Kreuzer (Editor), *Computerized symbolic manipulation in mechanics.* Springer Verlag, 262p., 1994.

[141] L. Kristensen, and S. Frandsen, "Model for power spectra of the blade of a wind turbine measured from the moving frame of reference." In *Journal of Wind Engineering and Industrial Aerodynamics*, Volume 10, pp. 249–262, 1982.

[142] T. Krüger, *Regelungsverfahren für Windkraftanlagen zur Reduktion der mechanischen Belastung.* PhD. Thesis, Universität Gesamthochschule Kassel, Germany, April 1998.

[143] M. Kühn (Institute for Wind Energy), *Dynamics of an Offshore Wind Turbine Digital Simulation.* Delft University of Technology, Institute for Wind Energy, IW 93.068 R, 102p., October 1993.

[144] M. Kühn (Institute for Wind Energy), *Dynamics and Design Optimisation of Offshore Wind Energy Conversion Systems.* PhD. Thesis, Delft University of Technology, Institute for Wind Energy, May 2001.

[145] W. Kuik (Stentec), "The wind turbine response program, called FKA-12 of Stentec, the Netherlands." In *Proceedings of the 28th IEA Meeting of Experts "State of the Art of Aerolelastic Codes for Wind Turbine Calculations"*, Technical University of Denmark, Lyngby, pp. 147-160, 11–12 April 1996.

[146] G.A.M. van Kuik, "Are wind turbines growing too fast?" In *Proceedings of European Wind Energy Conference and Exhibition, EWEC 2001*, Copenhagen, Denmark, July 2-6 2001.

[147] P. Kundur, *Power System Stability and Control*, McGraw-Hill, Inc., 1176p., 1994.

[148] J.C. Lagarias, J.A. Reeds, M.H. Wright, and P.E. Wright, "Convergence Properties of the Nelder-Mead Simplex Method in Low Dimensions." In *SIAM Journal on Optimization*, Volume 9, No. 1, pp. 112–147, 1998.

[149] J.-L. Lagrange, *Mécanique Analytique*, L'Académie Royal des Sciences, Paris, 1788.

[150] T.J. Larsen (Risø), email contact, August 12, 2002.

[151] J.P. Lauffer, and T.C. Carne (National Renewable Energy Laboratory), "Modal testing in the design evaluation of wind turbines." In *Windpower 1985*, San Fransisco, California, USA, pp. 323–332, 1985.

[152] J.P. Lauffer, T.G. Carne, T.D. Ashwill (Sandia National Laboratories), *Modal Testing in the Design Evaluation of Wind Turbines.* Sandia Report SAND87-2461, 25p., April 1988.

[153] L.X. Le, and W.J. Wilson, "Synchronous machine parameter identification: a time-domain approach.", In *IEEE Trans. on Energy Conversion*, Vol. 3, No. 2, pp. 241–248, 1988.

[154] E. Lee, *Self-regulating Wind Machine*, British patent No. 615, 3p., 9 December 1745.

[155] J.L. van Leeuwen, and D.R.V. van Delft (Stevin Laboratorium, Delft University of Technology), *Full scale tests on the APX45 rotor blade part I; Blade data, root fixing and test rig.* Stevin report 6-96-8, 13p., 8 September 1997.

[156] J.L. van Leeuwen, and D.R.V. van Delft, *Full scale tests on the APX45 rotor blade part II; Natural frequency tests.* Stevin report 6-96-9, 6p., 10 September 1997.

[157] J.G. Leishman, and T.S. Beddoes (Aerodynamics Department, Westland Helicopters Ltd., Yeovil, Somerset, United Kingdom), "A Semi-Empirical Model for Dynamic Stall." In *Journal of American Helicopter Society*, Volume 34, No. 2, pp. 3–17, July 1989.

[158] D.J. Leith, and W.E. Leithead (Department of Electronic and Electrical Engineering, University of Strathclyde, Glasgow, United Kingdom), "Appropriate realization of gain-scheduled controllers with application to wind turbine regulation." In *International Journal of Control*, Volume 65, No. 2, pp. 223–248, 1996.

[159] W. Leonhard, *Control of Electrical Drives.* Springer-Verlag Berlin Heidelberg, 430p., 1996.

[160] C. Lindenburg (Netherlands Energy Research Foundation ECN), Personal communication, May 15, 2001.

[161] C. Lindenburg (Netherlands Energy Research Foundation ECN), *PHATAS-III User's Manual - Program for Horizontal Axis wind Turbine Analysis and Simulation - version III.* ECN Unit Renewable Energy, P.O. Box 1, Petten, The Netherlands, ECN-C-95-040, 124p., May 1996.

[162] C. Lindenburg (Netherlands Energy Research Foundation ECN), *Results of the PHATAS-III development.* ECN Unit Renewable Energy, P.O. Box 1, Petten, The Netherlands, 7p., 1996.

[163] C. Lindenburg, and T. Hegberg (Netherlands Energy Research Foundation ECN), *PHATAS-IV User's Manual - Program for Horizontal Axis wind Turbine Analysis and Simulation - version IV*. ECN Unit Renewable Energy, P.O. Box 1, Petten, The Netherlands, ECN-C-99-093, 137p., May 2000.

[164] C. Lindenburg, and J.G. Schepers (Netherlands Energy Research Foundation ECN), *PHATAS-III: Program for horizontal axis wind turbine analysis and simulation, version III - aero-elastic modeling*. ECN-C-96-025, 50p., July 1996.

[165] C. Lindenburg, and J.G. Schepers (Netherlands Energy Research Foundation ECN), *Status of PHATAS-III Release "MAR-1995" - SUN and DOS version.* ECN-C-95-015, 44p., May 1996.

[166] L. Ljung, *System Identification - Theory for the User*. Prentice-Hall, Englewood Cliffs, New Jersey, 519p., 1987.

[167] L. Ljung, and T. Glad, "On Global Identifiability for Arbitrary Model Parametrizations." In *Automatica*, Volume 30, No. 2, pp. 265–276, 1994.

[168] R.P. Luijendijk (Stentec), *TWISTER - Dynamic Response Program for Horizontal Axis Wind Turbines*. Raadgevend Ingenieursbureau Stentec B.V., Heeg, The Netherlands, R6.24/01.05.97, 15p., 12 May 1997.

[169] J.M. Maciejowski, *Multivariable feedback design*. Addison-Wesley Publishing Company, Great Britain, 424p., 1991.

[170] N.M.M. Maia, J.M.M. Silva, J. He, N.A.J. Lieven, R.M. Lin, G.W. Skingle, W-M. To, and A.P.V. Urgueira, *Theoretical and Experimental Modal Analysis*. Research Studies Press Ltd., Taunton, Somerset, England, 468p., 1997.

[171] D.J. Malcolm, "Modal response of 3-bladed wind turbines." In *Proceedings of the 2002 AIAA/ASME Wind Energy Symposium*, Reno, NV, pp. 246–255, January 14-17, 2002.

[172] D. Manor, A. Croxson, and C. Carpmael, *European wind-turbine manufactures*, Credit Suisse First Boston Corporation, 90p., 26 March 2001.

[173] J. Mann (Risø National Laboratory), *Models in Micrometeorology*. Risø National Laboratory, Roskilde, Denmark, Risø-R-727(EN), 127p., March 1994.

[174] J. Mann (Risø National Laboratory), *Wind Field Simulation*. Risø National Laboratory, Roskilde, Denmark, 31p., 28 November 1997.

[175] B.A.H. Marrant, Th. van Holten, and G.A.M. van Kuik, *Smart Dynamic Rotor Control of Large Offshore Wind Turbines*. Duwind Report 2002.012, 43p., May 2002.

[176] MARC Analysis Research Corporation, *Online Documentation: Mentat 3.1-MARC K7.1*, 1997.

[177] J. Mathews, *Guide to accelerometer installation*, Endevo Technical Paper TP 319, Endevco Corporation, 30700 Racho Viejo Road, San Juan Capistrano, CA 92675, USA, 4p., 2001.

[178] J. Mathews, *Guide to adhesively mounting accelerometers*, Endevo Technical Paper TP 312, Endevco Corporation, 30700 Racho Viejo Road, San Juan Capistrano, CA 92675, USA, 10p., 2001.

[179] S.E. Mattsson, *Modelling and Control of Large Horizontal Axis Wind Power Plants*. PhD. Thesis, Department of Automatic Control, Lund Institute of Technology, 176 p., 1984.

[180] R.M. Mayer, *Design of Composite Structures Against Fatigue - Applications to Wind Turbine Blades*, Mechanical Engineering Publications Limited, Suffolk, United Kingdom, 246p., 1996.

[181] K.I.M. McKinnon, "Convergence of the Nelder-Mead simplex method to a nonstationary point." In *SIAM Journal on Optimization*, Volume 9, No. 1, pp. 148–158, 1998.

[182] Ministerie van Economische Zaken, *Derde Energienota*, 1995.

[183] Ministerie van Economische Zaken, http://www.ez.nl/groeneenergie/html/, January 2002.

[184] Ministerie van Economische Zaken, *Partiële herziening Tweede Structuurschema Elektriciteitsvoorziening (Locatiekeuze Demonstratieproject Near Shore Windpark) - Deel 3 Kabinetsstandpunt*. Tweede Kamer, vergaderjaar 2000-2001, 27 041, Sdu Uitgevers, 's-Gravenhage nr.4, 41p., 2001.

[185] S.H. Minnich, "Small signals, large signals, and saturation in generator models." In *IEEE Transactions on Energy Conversion*, Volume EC-1, No. 1, pp. 95–103, March 1986.

[186] D-P. Molenaar, *Control design: a way of reducing fatigue loads on a wind turbine? - NedFlex: a flexible, variable rotational speed wind turbine*. Mechanical Engineering, Systems and Control Group, Delft University of Technology, The Netherlands, TUD-WBMR-S-746, November 1995.

[187] D-P. Molenaar, *DAWIDUM User's Guide*, Version 1, Mechanical Engineering, Systems and Control Group, Delft University of Technology, The Netherlands, TUD-WBMR-N-552, December 2000.

[188] D-P. Molenaar, *Modeling and control of the NedFlex turbine - NedFlex: a flexible, variable rotational speed wind turbine*. Mechanical Engineering, Systems and Control Group, Delft University of Technology, The Netherlands, TUD-WBMR-A-746, August 1996.

[189] D-P. Molenaar, *Modeling the structural dynamics of the Lagerwey LW-50/750 turbine.* Mechanical Engineering, Systems and Control Group, Delft University of Technology, The Netherlands, Report N-522, October 1998.

[190] D-P. Molenaar, *State-of-the-art of wind turbine design codes.* Mechanical Engineering, Systems and Control Group, Delft University of Technology, The Netherlands, Report N-523, March 1999.

[191] D-P. Molenaar, *Validation of the structural model of the Lagerwey LW-50/750 turbine using modal analyis.* Mechanical Engineering, Systems and Control Group, Delft University of Technology, The Netherlands, Report N-531, March 2001.

[192] B. Montgomerie (Netherlands Energy Research Foundation ECN), *Dynamic stall model called "Simple"*, ECN-C-95-060, 48p., January 1996.

[193] B. Montgomerie, and A. Zdunek (FFA The Aeronautical Research Institute of Sweden), "Dynamic response in horizontal-axis wind turbines including instationairy aerodynamic effects in the stream tube." In *Proceedings of European Community Wind Energy Conference 1984*, Hamburg, Germany, pp. 259–264, October 22–26 1984.

[194] J.J. Moré, and S.J. Wright, *Optimization Software Guide.* Society for Industrial Applied Mathematics (SIAM), Philadelphia, 154p., 1993.

[195] D.J. Murray-Smith, "Enhanced environments for the development and validation of dynamic system models", In *Mathematics and Computers in Simulation*, Volume 39, Issues 5-6, pp. 459–464, November 1995.

[196] D.J. Murray-Smith, "Methods for the External Validation of Continuous System Simulation Models: A Review." In *Mathematical and Computer Modelling of Dynamical Systems*, Volume 4, No. 1, pp. 5–31, 1998.

[197] *NAG Foundation Toolbox*, Numerical Algorithms Group Ltd., September 1996.

[198] Nederlandse voornorm, *NVN 11400-0, Wind turbines - Part 0: Criteria for type-certification - technical criteria*, Issue April 1999.

[199] J.A. Nelder, and R. Mead, "A simplex method for function minimization." In *Computer Journal*, Volume 7, pp. 308–313, 1965.

[200] I. Newton, *Philosophiæ Naturalis Principia Mathematica.* Jussu Societatis Regiæ ac Typis Josephi Streater, London, 1687.

[201] P.E. Nielan (Stanford University and Sandia National Laboratories), and T.R. Kane (Stanford University), "Symbolic Generation of Efficient Simulation/Control Routines for Multibody Systems." In *G. Bianchi, and W. Schiehlen (Eds.) - Dynamics of Multibody Systems - IUTAM/IFToMM Symposium, Udine, 1985*, Springer, Berlin Heidelberg, 1986.

[202] D.W. Novotny, and T.A. Lipo, *Vector Control and Dynamics of AC Drives*. Clarendon Press, Oxford, Great Britain, 440p., 1998.

[203] *Offshore Wind Energy Ready to Power a Sustainable Europe.* Final Report Concerted Action on Offshore Wind Energy in Europe, Duwind 2001.006, December 2001.

[204] C. Onwubiko, *Introduction to Engineering Design Optimization*. Prentice Hall, Upper Saddle River, New Jersey, 312p., 2000.

[205] E. Overaa, S.E. Mattsson, and A. Rantzer (Department of Automatic Control, Lund Institute of Technology, Lund, Sweden), "Robustness analyis of a wind power plant." In *Proceedings of European Control Conference 1997*, Brussels, Belgium, 1–4 July 1997.

[206] S. Øye (Technical University of Denmark), "Dynamic stall - simulated as time lag of separation". In *IEA Synposium on the aerodynamics of wind turbines*. Great Britain, November, 1990.

[207] S. Øye (Technical University of Denmark), *FLEX 4 - Metoder*. 10 p., 1998.

[208] S. Øye (Technical University of Denmark), "FLEX 4 - Simulation of Wind Turbine Dynamics." In *Proceedings of the 28th IEA Meeting of Experts "State of the Art of Aerolelastic Codes for Wind Turbine Calculations"*, Technical University of Denmark, Lyngby, pp. 71-76, 11–12 April 1996.

[209] S. Øye (Technical University of Denmark), "Unsteady effects caused by pitch angle changes". In *IEA Synposium - joint action on aerodynamics of wind turbines*. London, Great Britain, October 15, 1986.

[210] M.J.D. Powell, "An efficient method for finding the minimum of a function of several variables without calculating derivatives." In *Computer Journal*, Volume 7, pp. 155–162, 1964.

[211] R.H. Park, "Two-Reaction Theory of Synchronous Machines, Generalized Method of Analysis." Part I: In *AIEE Transactions*, Vol. 48, pp. 716-730, July 1929.

[212] R.H. Park, "Two-Reaction Theory of Synchronous Machines, Generalized Method of Analysis." Part II: In *AIEE Transactions*, Vol. 52, pp. 352-355, June 1933.

[213] M. Päsler, *Prinzipe der Mechanik*, Walter de Gruyter & Co., Berlin, 147p., 1968.

[214] B.M. Pedersen. "State of the Art of aero-elastic Codes for Wind Turbine Calculations - summary". In *Proceedings of the 28th IEA Meeting of Experts "State of the Art of aero-elastic Codes for Wind Turbine Calculations"*, Technical University of Denmark, Lyngby, pp. 207-208, 11–12 April 1996.

[215] J.T. Petersen, "The aero-elastic code HawC - Model and Comparisons." In *Proceedings of the 28th IEA Meeting of Experts "State of the Art of Aerolelastic Codes for Wind Turbine Calculations"*, Technical University of Denmark, Lyngby, pp. 129-135, 11–12 April 1996.

[216] D. Petot (Onera, Châtillon Cedex), "Modélisation du décrochage dynamique par équations différentielles." In *La Recherche Aérospatiale*, Année 1989, No. 5 (Septembre-Octobre), pp. 59–72, 1989.

[217] D. Petot, "Progress in semi-empirical prediction of the aerodynamic forces due to large amplitude oscillations of an airfoil in attached or separated flow." In *Ninth European Rotorcraft Forum*, Paper No. 12, Stresa, Italy, 1983.

[218] D.M. Pitt (U.S. Army Aviation Research and Development Command, St. Louis), and D.A. Peters (Washington University, St. Louis), "Theoretical prediction of dynamic-inflow derivatives". In *Vertica*, Volume 5, pp. 21–34, 1981.

[219] H. Polinder, *On the losses in high-speed permanent-magnet generator with rectifier - with special attention to the effect of a damper cylinder*. PhD. Thesis, Delft University of Technology, Faculty of Electrical Engineering, Power Electronics and Electrical Machines department, June 1998.

[220] H. de la Vallée Poussin, D. Grenier, F. Labrique, and J-D. Legat, "Looking into the implementation of AC motor control on a fixed point processor." In *Proceedings of the IEEE International Electric Machines and Drives Conference IEMDC'99*, Seattle, Washington USA, pp. 519-521, May 9–12, 1999.

[221] L. Prandtl, Appendix to "Schraubenpropellor mit gerngstein Energieverlust" by A. Betz, Gottinger Nachr., pp. 193–217, 1919.

[222] B.R. Prentice, "Fundamental concepts of synchronous machine reactances." In *AIEE Transactions*, Volume 56 (Suppl. 1), pp. 716–720, 1929.

[223] A. Pubanz, "Specifications for the LW-50/750 Back to back convertor - version 1.0." Lagerwey Windturbine B.V., P.O. Box 279, 3770 AG, Barneveld, The Netherlands, July 1, 1997.

[224] A. Pubanz, "Calculated machine parameters - Lagerwey 50/750 B2 generator" Lagerwey Windturbine B.V., P.O. Box 279, 3770 AG, Barneveld, The Netherlands, February 28, 2000.

[225] P.C. Putnam, *Final Report on the Smith-Putnam Wind Turbine*. Engineering Research Division, New York University, War Production Board, 1948.

[226] D.C. Quarton (Garrad Hassan & Partners Ltd., Bristol, United Kingdom), "Calculation of Wind Turbine aero-elastic Behaviour - The Garrad Hassan Approach." In *Proceedings of the 28th IEA Meeting of Experts "State of the Art of Aerolelastic Codes for Wind Turbine Calculations"*, Technical University of Denmark, Lyngby, pp. 3-12, 11–12 April 1996.

[227] D.C. Quarton (Garrad Hassan & Partners Ltd.), "The Evolution of Wind Turbine Design Analysis - A Twenty Year Progress Review." In *Wind Energy*, Volume 1, pp. 5–24, 1998.

[228] D.C. Quarton (Garrad Hassan & Partners Ltd.), F. Rasmussen (Risø National Laboratory), C. Nath, and K. Argyriadis (Germanischer Lloyd), "Wind turbine design calculations - The state of the art." In *Proceedings of European Union Wind Energy Conference, EUWEC 1996*, Göteborg, Sweden, pp. 10–15, May 20–24, 1996.

[229] L.W.M.M. Rademakers and A.P.W.M. Curvers, *Global verification of the "Handbook wind data for the design of wind turbines"*. ECN-C-91-037, June 1991.

[230] L.W.M.M. Rademakers and P.A. van der Werff (Netherlands Energy Research Foundation ECN, *Verification of wind turbine design codes with the "Dutch handbook wind data for wind turbine design"*. ECN-I-92-048, 12p., December 1992.

[231] W.J.M. Rankine, "On the mechanical principles of the action of propellors." In *Transactions of the Institute of Naval Architects*, Volume 6, p. 13, 1865.

[232] J. Rauh, *Ein Beitrag zur Modellierung elastischer Balkensysteme.* Fortschritt-Berichte VDI, VDI-Verlag GmbH, Düsseldorf, Reihe 18: Mechanik/Bruchmechanik, Nr. 37, 126p., 1989.

[233] J. Rauh, and W. Schiehlen, "Various approaches for the Modeling of Flexible Robot Arms." In *Proceedings of the Euromech-Colloquium 219 on Refined Dynamical Theories of Beams, Plates, and Shells and their Applications, Kassel, 1986*, Springer-Verlag, Berlin Heidelberg, pp. 420–429, 1987.

[234] K.J. Reckdahl, and P.C. Mitiguy, *AUTOLEV 3 Tutorial*. OnLine Dynamics, Inc., Sunnyvale, CA, United States of America, 64p., March 12, 1996.

[235] M. Rees (*aerodyn* Energiesysteme GmbH, Rendsburg, Germany), and A. Vollan (Pilatus Flugzeugwerke, Stans, Switzerland), "Garos: an aero-elastic code for coupled fixed rotating structures." In *Proceedings of the 28th IEA Meeting of Experts "State of the Art of Aerolelastic Codes for Wind Turbine Calculations"*, Technical University of Denmark, Lyngby, pp. 97-104, 11–12 April 1996.

[236] V.A. Riziotis, and S. Voutsinas (National Technical University of Athens, Hellas), "GAST: A General Aerodynamic and Structural Prediction Tool for Wind Turbines." In *Proceedings of European Wind Energy Conference, EWEC 1997*, Dublin, Ireland, pp. 448–452, October 6–9 1997.

[237] V.A. Riziotis, and S.P. Voutsinas (National Technical University of Athens, Hellas), "Dynamic Stall on Wind Turbine Rotors: Comparative Evaluation Study of Different Models." In *Proceedings of European Wind Energy Conference, EWEC 1997*, Dublin, Ireland, pp. 481–484, October 6–9 1997.

[238] S.M. Rock, A.J. Eggers, P.J. Moriarty, and K. Chaney (RANN Incorporated, Palo Alto, CA), "Tradeoffs in Active Control of Aerodynamic Power and Loads on a HAWT Rotor." In *Proceedings of the 2000 AIAA/ASME Wind Energy Symposium*, Reno, NV, pp. 75–83, January 10-13, 2000.

[239] R.V. Rodenburg (Institute for Wind Energy, Delft University of Technology), "FOCUS, a design tool for structural optimization of rotor blades."

[240] R.V. Rodenburg (Institute for Wind Energy, Delft University of Technology), *FOCUS 3.0 manual*. Manual for the use of FOCUS 3.0, IW 94081R, November 1994.

[241] R.V. Rodenburg, C. Biever, and J.K. de Boer, "Design of the APX45/750 rotor blade with the integrated design tool FOCUS." In *Contributions European Union Wind Energy Conference, EUWEC 1996, Göteborg, Sweden*, IW-96106, pp. 37–40, May 1996.

[242] R.P.J.O.M. van Rooij, and W.A. Timmer, *Aerodynamic design of the APX-45 and APX-48 rotors*. Delft University of Technology, Institute for Wind Energy, IW 97.129 R, 43p., Oktober 1997.

[243] D.E. Rosenthal, and M.A. Sherman (Symbolic Dynamics, Inc., California), "High Performance Multibody Simulations via Symbolic Equation Manipulation and Kane's Method." In *Journal of the Astronautical Sciences*, Volume 34, No. 3, pp. 223–239, July-September, 1986.

[244] S. Rozendaal, "De Windoorlog." In *Elsevier*, pp. 108–111, 7 October 2000.

[245] S.A. de la Salle, D. Reardon, W.E. Leithead, and M.J. Grimble (Industrial Control Unit, Department of Electronic and Electrical Enginering, University of Strathclyde, Scotland, United Kingdom), "Review of wind turbine control." In *International Journal of Control*, Volume 52, No. 6, pp. 1295–1310, 1990.

[246] M.S. Sarma, *Synchronous Machines - Their Theory, Stability, and Excitation Systems*. Gordon and Breach, Science Publishers, Inc., New York, 582p., 1979.

[247] T. Sarpkaya, and M. Isaacson, *Mechanics of Wave Forces on Offshore Structures*, Van Nostrand Reynold Company, 651p., 1981.

[248] R.M. Saunders, "Synchronous-machine standstill frequency-response test data analysis", In *IEEE Trans. on Energy Conversion*, Vol. 6, No. 3, pp. 564–571, 1991.

[249] Scadas II User Manual (Version 8906 Rev. 9111), Difa Measuring Systems B.V., P.O. Box 3132, 4800 DC, Breda, The Netherlands, 1991.

[250] D.B. Schaeter, D.A. Levinson, and T.R. Kane, *Autolev user's manual*. Online Dynamics, Inc. Sunnyvale, CA 94087, United States of America, 1991.

[251] J.G. Schepers, H.J. van Grol, and H. Snel (ECN), *Kwalificatie rekenpro-gramma's horizontale as turbines (KRH)*. Report ECN-89-96, Petten, The Netherlands, June 1989.

[252] W. Schiehlen (Editor), *Multibody Systems Handbook*. Springer Verlag, Berlin Heidelberg, 432p., 1990.

[253] W. Schiehlen, *Anleitung Programmsystem NEWEUL*, Institut B für Mechanik, Universität Stuttgart, Pfaffenwaldring 9, 70550, Stuttgart, 79p.

[254] S.C.S. Technical Committee on Model Credibility, "Termininology for model credibility." In *Simulation*, Volume 32, pp. 103–104, 1979.

[255] SD/FAST Interface. The MathWorks, Inc., 18p., May 1994.

[256] R. Serban, and J.S. Freeman, "Identification and Identifiability of Unknown Parameters in Multibody Dynamic Systems." In *Multibody System Dynamics*, Volume 5, pp. 335–350, 2001.

[257] A.A. Shabana, "Flexible Multibody Dynamics: Review of Past and Recent Developments." In *Multibody System Dynamics*, Vol. 1, Issue 2, pp. 189–222, June 1997.

[258] A.A. Shabana, "Substructure synthesis methods for dynamic analysis of multi-body systems." In *Computers and Structures*, Vol. 20, No. 4, pp. 737–744, 1985.

[259] D.J. Sharpe (CREST, Loughborough University, United Kingdom), "Basic wind turbine aerodynamics." In *Wind Power Technology Course*, Centre for Renweable Energy Systems Techmology, Loughborough University, United Kingdom, 29 June - 3 July 1998.

[260] Shell International Limited, *The Evolution of the World's Energy Systems*, 7p., 1996.

[261] D.G. Shepherd, "Wind Power." In *P. Auer - Advances in Energy Systems and Technology*, Volume 1, Academic Press, New York, pp. 2–124, 1978.

[262] Y. Shimizu, H. Imamura, S. Matsamura, T. Maeda (Department of Mechanical Engineering, Mie University, Tsu-shi, Mie-ken, Japan) and G.J.E. van Bussel (Institute for Wind Energy, Delft University of Technology, Stevinweg 1, The Netherlands), "Power augmentation of horizontal axis wind turbine by Mie (tip) vane: velocity distribution around tip of HAWT blade with and without Mie (tip) vane." In *Proceedings of the 16th Annual Energy - Sources Technology Conference and Exhibition*. Houston, Texas, United States of America, Solar Energy Division, SED-Volume 14, pp. 143–148, ASME 1993.

[263] M. Shinozuka, and C.-M. Jan, "Digital Simulation of Random Processes and its Applications." In *Journal of Sound and Vibration*, Volume 25, No. 1, pp. 111-128, 1972.

[264] SIMULINK, *Using SIMULINK- version 4.1.* The Mathworks Inc., Natick, MA, United States of America, 6 April 2001.

[265] J.D. Smith, *Vibration Measurement and Analysis.* Butterworths & Co. (Publishers) Ltd., 166p., 1989.

[266] H. Snel (Netherlands Energy Research Foundation ECN), "Heuristic Modelling of Dynamic Stall Characteristics." In *Proceedings of European Wind Energy Conference, EWEC 1997*, Dublin, Ireland, pp. 429-433, October 6–9 1997.

[267] H. Snel (Netherlands Energy Research Foundation ECN), "Review of the Present Status of Rotor Aerodynamics." In *Wind Energy*, Volume 1, pp. 46–69, 1998.

[268] H. Snel (Netherlands Energy Research Foundation ECN), R. Houwink, J. Bosschers, W.J. Piers (National Aerospace Laboratory NLR), G.J.W. van Bussel, and A. Bruining (Delft University of Technology) "Sectional prediction of 3D-effects for stalled flow on rotating blades and comparison with measurements." In *Proceedings of European Community Wind Energy Conference 1993*, Lübeck-Travemünde, Germany, pp. 395–399, March 8–12 1993.

[269] H. Snel and J.G. Schepers (Netherlands Energy Research Foundation ECN), *Engineering models for dynamic inflow phenomena.* ECN report ECN-RX-91-064, 9p., June 1991.

[270] H. Snel and J.G. Schepers (Netherlands Energy Research Foundation ECN), "Investigation and Modelling of Dynamic Inflow Effects." In *Proceedings of European Community Wind Energy Conference 1993*, Lübeck-Travemünde, Germany, pp. 371–375, March 8–12 1993.

[271] H. Snel and J.G. Schepers (Netherlands Energy Research Foundation ECN), *Joint investigation of dynamic inflow effects and implementation of an engineering method.* ECN-C-94-107, 326p., April 1995.

[272] H. Snel and J.G. Schepers (Netherlands Energy Research Foundation ECN), *Joint investigation of dynamic inflow effects and implementation of an engineering method for response calculations.* PE-Memo-91-26, 17p., June 1991.

[273] H. Snel and J.G. Schepers (Netherlands Energy Research Foundation ECN), *Short description of aerodynamic research in the Joule dynamic inflow projects and of the results obtained.* ECN-R-93-014, 11p., September 1993.

[274] H. Snel, R. Houwink, and J. Bosschers (Netherlands Energy Research Foundation ECN), *Sectional prediction of lift coefficients on rotating wind turbine blades in stall.* ECN-C-93-052, 72p., December 1994.

[275] H. Snel, and C. Lindenburg (Netherlands Energy Research Foundation ECN), *PHATAS-II: Program for horizontal axis wind turbine analysis and simulation, version II - aero-elastic modeling.* ECN-C-92-027, 73p., May 1992.

[276] Y.D. Song, "Control of Wind Turbines Using Memory-Based Method." In *Proceedings of the American Control Conference*. Philadelphia, Pennsylvania, pp. 1715–1719, June 24–26, 1998.

[277] J.N. Sørensen, and M.O.L. Hansen (Department of Energy Engineering, Technical University of Denmark), "VISCWIND: A European Collaborate Effort on Viscous Effects of Wind Turbine Blades." In *Proceedings of European Wind Energy Conference, EWEC 1997*, Dublin, Ireland, pp. 440–443, October 6–9 1997.

[278] W. Spendley, G.R. Hext, and F.R. Himsworth, "Sequential application of simplex designs in optimization and evolutionary operation." In *Technometrics*, Volume 4, pp. 441-461, 1962.

[279] D.A. Spera (Editor), *Wind turbine technology: fundamental concepts of wind turbine engineering*. The American Society of Mechanical Engineers (ASME), 638p., 1994.

[280] D.A. Spera (Editor), *Wind turbine technology: fundamental concepts of wind turbine engineering - Chapter 5 - Aerodynamic Behavior of Wind Turbines*. The American Society of Mechanical Engineers (ASME), pp. 215–260, 1994.

[281] M. Steinbuch, *Dynamic modeling and robust control of a wind energy conversion system*. PhD. Thesis, Delft University of Technology, Faculty of Mechanical Engineering and Marine Technology, Measurement and Control group, November 1989.

[282] F.S. Stoddard (University of Massachusetts), "Momentum theory and flow states for windmills." In *Wind Technology Journal*, Volume 1, No. 1, pp. 3–9, Spring 1977.

[283] K. Stol, *Dynamics Modeling and Periodic Control of Horizontal-Axis Wind Turbines*, PhD. thesis, Department of Aerospace Engineering Sciences, Faculty of the Graduate School of the University of Colorado, 2001.

[284] H.J. Sutherland (Wind Energy Technology, Sandia National Laboratories, Albuquerque, New Mexico, United States of America), *On the Fatigue Analysis of Wind Turbines*". Sandia National Laboratories, SAND99-0089, 133p., June 1999.

[285] H.J. Sutherland, and P.S. Veers (Wind Energy Department, Sandia National Laboratories), "Fatigue Case Study and Reliability Analyses for Wind Turbines." In *1995 International Solar Energy Conference*, ASME/JSME/JSES, 7p., 1995.

[286] J. Svensson, *Grid-Connected Voltage Source Converter - Control Principles and Wind Energy Applications*. Technical report No. 331, Department of Electric Power Engineering, Chalmers University of Technology, Göteborg, Sweden, March 1998.

[287] System Identification Toolbox User's Guide. The MathWorks, Inc. August 1995.

[288] I. Szabó, *Geschichte der mechanischen Prinzipien*, Birkhäuser, Basel, 1977.

[289] K. Thomsen, F. Rasmussen, S. Øye, and S.M. Petersen (Risø National Laboratory, Roskilde, Denmark), "Loads and Dynamics for Stall Regulated Wind Turbines." Risø-R-655(EN), 43p., July 1993.

[290] W.A. Timmer, and R.P.J.O.M. van Rooij, *De profielgegevens voor de Aërodynamische Tabel Generator*. Sectie Windenergie, Faculteit Civiele Techniek en Geowetenschappen, Technische Universiteit Delft, rapport WE-011079, 30p., November 2001.

[291] O. Touhami, H. Guesbaoui, and C. Iung, "Synchronous Machine Parameter Identification by a Multitime Scale Technique." In *IEEE Trans. on Industrial Applications*, Volume 30, No. 6, pp. 1600–1608, 1994.

[292] M.A. Townsend (University of Virginia, Charlottesville, Virginia), "Kane's Equations, Lagrange's equations, and Virtual work." In *Journal of Guidance and Control*, Volume 15, No. 1, pp. 277–280, January-February 1992.

[293] C.T. Tran and D. Petot, "Semi-empirical model for the dynamic stall of airfoils in view of the application to the calculation of responses of a helicopter blade in forward flight." In *6th European Rotorcraft and Powered Lift Aircraft Forum*, Paper No. 48, Bristol, England, 1980.

[294] A. Tumageanian, and A. Keyhani, "Identification of synchronous machine linear parameters from standstill step voltage input data.", In *IEEE Trans. on Energy Conversion*, Vol. 10, No. 2, pp. 232–240, June 1995.

[295] P. Valk, "SD/FAST - Matlab 6.0 Interface." Mechanical Engineering Systems and Control Group, Delft University of Technology, The Netherlands, 6p., 19 July 2001.

[296] P.S. Veers, *Three-Dimensional Wind Simulation*. Sandia National Laboratories, SAND88-0152, March 1988.

[297] D. Veldkamp (NEG Micon), personal communication, May 15, 2001.

[298] A.T. Veltman, and P.P. Souillé (Netherlands Energy Research Foundation ECN), "Cost-performance of direct drive wind turbine generators." In *Proceedings of European Union Wind Energy Conference, EUWEC 1996*, Göteborg, Sweden, pp. 410–413, May 20–24, 1996.

[299] B. Visser (Stork Product Engineering), "The aero-elastic code FLEXLAST." In *Proceedings of the 28th IEA Meeting of Experts "State of the Art of Aerolelastic Codes for Wind Turbine Calculations"*, Technical University of Denmark, Lyngby, pp. 161-166, 11–12 April 1996.

[300] L.A. Viterna, and R.D. Corrigan (NASA Lewis Research Center, Cleveland, Ohio), "Fixed pitch rotor performance of large horizontal axis wind turbines." *Presented at DOE/NASA Workshop on large horizontal axis wind turbines*, Cleveland, United States of America, pp. 69–85, 1981.

[301] J.M. Vleeshouwers, *Synchronous machine identification by a simple step-response test.* PhD. Thesis, Eindhoven University of Technology, April 1998.

[302] S. Voutsinas (National Technical University of Athens, Hellas), personal communication, January 29, 1998.

[303] E. Walter, *Identifiability of state space models; with applications to transformation systems.* Series Lecture notes in biomathematics 46, Springer, Berlin, 202 p., 1982.

[304] F.H. Walter, S.L. Morgan, L.R. Parker Jr., and S.N. Deming, *Sequential Simplex Optimization.* Electronic reprint MultiSimplex AB "www.multisimplex.com", 404p., June 1999.

[305] W. Weaver, S.P. Timoshenko, and D.H. Young (Stanford University), *Vibration problems in engineering.* John Wiley & Sons, Inc., New York, 610p., 1990.

[306] B. Wilson (Oregon State University), *FAST-AD - An aerodynamics and dynamics analysis code for horizontal-axis wind turbines.* http://www.nrel.gov/wind/software/fastaddesc.html, 1p., 6 Februari 1998.

[307] R.E. Wilson, P.B.S. Lissaman, and S.N. Walker, *Aerodynamic Performance of Wind Turbines.* ERDA/NSF/04014-76/1, Washington, DC: U.S. Department of Energy, 1976.

[308] R.E. Wilson, and S.N. Walker, *Performance Analysis of Horizontal Axis Wind Turbines.* Corvallis, Oregon: Oregon State University, 1984.

[309] R.E. Wilson, S.N. Walker, and P. Heh (Department of Mechanical Engineering, Oregon State University, Corvallis), "Technical and user's manual for the FAST-AD advanced dynamics code." OSU/NREL Report 99-01, 185p., May 1999.

[310] Wind farm closes down after blade snaps. In *BBB NEWS - news.bbc.co.uk*, 23 January 2002.

[311] "Windmolens Eemshaven metaalmoe", In *De Telegraaf*, 18 September 1996.

[312] Windpower Monthly News Magazine, "Search archives", http://www.windpower-monthly.com/.

[313] G.D. de Winkel, P.A. Joosse, and D.R.V. van Delft, *STABTOOL project. Part: Determination eigenfrequencies of the APX70 rotor blade using FEM (confidential).* WMC group, Delft University of Technology, Report WMC 6-01-19, 26 June 2001.

[314] D. Winkelaar, "ROWS: Random Ocean Wave Simulator." ECN-x-xx-xxx, *In Preparation.*

[315] D. Winkelaar, "SWIFT: Program for the three dimensional wind simulation, Part 1: Model description and program verification." ECN-R-92-013, December 1992.

[316] P.Th.L.M. van Woerkom, "Modified dynamics modelling for maneuvering flexible space manipulators." In *Journal of Sound and Vibration*, Volume 179, No. 5, pp. 777–792, 1995.

[317] L.R. Brown, C. Flavin, H. French, J.N. Abramovitz, S. Dunn, G. Gardner, L. Mastny, A. Mattoon, D. Roodman, P. Sampat, M.O. Sheehan, and L. Starke, *State of the world 2001.* A Worldwatch Institute report on Progress Toward a Sustainable Society, Earthscan Publications Ltd, London, 275p., 2001.

[318] A.D. Wright (National Renewable Energy Laboratory, Golden, Colorado), "aero-elastic code development activities in the United States." In *Proceedings of the 28th IEA Meeting of Experts "State of the Art of Aerolelastic Codes for Wind Turbine Calculations"*, Technical University of Denmark, Lyngby, pp. 25-36, 11–12 April 1996.

[319] A.D. wright, N.D. Kelley, and R.M. Osgood (NREL), "Validation of a model for a two-bladed flexible rotor system: progress to date." In *Proceedings 1999 ASME Wind Energy Symposium AIAA/ASME*, Reno, Nevada, pp. 293–307, January 11–14 1999.

[320] A.D. Wright, C.E. Smith, R.W. Thresher, and J.L.C. Wang, "Vibration Modes of Centrifugally Stiffened Beams." In *Journal of Applied Mechanics*, Volume 49, pp. 197–202, March 1982.

[321] H.E. Wulff, *Traditional Crafts of Persia, Their Development, Technology, and Influence on Eastern and Western Civilization*, The MIT Press, Cambridge, Massachusetts, 304p., 1966.

[322] A. Yeznasni, R. Derdelinckx, and Ch. Hirsch, "Influence of dynamic stall in the aerodynamic study of a HAWT." In *Proceedings of Wind Energy: Technology and Implementation, EWEC 1991.* Amsterdam, The Netherlands, pp. 56–60, 1991.

Definitions

Aerofoil: Shape of a cross-section of a rotor blade.

Angle of attack (α): Angle between the resultant (or relative) wind velocity and the chord line of a blade section.

Aspect ratio (AR): Ratio of the rotor blade radius R to the average blade chord length $\bar{c}$ (large aspect ratio: $\bar{c}/R \ll 1$).

Capacity factor: The capacity factor is defined as the wind turbine's annual electricity yield (in kWh) divided by the electricity output if the turbine would have operated at its rated power output for the entire year (*i.e.* the installed power times 365 days times 24 hours). Reasonable capacity factors range from 0.25 to 0.30, while a very good capacity factor would be 0.40.

Capital cost: The capital cost include the purchase price, cost of transporting, assembling, and erecting a wind turbine on site, as well as the cost of installing grid lines and connecting the turbine to the grid.

Chord (c): Width of a cross-section of a rotor blade, *i.e.* local dimension perpendicular to the blade radius R.

Coherent gusts: Gusts of wind with dimensions larger than the rotor swept area, *see* non-coherent gusts.

Control system: Device of which the dynamics interact with the dynamics of a physical system (*e.g.* a wind turbine), and so have implications for the obtained performance.

Damping: Damping is the dissipation of energy with time or distance.

Degrees of freedom: The number of degrees of freedom of a mechanical system is equal to the minimum number of independent coordinates required to define completely the positions of all parts of the system at any instant of time. In general, it is equal to the number of independent displacements that are possible.

Downwind: Used to indicate that the rotor is placed at the back of the tower as seen from the main wind direction, *cf.* upwind.

Drive-train: Part of a wind turbine consisting of the rotor shaft, rotor inertia, transmission, and generator.

dSPACE: dSPACE$^®$ is a real-time system for data-acquisition, controller implementation, and hardware-in-the-loop (HIL) simulation.

Dynamic stall: Dynamic stall or stall hysteresis is a dynamic effect which occurs on aerofoils if the angle of attack changes more rapidly than the air flow around the blade (or blade element) can adjust to. The result is aerofoil lift and drag coefficients which depend not only on the instantaneous angle of attack (quasi-steady aerodynamics assumption), but also on the recent angle of attack history.

Euler-Bernoulli beam: A prismatic beam with length L, cross-section area $A = \pi \cdot R^2$, constant flexural rigidity EI, and uniformly distributed mass per unit length $\rho = m/L$, where m is the total mass of the beam. It is assumed that both the shear deformation and rotational inertia of the cross-sections are negligible if compared with bending deformation and translational inertia, respectively. This assumption leads to a good approximation if the beam is very slender (*i.e.* $R \ll L$).

External cost: Cost associated with damage and health to the environment with are not included in the electricity price, for example the cost due to greenhouse gas emissions which may cause global warming.

Extreme loads: Highest loads that are likely to be experienced by a wind turbine within its life-time (*i.e.* extreme operating conditions).

Fatigue loads: Dynamic loads that are experienced by a wind turbine repeatedly during its life-time (*i.e.* normal operating conditions).

Flap motion: Out-of-plane (elastic) bending of the blade, *i.e.* normal to the plane of rotation (*cf.* lead-lag motion).

Flexible body: A body in a system has to be treated as flexible when the rigid body assumption is not valid. In other words: the deformation of the body has a significant effect on the dynamic behavior of the system, *cf.* rigid body.

Generator: Device which converts mechanical power into electrical power.

Horizontal-axis wind turbine: Wind turbine of which the rotor shaft is substantially parallel to the wind flow, *cf.* vertical-axis wind turbine.

Hub: Fixture for attaching the blades or blade assembly to the rotor shaft.

Hub height (H): Height of the center of the horizontal-axis wind turbine rotor above the terrain surface.

Infinite bus: Voltage source of constant voltage and frequency.

Kinematics: The study of the geometry of motion. Kinematics is used to relate displacement, velocity, acceleration, and time without reference to the cause of the motion.

Lead-lag motion: In-plane (elastic) bending of the blade, *cf.* flap motion.

Leakage: Leakage is a problem which is a direct consequence of the fact that the Fast Fourier Transform (FFT) assumes that the discrete set of N point comes from a trigonometric polynomial of frequencies that are multiples of the sample frequency $f_s = \frac{1}{T}$. Thus the FFT assumes that the finite record of length T is periodic over the sampling interval chosen with period T. In general this will not be true, and leads to a problem known as leakage. Leakage leads to an overestimate of the damping. Leakage can be corrected to some degree by the use of a window function (*e.g.* Hanning window or Exponential window) which forces the signal to damp at the end of the time record. But windowing adds its own damping, causing additional leakage. Nevertheless, it is recommended that a window should always be used except when the signal is truly periodic in time, or the signal is a transient which has died away within the record length.

Load: Force or moment on a component (or section of a component) of a wind turbine.

MATLAB: MATLAB® is an integrated environment for numeric computation that specializes in working with matrices. With application specific toolboxes that cover (almost) everything from plant modeling to optimization. Powerful plotting routines are built in.

Multibody system: An approximation of a real mechanical system by a series of interconnected rigid and flexible bodies.

Nacelle: Housing which contains the stationary part of the generator (or: stator), and the ground plate at which the yaw mechanism has been placed. The nacelle mass equals the sum of the mass of the chassis (including yaw motor, yaw bearing, flanges *et cetera*) and the generator stator mass.

Non-coherent gusts: Gusts of wind with dimensions smaller than the rotor swept area, *see* coherent gusts.

Operation and maintenance (O&M) cost: The O&M cost include all troubleshooting, inspections, adjustments, retrofits, preventive as well as unscheduled maintenance performed on wind turbines, and the downtime that accumulates while waiting for parts, instructions, or outside services that are not available on site but are required to bring the turbine back in operation.

Particle: The most simple approximation of (an element of) a system is a free particle (or point mass). A particle is assumed to have no dimensions and accordingly can be treated as point in the three-dimensional space. In other words: it is assumed that the mass could be concentrated in one point, and that all forces act at that point (*i.e.* rotation about the mass center is neglected).

Pitch-flap flutter: Pitch-flap flutter is defined as the combined bending and torsional vibration of a rotor blade in steady air flow. It arises when the inertia axis (locus of the mass centers of the cross-sections along the blade) does not coincide with the elastic axis (locus of the shear centers, where a shear center is a point such that a shearing force passes through it produces pure bending and a moment about it produces pure torsion). Note that if the cross-section is symmetric, the shear center coincides with the mass center of the cross-section (assuming that the mass center is identical with the area center of the cross-section).

Point mass: *see* particle.

Power electronics: The task of power electronics is to process and control the flow of electric energy by supplying voltages and currents in a form that is optimally suited for user loads.

Reynolds number (Re): The Reynolds number is a dimensionless number that determines whether the flow around a wind turbine rotor blade (or blade element) is laminar or turbulent, and is defined as: $\text{Re} = (Wc)/\nu$, where W the relative wind velocity, c the local chord, and ν the kinematic velocity. The kinematic velocity is, in turn, defined as $\nu = \rho/\mu$ where ρ the density of air, and μ the dynamic viscosity. The Reynolds number can be interpreted as the ratio of inertial to viscous forces acting on the air flow. For air at standard, sea-level conditions, $\text{Re} = 69000\, Wc$. It is important to stress that aerofoil data used in rotor modeling must be near the correct Reynolds number, because otherwise accurate results cannot be expected.

Rigid body: A body in a system can be treated as rigid when the deformation is to small such that it can be neglected. For a rigid body, the distance between any two points on the body remains constant, and accordingly the kinematics of the rigid body is the same as the kinematics of its reference. The dynamic motion of a rigid body is described by a set of ordinary differential equations, *see* flexible body.

Rotational sampling: The phenomenon that air vortices, with dimensions smaller than the rotor swept area, are locally hit during each cycle by the rotation of the wind turbine blades.

SD/FAST: SD/FAST®, a product of Symbolic Dynamics, Inc., is a *general-purpose* multibody program whose function it is to create *special-purpose* simulation code employing explicit equations of motion for particular multibody configurations of interest. Computer symbol manipulation is used to simplify the general form of the equations of motion as appropriate to the system at hand (*i.e.* repeated terms are removed in order to arrive at the computationally simplest equations).

Any mechanical system that can be described as a collection of hinge-connected rigid bodies can be modeled in SD/FAST®. SD/FAST® generates the equations of motion describing the dynamic behavior of the system in either C or FORTRAN as requested, based on a user-written input file (sdinputs()), a system description file (System Description), and a user-written output file (sdoutputs()).

SIMULINK: SIMULINK® is an interactive environment integrated in MATLAB® for modeling, analyzing, and off-line simulation. It provides a graphical user interface for constructing block diagrams using drag-and-drop operations.

Solidity: The ratio of the total blade area to the swept area, *see* swept area.

Superelement: A superelement is a multibody approximation of a (part of a) flexible body consisting of three (describing bending only) or four (describing bending, axial deflection, and torsion) rigid bodies connected by ideal springs, and dampers.

Stall: Reduction of lift (or change in pitching moment or decrease in drag) associated with separation of airflow from the surface of the rotor blade.

Stall hysteresis: *see* dynamic stall.

Stiffness: Stiffness is the ratio of change of force (or torque) to the corresponding change on translational (or rotational) deflection of an elastic element.

Support structure: Part of a wind turbine comprising the tower (up to the yaw bearing) and the foundation.

Swept area (A): Area of the projection, upon a plane perpendicular to the wind velocity vector, of the disc along which the rotor blade tips move during rotation.

Theoretical modeling: In theoretical or fundamental modeling the relevant physical properties of the system are derived from first principles (*e.g.* conservation laws).

Tip loss: Loss of lift relative to 2-D aerodynamic profile data at the blade tip due to three-dimensional induced effects.

Total harmonic distortion (THD): Current or voltage THD is the root-sum-square of the harmonic components divided by the fundamental component.

Twist: Twist is applied to maintain the optimum angle of attack α, and hence the maximum lift coefficient C_l^{max}, constant along the rotor blade.

Unsteady aerodynamics: Wind turbines operate at all times in an unsteady environment. Two main areas can be discriminated: dynamic inflow and dynamic stall.

Upwind: Used to indicate that the rotor is placed in front of the tower as seen from the main wind direction, *cf.* downwind.

Validation: The process of determining whether or not the verified mathematical model of a system behaves similar to the real behavior associated with the intended model use.

Verification: The process of determining whether or not a computer simulation model is consistent with the underlying mathematical model to a specified accuracy level.

Vertical-axis wind turbine: Wind turbine of which the rotor shaft is vertical, *cf.* horizontal-axis wind turbine.

Wind Energy Conversion System (WECS): *see* wind turbine.

Windmill: System that converts kinetic energy in the wind into mechanical energy. The mechanical energy is typically used for grain-grinding, pumping water, and sawing wood. The term "windmill" comes from the fact that to "mill" means to grind.

Wind turbine: System that converts kinetic energy in the wind into electrical energy. Note that "turbine" in the definition of wind turbine is used as pars pro toto for the whole structure (*i.e.* from the rotor blades to foundation).

Wind Turbine Generator (WTG):   *see* wind turbine.

Glossary of symbols

Part I: Modeling of flexible wind turbines

Wind module:

V_w	Undisturbed wind velocity	[m/s]

Aerodynamic module:

$a = \frac{v}{V_w}$	Axial induction factor	[–]
a'	Tangential induction factor (represents induced swirl)	[–]
$A = \pi R^2$	Rotor swept area, or equivalently actuator disk area	[m^2]
AR	Aspect ratio of blade, $\frac{R}{c_{0.75}}$ (based at chord length at 75 % radius)	[–]
c	Local blade chord	[m]
C_d	Blade element drag coefficient	[–]
C_{dax}	Thrust coefficient	[–]
C_l	Blade element lift coefficient	[–]
C_m	Blade element moment coefficient	[–]
C_p	Power coefficient	[–]
C_t	Thrust coefficient	[–]
D	Rotor diameter	[m]
D	Drag force	[N]
D_{ax}	Rotor thrust or axial force on rotor	[N]
F	Force	[N]
F_{aero}	Aerodynamic forces	[N]
F_L	Effective total loss factor	[–]
F_{root}	Prandtl root-loss factor	[–]
F_{tip}	Prandtl tip-loss factor	[–]
H	Hub height	[m]
L	Length	[m]
L	Lift force	[N]
M	Pitching moment	[Nm]

Ma	Mach number	[–]
N_b	Number of rotor blades	[–]
N_s	Number of blade elements	[–]
p_0	Static pressure	[N/m^2]
P	Power extracted from the wind	[W]
q	Dynamic pressure	[N/m^2]
r	Radius of rotor blade section (*i.e.* local radius)	[m]
$R = \frac{1}{2}D$	Rotor radius	[m]
Re	Reynolds number	[–]
S	Cross-sectional area of cylindrical control volume	[m^2]
v	Axial induced wind velocity	[m/s]
V_{ax}	Wind velocity at rotor disk position	[m/s]
V_p	Local, undisturbed, perpendicular wind velocity	[m/s]
V_r	Rated wind velocity	[m/s]
V_t	Local, undisturbed, tangential wind velocity	[m/s]
V_w	Undisturbed wind velocity	[m/s]
V_∞	Wind velocity in the turbine wake	[m/s]
W	Local, undisturbed, aerodynamic wind velocity	[m/s]
$\dot{x}$	Velocity	[m/s]
α	Angle of attack of aerodynamic velocity	[deg]
ΔD	Element drag force	[N]
ΔF	Axial components of aerodynamic forces	[N]
ΔL	Element lift force	[N]
ΔQ	Tangential components of aerodynamic forces	[N]
Δr	Small section of rotor blade	[m]
θ	Pitch angle of rotor blade	[deg]
η_{ad}	Actuator disk efficiency	[–]
λ	Tip-speed ratio	[–]
μ	Dynamic viscosity	[Ns/m^2]
ν	Kinematic viscosity	[m^2/s]
ρ	Air density	[kg/m^3]
τ	Time constant	[s]
ϕ	Direction of aerodynamic velocity	[deg]
Φ_f	Net flow outside streamtube	[m^3/s]

Mechanical module:

A	Cross-sectional area	[m^2]
c	Torsional spring constant	[Nm/rad]
C	Torsional spring constant	[Nm/rad]
$C_{1,\cdots,4}$	Constants	[–]
D	Diameter	[m]

E	Modulus of elasticity	[N/m^2]
f_s	Sample frequency	[Hz]
F	Force, load	[N]
F_{aero}	Aerodynamic forces	[N]
G	Shear modulus of elasticity	[N/m^2]
h	Local flexible body height	[m]
I	Area moment of inertia about an axis	[m^4]
I_p	Polar moment of inertia of the cross-section	[m^4]
k	Partitioning coefficient	[–]
K	Viscous damping coefficient	[kg/s]
L	Length	[m]
L_{fb}	Flexible body length	[m]
L_{se}	Superelement length	[m]
m	Mass	[kg]
M	Mass	[kg]
M	Bending moment, couple	[Nm]
N_b	Number of rotor blades	[–]
N_{dof}	Number of degrees of freedom	[–]
N_{iter}	Number of iterations	[–]
N_{rb}	Number of rigid bodies	[–]
N_{se}	Number of superelements	[–]
r	Radius of rotor blade section (*i.e.* local radius)	[m]
R	Radius	[m]
t	Wall thickness	[m]
T_{em}	Electromechanical torque	[Nm]
v	Transverse displacement ($v \perp y$)	[m]
$\dot{x}$	Velocity	[m/s]
y	Distance from the origin	[m]
Y	Mode shape	[–]
δ	Total deflection (*i.e.* deflection @ $y = L$)	[m]
$\Delta \omega_f$	Relative frequency shift	[%]
η	Dimensionless rotation rate	[–]
θ	Total angle of rotation (*i.e.* angle @ $y = L$)	[rad]
ν	Poisson's ratio	[–]
ρ	Mass density	[kg/m^3]
ω_m	Mechanical rotational speed	[rad/s]
ω_n	Natural frequency	[rad/s]

Electrical module:

c	Constant	[–]
$\mathbf{C}$	Transformation matrix	[–]

f	Frequency	[Hz]
f_s	Sample frequency	[Hz]
i	Current	[A]
i_a, i_b and i_c	Stator current of the a-phase, b-phase, and c-phase	[A]
i_d	Direct-axis current	[A]
i_f	Field-winding current	[A]
i_q	Quadrature-axis current	[A]
L	Inductance (H=kg·m^2/(A^2·s^2))	[H]
$\mathbf{L}$	Inductance matrix	[H]
L_d	Direct-axis synchronous inductance	[H]
L_0	Zero-sequence inductance	[H]
L_q	Quadrature-axis synchronous inductance	[H]
$\mathbf{L_{rr}}$	Rotor self-inductance matrix	[H]
$\mathbf{L_{ss}}$	Stator self-inductance matrix	[H]
$\mathbf{M_{rs}}$	Rotor-stator mutual inductance matrix	[H]
$\mathbf{M_{sr}}$	Stator-rotor mutual inductance matrix	[H]
n	Rotor speed	[r.p.m.]
p	Number of pole-pairs	[–]
P_{elec}	Electrical power	[W]
R	Initial magnetic state	[]
$\mathbf{R}$	Resistance matrix	[Ω]
R_a, R_b and R_c	Stator resistance of the a-phase, b-phase, and c-phase	[Ω]
R_{1d}	Direct-axis damper resistance	[Ω]
R_f	Field-winding resistance	[Ω]
R_{1q}	Quadrature-axis damper resistance	[Ω]
R_s	Stator-winding resistance	[Ω]
S	Switch	[0,1]
t	Time	[s]
$\mathbf{T}_{0dq}$	Park's power-invariant transformation matrix	[–]
T_{em}	Electromechanical torque	[Nm]
u_a, u_b and u_c	Stator voltage of the a-phase, b-phase, and c-phase	[V]
u_d	Direct-axis voltage	[V]
u_{1d}	Direct-axis damper winding voltage	[V]
u_f	Field-winding voltage	[V]
u_q	Quadrature-axis voltage	[V]
u_{1q}	Quadrature-axis damper winding voltage	[V]
U_{dc}	DC link voltage	[V]
ϵ_a	Current error of phase a	[A]
η_{conv}	Frequency converter efficiency	[–]
θ_e	Angle between the direct-axis and the magnetic axis of phase a	[deg]
ψ_a, ψ_b and ψ_c	Stator flux linkages of the a, b, and c-phase	[Vs]
ψ_d	Direct-axis stator flux	[Vs]

ψ_{1d}	Direct-axis damper flux	[Vs]
ψ_f	Direct-axis field winding flux	[Vs]
ψ_q	Quadrature-axis stator flux	[Vs]
ψ_{1q}	Quadrature-axis damper flux	[Vs]
ω_m	Mechanical rotational speed	[rad/s]
Δi	Width hysteresis band	[A]

Wave module:

d	Water depth	[m]
D	Cross-section dimension	[m]
g	Gravity constant	[m/s^2]
H	Wave height	[m]
L	Wave length	[m]
T	Wave period	[s]

Part II: Model validation issues

Model verification, validation and model parameter updating:

A1, $\cdots$, A7	Accelerometer locations	
A	State or system matrix $(n \times n)$	
B	Input matrix $(n \times r)$	
C	Output matrix $(p \times n)$	
$C(q,t)$	Generalized stiffness matrix	
D	Direct feedthrough matrix $(p \times r)$	
A, B, C, D, F	Polynomials in the delay operator q^{-1}	
$e(t)$	White noise signal	
e_{oe}	Output error	
$e_{sim}(t)$	Simulation error	
Ex	Mathematical expectation of the random vector x	
F_{cable}	Force in TWARON cable	
F_{obj}	Objective function	
$G(q)$	Input-output transfer function	
H	Hessian	
$H(s)$	Transfer function	
$H(q)$	Noise transfer function	
$H(\omega)$	Frequency response function	
$\mathbf{I_n}$	Identity matrix of size $(n \times n)$	
j	Imaginary number	

J	Mass moment of inertia
k	Viscous damper coefficient
$K(q, \dot{q}, t)$	Generalized coriolis/centripetal array
l	Length
L	Length
L	Lagrangian ($L = T - U$)
m	Mass
$M(q, t)$	Generalized inertia matrix
$\mathcal{M}$	Model class
M_{gof}	Measure of the "goodness" of fit
$M(\theta)$	Specific model
n	Number of tunable parameters
n	Number of states
$n_{a,b,c,d,f}$	Orders of the polynomials A, B, C, D, and F respectively
n_k	Number of delays from input to output
N	Number of datapoints
$\mathbb{N}$	Set of natural numbers
p	Number of outputs
q	Generalized coordinate
q^{-1}	Delay operator
Q	Nonconservative forces
r	Number of inputs
$\mathbf{R_n}$	Toeplitz matrix
$\mathbb{R}$	Set of real numbers
$\mathbb{R}^+$	Subset of positive real numbers
s	Laplace variable
$\mathsf{S1}, \cdots, \mathsf{S7}$	Sensor locations
t	Time
T	Final time
T	Kinetic energy
U	Potential energy
$u(t)$	Input signal
$v(t)$	Disturbance signal
$V_N(\theta)$	Criterion value
x_0, x_1, x_2	Vertices (or points) forming a Simplex
$y(t)$	Output signal
y_{diff}	Difference (or error) between measured and simulated output
y_{meas}	Measured output
y_{sim}	Simulated output
$\hat{y}(t\vert t-1, \theta)$	One-step ahead prediction error
$Y_d(s)$	Direct-axis transfer function
$\epsilon(t)$	Prediction error
$Y_q(s)$	Quadrature-axis transfer function

Z_N	Data set $(i.e. = \{y(1), u(1), y(2), u(2), \cdots, y(N), z(N)\})$
α	Angle of TWARON cable with horizontal
Δ	Deviation
θ	(Physical) parameter vector
θ_0	Real parameter vector
$\hat{\theta}$	Estimated parameter vector
λ	Variance of the white noise signal $e(t)$
Π	Parametrization, mapping
∇	Gradient vector
ω_n	Undamped natural frequency
$\|\cdot\|$	Euclidian norm

Part III: Model based control design

Model based control design:

C	Controller
e	Error signal
F	Filter
L	Loop gain
P	Plant
P	Rotor power
P_{ci}	Start power
P_r	Rated aerodynamic power
r	Reference signal
P	Rotor power
P_{ci}	Start power
P_r	Rated aerodynamic power
r	Reference signal
S	Sensitivity function of the closed-loop system
T	Complementary sensitivity function of the closed-loop system
u	Input signal
v	Disturbance
V_{ci}	Cut-in wind velocity
V_{co}	Cut-out wind velocity
V_r	Rated wind velocity
V_w	Undisturbed wind velocity
y	Measured output
λ	Tip-speed ratio

Subscripts:

a	Axial
ad	Actuator disk
$aero$	Aerodynamic
a, b, c	a-phase, b-phase, and c-phase
$apx45$	APX-45 rotor blade
$apx48$	APX-48 rotor blade
b	Blade
$bottom$	Bottom of beam/tower
$b2j$	Bodytojoint
c	Chassis
$cable$	(TWARON) cable
co	Cutoff
$conv$	Frequency converter
cu	Copper
C_g	Center of gravity
d	Direct-axis
d	Drag
dax	Thrust
$diff$	Difference
dc	Direct current
d, q, o	Direct-axis, quadrature-axis, and zero-sequence
$e, elec$	Electrical
em	Electromechanical
eq	Equivalent
f	Field or excitation winding
f	Final
f	Foundation
fb	Flexible body
F	Load
Fe	Iron
$fric$	Friction
g	Generator
gof	Goodness of fit
$iter$	Iterations
l	Lift
m	Mechanical
min	Minimum
max	Maximum
$meas$	Measured
M	Bending moment, couple
obj	Objective

oe	Output error
opt	Optimal
O	Point about pin joint rotates
p	Perpendicular
p	Polar (moment of inertia)
p	Power
pi	Proportional-integral
q	Quadrature-axis
r	Rated
rb	Rigid body
s	Stator
se	Superelement
set	Set-point value
sim	Simulated
sp	Spacer
st	Steel
t	Tangential
t	Tower
T	Tower
top	Top of beam/tower
$x,\ y,\ z$	x-axis, y-axis, and z-axis
0	Real value
$1d$	Direct-axis damper
$1q$	Quadrature-axis damper

Superscripts:

DC	Steady-state (or DC) value
m	Mechanical
r	Rotor
r	Rated
s	Stator
set	Set-point value
ss	State-space
th	Threshold
wt	Wind turbine
-1	Inverse
2-D	2-dimensional
3-D	3-dimensional
$\dot{x}$	Derivative w.r.t. time $\left(\frac{dx}{dt}\right)$
$v',\ v''$	Derivative w.r.t. place $\left(\frac{dv}{dy},\ \frac{d^2v}{dy^2}\right)$
$^-$	Average value

ˆ	Estimate
+	Positive
∗	Non-dimensional

Acronyms and abbreviations:

AC	Alternating current
A.D.	Anno Domini
A/D	Analogue-to-digital
ADAMS/WT	Automatic Dynamic Analysis of Mechanical Systems - Wind Turbine
Aerpac	Aerodynamic Products and Consultancy
ARX	Autoregressive with external input
ATG	Aërodynamische Tabel Generator
B.C.	Before Christ
BEM	Blade-Element-Momentum theory
BFGS	Broyden-Fletcher-Goldfarb-Shanno
CAD	Computer Aided Design
CC	Capital cost
CCGT	Combined cycle gas turbine
cf.	Confer (compare)
CFD	Computational Fluid Dynamics
CoE	Total cost of electricity
COS	Continuous System
CPU	Central processing unit
DAE	Differential-algebraic equations
DC	Direct current
DFP	Davidon-Fletcher-Powell
DNS	Direct Numerical Simulation
DOF	Degrees of freedom
DSP	Digital Signal Processor
DUWECS	Delft University Wind Energy Convertor Simulation program
DUWIND	Delft University Wind Energy Research Institute (*see* www.duwind.tudelft.nl)
ECN	Dutch Energy Research Foundation
EEZ	Exclusive Economic Zone
e.g.	Exempli gratia (for example)
ELL	Elliptical
EMF	Electromagnetic force
FAROB	Fatigue rotor blades (part of FOCUS)
FAST	Fatigue, Aerodynamics, Structures, and Turbulence

FCR	Annual fixed charge rate
FES	Finite Element System
FFT	Fast Fourier Transform
FIR	Finite impulse response
FLEXLAST	Flexible load analysing simulation tool
FOCUS	Fatigue Optimization Code Using Simulations
FOS	First-Order-System
FRF	Frequency response functions
GAROS	General Analysis of ROtating Structures
GAST	General Aerodynamic and Structural Prediction Tool for Wind Turbines
GRE	Glass fibre reinforced epoxy
GUI	Graphical User Interface
HIL	Hardware-in-the-loop
HMBS	Hybrid Multibody System
ICC	Installed capital cost
i.e.	Id est (that is)
IEC	International Electrotechnical Commission
IIR	Infinite impulse response
IGBT	Insulated gate bipolar transistor
I/O	Input-output
ISD	Inertia-Spring-Damper system
JONSWAP	Joint North Sea Wave Project
KC	Keulegan-Carpenter number
kW	Kilowatt
LES	Large Eddy Simulation
LRC	Levelized replacements cost
LS	Least-squares
LTI	Linear, time invariant
LVDT	Linear variable differential transducers
LW	Lagerwey
MATLAB	Matrix laboratory
MBS	Multibody System
MDI	Mechanical Dynamics Inc.
MESC	Mechanical Engineering Systems and Control Group
MIMO	Multi-input-multi-output
ML	Maximum-likelihood
MW	Megawatt
MSD	Mass-Spring-Damper system
MSR	Modified step-response test
NACA	National Advisory Committee for Aeronautics
NAG	Numerical Algorithms Group

NIMBY	Not-in-my-backyard
NM	Nelder-Mead
NREL	National Renewable Energy Laboratory
NSW	Near Shore Wind Farm
OOC	Other operating cost
ODE	Ordinary differential equations
OECD	Organisation for Economic Co-operation and Development
O & M	Operation and maintenance cost
ONERA	Office National d'Etudes et de Rechereche Aérospatialers
PC	Personal Computer
PHATAS-III	Program for Horizontal Axis wind Turbine Analysis and Simulation
PI	Proportional-integral
PID	Proportional-integral-derivative
PMC	Preventive maintenance cost
PSD	Power spectral density
PWM	Pulse-width modulation
RIM	Resin-infusion moulding
RK	Runge-Kutta
ROWS	Random Ocean Wave Simulator
SCS	Society for Computer Simulation
SDOF	Single-degree-of-freedom
SG	Synchronous generator
SISO	Single-input-single-output
SITB	Graphical user interface to the System Identification Toolbox
SL-DUT	Stevin Laboratory of Delft University of Technology
S/N-ratio	Signal-to-noise ratio
SPE	Stork Product Engineering
SSFR	Standstill frequency response
SWIFT	Simulation of wind fields in time
SWING	Stochastic WINd Generator
SWL	Still water level
THD	Total harmonic distortion
TNO	Netherlands Organization for Applied Scientific Research
UMC	Unscheduled maintenance cost
UNIWEX	UNIversal Wind turbine for EXperiments
US	Ultra sharp
VOC	Verenigde Oost-Indische Compagnie
VSC	Voltage-source converter
YawDyn	Yaw Dynamics computer program
2-D	2-dimensional
3-D	3-dimensional

Index

Samenvatting

De windindustrie heeft zich in de afgelopen decennia ontwikkeld van een niche markt tot een van de meest aantrekkelijke vormen van duurzame energie. Wind heeft de capaciteit om in een belangrijk deel van de wereldwijde vraag naar elektriciteit te voorzien mits de kostprijs per kilowattuur verder wordt gereduceerd. De kosten per kilowattuur kunnen effectief gereduceerd worden door enerzijds het ontwerp verder te verbeteren en anderzijds de besturing te optimaliseren aangezien de conversie van windenergie in elektriciteit een kapitaalintensive en onderhoudseisende technologie is.

De uitdaging aan het onderzoek naar windenergie is het ontwikkelen van windturbines die geoptimaliseerd zijn met betrekking tot kosten en prestatie. Een noodzakelijke voorwaarde voor het ontwikkelen van zulke kosten-effectieve windturbines is het beschikbaar zijn van een methodiek die het mogelijk maakt tijdens de ontwerpfase snel en eenvoudig accurate modellen te genereren op basis van de dan aanwezige informatie. Deze modellen kunnen gebruikt worden om de invloed van bepaalde ontwerpkeuzes op de kosten-effectiviteit te evalueren en vervolgens het integrale turbine gedrag van de gekozen configuratie onder uiteenlopende (extreme) omstandigheden te onderzoeken en, indien nodig, te verbeteren.

In dit proefschrift is een dergelijke methodiek ontwikkeld voor het modelleren van de klasse van turbines die het grootste potentieel heeft kosten-effectiviteit in de (nabije) toekomst te realiseren. De validiteit van de methodiek is beoordeeld aan de hand van experimenten uitgevoerd aan een direct aangedreven synchrone generator, diverse rotor bladen en aan de Lagerwey LW-50/750 windturbine. Daarnaast is de eerste stap gezet in het gebruiken van de ontwikkelde modellen voor regelaarontwerp. De ontwikkelde methodiek is geïmplementeerd in een gebruikersvriendelijk ontwerppakket dat DAWIDUM genoemd is. DAWIDUM is ontwikkeld in de MATLAB®/SIMULINK® omgeving.

Geconcludeerd kan worden dat in dit proefschrift een basis is gelegd voor het geïntegreerd ontwerpen en bedrijven van kosten-effectieve variabel toeren windturbines.

Abstract

In the past decades, the wind industry has grown from a niche business serving the environmental aware into one that has established itself as the most competitive form of renewable energy. Wind has the potential to play a more important role in the future world electricity supply provided that the cost per kilowatt-hour are further reduced. The cost of wind-generated electricity can be effectively reduced by steady improvements in both wind turbine design and operation since the conversion of wind energy into electricity is a highly capital-intensive and maintenance-demanding technology.

The challenge of wind energy research lies in developing wind turbines that are optimized with respect to both cost and performance. A prerequisite for the cost-effective design of such turbines is the availability of a systematic methodology that generates accurate and reliable dynamic models of the complete system within the design phase with relatively low modeling effort. The models, in turn, can be used to evaluate the impact that the design choices have on the economic viability. Subsequently, the dynamic behavior of the selected wind turbine configuration can be assessed under various (extreme) conditions and, when required, improved.

In this thesis such a methodology has been developed for the class of wind turbines that has the highest potential to reach cost-effectiveness in the (near) future. The validity of the methodology has been judged by means of experiments performed on a direct-drive synchronous generator, various rotor blades, and a full-scale wind turbine. In addition to this, the first step is made in using the developed models for control design. The developed methodology has been implemented in a user-friendly design code called DAWIDUM. DAWIDUM has been developed in the MATLAB®/SIMULINK® environment.

It can be concluded that in this thesis the basis has been laid for the cost-effective design and operation of variable speed wind turbines.

Curriculum vitae

David-Pieter Molenaar was born on November 23, 1971 in Middelie, The Netherlands.

1984–1990	Pre-University Education (VWO) at St.-Ignatiuscollege, Purmerend, The Netherlands.
1990–1996	MSc. student with the Mechanical Engineering subfaculty of Delft University of Technology, The Netherlands. Prior to the MSc. project at the Mechanical Engineering Systems and Control Group (MESC) a teaching practice has been done at the Automatic Control Group of Linköping University, Sweden. Title MSc. project: "Modeling and control of the NedFlex wind turbine." This project has been carried out at Stork Product Engineering, Amsterdam, The Netherlands.
1996–2003	Ph.D. student with Mechanical Engineering Systems and Control Group of Delft University of Technology, The Netherlands. This work is sponsored by Stork Product Engineering and Lagerwey The Windmaster b.v.
1/7/2001–11/4/2002	Part-time employed with Siemens N.V., The Netherlands. Responsible for the design of a cost-effective support structure for both the Enron Wind EW-1.5 and EW-3.6 wind turbine for the North Sea Wind Power (NSWP) project.